



Performance improvement of electrochemical capacitors through the integration of advanced materials and the cell configuration assessment



Doctoral Thesis
By
Tandra Panja

eman ta zabal zazu



Universidad del País Vasco Euskal Herriko
Unibertsitatea

Universidad del País Vasco
University of Basque Country

Facultad de Ciencia y Tecnología
Faculty of Science and Technology

Departamento de Química Inorgánica
Inorganic Chemistry Department

**Performance improvement of electrochemical
capacitors through the integration of advanced
materials and the cell configuration assessment**

*A dissertation submitted to the University of the Basque Country in partial fulfilments
of the requirements for the degree of Ph.D in Material Science and Technology*

By

Tandra Panja

Thesis supervisors:

Dr. Daniel Carriazo Martín

Dr. Eider Goikolea Núñez

Vitoria-Gasteiz, August 2020

DECLARATION

I, Tandra Panja, hereby declare that the research works presented in this thesis are original and carried out by me. Some of the works has been published in international journals as mentioned in “List of contributions” and the credit has been given to all the co-authors. The remaining works will be published in near future.

ACKNOWLEDGEMENTS

I would like to convey my deepest appreciation to my advisors, *Dr. Daniel Carriazo*, and *Dr. Eider Goikolea* for their constant guidance, encouragement, tremendous support, and understanding of my research work throughout the entire period of my Ph.D. study. I offer my sincere appreciation to both for their enormous effort to shape my scientific vision properly.

Daniel's calm nature made me realize that patience is highly essential in research to step into the next level. He has motivated me on how to make a decision when the situation is critical. His skillful guidance, innovative ideas and stoic patience are truly appreciable. On other side, *Eider* is not only a strong self-made woman but also a wonderful supervisor. Her continuous suggestion and motivations have inspired me to push my limits and explore new ideas. It's not only her careful supervision but also her care and affection that have given me a lot of confidence to proceed smoothly during this doctoral journey. It is my honor to have the chance to learn from them.

I am also grateful to the Spanish ministry of Science and Innovation (MINECO/FEDER) (RTI2018-096199-B-I00 and MAT2015-64617-C2-2R) and the Basque Government (Elkartek 2018) for the financial support to continue my research work and the CIC energiGUNE for this predoctoral position. This PhD thesis represents not only my research work but also the imperishable job experience of three- and half year with Electrochemical Energy Storage (EES) research groups at CIC. This professional journey helped to broaden my knowledge and also strengthen my self-esteem to work under such a diverse and multicultural environment. I'm highly obliged to CIC for this amazing journey. My sincere thanks also go to all the brilliant researchers I've met here who co-operated to develop my scientific interest in the different research fields. I would like to express my special thanks to *Jon Ajuria* for his kind help and advice not only on the research work and scientific paper but also in personal life too. In addition, I would also like to thank *Roman Mysyk* his expertise and thoughtful criticism which helped me to improve my work. A special acknowledgement goes to my darlings, *María Arnaiz*, and *María Echeverría* for their continuous assistance in experiments and measurements during my research work. I enjoyed the time we spent together by sharing our random thoughts. Besides, *Juan Luis*, *Marína*, *Cristina B.*, *Gelines*, *María J.*, *Fran*, *Alvaro*, *Agnieszka*, *Jakub*, and *Elena G.* has also

Acknowledgement

shown me their friendly behavior which made me extremely comfortable to work with them. I hope I can remember all of you!! I hope, you all will be there whenever I take a trip down my memory lane by visualizing the labs, corridors, cafeteria, office desks and those wonderful small occasions we celebrated in CIC.

When I arrived in Europe could not even imagine that my Indian colleagues and friends from Vitoria-Gasteiz would be keeping me company for next years with their genuine kindness and support. Thank you, *Roshan, Mona, Nithi, Sona, Ram* and *Nivi* for making my life easier here. I am grateful to have been to spend this memorable time in with all you people.

My joy knows no bounds in expressing my cordial thanks to my best friends *Udipta* and *Sreejan* for their constant love and support. I wish to stay as such with them for rest of my life.

Above ground, I am indebted to my parents and brother for their endless encouragements to pursue my dreams. Without my family's constant support and understanding, chasing a big dream wouldn't be possible. Their unconditional love and sacrifice helped me to reach this far. *Baba & Maa*, thank you for the freedom you gave me without thinking about the typical societal norms and taught me how to fight against all the discriminations. Words can't express the gratitude of my feelings when I think about what you all have done for me. Besides, I would also like thank to my other family members (in-laws) for their substantial moral support throughout this journey.

Most importantly, it's my privilege to thank my husband and my also colleague, *Dhrubajyoti* for pushing me to stand up for what I believe in. I owe his constant support, tolerance, understanding that he has offered me every single day until now. You were always there when I thought that it is impossible to continue, you assisted me to keep things in perspective. I won't be this stronger without you as my inspiration. Now, I believe on your words, "destiny decides destinations". Indeed, it is....

At the end and foremost of all, I wholeheartedly appreciate my baby boy, *Shreyash* for accepting my busy working schedule and the patience that he showed during the completion of my thesis. I've experienced your struggle when I was not there around you. I appreciate this more than you'll ever know. You are and always will be the most precious to me no matter what comes on my way. I consider myself truly fortunate in this world to have you in my life.

SUMMARY

To overcome fossil fuel exhaustion and global warming, renewable energy resources are taking lead to protect the environment and the global economy. The qualities of renewable energy generation are often surpassed by their intermittent nature and uneven geographic distribution, thus the development of clean energy technologies such as energy conversion and storage is considered as the most possible conservation choice for the development of sustainable energy policies to fulfil the worldwide demand. At present, the main challenge is in the technology development process by focusing on the improvement of their performances, stability, life expectancy, safety, and cost with the specific accents according to the application.

In this regard, electrochemical capacitors or supercapacitors are envisioned as potential next-generation energy storage systems because of their excellent storage capacity, power density, and long-term durability. However, all these advantages are overshadowed by their poor energy density. Therefore, currently, several efforts and research are aimed at the development of high-energy supercapacitor without compromising its power performance in order to make them more commercially viable for many applications. There are several factors which enhance the overall performance of this energy storage device, such as high surface area electrode material with heterochiral porosity is always preferable for electric double-layer capacitors (EDLCs) for high power, whereas the high-capacitive faradaic electrode materials demonstrates superior performances when high energy is required. Thus, towards the development of supercapacitor, the major challenge is the implementation of new materials along with the optimization of cell design.

The objective of this dissertation covers the research associated with the improvement of the supercapacitor device through the integration of advanced material and cell configuration to achieve high-power density as well as high energy density.

The manuscript is sectioned into seven chapters.

In the first chapter, the literature review briefly presents the background of energy storage systems and key concepts of electrochemical capacitors. This section also describes the different working principles and applications of the supercapacitors along with the most often used electrode materials and their different energy storage mechanisms. Special attention is devoted

to the importance of the various engineered carbonaceous electrode materials and the systematic cell configurations of supercapacitors.

In the second chapter, synthesis related chemicals, and reagents, characterization techniques (physicochemical and electrochemical), and instrumentation details are briefly described. Besides, the specific experimental procedure of electrode preparations and cell fabrication is also explained.

In the third chapter, the work demonstrates a development of simple synthesis route for highly porous carbon materials with good electronic conductivity as electrodes in standard symmetric **EDLC** and investigate its performance in different electrolytes to select the best active material/electrolyte match in terms of the capacitance value as well as rate capability and cyclability. Herein, the porous carbon spheres (PCS) is synthesized by carbonization of the sol-gel process of resorcinol-formaldehyde polymer in presence of a catalyst (*i.e.* FeCl₃). The physicochemical characterization of this PCS reveals that this PCS material contains mostly micro-and small amount of mesopores, which is intended as electrode material for the symmetric EDLC system. Thus, to understand the role of the electro-adsorption process of electrolyte ions with the pore size, a detailed electrochemical study is performed of the PCS electrodes both as positive and negative in three different electrolytes, *i.e.* 6M aq. KOH, 1M aq. Li₂SO₄ and 1.5 M TEABF₄/acetonitrile, based on their cation/anion size variation. The obtained findings exhibit that the positive electrode delivers more capacitance compared to the negative in KOH electrolyte, whereas the behavior is entirely opposite in the case of organic TEABF₄/acetonitrile electrolyte. On the other hand, similar capacitive behavior on both electrodes is noticed in the aq. Li₂SO₄ electrolyte. Therefore, this study reveals the selection of the appropriate electrolytes based on the porous texture of the material is effective to increase the overall charge storage performance of the electrode material.

In the fourth chapter, the work is focused on the development of **aqueous asymmetric supercapacitors (AAS)** in full cell configuration by making a variation in electrode mass balance. Besides, this work also introduces a facile and scalable one-step synthetic method of high surface area activated carbon and a simple synthesis approach of nickel cobalt oxide. To observe the overall electrochemical performance of the AAS, a full cell device is fabricated by combining a capacitive-type (high surface area activated carbon) and faradaic-type (nickel-cobalt

oxide) with different mass balance between positive and negative electrode. This hollow-core floral nickel cobalt oxide spheres consists of nanoribbons like crystalline sheets which allows unrestricted movement of the electrolyte ions during electrochemical process and this binary metal oxide shows high capacitance with faradaic behavior. Besides, our polymer derived activated carbon has very high surface area ($\sim 3000 \text{ m}^2/\text{g}$) and its electrochemical studies evidence the importance of the hierarchical structures of the active materials to maintain good capacity retention at high current densities. The optimization of the electrode mass balance within the AAS devices leads not only to both excellent energy and power densities but also to outstanding stability. The obtained results predict that the best positive: negative mass ratio in this particular AAS device is 1:2 ratio, which allow delivering maximum gravimetric energy density of 24.3 W h kg^{-1} . Most importantly, this 1:2 AAS device exhibits excellent long-term cycling stability up to 10,000 cycles with only 13% capacity decay. This study demonstrates that the electrochemical performance of asymmetric supercapacitors not only depends on the excellence of electrode materials but also on the smart strategy of assembling electrodes in full cell configuration.

In the chapter five and six demonstrates the development of the **dual carbon lithium-ion hybrid capacitor (LIC)** to improve the energy-power output with two different approaches, such as **cell voltage variation** (chapter five) and **electrode mass variation** (chapter six). Special attention is paid to the electrode material excellence and device engineering by aiming to extract the best performance of LICs.

In chapter five, the work introduces a dual carbon LIC device by assembling a polymer derived spongy hard carbon (HC) and an activated carbon (AC), as negative and positive electrodes, respectively. In this system, the semi-graphitic spongy-shaped HC is used for lithium intercalation (battery-type) and the high specific surface area AC for fast ions adsorption (capacitor-type), that conducts a remarkable capacity values and highly stable rate performances at high current rates. Apart from high energy-power density aim, to enhance the overall performance of the LIC device in terms of operational safety point of view, a comprehensive potential window variation study is also performed. Among the different tested potential ranges, the best-obtained results predict that 1.5-4.0V LIC device shows the safest operational potential range with very good reversibility without any chances of lithium plating even at high current density of 10 Ag^{-1} . At such high current density, this LIC device delivers specific cell capacity

of 25 mAh^{-1} within an incredibly discharge time of only 9 seconds. This corresponding to an energy density of 64 W h kg^{-1} at an extreme power density of 28 kW kg^{-1} . Furthermore, within this operational potential range, this hybrid device exhibited an excellent capacity retention of 82% even after 10,000 charge-discharge cycles. Thus, this potential window variation study of hybrid system demonstrates to improve the overall electrochemical performance LICs can be possible with the optimization the safe operational potential window.

In the chapter six, the work describes the importance of material excellence and the electrode mass variation approach to improve the overall dual carbon LIC performance. In general, most LICs include graphite or non-porous hard carbon as negative electrode often failing the demand of high energy at high power densities. This study introduces a new LIC device by the assembling of a polymer derived hollow carbon spheres (HCS) and a superactivated carbon (AC), as negative and positive electrodes, respectively. The obtained results from the individual electrode performance reveals that the hollow microstructure of HCS and the ultra large specific surface area of AC maximizes the lithium insertion/diffusion and ions adsorption in each of the electrodes that leads to remarkable capacity values and rate performances. Thus, to improve the performance of the LIC system from a stability point of view, an optimization in electrode mass balance study is also performed. Optimized LIC, using a 2:1 negative to positive electrode mass ratio, shows very good reversibility within the operative voltage region of 1.5–4.2 V and it is able to deliver an energy density of 68 W h kg^{-1} at an extreme power density of 30 kW kg^{-1} . Moreover, this LIC device shows an outstanding cyclability, still retaining more than 92% of the initial capacity after 35,000 charge–discharge cycles. This prolong cyclability performance indicates that the electrode mass variation approach is highly effective to enhance the self-life of the LIC device.

Finally, in chapter seven, a conclusive statement of each study explains briefly about the current challenges and opportunities for the development of the as high-performance supercapacitor.

RESUMEN

Las energías renovables como la eólica o la solar representan una alternativa más ecológica a los combustibles fósiles, responsables en gran medida del calentamiento global experimentado en las últimas décadas en nuestro planeta. Sin embargo, su producción tiene lugar de manera intermitente, por lo que implementación requiere del desarrollo de tecnologías de almacenamiento más eficientes que permitan la acumulación de energía cuando haya un exceso de producción para su uso en los momentos de escasez.

Los condensadores electroquímicos o supercondensadores son sistemas de almacenamiento de energía que presentan una serie de propiedades como su alta densidad de potencia, amplio rango de temperatura de operación, fiabilidad o alta ciclabilidad que las hacen muy atractivos en un cierto número de aplicaciones, sin embargo, su limitada densidad de energía restringe su uso en otros campos de aplicación.

El objetivo de esta tesis consiste en el estudio del impacto que tiene la integración de nuevos materiales sintéticos como electrodos, así como la influencia de algunos de los parámetros de celda, en el rendimiento de distintos condensadores electroquímicos.

La tesis se divide en siete capítulos que incluyen la revisión bibliográfica y estado del arte (primer capítulo), así como las técnicas y métodos utilizados para la caracterización físico-química de los materiales y la caracterización electroquímica de los sistemas (segundo capítulo).

El tercer capítulo se centra en el desarrollo de esferas de carbón altamente porosas a partir de resinas fenólicas a través de un procedimiento de síntesis simplificado. Su rendimiento como electrodo en condensadores electroquímicos de doble capa se investigó utilizando en tres electrolitos diferentes (KOH 6M, Li₂SO₄ 1M y TEABF₄ 1,5 M en acetonitrilo). El estudio del comportamiento individual llevado a cabo en cada uno de los electrodos muestra que cuando se utiliza KOH como electrolito el electrodo positivo presenta una mayor capacitancia que el negativo, al contrario que en el caso del electrolito orgánico TEABF₄/AN. Sin embargo, en el caso del sistema formado por Li₂SO₄ como electrolito se observó que ambos electrodos presentan capacitancias similares, poniendo de manifiesto la importancia en la selección del electrolito en función de las propiedades texturales de los materiales activos de electrodo.

En el cuarto capítulo se investiga la optimización de supercondensadores acuosos asimétricos formados por un óxido metálico como electrodo positivo y un carbón activado como electrodo negativo. Para ello se sintetizaron carbones altamente porosos mediante un procedimiento en una sola etapa y óxidos de níquel cobalto nanoestructurados. El rendimiento de la celda se optimizó mediante el ajuste en la relación de masas entre el electrodo positivo y el negativo. Los mejores resultados se obtuvieron para una relación 1:2 lo que permite alcanzar densidad de energía gravimétrica de $24,3 \text{ W h kg}^{-1}$. Lo más importante es que este dispositivo acuoso asimétrico optimizado es que presenta una estabilidad excelente durante más de 10,000 ciclos de carga y descarga con solo un 13% de disminución de la capacidad inicial.

Los capítulos cinco y seis se centran en la mejora de prestaciones de condensadores híbridos de litio (LIC) basados en electrodos de carbono a través de dos enfoques diferentes: (1) La variación de voltaje de la celda (capítulo cinco) y la variación de la relación de masas entre electrodos (capítulo seis).

En el capítulo cinco se desarrolla un LIC mediante el ensamblaje de un hard carbón (HC) derivado del pirólisis de un polímero y un carbón activado altamente poroso (AC), como electrodos negativo y positivo, respectivamente. Además del objetivo de mejora de la densidad de energía y potencia del sistema, se modificaron los rangos de voltaje para mejorar la estabilidad y seguridad del dispositivo. Los mejores resultados se obtienen en el sistema que opera en el rango 1.5-4.0 V de potencial, que muestra una excelente reversibilidad sin evidencias de deposición de litio incluso a densidades de corriente de 10 A g^{-1} . A estas densidades de corriente el LIC presenta capacidades específicas de 25 mA h^{-1} con tiempos de descarga de solo 9 segundos, lo que se corresponde con una densidad de energía de 64 Wh kg^{-1} a 28 kW kg^{-1} . Además, en este rango de potencial operativo, el dispositivo híbrido exhibe una excelente retención de la capacidad del 82% incluso después de 10.000 ciclos de carga y descarga.

En el sexto capítulo se estudia la importancia que tienen la estructura de los materiales en el dispositivo LIC y su relación en masa dentro de la celda. Para ello se sintetizaron esferas de carbono huecas (HCS) y un carbono superactivado (AC) que sirvieron como electrodos negativo y positivo, respectivamente. Los resultados de los estudios realizados en cada uno de los electrodos revelan que la microestructura de las HCS y la alta área superficial del AC maximizan tanto la inserción/difusión de litio como la adsorción de iones en cada uno de los electrodos, lo

que conduce a altos valores de capacidad a altas densidades de corriente. Mediante la variación en la relación de masas de los electrodos se optimizó un LIC capaz de almacenar una densidad de energía de 68 W h kg^{-1} a una potencia de 30 kW kg^{-1} . Este dispositivo presenta además una excelente ciclabilidad, conservando más del 92% de la capacidad inicial después de 35.000 ciclos de carga-descarga. Esta gran estabilidad confirma que el enfoque de variación de masa del electrodo es muy eficaz para mejorar la vida útil de estos dispositivos.

Finalmente, en el capítulo siete, se incluyen las conclusiones generales alcanzadas en esta tesis y los desafíos futuros para el desarrollo del supercondensador de alto rendimiento.

LABURPENA

Erregai fosilak gure planeta osoan azken hamarkadetan izandako berotze globalaren erantzule izan dira, eta hori ekidite aldera, haizea edo eguzki-energia bezalako energia berriztagarriak alternatiba berdeago bezala nabarmendu dira. Hala ere, energia berriztagarrien produkzioa aldizkakoa da, eta beraz, energia-sistema eraginkor bat izateko biltegitratze-teknologiak ezinbestekoak dira energiaren ekoizpena gehiegizkoa denean hori metatu eta ekoizpena baxua denean erabil ahal izateko.

Energia biltegitratzeko sistemen artean, kondentsadore elektrokimikoak edo superkondentsadoreak potentzia dentsitate altuko sistemak dira. Gailu hauek erabilera-tenperatura zabalak aurkezten dituzte, fidagarriak dira eta beraien bizitza-ziklo altuak direla eta karga/deskarga denbora azkarrak behar dituzten hainbat aplikaziotarako erabil daitezke. Hala ere, beraien energia dentsitatea mugatua da eta honek superkondentsadoreen aplikazio-eremua mugatu egiten du.

Tesi honen helburua, alde batetik, material sintetiko berriak elektrodo gisa erabiltzea litzateke, eta ondoren, elektrodo horiek eta gelaxka elektrokimikoaren beste zenbait parametrok kondentsadore elektrokimiko ezberdinen errendimenduan duten eragina aztertzea.

Tesia zazpi kapitulutan banatua dago. Lehenengo kapituluan berrikuspen bibliografikoa eta teknologiaren egungo egoeraren azterketa egiten dira. Bigarren kapituluak materialen karakterizazio fisiko-kimikoan eta sistemen karakterizazio elektrokimikoan erabiltzen diren teknikak eta metodoak biltzen ditu.

Hirugarren kapituluak, sintesi-prozedura sinplifikatu baten bidez erretxina fenolikoetatik lortutako karbono-esfera oso porotsuen garapena eta karakterizazioa ditu aztergai. Karbono-esfera horiek geruza bikoitzeko kondentsadore elektrokimikoetan elektrodo gisa duten funtzionamendua ikertu da hiru elektrolito ezberdinetan, 6M KOH (aq), 1M Li₂SO₄ (aq) eta 1.5M (C₂H₅)₄N(BF₄) (azetonitriloan) -laburbiltzeko TEABF₄ (AN)-, hurrenez hurren. Sistema elektrokimiko bakoitzean materialak duen portaeraren azterketak erakusten duenez, KOH (aq) elektrolito gisa erabiltzen denean elektrodo positiboak negatiboa baino kapazitantzia handiagoa

erakusten du, TEABF₄ (AN) elektrolito organikoaren kasuan kontrako egoera ematen delarik. Aldiz, Li₂SO₄ (aq) elektrolito gisa erabiltzean, bi elektrodoek antzeko kapazitantzia aurkezten dutela behatu da. Hortaz, emaitza hauek elektrolitoaren aukeraketa elektrodoetako materialen testura-propietateen arabera egin behar dela erakusten dute.

Laugarren kapituluan, NiCo₂O₄ oxido metalikoz (elektrodo positibo) eta ikatz aktibatuz (elektrodo negatibo) eraikitako eta elektrolito urtsua darabilten superkondentsadore asimetrikoen optimizazioa ikertu da. Horretarako, etapa bakarreko prozedura bat jarraituz ikatz oso porotsuak eta NiCo₂O₄ nanoegituratuak sintetizatu ziren. Ondoren, gelaxka elektrokimikoaren errendimenduaren optimizazioa elektrodo positibo eta negatiboen arteko masa erlazioa egokituz burutu da. Emaitza onenak 1:2 masa erlazioarekin lortu dira, 24.3 Wh kg⁻¹-ko energia dentsitatea lortuz. Datu aipagarrien artean, elektrolito urtsua darabilen sistema asimetriko optimizatuaren egonkortasun bikaina litzateke, izan ere, 10,000 karga/deskarga ziklo baino gehiagoren ostean hasierako kapazitantziarekin alderatuz %13ko beherakada soilik erakusten du.

Bost eta sei kapituluetan ikatzezko elektrodoetan oinarritutako litio ioi kondentsadore hibridoak (ingelesez *lithium ion capacitor*, LIC) errendimendua hobetzeko jarraitutako optimizazio bideak aztertzen dira: (1) gelaxkaren tentsioa (bosgarren kapitulua) eta elektrodoetako material aktiboen masa-erlazioaren eragina (seigarren kapitulua) aztertuz.

Bosgarren kapituluan garatutako LIC-ak polimero baten pirolisitik eratutako ikatz gogor bat (ikatz ez-grafitizagarria) eta ikatz aktibatu oso porotsu bat erabiltzen ditu elektrodo negatibo eta positibo gisa, hurrenez hurren. Sistemaren energia eta potentzia dentsitatea hobetzeaz gain, potentzial tarte ezberdinak aztertu dira gailuaren egonkortasuna eta segurtasuna hobetzeko. Emaitza onenak 1.5-4.0 V tentsioan lan egiten duen sistemarekin lortzen dira. Gainera, sistema horrek itzulgarritasun bikaina erakusten du, 10 A g⁻¹-eko korronte dentsitatean ere litio-metaketa arrastorik erakutsi gabe. Korronte dentsitate balio horietan LIC-ak 25 mAh g⁻¹-ko kapazitate espezifikoa aurkezten du, deskarga denbora 9 segundokoa baino ez delarik. Hau da, 64 Wh kg⁻¹-ko energia dentsitatea biltegira (edo eman) dezake 28 kW kg⁻¹-ko potentzian. Gainera, sistema hibridoak %82ko kapazitate-erretentzio bikaina erakusten du 10,000 karga/deskarga zikloren ondoren.

Seigarren kapituluan, materialen egiturak eta elektrodoetako materialen masa erlazioak LIC-aren funtzionamenduan duen garrantzia aztertzen dira. Horretarako, karbono-esfera hutsak (ingelesez *hollow carbon spheres*, HCS) eta gainaktibatutako ikatza sintetizatu ziren elektrodo negatibo eta positibo gisa erabiltzeko, hurrenez hurren. Elektrodo bakoitzaren gainean egindako ikerketen emaitzek agerian uzten dute HCS-ren mikroegiturak eta gainaktibatutako ikatzaren azalera altuek litioaren txertaketa/difusioa hala nola ioien adsortzioa ahalbidetzen dutela. Ondorioz, kapazitate balioa altuak lortzen dira korrante dentsitate handitan. Elektrodoen masa erlazioa egokituz, 30 kW kg⁻¹-ko potentzian 68 Wh kg⁻¹-ko energia dentsitatea biltegitatzeko gai den LIC bat eraiki ahal izan da. Gailu honek bizitza-ziklo bikaina erakusten du eta hasierako kapazitatearekin alderatuz %92 baino gehiago mantentzeko gai da 35,000 karga/deskarga zikloren ondoren. Egonkortasun altu honek elektrodoen masa-erlazioaren egokitzapenak gailuen bizitzan eragin nabarmena duen parametroa dela baieztatzen du.

Azkenik, zazpigarren kapituluan, tesi honetan lortutako ondorio orokorrak eta etorkizuneko errendimendu handiko superkondentsadorea garatzeko gaintitu beharreko erronkak jasotzen dira.

TABLE OF CONTENTS

Acknowledgements	i
Summary	iii
Table of Contents	xv

CHAPTER-1: Introduction

1.1. Energy overview	3
1.2. Energy storage technologies	4
1.3. Batteries <i>versus</i> electrochemical capacitors	5
1.4. Classification of electrochemical capacitors	7
1.5. Energy storage mechanism in electrochemical capacitors	8
1.6. Applications of electrochemical capacitors.....	15
1.7. Materials for electrochemical capacitors.....	17
1.7.1. Carbon based materials	18
1.7.2. Pseudocapacitive materials.....	24
1.7.3. Transition metal oxides	24
1.7.4. Conductive Polymers	26
1.8. Electrolytes	26
1.8.1. Aqueous electrolytes	27
1.8.2. Organic electrolytes.....	28
1.8.3. Ionic liquid electrolytes	29
1.9. Cell configurations of electrochemical capacitor	29
1.9.1. Symmetric and asymmetric capacitor	29
1.9.2. Hybrid capacitor	30
1.9.3. Lithium-ion capacitor	32
1.9.4. Working principles of dual carbon hybrid capacitors	35
1.10. Research motivation	37
1.11. Specific objectives.....	38
Bibliography	39

CHAPTER-2: Physicochemical and electrochemical characterizations techniques

2.1. Experimental section	47
2.1.1. Reagents	47
2.1.2. Apparatus	47
2.2. Physicochemical characterization techniques	48
2.2.1. Electron microscopy	48
2.2.1.1. Scanning electron microscopy	49
2.2.1.2. Transmission electron microscopy	51
2.2.2. X-ray diffraction.....	54
2.2.3. Raman spectroscopy.....	55
2.2.4. Elemental Analyzer	56
2.2.5. Gas adsorption desorption.....	57
2.3. Electrochemical characterization techniques	61
2.3.1. Cyclic voltammetry	61
2.3.2. Galvanostatic charge discharge	63
2.3.3. Electrochemical impedance spectroscopy	64
2.3.4. Electrode processing and cell assembly	65
Bibliography	69

CHAPTER-3: Synthesis of porous carbon spheres and their use as electrodes for EDLC in different electrolytes

3.1. Introduction	73
3.2. Material synthesis	75
3.3. Physicochemical characterization	76
3.4. Electrochemical characterization	79
3.4.1. Electrode processing and cell assembly	79
3.4.2. Electrochemical evaluation	80
3.5. Conclusion.....	88
Bibliography.....	89

CHAPTER-4: Optimization of aqueous asymmetric supercapacitors by using nickel cobalt oxide and superactivated polymer-derived carbon as electrode materials

4.1. Introduction	95
4.2. Material synthesis	96
4.3. Physicochemical characterization	97
4.4. Electrochemical characterization.....	101
4.4.1. Electrode processing and cell assembly	101
4.4.2. Electrochemical performance of the positive electrode (NiCo ₂ O ₄)	101
4.4.3. Electrochemical performance of the negative electrode (SAC).....	103
4.4.4. Electrochemical performance of the NiCo ₂ O ₄ //SAC asymmetric supercapacitor.....	105
4.5. Conclusion.....	111
Bibliography.....	112

CHAPTER-5: Optimization of a novel dual-carbon lithium hybrid capacitor by cell potential window approach

5.1. Introduction	119
5.2. Material synthesis	120
5.3. Physicochemical characterization	121
5.4. Electrochemical characterization.....	125
5.4.1. Electrode processing and cell fabrication.....	125
5.4.2. Electrochemical performance of anode (SHC)	126
5.4.3. Electrochemical performance of cathode (PAC)	128
5.4.4. Electrochemical performance of the SHC//PAC hybrid LIC.....	129
5.5. Conclusion.....	135
Bibliography.....	137

CHAPTER-6: Development of dual-carbon lithium-ion hybrid capacitor with electrode mass variation approach for the improvement of rate performance and cycling stability

6.1. Introduction	143
-------------------------	-----

6.2. Material synthesis	144
6.3. Physicochemical characterization	144
6.4. Electrochemical characterization	148
6.4.1. Electrode processing and cell assembly.....	148
6.4.2. Electrochemical performance of anode (HCS)	149
6.4.3. Electrochemical performance of cathode (AC).....	151
6.4.4. Electrochemical performance of the HCS//AC hybrid LIC	152
6.5. Conclusion.....	158
Bibliography	159
 CHAPTER-7: Conclusions and perspectives	
7.1. Conclusions	165
7.1.1. EDL system.....	165
7.1.2. Aqueous asymmetric system.....	166
7.1.3. Hybrid LIC system	166
7.2. Perspectives	168
 Appendix I: List of Tables	 169
Appendix II: List of Figures.....	171
Appendix I: List of Abbreviations	177
Appendix II: List of Contributions.....	181

CHAPTER – 1

Introduction

1.1. Energy overview

In last few decades, the ever-increasing global demand for energy is associated with the vast population and economic growth, and this rising trend in energy consumption contributes to environmental and economic risks.^[1-2] Excessive consumption of fossil fuels (such as coal, petroleum, natural gas, and crude oils) leads to higher greenhouse gas emissions (particularly carbon dioxide), which impacts global warming and pollutions.^[1, 3] For the sustainable development of human society, clean energy technology like energy conversion and storage plays the most important role in overcoming problems of fossil fuels.^[1, 3] Therefore, the replacement of conventional highly polluting energy sources has been possible with alternative greener energy sources like renewable ones, accompanying greater prosperity as well as new challenges. The most popular renewable energy sources currently are solar, wind, hydro, tidal and geothermal energy. The more widespread use of these renewable energy sources with better efficiency can only deal with these socio-economic issues. According to the *World Energy Balances: Overview*, published by the International Energy Agency, the share of renewables in final energy consumption is currently reached upto 26 % (Figure 1.1.) in the world, following the rapid rise in recent decade.^[4]

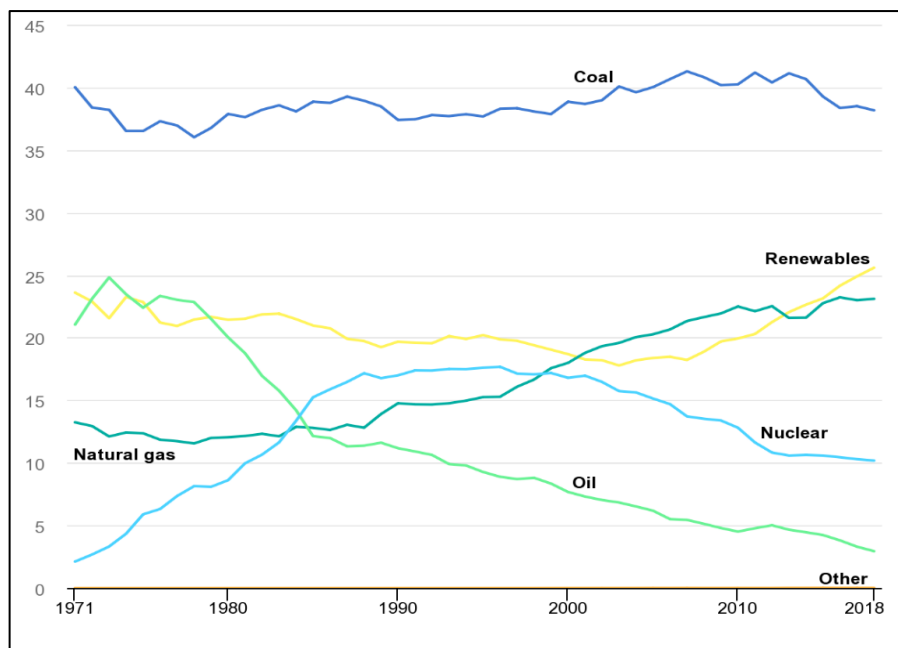


Figure 1.1. World electricity generation mix by fuel, 1971-2018 (World Energy Balances: Overview, International Energy Agency data up to 2019).^[4]

Renewable energy sources now cover 36% of the power mix in Europe, 26% in China and around 18% in the United States, India and Japan as presented by global energy statistical yearbook 2020.^[5] Forecast for the year 2024 shows that 50-60% of world energy demand would be fulfilled from energy obtained from renewable sources. This energy production will be led by solar photovoltaic (PV) and followed by wind energy, hydropower, and bioenergy. Beside this energy conversion sources, energy storage is also taking lead to fulfill the demand of renewable energy supplies.

1.2. Energy storage technologies

Most of the renewable energy sources are intermittent, for example, solar and wind power mainly depends on the time of the day and regional weather conditions, which can often cause power supply fluctuations.^[1, 6] Thus, energy storage devices are used as strong complementary systems to comprehend the eventual distribution and accessibility of these harvested renewable energies when it is needed. The main target of the energy storage system is to accumulate-store-integrate the electricity into the electrical grid on peak demand.^[6]

There are several technologies that can store energy through different mechanisms, showing distinct properties such as the amount of energy, power, lifetime, and cost. At large scale, compressed air energy storage, fireless locomotive, flywheel energy storage, solid mass gravitational, hydraulic accumulator, and pumped-storage hydroelectricity are the most common mechanical bulk energy storage systems.^[6-7] Among them, at present, the major bulk energy storage is controlled by hydroelectric dams, both conventionally as well as pumped.^[7]

On the other hand, supercapacitors and rechargeable batteries, which store the energy through the electrostatic and electrochemical mechanism, are used to store lower amounts of energy and typically bring into service as “portable” devices.^[6-8] Their applications in electronics, hybrid vehicles, aircrafts, and smart grids are widespread.^[8-9] For this reason, development of energy storage devices is on high demand in the last few decades because of their electric storing viability when needed and released as per required. Thus, the challenge is to improve the efficiency of energy storing technologies in case of both short term and long-term purposes.

For short term devices, inductors and capacitors are the known specimens for their energy-storing capacity through the magnetic field and electric field, whereas for long term purpose batteries and fuel cells takes the lead to provide high capacity for the industrial and personal demand.^[10]

Moreover, the different types of the large-capacity hybrid energy storage system are usually equipped with the power-conditioning system (PCS) to deliver energy efficiently as well as uninterrupted electric power generated through energy conversion technologies.^[10] Therefore, the generated power from the windmill or solar panel can be stored by hybridizing these energy storage devices for the supply of stable electric power without any frequent fluctuation.^[6, 10] In this regard, the performance of these energy storage devices need to be improved in order to fulfill the autonomy requirements of some of these integrated devices.

With the rising demands of long runtime portable energy storage devices, the energy research sector is being extended and integrated into new innovative technologies and cord-less applications. This need leads to the advancement in the high-performance energy storage system. Therefore, exploring highly efficient, prolong cycle life, reliable, and large-capacity energy storage devices are strongly demanded to encounter the current challenges of portable energy storage devices.^[6-7]

1.3. Batteries *versus* electrochemical capacitors

Batteries can be divided into two types, such as primary and secondary batteries, depending on whether they have single-use (galvanic cell, alkaline battery and dry cell) or rechargeable [nickel-metal hybrid (Ni/MH) batteries, lead acid battery (PbO₂/Pb) and lithium-ion battery (LIB)], respectively.^[11-12]

In rechargeable batteries energy storage depends on electrochemical redox reactions, that limits the charge transfer process due to its slow mass diffusion. However, the main drawback of batteries is their short cycle life (~2000 cycles) and very low power density that cannot meet the necessary demands for electronic devices.^[12-13] Consequently, supercapacitors that store energy electrostatically like common capacitors can utilize fast electrosorption processes on the surface of the electrode.

The importance of supercapacitors is that they can provide high power by utilizing the fast electrolyte ion transportation, but they always suffer from low-energy.^[11, 13] Thus, for the past few decades, the supercapacitor research field is focused on improving energy density without compromising its power density. Significantly, in recent times Hybrid capacitors (such as Lithium-ion capacitor or LIC) are rapidly approaching to forefront position by combining the

advantages of both lithium-ion battery and electrochemical capacitors such as long cycle life expectancy, reliability and superior energy efficiency.^[14]

The Ragone plot, displayed on Figure 1.2. shows the specific energy and specific power ranges of these technologies.

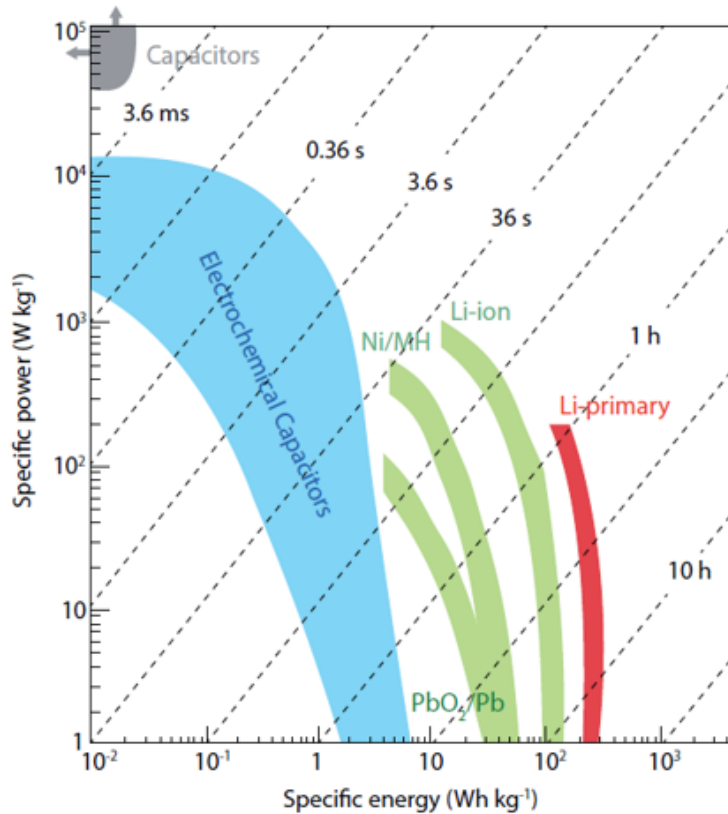


Figure.1.2. Ragone Plot of different energy storage devices.^[11]

Another advantage of supercapacitors is that they can work in a wide operating temperature range ranging from -40°C to 80°C , maintaining the stability, whereas battery operations is limited at low temperature for its kinetic issues.^[13] From a safe-handling perspective the use of supercapacitors is much more beneficial compared to batteries due to the use of low reactive species as electrode materials.

In the case of batteries, the use of highly reactive alkali-metal based materials struggles with thermal instability and flammability, which can cause serious concerns regarding safe and secure operations. Therefore, supercapacitors are highly efficient when fast charge-discharge operation is needed for high power application purposes over a longer time span. Despite the several

advantages of supercapacitor over batteries, cost reduction (20 € per watt hour) is a crucial issue for commercial scale-up.

Thus, the industrial R&D is highly focused on the advancement of electrode material-electrolyte and cell construction which can improve performance at a reduced cost for the global market. Thus, supercapacitor as energy storage devices retain several high-impact attributes such as prolong charge-discharge cycles, fast charging abilities and uninterrupted operational capacities at a broad range temperature. Comparison between the main characteristics of both technologies is shown in table 1.1.

Table 1.1. Comparative features of the electrochemical capacitors and lithium ion batteries.^[15-16]

Features	Lithium ion Batteries	Electrochemical Capacitors
Charge Time	~3-5 mins	~1 second
Discharge Time	~3-5 mins	~1 second
Cell Cycle Life	<5000 at 1C rate	>1,000,000
Specific Energy (Wh kg ⁻¹)	70-100	5-10
Energy Density (Wh l ⁻¹)	50-300	0.5-5
Specific Power (kW kg ⁻¹)	0.5-1	5-10
Power Density (kW l ⁻¹)	<0.5	1-3
Cycle Life Efficiency (%)	<50% to >90%	<75% to >95%
Energy-Cost/Wh	0.5-2 €/Wh	10-20 €/Wh
Power-Cost/kW	75-150 €/kW	25-50 €/kW

1.4. Classification of electrochemical capacitors

The advancement in capacitor technology over the years not only focuses on materials but also on the cell fabrication-design to ensure the performance over long periods of operation. Today many commercial capacitor/supercapacitor devices are available in the market but to reach this stage it has gone through several development steps. By looking up the history of capacitors, electrostatic and electrolytic capacitors could be considered as first- and second-generation capacitors.^[17]

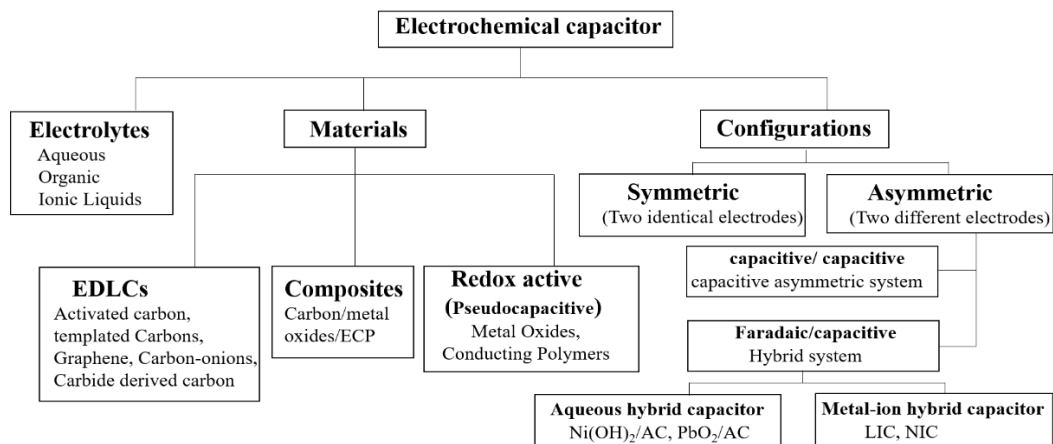


Figure.1.3. Classification of electrochemical capacitors based on materials, cell configurations and electrolytes.

In the 1830s, Michael Faraday reported the basic phenomenon for the charge storage mechanism of a capacitor system. After that, several types of capacitors started to become known, such as mica capacitor (1909), ceramic capacitor (1920), tantalum electrolytic capacitors (1930) and polymer film capacitors (1954).^[13, 18-19] In 1966, General Electric experimented with electrochemical capacitors (ECs) by using porous carbon electrodes to patent “low voltage electrolytic capacitors with porous carbon electrodes” and then NEC commercialized these devices in 1978.^[19] Since then scientists and engineers have invested tremendous effort for further improve their power density, energy density, reliability, safety and cost effectivity to reach the specific requirements for different ES applications. The third-generation or electrochemical capacitors, also known as supercapacitor or ultracapacitors, incorporate an electrolyte that allows to adsorb charges at the surface of the electrodes. Figure 1.3 represents the taxonomic classification of the supercapacitors.^[17] The supercapacitor can be classified, according to (i) the charge storage mechanism (electrode materials), (ii) electrolytes or (iii) device configurations storage theories, material properties, electrolyte categories, and device configurations, respectively.

1.5. Energy storage mechanism in electrochemical capacitors

Electrochemical capacitors are primarily formed by two electrodes (a positive and a negative) in combination with an electrolyte and a separator. Those electrodes consist of active materials along with conductive additives and a binder, coated onto a current collector. The separator

allows the electrolyte ion permeability through its pores and avoids direct contact between electrodes to prevent short circuit of the cell.^[13]

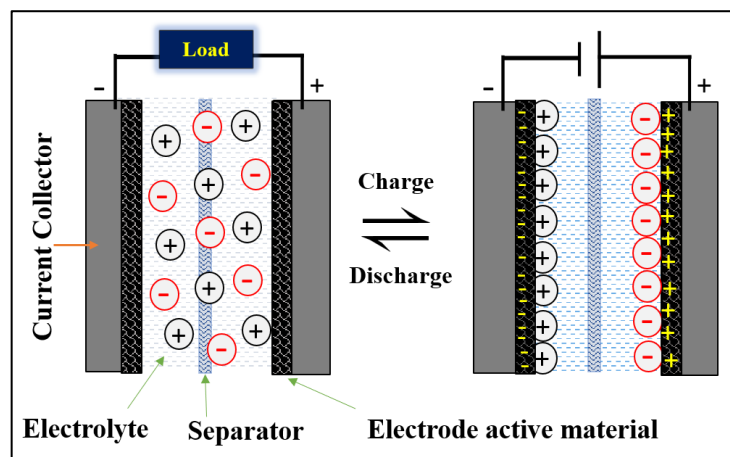


Figure.1.4. Schematic configuration and basic charge/discharge mechanism of the electrochemical capacitor.

Thereby, the opposite charges are accumulated at the electrode/electrolyte interface during the polarization of the electrode by the electrostatic charge separation process. Figure 1.4 shows a scheme of the inside components of the electrochemical capacitors and the basic charge/discharge process undergone upon the application of the potential difference.

There are two main types of charge storage mechanisms: “electric double layer (EDL) theory” and “Faradic charge transfer process”. The EDL theory is the principle foundation of the electrochemical processes taking place at the electrostatic interface between the charged electrode material and electrolyte. The German physicist Herman von Helmholtz (in 1853) proposed first of this EDL theory. Figure 1.5a schematically explains the double-layer interface model (Grahame model), which depicts an amalgamation of anions and cations charge distribution.^[20] Later, this theory was further developed by Gouy, Chapman, and Stern.^[13, 19] According to the Gouy-Chapman model (Figure 1.5b), the EDL refers two parallel layers of charges on the electrode-electrolyte interface. The first layer corresponds to the opposite charges accumulated by the surface chemisorption process of ions, whereas the second layer comprises the ions attracted *via* coulombic force after electrically screening the first layers. Thus, the second layer trends to loosely attached ions with the electrode surface, so they can move freely in the fluid medium under the influence of thermal motion and electric attraction. This scattered layer

along with the firmly anchored opposite charge array on the electrode-electrolyte interface is called the “diffuse layer”.

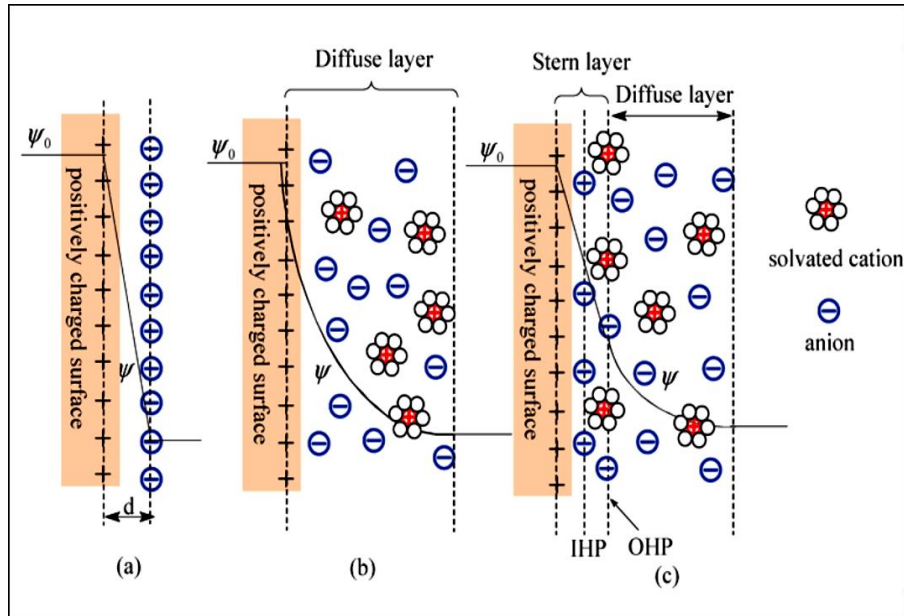


Figure 1.5. Different models of the EDL at a positively charged surface, (a) the Helmholtz model, (b) the Gouy–Chapman model, and (c) the Stern model, showing the IHP and OHP.^[21]

Afterwards the Stern model advances this surface charge storage mechanism by introducing the Stern layers. In Stern layers (Figure 1.5c), the “Inner Helmholtz Plane (IHP)” is known as the compactly attached solvent layer on the electrode surface, another side the term “Outer Helmholtz Plane (OHP)” expresses the association of solvent and solvated ions. The layer beyond the OHP is still considered as diffusing layer.

The total capacitance (C_{dl} , F) of the EDL interface is according to the following equation (Eq. 1),

$$\frac{1}{C_{dl}} = \frac{1}{C_{IHP}} + \frac{1}{C_{OHP}} + \frac{1}{C_{diff}} \quad 1$$

C_{dl} is equivalent to a series relationship in between C_{IHP} , C_{OHP} , and C_{diff} as shown in the following circuit pattern.



In Fact, C_{diff} is usually much larger than both C_{IHP} and C_{OHP} , so the contribution of the diffusion layer to the EDL capacitance is neglected in many cases. The IHP could be considered as a dielectric layer, so combination of the C_{IHP} and C_{OHP} represents C (total Capacitance), which is more realistic expression of double-layer capacitance and can be determined by the following equation (Eq. 2),

$$C = \frac{A\varepsilon}{d} \quad 2$$

Where, A is the surface area (m^2) of the interface between the electrode-electrolyte, ε is the permittivity of the dielectric material and d is the EDL thickness (m). The capacitance value depends on the surface area that differentiates supercapacitors from the other capacitors. In electric double layer capacitors (EDLCs), porous carbon materials with the large surface area are generally used as electrode materials to obtain high capacitance. The porosity of materials not only induces the adsorption of the ions from the electrolyte, but it also helps their access to the whole surface of the active material.

When a potential difference (V) is applied in supercapacitor systems, positive charges (Q_+) and negative charges (Q_-) are accumulated as a result of the movement of electrons in the outer circuit. The current passes to the electrodes until an equal balance is made between the potential difference and the supplied voltage, by generating opposite charges within supercapacitors. The total accumulated charges ($Q = |Q_+| + |Q_-|$) is considered in coulombs, C , and the applied potential difference in V , yields the capacitance values in farads, F . The capacitance values can be calculated as (Eq. 3):

$$C = \frac{Q}{V} \quad 3$$

Therefore, the stored energy (E) can be expressed by the following equation in the EDL system (Eq. 4),

$$E = \frac{CV^2}{2} \quad 4$$

Pseudocapacitors are a type of electrochemical capacitors in which charge storage is produced by fast and reversible faradaic reactions at the surface of the electrodes, where the “pseudocapacitance” generates by the faradic charge transfer process in the electrode materials

through thermodynamically and kinetically favored electrochemical reduction-oxidation (redox). Due to these interfacial redox reactions a larger quantity of charges can be stored and therefore the capacitance values achieved by pseudocapacitive materials are much higher than those obtained by EDLCs. C_{Pseudo} , can be calculated from the generated charges on the electrode (dQ) that depends on the applied potential difference (dV) and this derivation relation can be expressed by the following equation (Eq. 5)^[22],

$$C_{Pseudo} = \frac{dQ}{dV} \quad 5$$

Consequently, the energy (E , $W h$) stored by the pseudocapacitors can be calculated by the integral of voltage over the applied potential (Eq. 6 and 7)^[22]:

$$E = - \int_0^Q V dQ \quad 6$$

$$E = - \int_{V_{max}}^{V_{min}} V dCV = -C \int_{V_{max}}^{V_{min}} V dV = C \frac{(V_{max}^2 - V_{min}^2)}{2} \quad 7$$

The importance of using integration formulas for calculating pseudocapacitive energy efficiencies are highly essential for reporting the correct values of pseudocapacitive energy storage devices.

Furthermore, the power values (P) depend on the obtained energy and the discharge time (Δt , h) of the supercapacitor. The power (P) will be expressed as (Eq. 8):

$$P = \frac{E}{\Delta t} \quad 8$$

When the energy and power are represented in terms of the gravimetric or volumetric perspective of the EDLC device, they are denoted as energy density (E_{SP} , $W h kg^{-1}$ or $W h l^{-1}$) and Specific power (P_{SP} , $W kg^{-1}$ or $W l^{-1}$).

EDLCs generally suffer from limited energy density because the amount of charge storage is restricted to the surface of the active materials. Compared to EDLCs, pseudocapacitive materials provide much higher energy values due to the additional contribution of surface faradaic charge storage.^[23] The primary difference in the charge storage mechanism of battery electrodes from the supercapacitor electrode is that battery electrodes involve diffusion-controlled kinetics, while

the capacitive and pseudocapacitive electrodes have only surface-controlled processes during charge-discharge.^[23] Figure 1.6 illustrates the individual behavior of the electrochemical energy storage materials to understand the intrinsic operative charge storage mechanisms of energy storage systems.

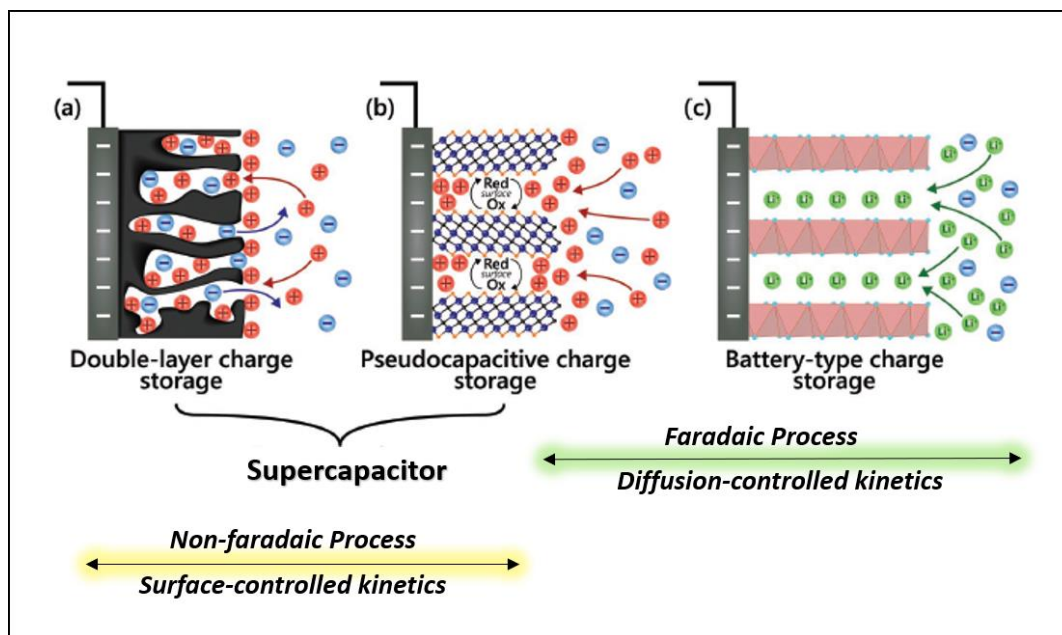


Figure 1.6. Schematics of the charge storage processes occurring at (a) electrical double-layer capacitive, (b) pseudocapacitive, and (c) battery-type electrodes.^[23]

Three types of pseudocapacitive mechanisms have been described in the literature depending on the intrinsic charge storage of the electrode materials.^[24] They are: (i) “under potential deposition”, where a monolayer of metal can be deposited on the working electrode, (ii) “Surface redox pseudocapacitance”, where the electrode surface participates in redox reaction by utilizing only the electrode materials oxidation states, and (iii) “intercalation pseudocapacitance”, where ions intercalate in the core structure of the electrode material to find the redox-active surface without any deformation in material structure and phase change.^[24-25]

The term “pseudocapacitance” is sometimes wrongly used for materials that store charges through a classical faradaic battery type mechanism. During the charge-discharge of pseudocapacitive materials, highly reversible redox reactions occur at the surface of host material without any phase transformations. However, in the classical battery electrode materials, reversible phase transformation takes place during the faradaic charge-discharge process.^[23-24]

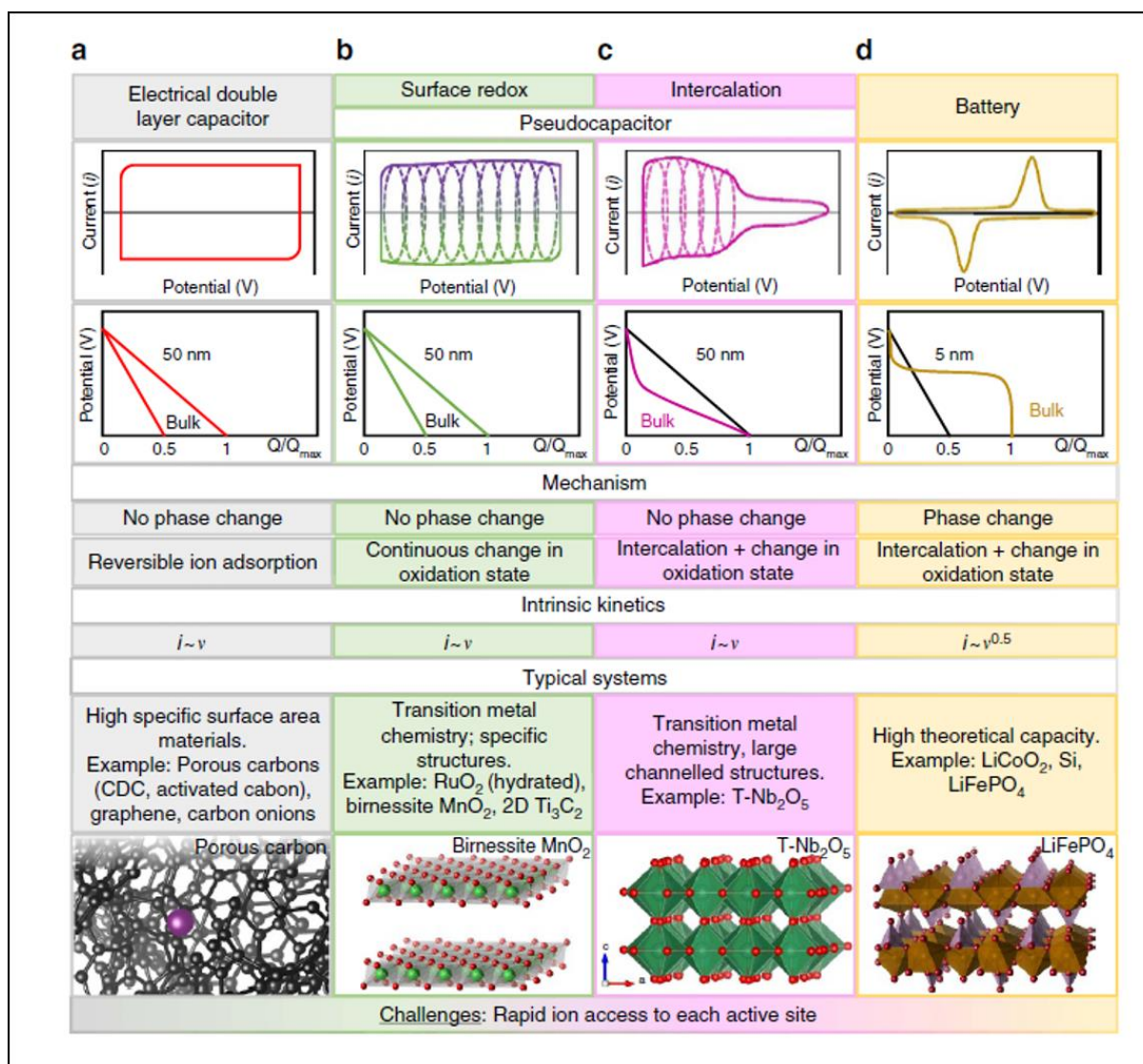


Figure 1.7. Comparative characteristics of the different types of charge storage materials, (a) electrical double-layer capacitive, (b) surface redox pseudocapacitance, (c) intercalation pseudocapacitance, and (d) batteries. ^[24]

Therefore, this electrochemical phenomenon is entirely different and is clearly distinguishable by the faradaic redox peaks in their cyclic voltammograms and the plateaus under constant applied current in charge-discharge profiles.

Figure 1.7 summarizes the distinguishable features of the different energy storage materials. According to pragmatic calculations, surface faradaic processes show prominent peaks only, that

can be more widened varying on the interaction between the reactants and electrolytes, but the capacitive response cannot be through that mechanism.

1.6. Applications of electrochemical capacitors

Electrochemical capacitors are very interesting energy storage technologies for some specific applications and can be used as alternative to batteries. When high-power shuttling applications are needed along with high energy source, the coupling with batteries can be a reliable and highly suitable configuration. Supercapacitors are very useful in a wide range of mobility applications purpose (backup power for a temporary UPS system, rail-tram transportation, shipping, automotive), semi-stationary (high power cranes, heavy excavators), stationary sector (wind/solar power plant grid and backup power of pitch system), and for regenerative braking for hybrid or electric vehicle.^[26, 29-30] However, the development of supercapacitors depends on not only the market demand but also on social needs. It is very promising that the present scenario is changing so fast towards market growth. Especially, in the automotive sector, the growth rate of the supercapacitor industry is exponentially increasing along with eco-friendly social demand. Nowadays numerous companies are involved in the development and manufacturing of power devices that can fulfill different application ranges to cover market growth, which is expected to increase from 1.2 to 5.5 billion euros in 2022. Figure 1.8 illustrates the probable future market demand of commercially available electrochemical capacitors and table 1.2 summarizes some of the important features of commercial cells.^[26-28]

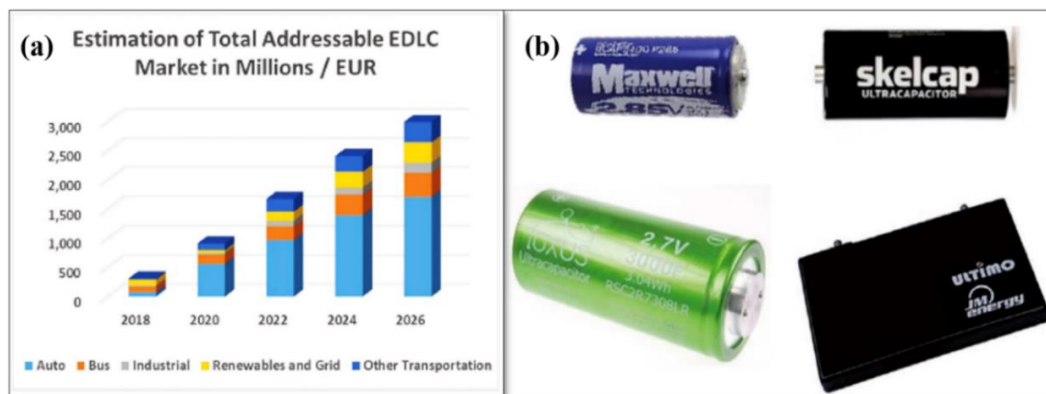


Figure 1.8. (a) Estimation of the future addressable market of EDLC (Skeleton Technological Group), and (b) commercially available supercapacitor cells [Maxwell 3400 F (top left), Skeleton 3200 F (top right), Ioxus 3000F (bottom left), and JM Energy 3300 F (bottom right)].^[26-27]

Table 1.2. Details of different commercial supercapacitors available in the market. ^[28]

Manufacturer	Voltage (V)	Capacitance (F)	ESR (Ω)
APowerCap	2.70	450	-
NipponChemii-Pon	2.50	1400	1.1
BatScap	2.70	2680	0.20
Fuji	3.80	1800	1.50
Ioxus	2.85	3150	0.22
LS Mtron	2.80	3200	0.25
Maxwell	3.00	3400	0.22
NessCap	2.70	3640	0.30
Skeleton	2.85	3200	0.12
Yunasko	2.70	7200	1.40
JM Energy	3.80	3300	0.7

Those applications differ according to their energy or power requirements for extended charge-discharge cycles with an interval range of 10-60 seconds in some cases, while other cases may need less than even 1 second. In the case of the heavy transportation sector (especially in trains and trams), the use of supercapacitor is extremely highly efficient in regenerative energy recovery systems where the braking energy is reused for the acceleration. In electric vehicles, high efficiency with low-cost power devices plays a huge role in eco-friendly transportation to reduce CO₂ emission.^[26] Thus, several countries like Spain, China, Taiwan, Germany, Austria, UK, USA are trying to implement supercapacitors for zero-emission electric transportations.^[26]

China is experimenting with the advanced design of electric buses by using EDLC supercapacitor systems, known as *Capabus*, which can run without any continuous overhead and are able to quickly recharge within a few seconds at any bus stop (each stop will be equipped with the charging system, so-called electric umbrellas).^[29, 31] The Chinese company Sunwin (a joint venture between Volvo and China's largest automaker SAIC) already developed and has been operating a fleet of electric buses equipped with a supercapacitor operative system.

In Graz, Austria, a few routes are successfully running with short intermediate recharging electric buses, using 24-32 kWh EDLCs.

Besides electric buses, Spanish manufacturer CAF developed catenary-free trams using supercapacitors to save energy from regenerative braking and preserve the historical heritage and urban environment, which has been successfully running on a 1.6 kilometer tramway in Seville since 2010 and is also successfully extended to other Spanish cities (Granada and Zaragoza).^[32] Likewise, the tramway in Kaohsiung (Taiwan) has also introduced supercapacitor operated trams in 2016.^[33] In each stoppage of the tramway has charging ports and it takes only 20 seconds to charge up the supercapacitor and then the tram can run until the next destination without any disturbance. Figure 1.9 shows pictures of the trams boosted by EDLC supercapacitors in Kaohsiung and Spain.



Figure 1.9. Fully operative supercapacitor trams in Taiwan and Spain.

Skeleton Technologies is well-known in the European market as a supercapacitor manufacturer and they will supply supercapacitor systems to Škoda Electric (a traction equipment manufacturer), for making 114 trams will operate in Mannheim, Heidelberg, and Ludwigshafen in Germany.^[34] The advancement in energy storage technologies will attract more commercial applications.

1.7. Materials for electrochemical capacitors

The most common electrode materials for supercapacitors are carbons, transition metal oxides, and conducting polymers.

1.7.1 Carbon-based materials

Carbon is the preferred material for the fabrication of supercapacitors because it has a high specific surface area, easily tailored porosity, high electronic conductivity, inertness, and it is cheap. Besides, they are mechanically and thermally very stable for longer operations. However, because of its electrostatic surface charging mechanism, EDLCs devices constructed with carbon electrodes always experience a limited energy density. Several studies focus on strategies to modify carbon morphologies or heteroatoms doping to further improve the performance *versus* pristine materials.

The electronic configuration of carbon is $1s^2 2s^2 2p^2$. In the case of the carbon atom, the hybridization of s and p orbital results in different crystalline (ordered) allotropes, such as diamond (sp^3), graphite (sp^2), fullerenes (distorted sp^2), carbyne (sp). Among those, graphite is a very common electrode material for energy storage applications (particularly in Li-ion batteries) but its slow kinetics is the main drawback for electrochemical operations. Thus, different carbon engineering with tailoring porosity has revealed promising results as a replacement of “graphite” because of its disordered structure along with limited aligned crystalline graphite-like layers.

Among them “soft” and “hard” carbons are well known materials for Li-ion hybrid capacitors as well as batteries and can be classified on the basis of heat treatment temperature that helps to increase the graphitization degree in carbon matrix.^[13, 35-36] For graphite, the pyrolysis temperature generally maintains at 2500°C to obtain high crystallinities. Consequently, graphitization states of “soft” carbons can be easily controlled during the heat-treatment at 1100-2000°C, where often layers are stacked with arbitrary orientations and this turbostratic misalignment delivers high rate charge-discharge.^[37-39]

On the other side, “hard” carbons or non-graphitizable carbons (temperature ca. ~600°C to 1000°C) contains mainly single layers arrangements with a larger space gap between the carbon layers than graphite.^[37-39] This disordered pattern leads to doubling the theoretical capacity compared to graphite because of its nutshell like morphology can utilize the more space for the insertion electrolyte ion on the graphite-like regions. In general, the electrodes are made of porous carbon materials with very large specific surface area (SSA) can store more charges on their electrode/electrolyte interphases. Pores can be classified depending on their pore size, such as

micropores (<2 nm), mesopores (2-50 nm), and macropores (>50 nm), which is described in Figure 1.10.^[40]

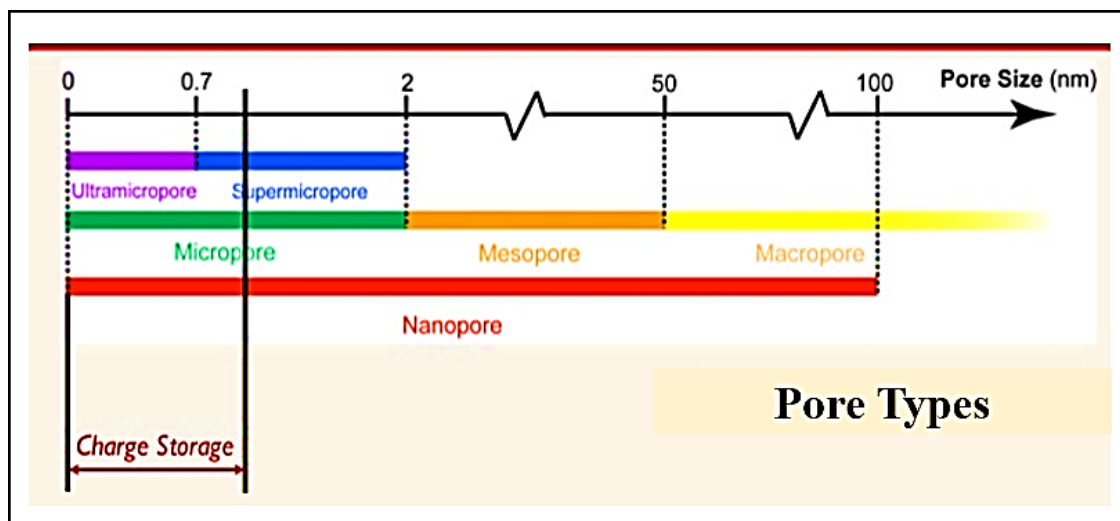


Figure 1.10. Pore classification of different pore size parameters.^[36]

They are typically synthesized by utilizing different carbon precursors by applying a heat treatment under an inert atmosphere, which results in different degrees of graphitization on their base frame. Figure 1.11. represents the several nanostructured carbons in EDLCs.^[41]



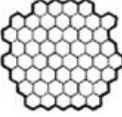
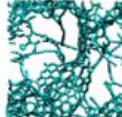
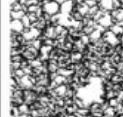

Material	Carbon onions	Carbon nanotubes	Graphene	Activated carbon	Carbide derived carbon	Templated carbon
Dimensionality	0-D	1-D	2-D	3-D	3-D	3-D
Conductivity	High	High	High	Low	Moderate	Low
Volumetric Capacitance	Low	Low	Moderate	High	High	Low
Cost	High	High	Moderate	Low	Moderate	High
Structure						

Figure 1.11. Different carbon structures are used in EDLCs.^[37]

Among the various forms of carbons, ‘**activated carbons**’ are widely used in industries because of their SSA ($\sim 1000 - 3000 \text{ m}^2 \text{ g}^{-1}$), which is required to maximize capacitance values. However, SSA is not the only relevant parameter to achieve high specific capacitance values, the presence of hierarchical porosity can also help to fasten the ions diffusion processes.^[35, 41] A high SSA carbon material along with mixed porosity (mesopores 20-30% along with micropores) enhances

the electrochemical performance to support high-power.^[42] Thus, porosity parameters are highly important to get a good performance in carbon electrodes. Precursors, such as coal pitch, petroleum pitch, and some polymers exhibit liquid phases during carbonization. Figure 1.12. represented the hierarchical porous structure of an activated carbon.

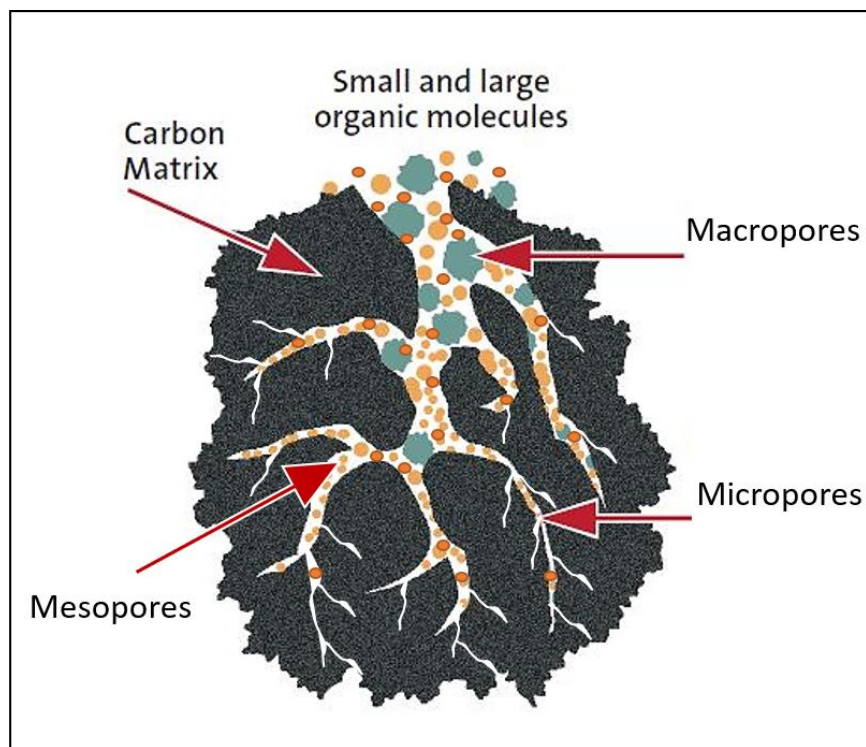


Figure 1.12. Hierarchical porosity distribution outline in activated carbons.^[43]

Consequently, the carbons made from those precursors can maintain highly ordered graphitic layers and are known as soft carbons. Whereas carbons from compound precursors, such as biomass (woods, coconut shells) and thermosetting polymers (PVC, PVDC) do not provide ordered graphitic structures, even by applying high-temperature treatments and are considered as hard carbons.^[21, 44] In such cases, the volatile component releases during the heat treatment that produces porous structures within the carbon frame.

Numerous activation approaches for the preparation of high SSA carbons are described in the literature. There are two typical activation processes: physical and chemical. In the physical activation process, the carbon reacts with the water molecules present on the carbon frame under heat treatment (temperature $\sim 700-1000^{\circ}\text{C}$) and releases H_2 , CO , or CO_2 gases. However, chemical activation needs an activating/dehydrating agent [MCl_n or $\text{M}(\text{OH})_n$ where M: Na, K,

Zn and n:1, 2], which reacts with carbon and produces M_2CO_3 , M_2O , and H_2 gases during the carbonization (temperature $\sim 400\text{-}700^\circ\text{C}$).^[21, 38, 44]

After carbonization, acid wash is required to remove the metal precursors and a high SSA carbon where the pores are much wider than the physical activations.

Templated microporous carbon has also drawn research attention for the past few decades. Template systems provide highly ordered pores within the carbon frame which fasten the charge rate capabilities and overall storage capacities. Templated porous carbons are generally prepared by two methods, known as hard and soft templated synthesis. In the case of the hard-templated method, silica, zeolite, and metal-organic framework are introduced as templates along with carbon precursors (Figure 1.13).^[21, 44]

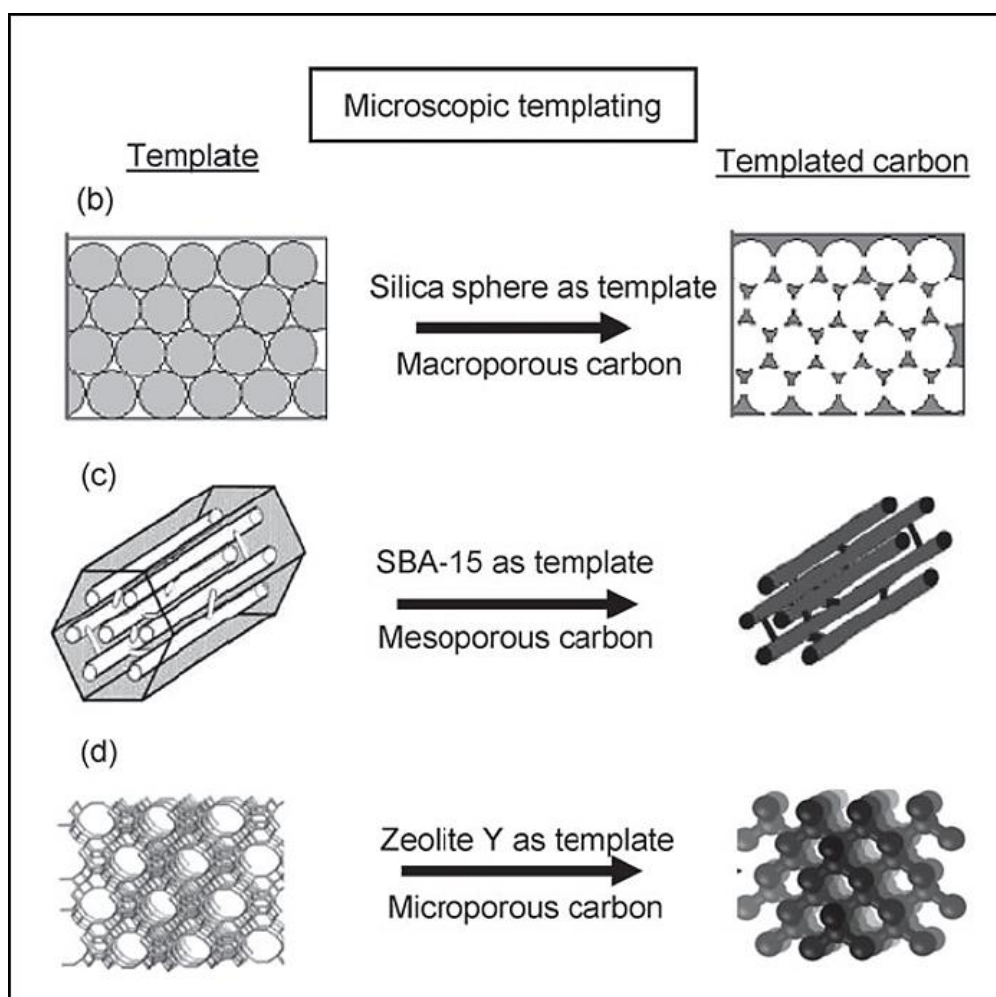


Figure 1.13. Schematic representation of the templating synthetic approach.^[39]

The carbonization is followed by an acid wash to obtain a template free highly ordered porous carbon replica. Consequently, the soft templated method requires an organic structure-directing agents to create porous carbon structures, such as surfactant molecules, block copolymers, or liquid crystals.^[21, 44-45]

The carbon surface morphology and ordered porosity can be tailored by carefully controlling the carbon precursor and the types of template. However, their synthesis usually involves several steps and the removal of the sacrificial template with strong acids is not environmentally benign. Thus, both are time-consuming approaches and difficult to scale up, and the cost of these methods limits their use for commercial energy storage applications.

Graphene and graphene oxide are new advanced carbon material with a special 2D hexagonal lattice that distinguishes them from other carbons.^[46] Graphite consists of tightly stacked sheets of a highly ordered carbon frame, which has angstrom level interspacing between the basal plane of each graphene layer due to strong π - π interactions. The combination of mechanical robustness, excellent electrical conductivity, and high theoretical SSA ($2630 \text{ m}^2\text{g}^{-1}$) makes graphene a promising electrode material for energy storage applications.^[47] However, the main drawback of graphene-based materials is their restacking tendency. Restacking reduces the surface area as well as capacitance. Thus, in most cases, these materials suffer from low-density issues which gives adverse effects in volumetric terms in performance indicators.

In literature, several methods are being studied to lower the agglomeration and restacking issues of graphene (Figure 1.14).^[48] Among them, “top-down”(Mechanical exfoliation/ milling of graphite, chemical exfoliation of graphite, etc.) and “bottom-up”(Epitaxial growth, chemical vapor deposition or CVD, etc.) are two types of approaches used in the fabrication of graphene.

The top-down approach involves the exfoliation of graphite into its graphene sheets, whereas the bottom-up approach implements carbon molecules as building blocks for the attainment of graphene layers. In the top-down approach, the most known methods are ‘graphene synthesis from modified hummer’s method and ultrasonication’.^[49-50] Bottom-up approach generally yields higher quality graphene than top-down synthetic routes, but in contrast, since they need ultra-high vacuum conditions they are more expensive and difficult to be scaled up.^[48]

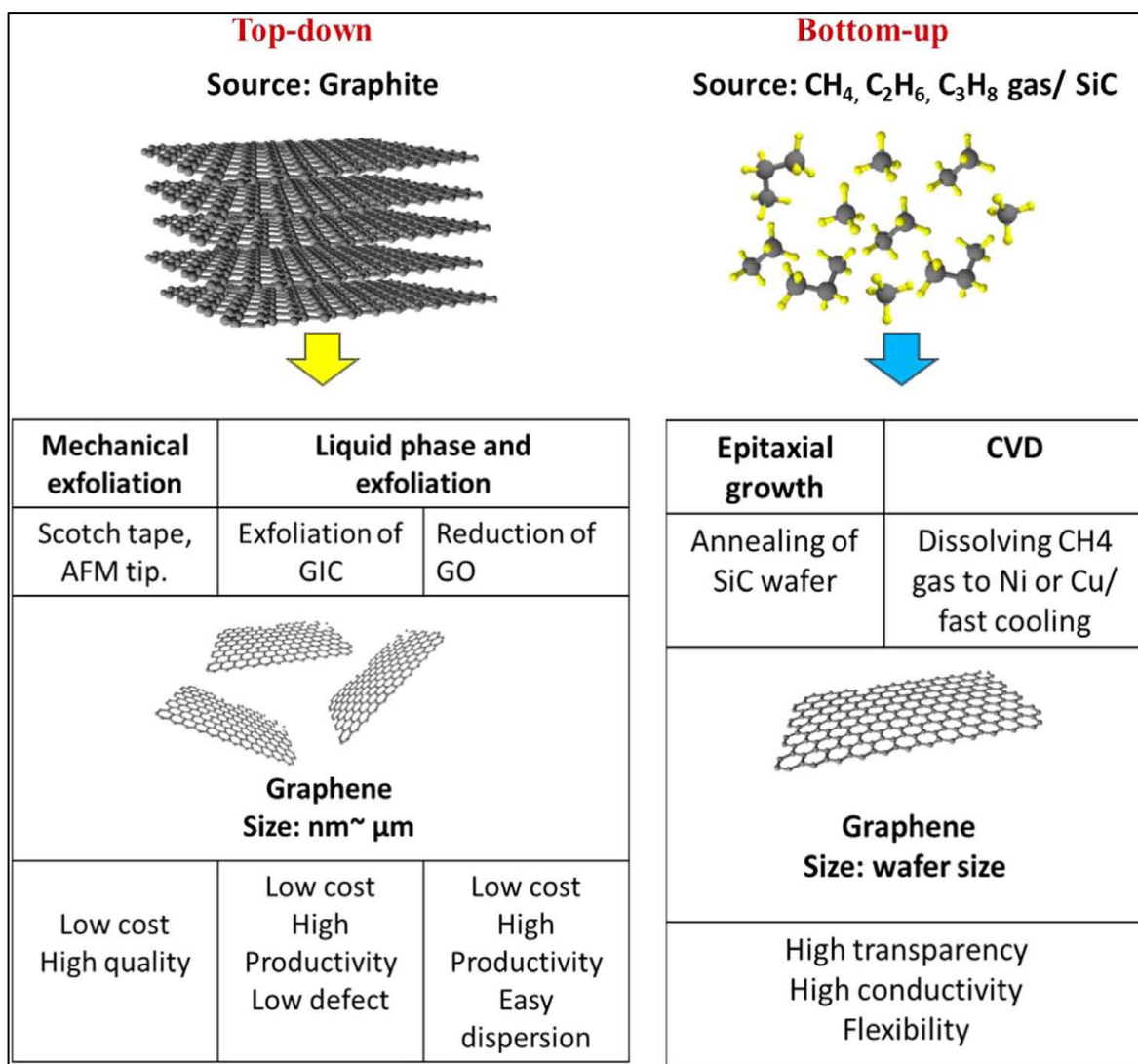


Figure 1.14. Schematic representation of several techniques involved in the production of graphene-based materials. ^[44]

Carbon nanotubes or CNTs as supercapacitor electrode material have drawn attention due to their relatively large SSA, excellent mechanical and thermal stability, and remarkable electrically conductive properties.^[21,35] CNTs can be categorized according to the number of graphitic walls, such as single-walled carbon nanotubes (SWCNTs) or multi-walled carbon nanotubes (MWCNTs). The graphitic planes generate electrically conductive carbon tubes. The most known method to produce CNTs is the CVD method. Compared to MWCNTs, SWCNTs show excellent capacitive performance, though the production process of SWCNTs generally suffers from high cost and scalable issues. Like CNTs, carbon onions have also quasi-spherical concentric graphitic

shells. The main advantage of carbon onions is the possibility to utilize the entire surface for electrolyte access very easily through its porous channels. Carbon onions, graphene, and CNTs are always a good choice for microsupercapacitors.^[21, 35, 51]

1.7.2. Pseudocapacitive materials

Some transition metal oxides and conductive polymers are additionally stored energy through interfacial redox reactions. Carefully selecting metal oxide components and their morphology, the charge storage can be boosted through easily accessible surface redox reactions. Whereas, in the case of conducting polymers charge storage mechanism includes the accumulation of charges *via* proton doping interactions on the overall material surface.

1.7.3. Transition metal oxides

Transition properties of different metal oxides, such as ruthenium (RuO_2), vanadium (V_2O_5), and manganese (MnO_2) are widely used as pseudocapacitive materials because of their multiple oxidation states.^[52-54] These crystalline metal oxides are also highly conductive, which helps charge propagations on their lattice structure. However, in the case of hydrous metal oxides, conductivity is a major issue. To overcome this problem, metal oxides crystalline properties can be increased by the reduction of the active surface area via the removal of water and pore spacing in material structure.

RuO_2 , both amorphous or crystalline, shows very interesting properties such as chemical-thermal stability, high catalytic activity, or high electronic conductivity.^[53] RuO_2 exhibits high reversible capacitance and good long-term stability. However, RuO_2 exhibits such outstanding properties that favor its pseudocapacitive performance, its scarcity, and its high cost limits its application as an electrode in supercapacitors.^[52-54]

Therefore, vanadium, manganese, cobalt, and nickel oxides have emerged as the best alternatives when working in aqueous electrolyte (Table 1.3).^[52-55] Among them, manganese oxides have shown the best balance between performance compared to other oxides such as vanadium and niobium oxides. However, the capacitive performance of MnO_2 is limited by poor electronic conductivity.^[52, 54]

Table 1.3. Comparative specific capacitance values of transition metal oxides reported in literature.

Transition metal Oxides	Specific capacitance (F g ⁻¹)	Specific capacity (mA h g ⁻¹)
RuO ₂	768 ^[54]	172 ^[54]
MnO ₂	350 ^[55]	50 ^[54]
V ₂ O ₅	910 ^[55]	540 ^[55]
NiO	309 ^[55]	198 ^[55]
Co ₃ O ₄	382 ^[53]	229 ^[53]
MnCo ₂ O ₄	346 ^[53]	173 ^[53]
NiCo ₂ O ₄	1400 ^[53]	672 ^[53]

In recent times, many research investigations have been accomplished to increase the capacitive performance along with better electronic conductivity by using of multi-metallic compounds of cobalt, such as Mn-Co, Co-Ru, Co-Mo, Co-Al, Ni-Zn-Co, and Ni-Co.^[56-61] These materials can significantly enhance the energy density by giving specific capacitance about 2-5 times higher than monometallic oxides and these materials are often considered as battery-type materials.

Moreover, cobalt in combination with lithium has also exhibited excellent performance, such as LiCoO₂ is the first layered oxide type cathode material for batteries.^[54] Among the multi-metallic compounds of cobalt, a binary metal oxide, NiCo₂O₄, has been investigated to be a potential electrode material in the electrochemical energy storage system due to its excellent capacitance with high rate capability and also higher electronic conductivity compared to its monometallic counterparts.^[59, 61] Furthermore, a complete understanding of the relationship between the electrochemical characteristics and the microstructure of binary Ni-Co oxides for supercapacitors is still lacking. Several research efforts are involved to find more affordable synthesis methods to prepare and nanostructure Ni-Co oxides with an excellent capacitor performance.

1.7.4. Conductive Polymers

Conducting polymers show relatively higher conductivity, and capacitance values compared to carbon-based electrode materials.^[62] Several electrode configurations can be used for conducting polymers, in the case of n/p type configurations, that is, the assembly between a negatively charged (n-doped) and a positively charged (p-doped) polymer, provides a high energy density. The most common conducting polymers are polypyrrole (PPy), polyaniline (PANI), and poly-(3,4)-ethylenedioxythiophene (PEDOT).^[62-63] Among them, PANI is considered as the most efficient supercapacitor electrode material due to its high conductivity, remarkable capacity, and easy synthesis process. However, its mechanical instability induces the rapid degradation of overall electrochemical performance during long-term cycling operations. To avoid this limitation, a combination of PANI with carbon materials can strengthen the overall electrical and mechanical stability of PANI.^[64]

1.8. Electrolytes

Electrolyte provides ionic conductivity which accelerates charge compensation on each electrode in the cell, where the salt and the solvent are the main components of electrolyte. In supercapacitors, the most common electrolytes are aqueous- and organic-based.^[12, 65-66] The major limitation of an aqueous electrolyte is its low operating voltage of *ca.* 1.0 V (due to the thermodynamic decomposition of H₂O), whereas organic medium allows a much higher voltage window of about 2.7 V.^[12] Thus, the recent trend in the development of supercapacitors is interested in switching to an organic medium in comparison with aqueous.

Mostly commercial supercapacitors use organic electrolytes with a wide cell voltage of 2.7-3.0 V, based on aprotic solvents, *i.e.* acetonitrile (ACN) or propylene carbonate (PC) as carbonate-based solvents.^[12, 66] Despite the advantage of non-aqueous electrolytes, they suffer from low conductivity and low dielectric constant compared to aqueous electrolytes, which leads to power deterioration and low capacitance.^[12, 66] From a safety perspective also, organic solvents are highly flammable and toxic. Besides this, the cost is a major issue for organic electrolytes. Ionic liquids (ILs) are also another type of electrolyte, consists of organic salts with a lower melting point than room temperature, which can be used as a liquid state.^[67-68] The main advantages of ILs are their non-volatility and broad operational potential window within a wide-ranging

temperature, though its low ionic conductivity, high viscosity, and high cost limit their applications. [67-68]

The electrolyte properties depend on: (a) the ionic size and mobility; (b) the solubility of the salt in a solvent; (c) the solvent and ion concentration; (d) viscosity; (e) reactions concerning the ion and the solvent; (f) electrode-electrolyte interactions; and (g) the operating potential window.^[12, 66] Those parameters have a significant influence on the overall capacitance as well as the energy/power densities and also on long term operation. Different characteristics of electrolyte ions are given in table 1.4.

Table 1.4. Relevant properties of ions commonly used in aqueous electrolytes. *a*, *b* and *c* sourced from [12], *d* sourced from [69]

Ion	Bare ion size (Å)	Hydrated ion size (Å)	Ionic conductivity (S cm ² mol ⁻¹)
H ⁺	1.15 ^a	2.80 ^a	350.1 ^b
Li ⁺	0.6 ^c	3.82 ^{a,c}	38.69 ^a
Na ⁺	0.95 ^c	3.58 ^{a,c}	50.11 ^a
K ⁺	1.33 ^c	3.31 ^{a,c}	73.5 ^a
SO ₄ ²⁻	2.90 ^c	3.79 ^c	160.0 ^a
Cl ⁻	1.81 ^c	3.32 ^{a,c}	76.31 ^a
NO ₃ ⁻	2.64 ^c	3.35 ^c	71.42 ^a
OH ⁻	1.76 ^d	6.3 ^d	198 ^a

1.8.1. Aqueous electrolytes

Aqueous electrolytes can be grouped into acidic, alkaline, and neutral. Within aqueous electrolytes, the most frequently used electrolytes are potassium hydroxide (KOH) as alkaline, sulfuric acid (H₂SO₄) as acidic, and sodium sulfate (Na₂SO₄) as neutral. The maximum ionic conductivity of 6M KOH is 0.6 S cm⁻¹ and 1 M H₂SO₄ is around 0.8 S cm⁻¹. [12, 66] Due to the

decomposition of the water molecule, the hydrogen evolution happens at 0.0 V *vs.* standard hydrogen electrode (SHE) and the oxygen evolution occurs at 1.23 V. Thus, the cell voltage of the aqueous electrolytes limited to *ca.* 1.0 V. Highly concentrated solutions are essential to minimize the equivalent series resistance or ESR, although acidic medium always tends to be more corrosive than the alkaline counterpart. Therefore, highly concentrated alkaline KOH or NaOH solutions are generally preferred. ^[12, 66] Unlike the low operational voltage window of both alkaline and acidic media, some neutral aqueous electrolytes (such as LiCl and Li₂SO₄) can provide higher stable cell voltages of up to 1.6-2.2V. ^[12, 66] This electrochemically stable extended potential window can be operated due to the presence of a lower concentration of H⁺ and OH⁻ in neutral pH electrolytes, which allows them to have a higher overpotential for H₂ and O₂ evolution reactions compared to the acidic and the alkaline electrolytes.^[70]

In general, the combination of ions size and high ionic conductivities of aqueous electrolytes benefits them compared to other types of electrolytes. Therefore, they can easily penetrate on to the electrode surface and this accessibility helps them to achieve higher capacitance values. ^[12, 66] Consequently, the presence of H⁺ and OH⁻ ions can also participate during the surface faradaic reactions by interacting with heteroatoms and their related functional groups, which also helps to obtain higher capacitance. ^[12, 66] Besides, the EDL capacitance in aqueous electrolytes is much higher due to their higher dielectric constant in an aqueous medium. For these reasons, the neutral electrolyte can be a promising choice for their non-corrosive properties but also highly cost-effective as well as environmentally friendly. ^[12, 66]

1.8.2. Organic electrolytes

Organic electrolytes are the most used ones in commercial devices. Tetraethylammonium tetrafluoroborate ((C₂H₅)₄NBF₄) salt dissolved in acetonitrile (ACN), or in propylene carbonate (PC) is the most common used electrolyte, where ACN is used because of its large dielectric constant which can provide high conductivity and PC is used for a better safety purpose though its conductivity is much lower than ACN, *i.e.* 15 mS cm⁻¹ *vs.* 60 mS cm⁻¹.

The operational voltage window of these solvents can easily reach up to 2.7~3.0 V. ^[12, 66] Moreover, organic electrolytes are less corrosive in nature because they allow the use of cheap and light current collectors, such as Al. Normally, organic-based electrolytes provide lower

specific capacitance compared to aqueous electrolytes, because of their larger solvated ion sizes and lower dielectric constants. Besides, in aqueous media, oxygenated functional groups undergo a fast redox reaction that contributes to additional pseudocapacitance due to the proton participation, but such contribution is not favored in the aprotic organic electrolytes. Therefore, adapting the ion size to the pore size of the electrode material can maximize the overall specific capacitance. [12, 66]

1.8.3. Ionic liquid (IL) electrolytes

ILs usually contain a large asymmetric organic cation and an inorganic/organic anion; thus, this special combination of cations and anions contributes to a low melting point. [67-68] IL can be classified into aprotic, protic, and zwitterionic according to their composition. Aprotic types are suitable for LIBs and supercapacitors, whereas protic is appropriate for fuel cells, and zwitterionic is useful for ILs based membranes. However, their highly viscous nature and low conductivity is the main drawback, that limits the overall rate performance and the power density in supercapacitor applications.

Mostly, Imidazolium based ILs have the highest conductivity, while pyrrolidinium based ones have a larger voltage window. [67-68] For practical applications, ILs still has limitation because of their high price and temperature-dependent phenomenon which involves ultra-stringent carbon drying process to go beyond the practical voltage of the solvent-based cell, resulting in the surplus overall cost of supercapacitors.

1.9. Cell configurations of electrochemical capacitor

Depending on the cell components and construction, supercapacitor technologies can be categorized into three different sections.

1.9.1. Symmetric and asymmetric capacitor

In symmetric systems, the charge storage mechanism should be the same in both electrodes. Mostly, the same type of electrode materials is used both as positive and negative, but the low potential window in this design persists a fundamental problem to maximize the energy density of the cell (Figure 1.15).

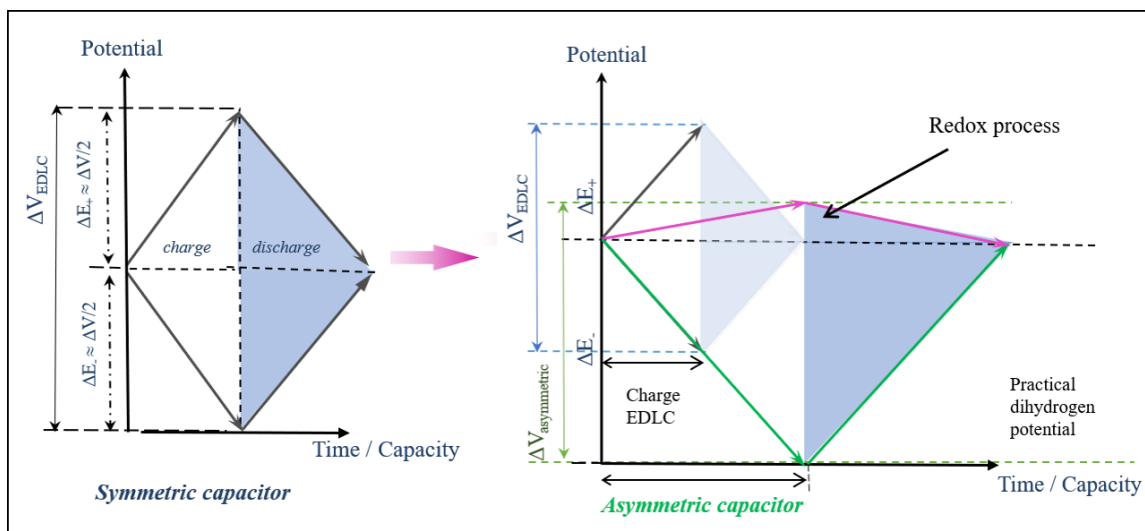


Figure 1.15. Schematic representation of the potential window span for the symmetric and asymmetric capacitor.^[22]

The development of an asymmetric system is a good alternative to improve performance in supercapacitor technology. This asymmetric system can be designed by various types of combinations, such as, ‘different nature capacitive-type electrodes’, ‘pseudocapacitive and capacitive-type’, and ‘capacitive-type and battery-type electrodes.’^[23-24] Among them, increasing the overall potential window by combining a pseudocapacitive material along with EDLC material has been proven to be an effective way to increase the energy density. The energy density is comparatively much higher (at least four to five times) than that of the asymmetric system. Despite these advantages, asymmetric systems restrain the stability for long term operations due to the degradation of the redox-active material, which affects the cycling performance of the cell.^[23-24]

1.9.2. Hybrid capacitor

A hybrid capacitor is a subclass of the asymmetric system with a special cell configuration, where one non-faradic and one faradic battery-type material are coupled in a single cell set-up.^[71] Figure 1.16 illustrates a hybrid system where one of the electrodes can store charges through ion insertion-extraction in the battery-type electrode material, while the capacitor-type electrode accumulates charge by ionic adsorption/desorption process. This configuration can store a high

amount of energy at low current by utilizing high-capacity battery-type material, simultaneously it can supply high power through non-Faradic material.

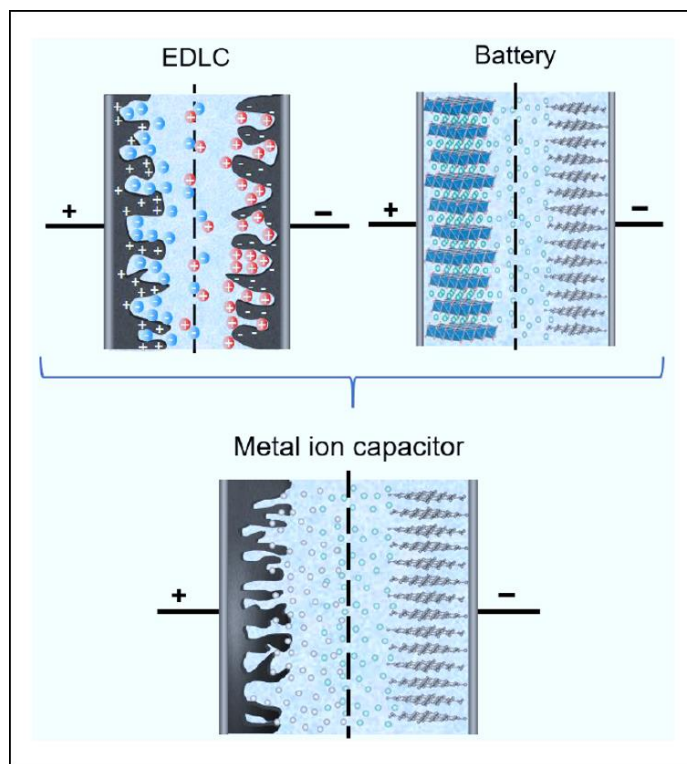


Figure 1.16. Hybridization of EDLC and Battery system to develop metal ion capacitors.

Hybridization of EDLC and battery type electrodes can be categorized into “internal series hybrids”/ISHs and “internal parallel hybrids”/IPHs.^[14] For ISH type, one battery-type electrode is coupled with one EDLC type electrode. The battery-type can work at a constant potential delivering high charge storage capacity, but their slow diffusion process limits capacity at high current.

On the other side, the capacitive-type material exhibits a linear (sloppy) potential profile, which limits their capacity but due to the fast ion diffusion process, they retain the capacity at high current. This ISH type hybridization can be seen in commercial LIC systems. Meanwhile, the IPH type hybridization uses a mixture of battery and capacitive electrode in each electrode, which provides much higher energy at low current, but it can also work at high current due to the capacitive electrode material. Thus, combining both faradic and non-faradaic mechanisms synergistically into a hybrid system allows not a moderate energy value at high power but also

able to maintain long-lasting cycle life. Therefore, their individual role can provide high energy density without compromising high power densities. A detailed comparative parameter of these different supercapacitor configurations is given in Table 1.5.

Table 1.5. Comparative parameters of the different supercapacitor configurations.^[13]

Parameters	Supercapacitor		Li-ion hybrid capacitor
	Symmetric	Asymmetric	
Internal resistance	Low	Low	medium
Voltage range	0-2.7	0-1.6	1.5-4.2
Discharge time	1-30 sec	1-30 sec	1-5 mins
Energy Density (W h Kg ⁻¹)	4-6	2-8	100-200
Power Density (kW Kg ⁻¹)	1-2	0.5-1	1-40
Cycle life	1000k	100k	100k
Self-Discharge	High	Medium	low
Safety	Highly stable	Highly safe	Moderately safe

1.9.3. Lithium-ion capacitor

Among the commercially available hybrid capacitor system, lithium-ion capacitors (LICs) are the most popular. Many different materials are evaluated as negative electrodes of the LIC system such as lithium titanium oxide (LTO), Lithium-compound and intermetallic-alloys, graphite, disordered carbon, etc.^[39, 71-72] On the other hand, high surface area activated carbons are mostly used as a positive electrode.

The LIC system comprising of lithium-intercalating carbons as negative, and high surface area carbon as positive is called “dual carbon LIC”. The energy storage capacity of dual carbon LICs is almost five times higher than the EDLCs with maintaining good power density and long cyclability. In this system, AC is generally used as a positive electrode, and various carbonaceous materials have been explored as battery-type negative electrodes, *eg.* Graphite, hard and soft

carbons, graphene.^[39, 73] Several carbonaceous battery-type materials can be pair with activated carbons (AC), such as graphite/ AC, hard carbon /AC, soft carbon /AC, Graphene/AC.^[35, 39, 72, 74] Figure 1.17 represents the schematic structural pattern of graphite soft carbon and hard carbon. It can be observed that the orientation of the graphitic layer is less parallel in soft carbons and the ultimate misorientation is prominent in hard carbon.

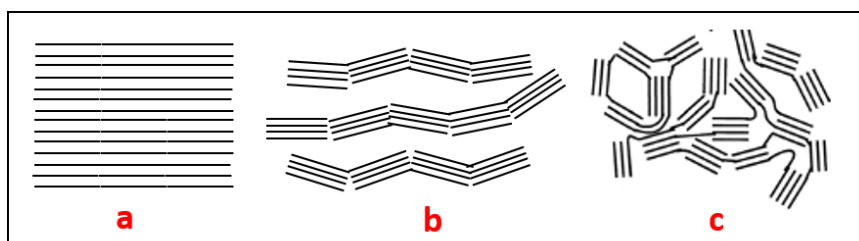


Figure 1.17. The textural pattern of (a) graphite, (b) soft carbon, and (c) hard carbon.^[75]

Among them, hard carbon (HC) has revealed promising results as a replacement of “graphite” is the most commonly used carbonaceous negative electrode material because of its disordered structure along with limited aligned crystalline graphite-like layers.^[74, 76-77]

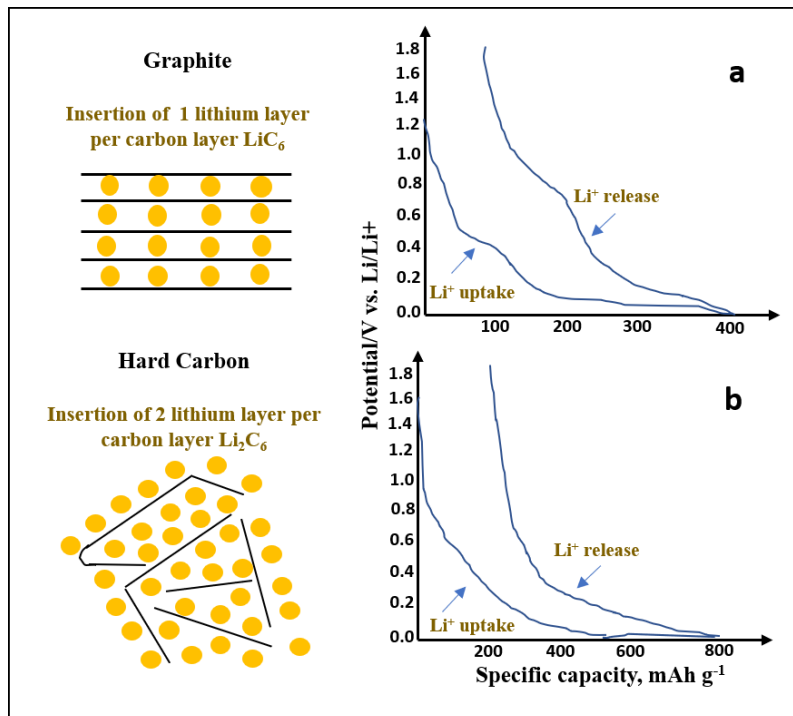


Figure 1.18. Structural illustration of the lithium consumption in the carbon layer and the typical charge/discharge profile of (a) graphite and (b) hard carbon.^[76]

This disordered pattern leads to doubling the theoretical capacity compared to graphite because of its nutshell like morphology can utilize more space for the insertion of the Li^+ ion on the graphite-like regions.^[71-72] Thus, using hard carbon can be the best alternative negative electrode instead of graphite in the dual carbon-LIC system. Figure 1.18 suggests that lithium ions can be placed on one side of a graphene layer in graphite, whereas in HC, each lithium layer can be inserted on both sides of it.

In contrast, disordered carbons as anode sometimes suffer from a steep decrease in cell voltage due to an imbalance of lithium-ion intercalation/de-intercalation process when associated with the voltage changes occurs in capacitive electrodes during the charge-discharge operations. This loss of anodic voltage range leads to a decrease in energy density.

To improve the energy density of the LIC device the pre-lithiation process in the anode can fulfill the excess demand of the lithium ions which cannot be achieved only from electrolytes. Thus, an additional internal sacrificial lithium metal electrode in the device helps to provide the abundant sources of Li^+ . This pre-lithiation not only suppresses the irreversible capacity of the negative electrode but also reduces the electrode resistance.^[78] Thus, a pre-doped carbon anode in LIC can provide 1.14 and 2.3 times higher the energy and power densities compared to using only pristine carbon LICs.^[79]

Besides lithium, other metals such as sodium (Na) are also getting attention in this hybrid supercapacitor research field. Although, the commercialization of this hybrid system is still relying on LICs.^[73, 80] Moreover, lithium-containing organic electrolytes are mostly used, which are almost the same as those used for LIBS, such as, salts of LiPF_6 , LiClO_4 , or LiTFSI in organic carbonate-based solvent mixtures chosen from ethylene carbonate, dimethyl carbonate, ethyl methyl carbonate, etc.^[66, 72]

Due to the wide electrochemical stability window obtained in these organic electrolytes (3-4.3V), these hybrid systems can deliver high energy densities (above 30 Wh kg^{-1}) than other supercapacitor configurations. The information regarding the commercial LIC cells available in the market several related based on different technology roadmaps are given in Table 1.6.

Table 1.6. Different parameters for state-of-art commercial LIC products.^[39]

Company	Cell Type	Work Voltage (V)	Capacitance (F)	Gravimetric Energy Density (Wh Kg ⁻¹)	Volumetric Energy Density (Wh L ⁻¹)	Cycles (n)
JM energy	Laminate	2.2-3.8	2100F	24	40	300 000
JM energy	Laminate	2.2-3.8	1100F	10	20	1000 000
General Capacitor	Laminate	2.2-3.8	3000	18	-	100 000
Taiyo Yuden	Laminate	2.2-3.8	200	10	20	100 000
Vina Technology	Cylinder	2.2-3.8	270	-	-	-
Aowei Technology	Module	2.2-3.8	9000	>20	>35	>30 000
Greenway	Cylinder	2.0-4.0	333	10.7	22.2	50 000

1.9.4. Working principles of dual carbon hybrid capacitors

Carbonaceous materials are always known for their mechanically and thermally very stable characteristics for a prolonged operation. In the organic EDLC system with a typical ACN based electrolyte, the obtained stable operating voltage is around 2.7V.

Meanwhile, in a hybrid system (an organic carbonate-based battery-type electrolyte), it can deliver around 4-5 times the higher energy density than EDLCs because of their wide potential range which is 4.2V. By modifying their internal configuration, a hybrid system can achieve a safe working potential window as schematically shown in Figure 1.19.

Using carbonaceous battery type material (such as Hard Carbon or graphite) provides higher capacities by storing charges through the insertion-deinsertion process, which widen the cell voltage output by increasing the upper potential. ^[39, 79, 81] Thus, the energy density is always higher compared to an EDLC system.

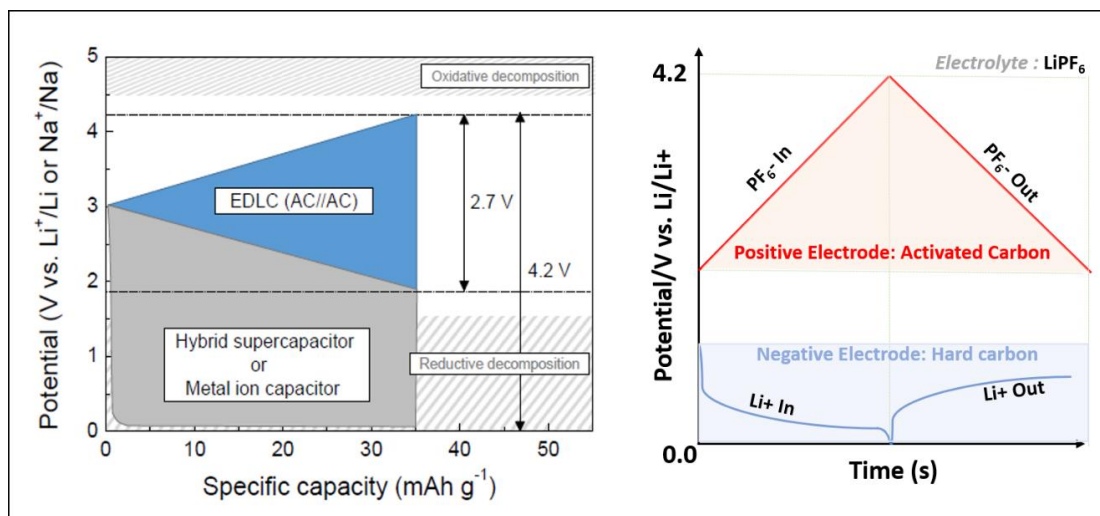


Figure 1.19. Typical voltage profiles of an EDLC and a hybrid supercapacitor (Left), and individual galvanostatic charge-discharge profile of a dual carbon LIC (hard carbon//AC).^[24]

On the other side, the capacitor-type electrode (Activated carbon/AC) can rapidly provide the fast-ionic diffusion process through its surface adsorption-desorption at a high current rate, which helps to obtain high power density. Combining both types of electrodes in a device facilitates not only its high-energy but also high-power densities along with a very stable cycle life. Thus, the dual carbon hybrid capacitor can work at high current densities without compromising its energy and power output.

In 2008, ULTIMO supercapacitors introduced the first commercialized LIC on the market and later they become known for their energy/power provider due to the improved energy density, higher cell voltage, and charge retention than the traditional EDLC supercapacitors. Besides, these LIC cells also contain incredible cycle life, fast charge/discharge rates, high power density, long-lasting with low maintenance cost. Their product line consists of both individual laminate and prismatic cells along with multi-cell modules and both designs differ significantly from the cylinder-shaped designs which are generally available in the LIC market. Some inherent defects directly affects the performance of the LIC unit (such as, limitation of anode material properties). It is quite challenging to overcome the defects of the material itself, such as graphite material suffers a poor compatibility issue with solvent and terrible C-rate performance. On the other way, hard carbon materials also have low efficiency for their highly irreversible capacity. Thus, to enhance the performance of the LIC, the development of applicable anode materials is crucial.

At present, several types of research are focused on the development of electrode materials and the improvement in production technology, which can help to reach the desired performance of high energy and high-power devices.

1.10. Research motivation

Although supercapacitors have the capability to provide high-power supply when it comes to high energy output there are still issues that need to be addressed. To overcome this issue most of the research and development have been focusing on the advancement of the high capacitive electrode materials, whereas smart design, selection of appropriate current collectors and deployment of the customized electrolyte can also make a significant improvement in the overall cell performance. However, these developments must also consider the cost and safety issues from the commercialization point of view. Thus, the general objective of this thesis is to contribute to the collective knowledge of the development efforts made in the arena of supercapacitors.

After the EDL system, asymmetric and hybrid systems in supercapacitors come forth with lots of attention in this era due to their excellent capability of providing high power density along with high energy density. Although in this sector, marked improvements can be noticeable in the area of electrode and electrolyte, there is still a lot of space for research to further upgrade the durability and safety issues. In this regard, EDL supercapacitors have a huge reputation for their very safe operation, whereas asymmetric and hybrid systems are still lacking full assurance. Thus, different approaches can be used to improve the safety of a hybrid system, such as variation in electrode masses or optimizing the operative potential window, etc. Careful optimization of these above-mentioned parameters during the development of the cell design needs to be considered for the sake of the best electrochemical performance.

Hence, the main focus of this thesis is not only to correlate the physicochemical properties of the new materials with its performance as an electrode, but also investigating the issues related to the applicability, development, or design of full cell systems from a perspective to understand the better electrochemical performance in different segments of supercapacitor configurations (EDL, asymmetric and hybrid). Therefore, this thesis emphasizes a detailed work on the improvement in the full cell performance by developing the high capacitive material of electrodes, selecting

the appropriate electrolytes, varying in the operative cell voltage, and optimizing the electrode mass balance. These different aspects can achieve not only the high energy and power densities but also to obtain good cycling stability without compromising its safety matters for the intended applications.

1.11. Specific objectives

To attain the main objective, several other partial intentions have been taken into considerations. Here in this thesis, four specific approaches are presented with different capacitive mechanisms, those will be developed and studied in detail for the supercapacitor application.

- Chapter 3 focuses on the development of a synthetic strategy of nanostructured carbon materials by a very simple method and the evaluation of their performance as electrode in **EDL capacitors** *using different electrolytes* to select the best active material/electrolyte match in terms of the capacitance value as well as rate capability and cyclability.
- Chapter 4 focuses on the synthesis of faradaic (metal oxide) and non-faradaic (porous carbon) material for the integration into a new **aqueous asymmetric supercapacitors**, and the optimization of the full cell by the *mass balance* between both electrodes.
- Chapter 5 focuses on the synthesis of battery-type and capacitive-type carbon electrode materials for the study of **dual-carbon hybrid LIC** performance. Here, the impact of *operative cell voltage optimization* is investigated to achieve the best electrochemical performance in terms of safe handling without compromising its energy and power output.
- Chapter 6 focuses the study of **dual-carbon hybrid supercapacitor** by *optimizing the electrode mass variation* in the negative and positive electrode in the LIC system and how this effort can make a significant change to utilize each electrode's working potential span which can be effective to improve the energy density at high current rates as well as its cycle life without worrying about safety issues.

Bibliography

1. Chu, S.; Cui, Y.; Liu, N., The path towards sustainable energy. *Nature materials* **2017**, *16*, 16-22.
2. Kuhns, R. J.; Shaw, G. H., *Navigating the Energy Maze*. Springer: 2018.
3. Raza, W.; Ali, F.; Raza, N.; Luo, Y.; Kim, K.-H.; Yang, J.; Kumar, S.; Mehmood, A.; Kwon, E. E., Recent advancements in supercapacitor technology. *Nano Energy* **2018**, *52*, 441-473.
4. IEA (2020), World Energy Balances: Overview, IEA, Paris <https://www.iea.org/reports/world-energy-balances-overview>.
5. Global Energy statistical Yearbook 2020, <https://yearbook.enerdata.net/renewables/renewable-in-electricity-production-share.html>.
6. Gür, T. M., Review of electrical energy storage technologies, materials and systems: challenges and prospects for large-scale grid storage. *Energy & Environmental Science* **2018**, *11*, 2696-2767.
7. Akinyele, D.; Rayudu, R., Review of energy storage technologies for sustainable power networks. *Sustainable Energy Technologies and Assessments* **2014**, *8*, 74-91.
8. Mahlia, T.; Saktisahdan, T.; Jannifar, A.; Hasan, M.; Matseelar, H., A review of available methods and development on energy storage; technology update. *Renewable and sustainable energy reviews* **2014**, *33*, 532-545.
9. Khan, N.; Dilshad, S.; Khalid, R.; Kalair, A. R.; Abas, N., Review of energy storage and transportation of energy. *Energy Storage* **2019**, *1*, e49.
10. Hitachi Chemical Technical report. **2013**, 55.
11. Simon, P.; Gogotsi, Y., Materials for electrochemical capacitors. *Nature Materials* **2008**, *7*, 845-854.
12. Wang, G.; Zhang, L.; Zhang, J., A review of electrode materials for electrochemical supercapacitors. *Chemical Society Reviews* **2012**, *41*, 797-828.
13. Béguin, F.; Frackowiak, E., *Supercapacitors: materials, systems, and applications*. John Wiley & Sons: 2013.
14. González, A.; Goikolea, E.; Barrena, J. A.; Mysyk, R., Review on supercapacitors: Technologies and materials. *Renewable and Sustainable Energy Reviews* **2016**, *58*, 1189-1206.
15. Divyashree, A.; Hegde, G., Activated carbon nanospheres derived from bio-waste materials for supercapacitor applications—a review. *Rsc Advances* **2015**, *5*, 88339-88352.
16. Miller, J. R.; Burke, A. F., Electrochemical capacitors: challenges and opportunities for real-world applications. *The Electrochemical Society Interface* **2008**, *17*, 53.

17. Shao, Y.; El-Kady, M. F.; Sun, J.; Li, Y.; Zhang, Q.; Zhu, M.; Wang, H.; Dunn, B.; Kaner, R. B., Design and Mechanisms of Asymmetric Supercapacitors. *Chemical Reviews* **2018**, *118*, 9233-9280.
18. Yu, A.; Chabot, V.; Zhang, J., *Electrochemical supercapacitors for energy storage and delivery: fundamentals and applications*. CRC press: 2017.
19. Conway, B. E., *Electrochemical supercapacitors: scientific fundamentals and technological applications*. Springer Science & Business Media: 2013.
20. Grahame, D. C., The electrical double layer and the theory of electrocapillarity. *Chemical reviews* **1947**, *41*, 441-501.
21. Zhang, L. L.; Zhao, X., Carbon-based materials as supercapacitor electrodes. *Chemical Society Reviews* **2009**, *38*, 2520-2531.
22. Goikolea, E.; Mysyk, R., Nanotechnology in Electrochemical Capacitors. In *Emerging Nanotechnologies in Rechargeable Energy Storage Systems*, Elsevier: 2017; pp 131-169.
23. Mathis, T. S.; Kurra, N.; Wang, X.; Pinto, D.; Simon, P.; Gogotsi, Y., Energy storage data reporting in perspective—guidelines for interpreting the performance of electrochemical energy storage systems. *Advanced Energy Materials* **2019**, *9*, 1902007.
24. Lukatskaya, M. R.; Dunn, B.; Gogotsi, Y., Multidimensional materials and device architectures for future hybrid energy storage. *Nature communications* **2016**, *7*, 1-13.
25. Liu, Y.; Jiang, S.; Shao, Z., Intercalation pseudocapacitance in electrochemical energy storage: recent advances in fundamental understanding and materials development. *Materials Today Advances* **2020**, *7*, 100072.
26. Schütter, C.; Pohlmann, S.; Balducci, A., Industrial requirements of materials for electrical double layer capacitors: impact on current and future applications. *Advanced Energy Materials* **2019**, *9*, 1900334.
27. Nybeck, C. N.; Dodson, D. A.; Wetz, D. A.; Heinzl, J. M., Characterization of Ultracapacitors for Transient Load Applications. *IEEE Transactions on Plasma Science* **2019**, *47*, 2493-2499.
28. Yassine, M.; Fabris, D., Performance of commercially available supercapacitors. *Energies* **2017**, *10*, 1340.
29. Kim, B. K.; Sy, S.; Yu, A.; Zhang, J., Electrochemical supercapacitors for energy storage and conversion. *Handbook of Clean Energy Systems* **2015**, 1-25.
30. Miller, J. R., Engineering electrochemical capacitor applications. *Journal of Power Sources* **2016**, *326*, 726-735.
31. Capa vehicle, https://en.wikipedia.org/wiki/Capa_vehicle.

-
32. GREENTECH TRAM, <https://www.caf.net/en/ecocaf/nuevas-soluciones/tranvia-greentech.php>.
 33. Kaohsiung's first steps to a tram future , <http://www.tautonline.com/kaohsiungs-first-steps-to-a-tram-future/>.
 34. Skeleton Technologies' Ultracapacitors to Power Škoda Trams in Mannheim.
 35. Pandolfo, A. G.; Hollenkamp, A. F., Carbon properties and their role in supercapacitors. *Journal of Power Sources* **2006**, *157*, 11-27.
 36. Wang, X.; Liu, L.; Niu, Z., Carbon-based materials for lithium-ion capacitors. *Materials Chemistry Frontiers* **2019**, *3*, 1265-1279.
 37. Dunn, B.; Kamath, H.; Tarascon, J.-M., Electrical energy storage for the grid: a battery of choices. *Science* **2011**, *334*, 928-935.
 38. Roberts, A. D.; Li, X.; Zhang, H., Porous carbon spheres and monoliths: morphology control, pore size tuning and their applications as Li-ion battery anode materials. *Chemical Society Reviews* **2014**, *43*, 4341-4356.
 39. Li, G.; Yang, Z.; Yin, Z.; Guo, H.; Wang, Z.; Yan, G.; Liu, Y.; Li, L.; Wang, J., Non-aqueous dual-carbon lithium-ion capacitors: a review. *Journal of Materials Chemistry A* **2019**, *7*, 15541-15563.
 40. Liu, T.; Zhang, F.; Song, Y.; Li, Y., Revitalizing carbon supercapacitor electrodes with hierarchical porous structures. *Journal of Materials Chemistry A* **2017**, *5*, 17705-17733.
 41. Simon, P.; Gogotsi, Y., Capacitive energy storage in nanostructured carbon–electrolyte systems. *Accounts of chemical research* **2013**, *46*, 1094-1103.
 42. Díez, N.; Mysyk, R.; Zhang, W.; Goikolea, E.; Carriazo, D., One-pot synthesis of highly activated carbons from melamine and terephthalaldehyde as electrodes for high energy aqueous supercapacitors. *Journal of Materials Chemistry A* **2017**, *5*, 14619-14629.
 43. Activated Carbon, <https://www.elgalabwater.com/technologies/activated-carbon>.
 44. Benzigar, M. R.; Talapaneni, S. N.; Joseph, S.; Ramadass, K.; Singh, G.; Scaranto, J.; Ravon, U.; Al-Bahily, K.; Vinu, A., Recent advances in functionalized micro and mesoporous carbon materials: synthesis and applications. *Chemical Society Reviews* **2018**, *47*, 2680-2721.
 45. Panja, T.; Bhattacharjya, D.; Yu, J.-S., Nitrogen and phosphorus co-doped cubic ordered mesoporous carbon as a supercapacitor electrode material with extraordinary cyclic stability. *Journal of Materials Chemistry A* **2015**, *3*, 18001-18009.
 46. Lv, W.; Li, Z.; Deng, Y.; Yang, Q.-H.; Kang, F., Graphene-based materials for electrochemical energy storage devices: opportunities and challenges. *Energy Storage Materials* **2016**, *2*, 107-138.

47. Choi, W.; Lahiri, I.; Seelaboyina, R.; Kang, Y. S., Synthesis of graphene and its applications: a review. *Critical Reviews in Solid State and Materials Sciences* **2010**, *35*, 52-71.
48. Mahmoudi, T.; Wang, Y.; Hahn, Y.-B., Graphene and its derivatives for solar cells application. *Nano Energy* **2018**, *47*, 51-65.
49. Zaaba, N.; Foo, K.; Hashim, U.; Tan, S.; Liu, W.-W.; Voon, C., Synthesis of graphene oxide using modified hummers method: solvent influence. *Procedia engineering* **2017**, *184*, 469-477.
50. Ciesielski, A.; Samori, P., Graphene via sonication assisted liquid-phase exfoliation. *Chemical Society Reviews* **2014**, *43*, 381-398.
51. Plonska-Brzezinska, M. E.; Echegoyen, L., Carbon nano-onions for supercapacitor electrodes: recent developments and applications. *Journal of Materials Chemistry A* **2013**, *1*, 13703-13714.
52. Jiang, Y.; Liu, J., Definitions of pseudocapacitive materials: a brief review. *Energy & Environmental Materials* **2019**, *2*, 30-37.
53. Augustyn, V.; Simon, P.; Dunn, B., Pseudocapacitive oxide materials for high-rate electrochemical energy storage. *Energy & Environmental Science* **2014**, *7*, 1597-1614.
54. Choi, C.; Ashby, D. S.; Butts, D. M.; DeBlock, R. H.; Wei, Q.; Lau, J.; Dunn, B., Achieving high energy density and high power density with pseudocapacitive materials. *Nature Reviews Materials* **2019**, 1-15.
55. Kate, R. S.; Khalate, S. A.; Deokate, R. J., Overview of nanostructured metal oxides and pure nickel oxide (NiO) electrodes for supercapacitors: a review. *Journal of Alloys and Compounds* **2018**, *734*, 89-111.
56. Mai, L.-Q.; Yang, F.; Zhao, Y.-L.; Xu, X.; Xu, L.; Luo, Y.-Z., Hierarchical MnMoO₄/CoMoO₄ heterostructured nanowires with enhanced supercapacitor performance. *Nature communications* **2011**, *2*, 1-5.
57. Wang, Y.-G.; Cheng, L.; Xia, Y.-Y., Electrochemical profile of nano-particle CoAl double hydroxide/active carbon supercapacitor using KOH electrolyte solution. *Journal of power sources* **2006**, *153*, 191-196.
58. Wang, H.; Gao, Q.; Hu, J., Asymmetric capacitor based on superior porous Ni-Zn-Co oxide/hydroxide and carbon electrodes. *Journal of Power Sources* **2010**, *195*, 3017-3024.
59. Wu, Z.; Zhu, Y.; Ji, X., NiCo₂O₄-based materials for electrochemical supercapacitors. *Journal of Materials Chemistry A* **2014**, *2*, 14759-14772.
60. Malak, A.; Fic, K.; Lota, G.; Vix-Guterl, C.; Frackowiak, E., Hybrid materials for supercapacitor application. *Journal of Solid State Electrochemistry* **2010**, *14*, 811-816.

61. An, C.; Wang, Y.; Huang, Y.; Xu, Y.; Xu, C.; Jiao, L.; Yuan, H., Novel three-dimensional NiCo₂O₄ architectures: solvothermal synthesis and electrochemical properties. *CrystEngComm* **2014**, *16*, 385-392.
62. Mastragostino, M.; Arbizzani, C.; Soavi, F., Conducting polymers as electrode materials in supercapacitors. *Solid state ionics* **2002**, *148*, 493-498.
63. Li, J.; Xie, H.; Li, Y.; Liu, J.; Li, Z., Electrochemical properties of graphene nanosheets/polyaniline nanofibers composites as electrode for supercapacitors. *Journal of Power Sources* **2011**, *196*, 10775-10781.
64. Cheng, Q.; Tang, J.; Shinya, N.; Qin, L.-C., Polyaniline modified graphene and carbon nanotube composite electrode for asymmetric supercapacitors of high energy density. *Journal of Power Sources* **2013**, *241*, 423-428.
65. Béguin, F.; Presser, V.; Balducci, A.; Frackowiak, E., Carbons and electrolytes for advanced supercapacitors. *Advanced materials* **2014**, *26*, 2219-2251.
66. Zhong, C.; Deng, Y.; Hu, W.; Sun, D.; Han, X.; Qiao, J.; Zhang, J., *Electrolytes for electrochemical supercapacitors*. CRC press: 2016.
67. Eftekhari, A., Supercapacitors utilising ionic liquids. *Energy Storage Materials* **2017**, *9*, 47-69.
68. Balducci, A., Electrolytes for high voltage electrochemical double layer capacitors: A perspective article. *Journal of Power Sources* **2016**, *326*, 534-540.
69. Garcia-Gomez, A.; Barranco, V.; Moreno-Fernandez, G.; Ibañez, J.; Centeno, T.; Rojo, J., Correlation between capacitance and porosity in microporous carbon monoliths. *The Journal of Physical Chemistry C* **2014**, *118*, 5134-5141.
70. Lewandowski, A.; Olejniczak, A.; Galinski, M.; Stepniak, I., Performance of carbon-carbon supercapacitors based on organic, aqueous and ionic liquid electrolytes. *Journal of Power Sources* **2010**, *195*, 5814-5819.
71. Ding, J.; Hu, W.; Paek, E.; Mitlin, D., Review of hybrid ion capacitors: from aqueous to lithium to sodium. *Chemical reviews* **2018**, *118*, 6457-6498.
72. Cericola, D.; Kötz, R., Hybridization of rechargeable batteries and electrochemical capacitors: Principles and limits. *Electrochimica Acta* **2012**, *72*, 1-17.
73. Ajuria, J.; Redondo, E.; Arnaiz, M.; Mysyk, R.; Rojo, T.; Goikolea, E., Lithium and sodium ion capacitors with high energy and power densities based on carbons from recycled olive pits. *Journal of Power Sources* **2017**, *359*, 17-26.
74. Kim, J.-H.; Kim, J.-S.; Lim, Y.-G.; Lee, J.-G.; Kim, Y.-J., Effect of carbon types on the electrochemical properties of negative electrodes for Li-ion capacitors. *Journal of Power Sources* **2011**, *196*, 10490-10495.

75. Crabtree, G.; Kocs, E.; Trahey, L., The energy-storage frontier: Lithium-ion batteries and beyond. *Mrs Bulletin* **2015**, *40*, 1067-1078.
76. Loeffler, B. N.; Bresser, D.; Passerini, S.; Copley, M., Secondary lithium-ion battery anodes: From first commercial batteries to recent research activities. *Johnson matthey technology review* **2015**, *59*, 34-44.
77. Azuma, H.; Imoto, H.; Yamada, S. i.; Sekai, K., Advanced carbon anode materials for lithium ion cells. *Journal of power sources* **1999**, *81*, 1-7.
78. Holtstiege, F.; Bärman, P.; Nölle, R.; Winter, M.; Placke, T., Pre-lithiation strategies for rechargeable energy storage technologies: Concepts, promises and challenges. *Batteries* **2018**, *4*, 4.
79. Sivakkumar, S. R.; Pandolfo, A., Evaluation of lithium-ion capacitors assembled with pre-lithiated graphite anode and activated carbon cathode. *Electrochimica Acta* **2012**, *65*, 280-287.
80. Arnaiz, M.; Shanmukaraj, D.; Carriazo, D.; Bhattacharjya, D.; Villaverde, A.; Armand, M.; Ajuria, J., A transversal low-cost pre-metallation strategy enabling ultrafast and stable metal ion capacitor technologies. *Energy & Environmental Science* **2020**.
81. Arnaiz, M.; Nair, V.; Mitra, S.; Ajuria, J., Furfuryl alcohol derived high-end carbons for ultrafast dual carbon lithium ion capacitors. *Electrochimica Acta* **2019**, *304*, 437-446.

CHAPTER – 2

Physicochemical and electrochemical characterization
techniques

2.1. Experimental section

2.1.1. Reagents

Lists of chemicals and reagents used for the experiments are given in the following table 2.1.

Table 2.1. The details of the general materials used for the experiments.

Chemicals	Company
Resorcinol (mol wt. 110.11)	Sigma-Aldrich
Formaldehyde (≥ 36 wt.% in H ₂ O)	Sigma-Aldrich
FeCl ₃ ·6H ₂ O (97%)	Sigma-Aldrich
Hydrochloric acid (37%)	Sigma-Aldrich
Melamine (mol wt. 126.12)	Sigma-Aldrich
Terephthalaldehyde (mol wt. 134.13)	Sigma-Aldrich
Potassium hydroxide or KOH (mol wt. 56.11)	Sigma-Aldrich
Nickel (II) nitrate hexahydrate or Ni (NO ₃) ₂ ·6H ₂ O (mol wt. 290.79)	Sigma-Aldrich
Cobalt (II) nitrate hexahydrate or Co (NO ₃) ₂ ·6H ₂ O (mol wt. 291.03)	Sigma-Aldrich
Urea (mol wt. 60.06)	Sigma-Aldrich
Triton-X-100	Sigma-Aldrich
Aniline ($\geq 99.5\%$ -mol wt. 93.13)	Sigma-Aldrich
Pyrrole (98% -mol wt. 67.09)	Sigma-Aldrich
Ammonium persulfate ($\geq 98\%$ -mol wt. 228.20)	Sigma-Aldrich
Phosphoric acid (85% - mol wt. 98.00)	SAFC
Ethanol ($\geq 99.5\%$ -mol wt. 46.07)	Sigma-Aldrich
Glass fiber, Z242063	Whatmann®
Lithium metal foil, battery grade 7439-93-2	Rockwood
N-Methyl-2-pyrrolidone (NMP) 99.5%, 872-50-4	Sigma-Aldrich
Poly(vinylidene fluoride), 24937-79-9	Solef®

Carbon Black Super P®1333-86-4	TIMCAL, TIMREX®
1M LiPF ₆ in EC/DMC (1:1 v/v)	Solvionic
Li ₂ SO ₄	Sigma-Aldrich
1M TEABF ₄ in acetonitrile	Sigma-Aldrich

2.1.2. Apparatus

Huanyu teflon lined hydrothermal autoclave reactor, MMERT drying oven, CARBOLITE horizontal tubular furnace, TELSTAR LYOQUEST freeze dryer, THERMO SCIENTIFIC™ centrifuge, and HEIDOLPH hotplate & magnetic stirrer was used as the general equipment for the synthesis of materials.

2.2. Physicochemical characterization techniques

The development and optimization of supercapacitors require the understanding and correlation between the properties of the materials and their electrochemical behavior. Standard characterization techniques and protocols have been followed in order to optimize the electrode materials morphology-chemical compositions-textural parameters and its electrochemical behavior. Materials synthesized along this thesis have been characterized by different analysis methods. For physicochemical characterization, Electron microscopies (SEM and TEM), X-ray diffraction, Raman spectroscopy and Gas adsorption-desorption process are used. Synthesized materials have been processed to make electrodes and electrochemically characterized by cyclic voltammetry, galvanostatic charge-discharge and impedance spectroscopy to extract the essential information about their electrochemical behavior in electrolytes. The details of these techniques are briefly explained in the following section.

2.2.1. Electron microscopy

Electron microscopy is the most recognized standard tool to characterize morphology, particle size or shape of nanomaterials.^[1] The technique is widely well-known and considered for an wide range of analysis, from biomaterials to organic-inorganic materials. It can offer exceptionally high-resolution in nanometer range down to single atoms. For the design and synthesis of nanomaterials requires fundamental understanding of the relationship between their diffusion

differences and their structural properties. The optimization of material properties in nanoscale can only be realized by precise interpretation and control over size, composition, phase, strains. Thus, electron microscopy techniques are highly useful to study the core material morphological characteristics. Figure 2.1. provides the comparative characterization resolution regimes of the optical and electron microscope.

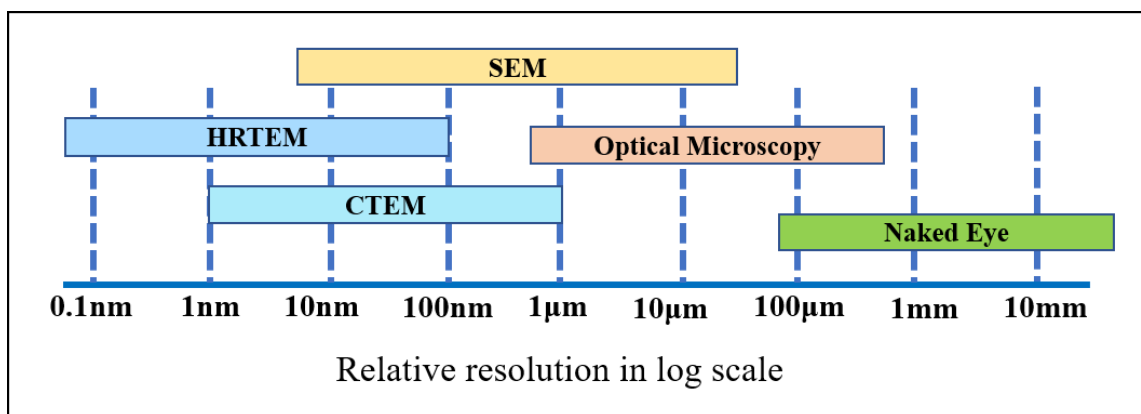


Figure 2.1. Working range of various microscopy techniques; CTEM: conventional transmission electron microscopy; HRTEM: high resolution electron microscopy.

A typical microscope includes several parts, such as electron beam, electron column, electromagnetic lenses, specimen holder, and a set of detectors. Besides, the methods generally require a proper inside vacuum environment. There are two main different types of EM are particularly useful in material characterization techniques: scanning electron microscopy and transmission electron microscopy.

2.2.1.1. Scanning electron microscopy

In scanning electron microscopy (SEM), the electron beam scans the sample in a raster pattern. Firstly, the electron source generates electrons, which are emitted due to their thermal energy when overcomes the work function of the source material. when, the primary electron beam penetrates the sample, the electrons are scattered and get absorbed in a zone, which is called as “interaction volume region”. ^[1] This interaction of the primary electron beam with the sample causes electron elastic scattering. Other side, the emission of secondary electrons results in inelastic scattering, and X-ray photon emission, each of which can be spotted by specialized detectors. A schematic representation of the technology of a SEM is shown in Figure 2.2.

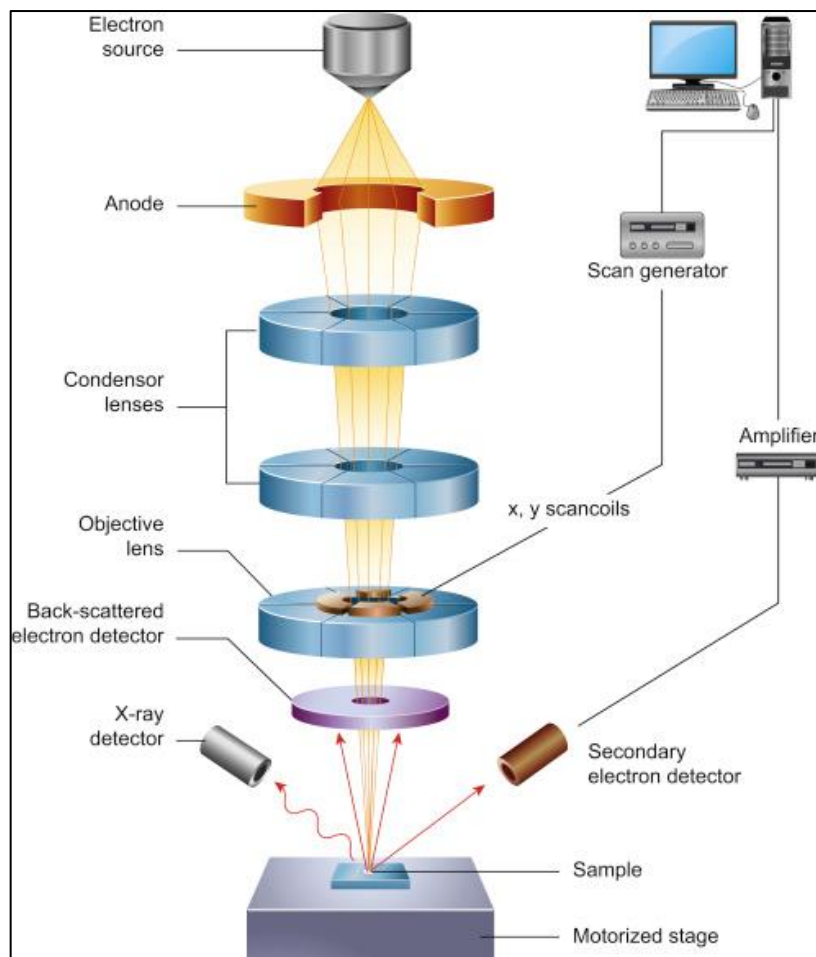


Figure 2.2. Schematic representation showing the core component of a SEM.^[2]

Secondary electrons can provide high-resolution images while backscattered electrons give lower resolution images. Though, backscattered electrons present different contrast pattern that depends on the composition of the multiphase of the topographic images. The information about crystal structure and the orientation of the minerals can be obtained from diffracted backscattered electrons while characteristic X-rays are generally used for elemental analysis. The maximum resolution of SEM images mainly depends on the electron spot size and the volume of the electron beam during the contact with the sample. It can resolve below 1 nm scale, but on average it is able to provide the image with a high resolution of 1-20 nm.

Energy-dispersive X-ray (EDX) spectroscopy is used to identify and quantify the elements present in the sample. This technique can be also used to evaluate the element distribution on the sample through map drawing. The chemical composition can be discerned by the X-ray emission,

during the interaction of electron beams with the specimen. When the sample is bombarded by the SEM electron beam, electrons are emitted from the atoms comprising the surface of the sample. Then, the electron vacancies are filled by electrons from a higher energy state. During this transition state from a higher energy state to a lower energy state, the created energy difference can be released as X-rays.

The SEM and EDX analysis data provided in this thesis were taken in FEI Quanta 200 FEG high resolution microscope (Figure 2.3.). The working voltage in this microscope is in the range of 3-30 kV and the maximum resolution is 3-5 nm.



Figure 2.3: FEI Quanta 200 FEG SEM (Themofischer).

2.2.1.2. Transmission electron microscopy

Transmission electron microscope (TEM) can acquire high resolution in the nanoscale range for the extremely shorter wavelength when applied electron beams can accelerate at several hundred kilovolts ($\sim 300\text{kV}$).^[3] Unlike SEM, in TEM the transmitted electrons beam pass through the

sample. TEM shows many characteristics of the sample, such as morphology, crystallization, or even magnetic domains, whereas SEM only shows the morphology of samples.

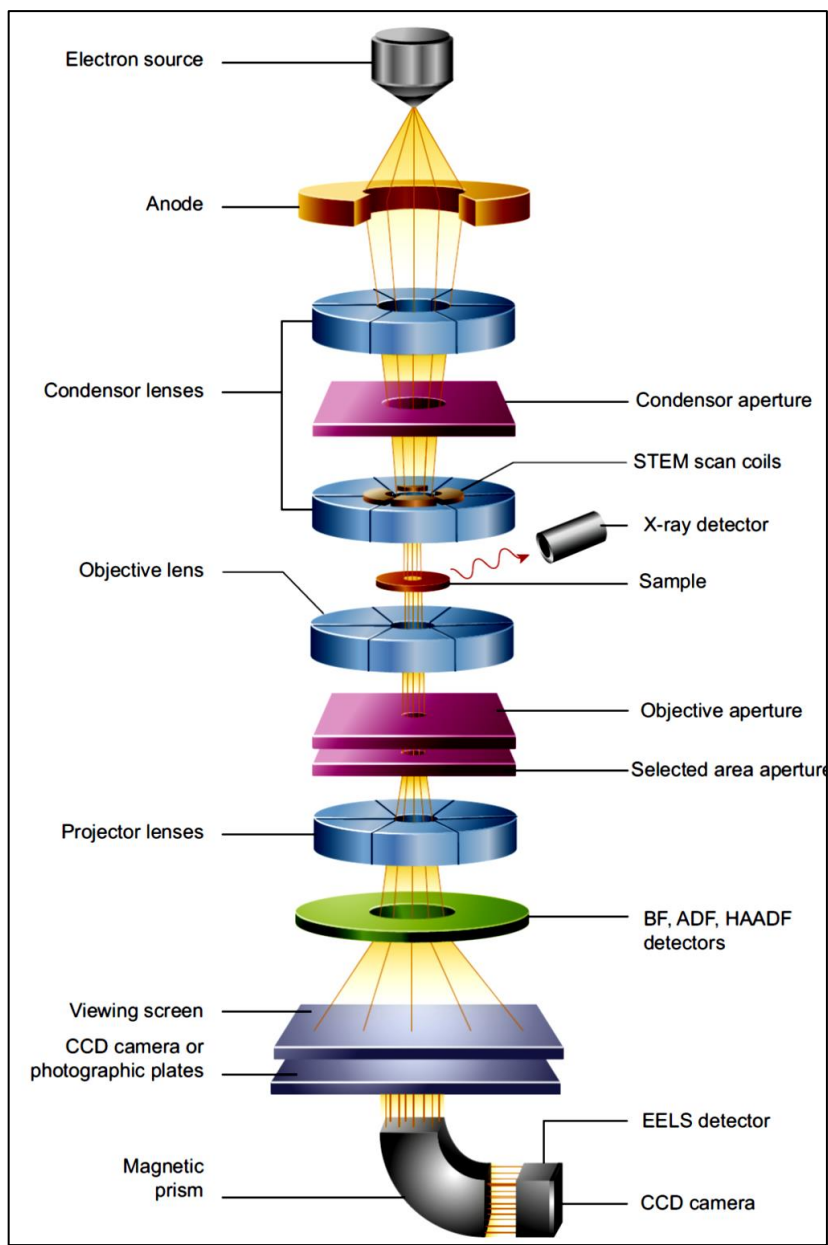


Figure 2.4. Schematic representation of the core components of a TEM.^[2]

Figure 2.4 shows the schematics diagram of a typical TEM microscope and the mechanism of its imaging system. TEM can also be utilized to detect the crystal structure and chemical composition of the materials. A high energy beam of electrons is transferred through a thin sample and the interaction between the specimen and the electrons produces the image. The

mechanism of the focusing of electrons is generally based on the wavelike characteristics of electrons, as they are negatively charged particles, they can be directly deflected by magnetic/electric fields. By applying condenser lenses in a TEM, the crystal structure information of a sample could also be obtained from parallelized electrons beams. The magnification of TEM varies within the range of 100X to more than 1000,000X. The image producing system contains electromagnetic lenses such as a condenser, objective, and a projective lens, as well as a movable sample stage, which helps to focus the electron beam through the sample. Finally, high-magnified TEM images can be obtained in a phosphorescent screen or charge-coupled device (CCD) camera.



Figure 2.5. FEI Tecnai G2 F20 S-TWIN TEM (Thermofischer).

The TEM analysis data provided in this thesis was taken in FEI Tecnai G2 F20 S-TWIN microscope equipped with a field emission gun operating at 200 kV (Figure 2.5.). The sample preparation was carried out by ultra-sonication of the powdered samples in ethanol followed by casting a few droplets of the dispersion on a holey carbon film fixed on a 3 mm copper TEM grid of 200 mesh.

2.2.2. X-ray diffraction.

X-ray diffraction (XRD) is a non-spectroscopic technique that is most widely used for the identification of unknown crystalline materials. The patterns registered from the interactions between the X-ray and the atoms provide information about the atomic structure of crystalline materials.^[4]

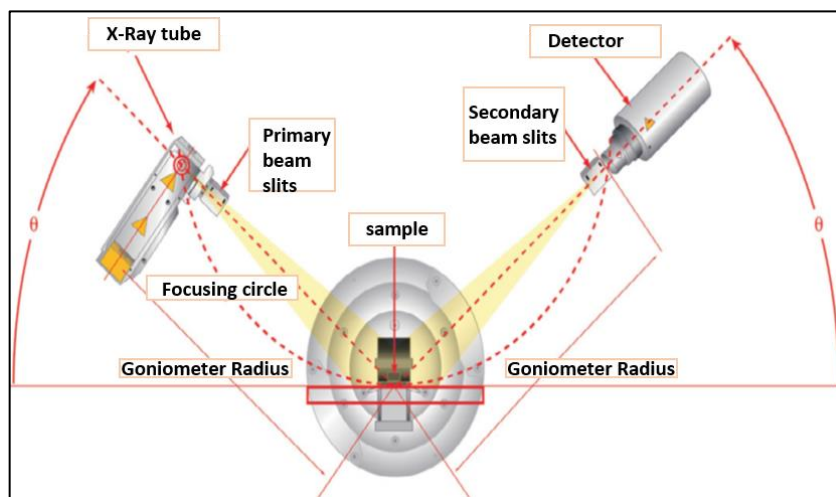


Figure 2.6. Schematic representation of the core components of X-ray diffractometer.^[5]

The X-ray diffractometer consists of three basic parts, which are X-ray tube, a sample holder and a detector (Figure 2.6). X-rays are generated in the X-ray tube by heating a filament to produce electrons and accelerates directly towards the target by applying voltage and then bombards the target material with electrons. When these electrons acquire sufficient energy to disrupt inner shell electrons of the target material, this produces the characteristic X-ray spectra. These X-rays are filtered through a monochromator to produce monochromatic X-rays required for diffraction analysis. The target used in most of the modern powder X-ray diffractometers are Cu, and it produces characteristic monochromatic radiation called Cu K_{α} with a wavelength of 1.5418 Å. Then this radiation is collimated and targeted to the sample holder. Then the radiations are reflected from the sample and recorded on intensity. Through the rotation of the sample holder, the interaction of the incident X-rays with the targeted sample produces constructive interference. This interference is recorded in a detector based on intensity in the form of diffraction peaks by fulfilling the Bragg's Law. ($n\lambda=2d \sin \theta$), where n is the integer, λ is the wavelength of electromagnetic radiation and θ is the diffraction angle, d is the lattice spacing in a crystalline

sample. The intensity vs. 2θ ($^{\circ}$) archetype attained from this technique provides a fingerprint of the crystal pattern of the studied material that gives more knowledge about the structure-phase and its crystallinity.

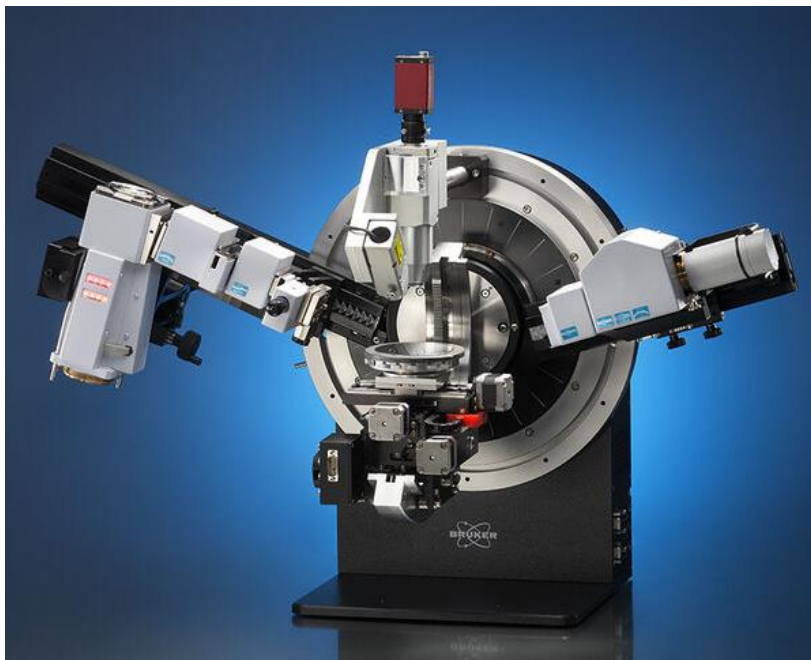


Figure 2.7. Bruker D8 discover XRD system.

The XRD patterns of the synthesized samples included in this thesis were measured by using Bruker D8 discover X-ray diffractometer (Figure 2.7.) for powdered samples and the data were attained at 40 kV and 30 mA using $\text{CuK}\alpha$ radiation over 2θ range from 5 to 90° with a step of 0.02° and a residence time of 5 seconds.

2.2.3. Raman Spectroscopy

Raman spectroscopy is a non-destructive analysis technique depend on the scattering interaction of light with the chemical bonds within a material. It can provide detailed information about chemical structure, crystallinity, phase, and molecular interactions in different types of materials ranging from inorganic to biological. It is primarily used to identify the vibrational modes of the different energy states of the studied molecule, while rotational and additional low-frequency modes of systems may also be uncovered.^[6] When a monochromatic light from a high-intensity laser light source hits an analyte molecule, inelastic and elastic scattering of light takes place. While most of the scattered light has the same wavelength as incident light (Rayleigh scattering)

and does not give any useful information, a small amount of light is scattered at different wavelength depending on the chemical structure of the analyte molecule (Raman scattering). Figure 2.8 shows the schematic outlook of basic Raman spectroscopic configuration. A typical Raman spectrum consists of several peaks, displaying the intensity and wavelength position of the Raman scattered light. Each of the peaks is a fingerprint of specific molecular bond vibration, including individual bonds (C-C, C=C, N-O, C-H) as well as a group of bonds (benzene ring breathing mode, polymer chain vibrations, lattice modes, etc.).^[7] Figure 2.4. shows the schematic diagram of the basic Raman spectroscopic configuration.

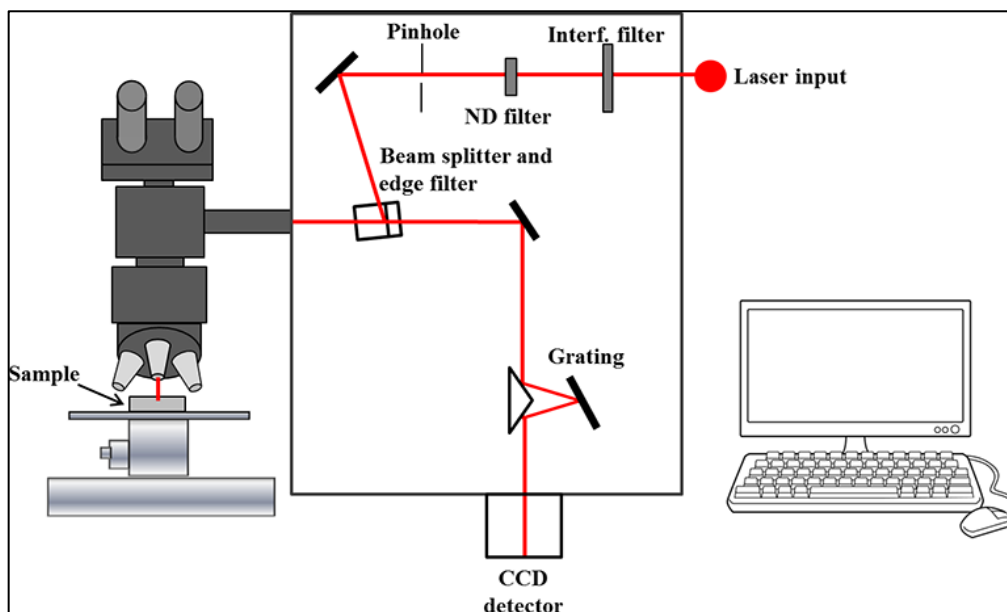


Figure 2.8. Schematic representation of the basic Raman spectroscopy configurations.^[6]

All the Raman spectra data for this thesis were recorded by a Renishaw spectrometer (Nanonics Multiview 2000), operating with an excitation wavelength of 532 nm under an Ar ion laser. The spectra were assimilated with an exposition time of 10 seconds of the laser beam to the sample.

2.2.4. Elemental Analyzer

Elemental analysis technique is used for the interpretation of the chemical elements in the organic and inorganic samples. By using the Elemental analyzer, the major elements such as carbon, hydrogen, nitrogen, and sulfur can be detected through gas chromatographic techniques.^[8] In commercial CHN and CHNS-O analyzers, oxidative decomposition starts after insertion of the

samples which leads to the subsequent reduction to form the final products, such as carbon dioxide (CO₂), water (H₂O), elemental nitrogen (N₂), and sulfur dioxide (SO₂) measured. An autosampler is generally connected to a reactor placed in the pre-set furnace (temperature ~900°C), once the gasification of the sample begins in the furnace, the chromatographic column starts to detect the analyzing component through a thermal conductivity detector. It also can identify different isotopes of the same element, which makes this instrument a versatile tool for isotopic labeling. The Flash 2000 elemental analyzer is used for the elemental analysis purpose in the thesis (Figure 2.9).



Figure 2.9. The Flash 2000 Elemental Analyzer.

2.2.5. Gas adsorption-desorption

Gas adsorption is a very well-known technique for the characterization of porous materials.^[9-10] In general, the physisorption takes place when an absorbable gas is approached to direct contact with the surface of a material. The information related to the specific surface area (SSA) and pore size distribution (PSD) of the material can be extracted from the adsorption-desorption isotherm.

N₂ gas adsorption at the temperature of -195.8°C is the widely used technique to determine the porosity of the material.

An updated classification of adsorption-desorption isotherm can be categorized into six types (Figure 2.10).

Type I has a prominent steep uptake at very low relative pressure P/P_o , which draws a concave curve with respect to the gas amount absorbed at Y-axis, and this typical isotherm is the characteristics of microporous materials. This is a very typical isotherm for high surface area activated carbon.

Type II isotherms are the characteristics of non-porous or macroporous absorbents, due to unrestricted adsorption of monolayer-multilayer at high relative pressure P/P_o . This type of isotherms can be seen in the case of CNT and carbon black.

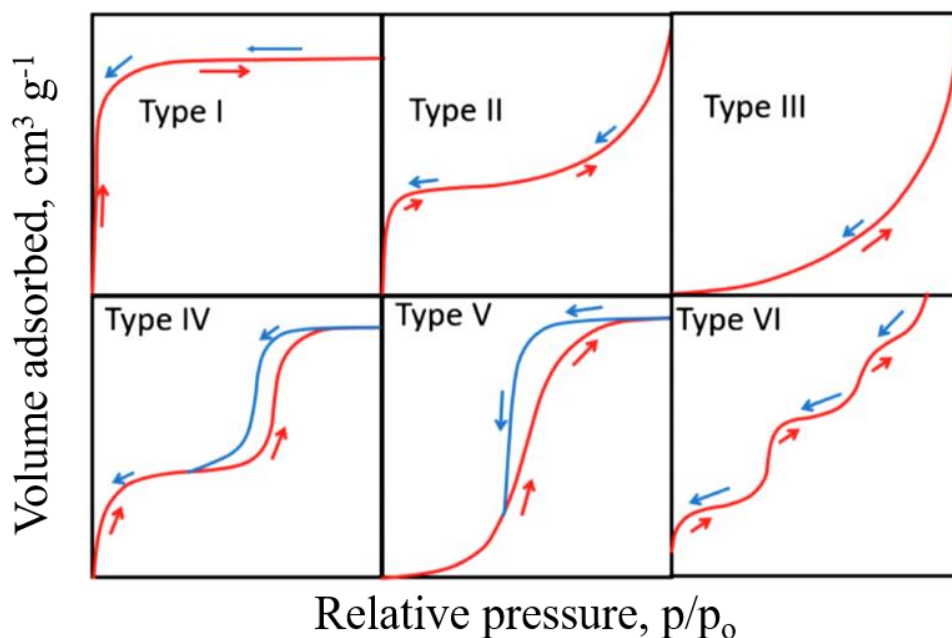


Figure 2.10. Different types of adsorption isotherms as classified by IUPAC.^[11]

Type III isotherms appear with a convex shape throughout the entire range of relative pressure. This also another characteristic for nonporous or macroporous solids, but those are very rare

cases. The interactions between adsorbent-adsorbate are generally very weak, thus the amount adsorbed at P/P_0 remains finite.

Type IV isotherms are very prominent characteristics of mesoporous adsorbents. First, capillary condensation occurs in mesopore, which limits the adsorption capacity over a broad range of relative pressure P/P_0 . The very initial steep path at a low relative pressure of this isotherm is quite resembled with the type II isotherm, thus this pattern can be attributed to the transition of adsorption from monolayer to multilayer. This type of isotherms is typical for templated carbons where mesopores are the main substance for tailoring the porosity.

Type V isotherm is the characteristic of weak adsorbent-adsorbate interactions like type III, mostly observed in the case of hydrophobic microporous and mesoporous adsorbents.

Type VI isotherm is typical of layer-by-layer adsorption on an extremely uniform non-porous surface.

Hysteresis is also an important factor like isotherms when the adsorption and desorption do not follow the same direction. It delivers information about the nature of patterns of pore present in the material.

H1 is known for well-defined cylindrical pore channels or agglomeration of uniform spheres. Mostly it is observed where the material consists of typical tubular-shaped pores open on both sides.

H2 is the type of disordered distribution of pores that are quite complicated to interpret. It is typical of “bottleneck” pores with a large body and narrow neck.

H3 differs from the above two hysteresis. It represents the slit-shaped pores or pores produced by plate-like agglomerations.

H4 is generally parallel with relative pressures but gas amount adsorbed vertical cycles resemble with H3 type, *i.e.* narrow slit form. In addition, this hysteresis with a type I adsorption isotherms indicates the presence of micropores.

According to the hysteresis pattern, we can determine the nature of pores present in the samples, which is given in Figure.2.11.

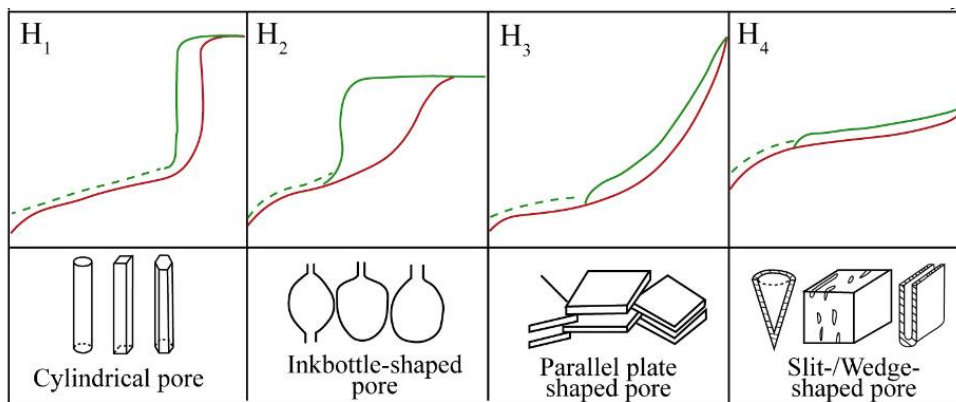


Figure 2.11. Schematic representation of different types of hysteresis patterns and the corresponding pore structures.^[12]

For this thesis, all the synthesized materials were characterized by N₂ adsorption/desorption technique. The analysis was carried out by using N₂ gas -195.8°C (77 K) using a Micromeritics ASAP 2020 instrument. Before the analysis samples were outgassed for 12 h at 250°C. Specific surface area values of some samples were calculated using the Brunauer, Emmett, and Teller (BET) model within a range of relative pressure 0.05–0.2, where P/P₀=0.95 in two steps. In the first step, the adsorption isotherm was transformed into the BET plot by using the following BET equation:

$$\frac{p/p^0}{n(1-p/p^0)} = \frac{1}{n_m C} + \frac{C-1}{n_m C} (p/p^0) \quad 1$$

Where n is the specific amount adsorbed at the relative pressure p/p^0 , n_m specific monolayer capacity and C is a parameter related to the energy of monolayer adsorption. In the second step the BET area was calculated from the monolayer capacity

$$a_s(BET) = n_m L \sigma_m / m \quad 2$$

For evaluation of pore size distribution of slit, cylindrical and spherical pores, several semi-empirical methods have been proposed by Horvath and Kawazoe (the HK method), Saito and Foley, and Cheng and Yang, respectively.

Despite their inaccuracy for pore size estimation, they have been popularly used to compare microporous materials. For more reliable analysis of pore size over the entire pore range, the microscopic analysis applied to the molecular behaviour of constrained fluids such as density

functional theory and molecular simulation are considered as better methods. Among the different models used to study different pore shapes, the non-local density functional theory (NLDFT) is extended in commercial software and allows more accurate measurement.

In this method, the pore size distribution function is calculated by correlating an experimental adsorption isotherm $N(p/p^0)$ with the core of a theoretical adsorption or desorption isotherms $N(p/p^0, W)$ based on the following equation:

$$N(p/p^0) = \int_{W_{min}}^{W_{max}} N(p/p^0, W) f(W) dW \quad 3$$

In this thesis, recently established 2D-NLDFT was used to measure SSA and PSD of the porous carbon materials from the adsorption isotherm using the data reduction software ‘SAIEUS’ (developed by Jacek Jagiello)

2.3. Electrochemical characterization techniques

All electrochemical measurements for this thesis were made using a VMP3 Potentiostat/Galvanostat/EIS (from BioLogic Science Instruments).

2.3.1. Cyclic voltammetry

Cyclic voltammetry (CV) can be considered as a qualitative and quantitative technique that provides the information during the interactions between the surface and solution of an electrochemical reaction. Thus, we can obtain the details about electrochemical kinetics, reaction reversibility, and mechanism. During CV measurements, the potential of a target/working electrodes can be measured in an electrochemical set up against the reference electrode through linear scanning back and forth between a specific potential range. As result of a recorded CV, the passing current via the working electrode is plotted as a function of the electrode potential.

In the case of ideal electrochemical double-layer capacitors (EDLCs), a typical rectangular profile can be noticed clearly. So, as the capacitance is constant, CV is formed by a straight line, and the capacitance (C) can be calculated from the following equation:^[13]

$$c (F) = \frac{q}{\Delta E} = \frac{\int_0^t I . dt}{\Delta E} = \frac{I}{v} \quad 4$$

where, q is the stored charge (c, coulomb), ΔE is a potential difference (V), I is the current (A), t is time (s), and v is the potential scan rate ($V s^{-1}$).

On an ideal supercapacitor, the increase in the sweep rate would produce a proportional increase in the current. However, in the case of a real device, if the potential scan rate is too fast, there is a restriction of ion diffusion on the entire surface area of the material resulting in slowing down the electrochemical kinetics. Thus, a decay of capacitance is noticed at higher scan rates.

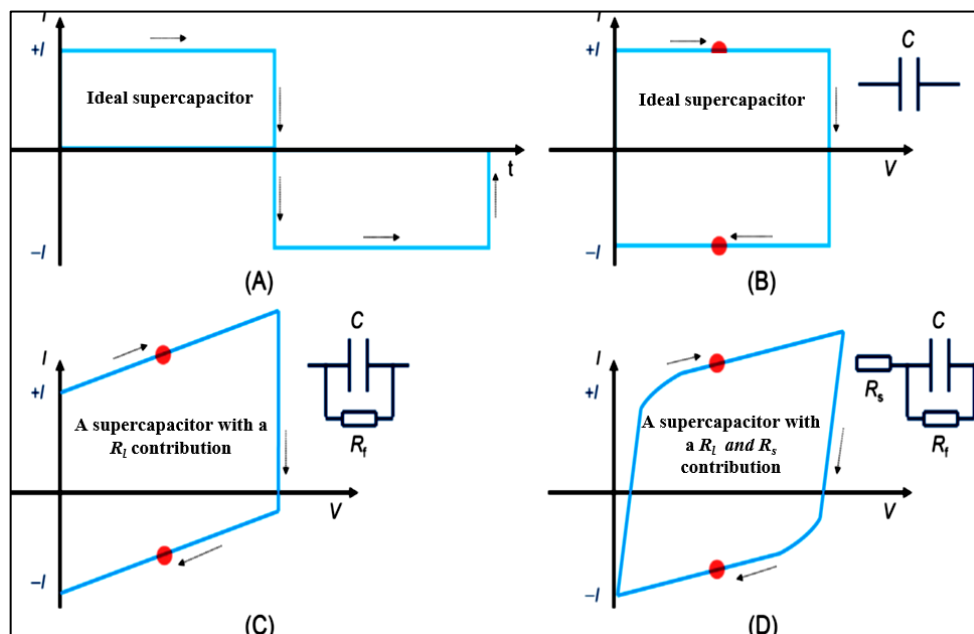


Figure 2.12. (a) i - t plot and (b) cyclic voltammograms and the respective equivalent circuits of an ideal supercapacitor. Cyclic voltammograms of a supercapacitor (c) with series resistance (R_s), and of (d) with series and leak resistance(R_l). [13]

Additionally, the continuous cycle of the CVs also provides the self-life of the studied material. If the material starts to degrade or decompose for a longer period, the loss in capacitance will be noticed in consecutive CV plots. Besides this, the shapes of CV cycles become much thinner or tilted which gives the indications of the resistive behavior of the material. However, CVs cannot be fully reliable as a precise electrochemical technique to determine capacitance values, especially for real supercapacitors. CVs can present leak resistance as R_l , and series resistance as R_s , which causes the distortions from the ideal rectangle shape. These deviations are increased at high scan rates, which make it more complicated to interpret the value of capacitance. The differences can be seen in figure 2.12.

2.3.2. Galvanostatic charge-discharge

Galvanostatic charge-discharge (GC/GD) measurements can be performed by using a fixed current within a potential range. In this technique, a constant current is applied within the fixed potential range to the working electrode and its resulting potential is measured against a reference electrode as a function of time. GC/GD measurements can be carried out in half-cell or full configuration. The typical curve provides the variation of the ‘potential vs. time’, from where we can calculate the stored charge, the capacitance and capacity values, the equivalent series resistance (ESR) of the working electrode along with the specific energy and power of the overall device.

The charge stored, q on electrodes can be calculated by the integral of the applied constant current and the consumed charge/discharge time. So, the capacitance (C) value of a device can be expressed as the following equations (Eq. 5 and 6)^[13]:

$$q = \int_0^t I(t) dt \quad 5$$

$$C (F) = \frac{q}{\Delta E} \quad 6$$

Furthermore, when charge/discharge cycles perform for a longer period, degradation in electrodes is often noticed, which can cause irreversible loss of capacity due to the continuous electrode-electrolyte reactions. Thus, Coulombic Efficiency (CE) is an important parameter to observe those capacity decay (Eq. 7).

$$CE (\%) = \frac{Q_{discharge}}{Q_{charge}} \quad 7$$

The specific cell capacitance (C_{SP}) values of supercapacitors studied in this thesis are calculated by the data obtained from the slope of the discharge curve, as shown in Eq. 8, where I is the applied current (A) and m_{AM} (mg) the mass of the active material. Moreover, the specific capacity (Q_{SP}), is calculated from the total discharge time, t_d , and the applied current, I , as shown in Eq. 9^[14]

$$C_{SP} (F g^{-1}) = \frac{I/m_{AM}}{dV/dt} = \frac{I}{Slope_{discharge} \cdot m_{AM}} \quad 8$$

$$Q_{SP} (mAh g^{-1}) = \frac{I \times (td)}{m_{AM}} \quad 9$$

The specific electrode capacitance in an asymmetric EDLC system can be measured by multiplying the specific cell capacitance by the factor of 4.

While the ESR values of GC/GD curves are calculated from the potential/voltage drop during the current inversion as shown in (Eq. 10),

$$ESR (\Omega) = \frac{\Delta E_{drop}}{\Delta I} \quad 10$$

In capacitors, the resistance in a system can be expressed as the ESR, which generates from interfacial contact, ionic diffusion hindrance, and electrolyte ionic resistances. Thus, a voltage drop can be seen during the charge or discharge steps.

For the capacitive type storage mechanism of EDL capacitors, the energy density is calculated from the linear type GC/GD plots following the (Eq. 11) by using the capacitance value and the square potential difference, where V_f is the voltage after iR drop and V_i is the lower cut-off voltage.. However, for the non-linear GC/GD characteristics of asymmetric and hybrid capacitor system with faradaic contribution, the energy density is calculated from integral calculation of the area under the GD curve (Eq. 12).^[14]

$$E (Wh Kg^{-1}) = \frac{C_{SP} \times (V_f^2 - V_i^2) \times 1000}{2 \times 3600} \quad 11$$

$$E (Wh Kg^{-1}) = \frac{I}{m_{AM}} \int_{t_1}^{t_2} V (t) dt \quad 12$$

Power density of hybrid devices has been calculated from the energy density and the discharge time (Eq. 13).

$$P (W Kg^{-1}) = \frac{E \times 3600}{\Delta t} \quad 13$$

2.3.3. Electrochemical impedance spectroscopy

Electrochemical impedance spectroscopy (EIS) is generally used to measure the ability of an equivalent circuit to resist to an electric current (AC) flow, which can provide accurate information about the charge transport properties in an energy storage device. In EIS process, the

response of an AC current signal is measured by applying a sinusoidal potential excitation. This sinusoidal signal is consecutively applied at different frequency range. The impedance ($Z(\omega)$) can be specified as a complex resistance of AC current and voltage and is expressed by Eq. 14:

$$z = \frac{\Delta V}{\Delta I} = |Z(\omega)|e^{-j\phi} = Z' + jZ'' \quad 14$$

Nyquist plot is a very well-known EIS plot, which demonstrates the absolute imaginary impedance vs. the real impedance. Figure 2.13. illustrates the Nyquist plots of capacitors.

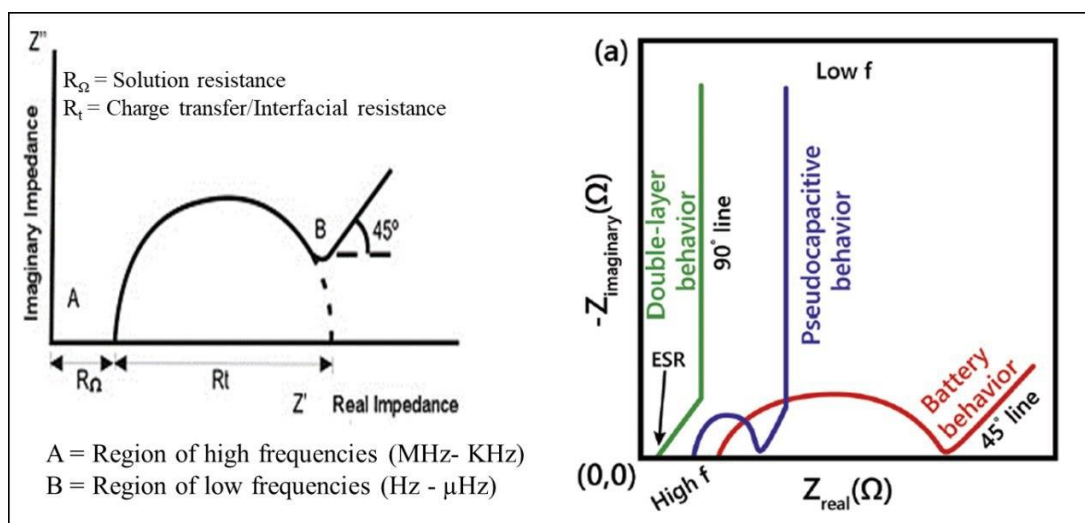


Figure 2.13. Illustration of Nyquist diagram.^[15]

When porous materials are used as electrode materials, the plot line tends to go upwards ($\sim 45^\circ$ angle) at the high frequency region that is followed by a quasi-vertical line, represents the ionic resistance inside the pores (diffusion kinetics). Additionally, a semicircle at high frequency represents the charge transfer resistance characteristics between the electrode and the current collector.

2.3.4. Electrode processing and cell assembly

For this thesis, different electrochemical set-ups were used for studying the electrochemical behavior of the material. Those are: (1) three-electrode configuration (Figure 2.9.), (2) two electrode configurations (Figure 2.10.). The three-electrode configurations were carried out either in a beaker cell or in a SwagelokTM T-type cells in aqueous or organic electrolytes using a working, counter and a reference electrode (Figure 2.14). The electrodes were prepared by mixing

Active material along with carbon black (CB) and polytetrafluorethylene (PTFE) in the presence of a few drops of ethanol. The dough was kneaded continuously until reaching plasticity, uniformly rolled until a thickness of 40-60 μm , punched out into disk shaped (12 mm in diameter), and finally dried at 120 $^{\circ}\text{C}$ overnight.

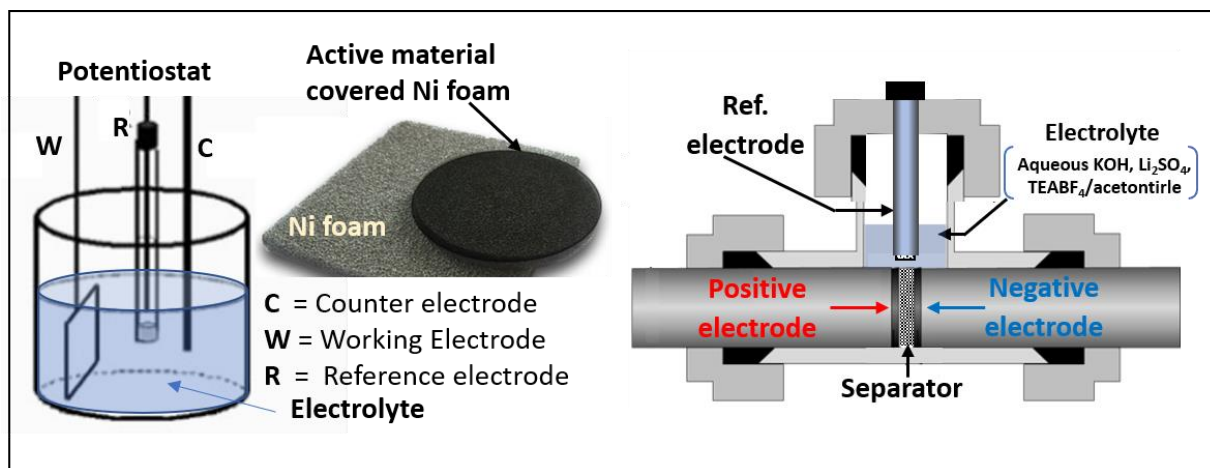


Figure 2.14. Three electrode configurations in a beaker cell (left) and Swagelok™ T-type cell for testing symmetric and asymmetric supercapacitor.

Working electrodes for beaker type cells were prepared by compressing these disk-shaped electrodes (2-4 mg cm^{-2}) onto a 2 mm thick Nickel foam (99.8% pure, MTI Corp.) that served as a current collector.

A Pt coiled wire was used as a counter electrode in the beaker type cell, which was cleaned prior to the measurements with acidic piranha solution (3:1 mixture of conc. H_2SO_4 conc and H_2O_2 (30 v/v %)) to remove any surface impurities. For Swagelok™ T-type cell, working and counter electrodes were made of the same carbon material. When aqueous alkaline electrolyte was used, a Hg/HgO (saturated in 1 M NaOH) electrode served as the reference electrodes, whereas a Hg/HgSO₄ in 0.1M K₂SO₄ served as the reference electrode for an aqueous neutral electrolyte. For Organic electrolyte Ag wire was used as a quasi reference electrode, which was polished with emery paper followed by surface etching in aqueous nitric acid to remove surface oxides.

In the case of a two-electrode configuration symmetric system, electrodes with similar masses were assembled into Swagelok™-type cells (Figure 2.15).^[16] The disk-shaped electrodes were prepared following the above-mentioned process by mixing Active material along with CB and

PTFE binder. A porous glass fiber (Whatman GFB) membrane was used as a separator between them and stainless-steel rods as current collectors. The electrodes and the separator were wetted with a few drops of aqueous electrolytes.

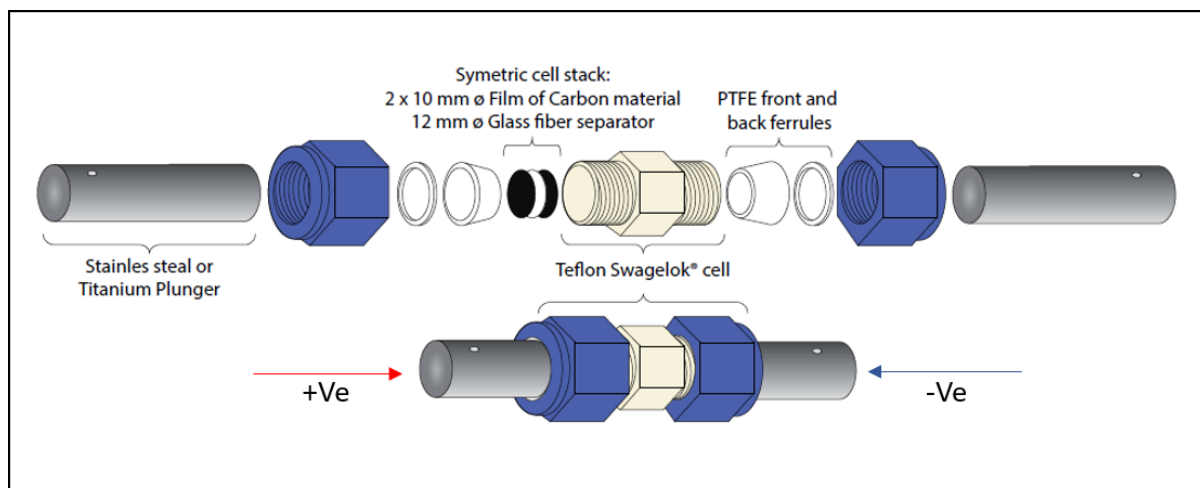


Figure 2.15. Two electrode configurations in a SwagelokTM-type cell.^[16]

For hybrid capacitor testing, three-electrode configuration SwagelokTM-type cells were used. The negative electrode slurry was prepared by mixing in a weight mass ratio of 90:5:5, (active material + Super-C C65 + CB) in presence of polyvinylidene fluoride (PVdF) binder in N-methyl-2-pyrrolidone (NMP) solvent. The components were mixed under vigorous stirring for at least 1 h using a magnetic stirrer. The obtained negative electrode material slurry was coated onto a copper foil current collector.

For the positive electrode slurry, the activated carbon, Super-C C65 and PVdF was mixed by following the same above-mentioned weight mass ratio in NMP solution under continuous stirring for 1 h and then the positive electrode material-based slurry was laminated onto an aluminum foil. Laminates were placed immediately into a vacuum oven for drying at 80 °C for 12 h under constant vacuum. The mass loading of the positive electrode was 1-1.5 mg cm⁻² while the loading in the negative electrode ranged from 1.5 - 3 mg cm⁻².

The electrochemical characterization of the anode was evaluated in a three-electrode configuration using an airtight Swagelok T-cell. Metallic Li was used as both the counter and the reference electrode, and the anode was cycled within the potential range of 0.002 V to 2V vs.

Li⁺/Li. The same cell assembly procedure was followed to perform the electrochemical characterization of the cathode within the 1.5-4.2 V vs. Li⁺/Li potential range.

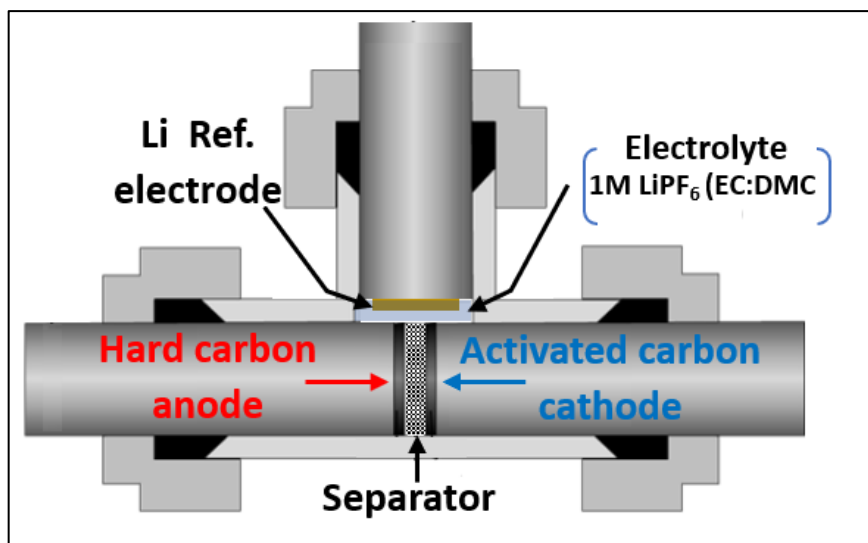


Figure 2.16. Three electrode SwagelokTM-type cell configurations for testing hybrid Lithium-ion capacitor.

Lithium hybrid supercapacitor full cells (negative//positive) were assembled using a three-electrode configuration (Swagelok T-cell) with a metallic Li reference that was chosen to record the individual electrode potential changes (Figure 2.16.). Stainless steel current collectors and a porous glass fiber separator (Whatman GFB) were used and the electrolyte used was 1 M LiPF₆ in EC:DMC (1:1). Before testing, both negative and positive electrodes were preconditioned to maximize the output voltage. Thus, the negative electrode was cycled at least five times between 0.002 and 2 V vs. Li/Li⁺ at 0.1C rate in order to form solid electrolyte interphase (SEI) and supply enough lithium to compensate the first irreversible cycle. After that, a cut-off potential of 0.2 V vs. Li/Li⁺ was set in order to evade any chances of lithium plating. The positive electrode was also charged up to a cut-off potential of 4.2 V vs. Li/Li⁺. After this pre-lithiation process, the LICs full cells were built for their extensive electrochemical characterization.

Bibliography

1. Bittner, A.; Koroteev, V., Characterization of Nanomaterials for Energy Storage. In *Emerging Nanotechnologies in Rechargeable Energy Storage Systems*, Elsevier: 2017; pp 171-193.
2. Inkson, B., Scanning electron microscopy (SEM) and transmission electron microscopy (TEM) for materials characterization. In *Materials characterization using nondestructive evaluation (NDE) methods*, Elsevier: 2016; pp 17-43.
3. Tang, C.; Yang, Z., Transmission electron microscopy (TEM). In *Membrane Characterization*, Elsevier: 2017; pp 145-159.
4. Epp, J., X-ray diffraction (XRD) techniques for materials characterization. In *Materials characterization using nondestructive evaluation (NDE) methods*, Elsevier: 2016; pp 81-124.
5. Powder X-ray Diffraction (XRD) <https://static.thermoscientific.com/images/D02513~.pdf>.
6. Downes, A.; Elfick, A., Raman spectroscopy and related techniques in biomedicine. *Sensors* **2010**, *10*, 1871-1889.
7. What is Raman Spectroscopy, https://www.horiba.com/en_en/raman-imaging-and-spectroscopy.
8. Fadeeva, V.; Tikhova, V.; Nikulicheva, O., Elemental analysis of organic compounds with the use of automated CHNS analyzers. *Journal of analytical chemistry* **2008**, *63*, 1094-1106.
9. Sing, K. S., Reporting physisorption data for gas/solid systems with special reference to the determination of surface area and porosity (Recommendations 1984). *Pure and applied chemistry* **1985**, *57*, 603-619.
10. Thommes, M.; Kaneko, K.; Neimark, A. V.; Olivier, J. P.; Rodriguez-Reinoso, F.; Rouquerol, J.; Sing, K. S., Physisorption of gases, with special reference to the evaluation of surface area and pore size distribution (IUPAC Technical Report). *Pure and Applied Chemistry* **2015**, *87*, 1051-1069.
11. Kumar, K. V.; Gadipelli, S.; Wood, B.; Ramisetty, K. A.; Stewart, A. A.; Howard, C. A.; Brett, D. J.; Rodriguez-Reinoso, F., Characterization of the adsorption site energies and heterogeneous surfaces of porous materials. *Journal of Materials Chemistry A* **2019**, *7*, 10104-10137.
12. Wang, Z.; Jiang, X.; Pan, M.; Shi, Y., Nano-Scale Pore Structure and Its Multi-Fractal Characteristics of Tight Sandstone by N₂ Adsorption/Desorption Analyses: A Case Study of Shihezi Formation from the Sulige Gas Field, Ordos Basin, China. *Minerals* **2020**, *10*, 377.
13. Goikolea, E.; Mysyk, R., Nanotechnology in Electrochemical Capacitors. In *Emerging Nanotechnologies in Rechargeable Energy Storage Systems*, Elsevier: 2017; pp 131-169.

14. Laheäär, A.; Przygocki, P.; Abbas, Q.; Béguin, F., Appropriate methods for evaluating the efficiency and capacitive behavior of different types of supercapacitors. *Electrochemistry Communications* **2015**, *60*, 21-25.
15. Mathis, T. S.; Kurra, N.; Wang, X.; Pinto, D.; Simon, P.; Gogotsi, Y., Energy storage data reporting in perspective—guidelines for interpreting the performance of electrochemical energy storage systems. *Advanced Energy Materials* **2019**, *9*, 1902007.
16. Estabén, D. A. Composite materials based on disordered carbon as supercapacitor electrodes. Universidad Complutense de Madrid, Madrid, 2019.

CHAPTER – 3

Synthesis of porous carbon spheres and their use as electrodes
for EDLC in different electrolytes

This chapter presents a facile and scalable approach for the preparation of uniform porous carbon spheres with 3D interconnected pore architecture from the pyrolysis of phenolic resins obtained through the sol-gel process between resorcinol and formaldehyde catalyzed by FeCl_3 . The resulting porous carbon spheres (PCS) exhibit a high specific surface area of $2072 \text{ m}^2 \text{ g}^{-1}$ and a pore volume of $1.33 \text{ cm}^3 \text{ g}^{-1}$. The pore size distribution also confirms the combination of micro/meso sized pores centered around 0.9-2.0 nm, which is suitable for supercapacitor applications. To study their charge storage behavior on the electrode surface s PCS have been used as electrode and tested in symmetric EDLCs using three different electrolytes, i.e. 6M aq. KOH, 1M aq. Li_2SO_4 and 1.5 M TEABF₄/acetonitrile, based on their cation/anion size variation. The electro-adsorption of electrolyte ions on the positive and negative electrode was individually monitored during the cyclic voltammetry and galvanostatic charge-discharge test using a reference electrode. The PCS electrodes show an excellent specific capacitance of 168, 110, 114 F. g^{-1} in KOH, Li_2SO_4 , and TEABF₄/acetonitrile electrolyte at the current density of 0.1 A g^{-1} , and able to maintain good capacitance retention even at a high current density of 10 A g^{-1} . Due to the high surface area and suitable micro/mesoporosity, these electrodes exhibit superb cycling performance even after 5000 charge-discharge cycles.

3.1. Introduction

Among the different supercapacitor systems, electrochemical double layer capacitors (EDLCs) based have drawn the tremendous attention due to their fast charge-discharge rates over unlimited cycles, which is required not only for the development of hybrid electric vehicles but also for the portable electronics and industrial power-energy management purpose.^[1-3] Porous carbon are the most used materials for the fabrication of electrodes for EDLC due to their low toxicity, good electronic conductivity, high accessible surface area and optimum porous architecture, which are extremely desirable for charge storage purposes in the electrode/electrolyte interface.^[4-5] Porous carbons can be synthesized by several methods, such as hard or soft templated method, carbonization of polymer blends, chemical activations and also through the catalytic activation by using metal salts.^[6] Development of simple and cost-effective strategies are highly challenging to synthesize the nanostructured carbon materials to save time and energy as well as to reduce the consumption of expensive precursor.

In this context, carbons synthesized from the polycondensation polymerization reaction of the resorcinol (R) and formaldehyde (F) precursor are quite well known for the synthesis of carbon aerogels and xerogels.^[7-11] Several studies have reported how the nanoporous structure of RF carbon controls the performance of EDL behavior.^[9, 11] This synthesis process involves three major steps. These are, 1) preparation of the solution mixture, where ‘gelation and curing’ happens, 2) drying of the wet gel, 3) and carbonization of the dry gel. The main factor of this synthesis process depends on the ‘gelation and curing’ step, where endothermic, polycondensation and polymerization reaction takes place in presence of a catalyst.^[7, 11] Different types of acid and base catalysts can be used for this polymerization reaction. Among the base catalysts, (Na_2CO_3 , NaOH , KOH) are predominantly used, which reduces the gelation time by accelerating the reaction and also improves the crosslinking of the polymer particles.^[7, 9, 12-14] The crosslinking process during the condensation reaction is referred as an ‘ageing step’, reducing this ageing step in presence of an acid catalyst also plays an important role to increase the EDL capacitance.

In this regard, various acid catalysts and salts of transition metals (*e.g.* $\text{Pt}(\text{NH})_3$, PdCl_2 , or $\text{Ag}(\text{COO-CH}_3)_2$, $\text{Fe}(\text{COO-CH}_3)_2$, FeCl_3) are also utilized.^[8, 15-17] The main advantages of using

these acid catalysts are decreasing in reaction temperature, increase in the surface area as well as micro- and mesopore volumes, and the reduction of gelation time.^[18] Among them, FeCl₃ is highly promising due to its widely regarded chemical activation effect to produce activated carbon.^[19-21] It has many advantages compared to traditional activation agent such as lower cost and environment friendliness.^[22-23] Furthermore, use of iron containing salt can also act as a catalyst for producing localized graphitic domains in the carbons obtained from the dry gel during the pyrolysis process at relatively low pyrolysis temperature (<1000°C).^[18, 24-27] This induced graphitization in carbon can enhance the electrical conductivity, which helps to achieve better electrochemical performance compared to the conventional amorphous activated carbons. Generally, the carbon obtains from the RF gel usually has poor porosity because of the non-porous nature of polymeric precursors. However, this issue can be resolved by using polymeric gels impregnated with the transition metal salts resulting in carbon materials having both graphitic domains as well as significant porosity.^[8, 24]

As the energy density of supercapacitors depends on the capacitance and the potential window of the system, thus increasing the operating voltage is the prime challenge for the performance improvement of this energy storage device. In fact, the cell voltage of the EDLC system is mainly limited to the stability potential window of the electrolytes. Therefore, the careful selection of aqueous and non-aqueous mediums can restrain the overall electrochemical performance. In aqueous medium, the practical operating voltage is limited at *ca.* 1.0 V because of the thermodynamic instability of water, whereas the organic electrolytes are ranging ~2.5–2.7 V but their main drawbacks are the low conductivity and larger ionic size.

Generally, H₂SO₄ and KOH are quite common and most studied aqueous electrolytes for supercapacitors. The high over-potential for dihydrogen evolution reaction can improve the operating voltage in the carbon electrode, however, the corrosive property of H₂SO₄ prevents the wide-ranging applications. In this regard, KOH is comparatively safer, but it also degrades the electrode material and the current collector during prolonged application.^[28] Though these acidic and alkaline electrolytes have much higher ionic conductivities, which help to achieve the high specific capacitance, they exhibit adverse effects in cycle performance. On the other side, neutral electrolyte (LiCl, Li₂SO₄, Na₂SO₄, *etc.*) contains the negligible concentration of H⁺ and OH⁻ compared to the acidic and alkaline aqueous electrolytes, thus high overpotential of gas evolution

(H₂ and O₂) reaction can be expected that helps to increase the working potential window.^[28-30] Although neutral electrolytes provide much lower specific capacitance, their higher cell voltage (~1.7 V), less corrosive nature, stability resulted in an enhanced energy storage performances of the devices.^[1, 28] Apart from these aqueous electrolytes, an organic electrolyte such as tetraethylammonium tetrafluoroborate (TEABF₄) in acetonitrile or propylene carbonate (PC) solvent is used in most of the commercial EDLCs.^[31] Despite having lower specific capacitance, higher cost, volatility issues, still they dominate the commercial market because of their much better operation potential window around 2.7 V, which provides not only high energy density but also better cycle life.^[28, 32]

In this chapter, porous carbon spheres were synthesized by using resorcinol and formaldehyde in a sol-gel process with the aid of FeCl₃ as an acid catalyst followed by carbonization. FeCl₃ serves as a catalyst during the gel condensation and as activating agent during its carbonization. These synthesized porous carbon spheres were used as the electrode material to study its electrochemical behavior in different voltage limits by using various electrolytes. We selected KOH as alkaline, Li₂SO₄ as neutral, and TEABF₄/acetonitrile as organic electrolyte respectively to observe the intrinsic and extrinsic behavior of the full cell performance of the porous carbon sphere electrode. In this regard, the detailed electrochemical analyses were performed to understand the relationship of the different electrolyte ions with the porous textural properties of this catalytic graphitic carbon.

3.2. Material synthesis

The porous carbon spheres (PCS) were synthesized by the carbonization of the dry polymeric gel under a dynamic inert atmosphere. In this typical synthesis, 880 mg of resorcinol, 1.2 mL of formaldehyde, and 216 mg of FeCl₃·6H₂O were dissolved in the mixture solvent of DI water and ethanol. After the complete mixing, the resultant solution was kept it in an oven at 60 °C for 48 h in a closed container to form a gel. Then this wet gel was kept under the same heating condition for a sufficient period to dry properly. After that, this dried gel was carbonized at 950 °C for 3 h under the stream of N₂ gas (0.5 L min⁻¹) with a heating rate of 4 °C min⁻¹. Then the carbonized sample was washed with 3 M HCl in EtOH/H₂O (1/1 in volume) to remove Fe species from the obtained carbon.

3.3. Physicochemical characterization

Figure 3.1.a shows the XRD patterns of the carbonized sample prepared from the RF precursor in the presence of a certain amount of FeCl_3 , which served as both catalyst and an activating agent. The smooth XRD pattern without any graphitic peaks shows that the synthesized porous carbon spheres are amorphous in nature high porous surface. A few sharp diffraction peaks can be seen in the XRD patterns, which are assigned to Fe-oxide species (Fe_3O_4 and Fe_2O_3). During the carbonization process, some FeCl_3 catalyst reacts with the other functional groups of the resin forming these Fe-oxides. Although extensive washing with an acidic solution was done post carbonization, the presence of these residual Fe-oxide species are observed, which are difficult to be accessed and leached from the carbonaceous matrix.

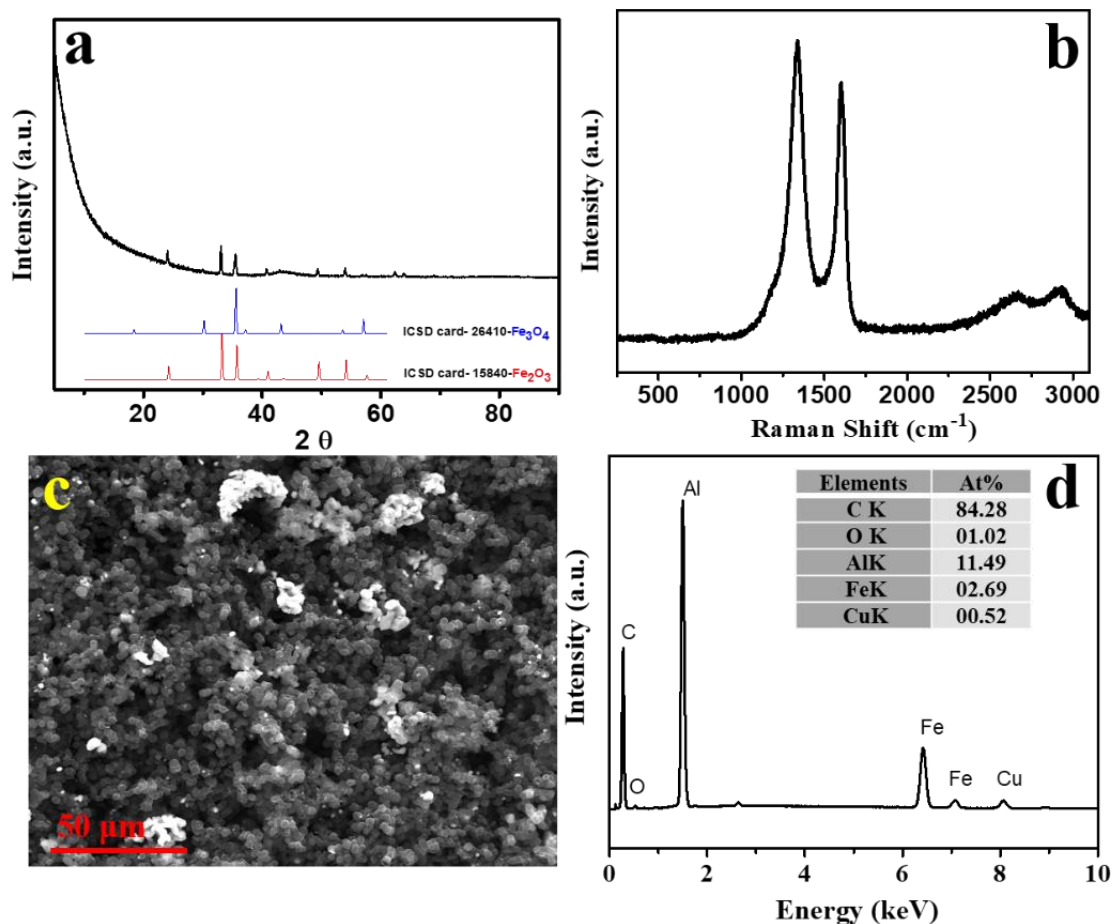


Figure 3.1. (a) XRD profile, (b) Raman spectra, (c) low magnification SEM image, and (d) EDX spectra of the PCS.

Figure 3.1.b shows the Raman spectrum registered for PCS. The bands registered at around ~ 1340 and $\sim 1600\text{ cm}^{-1}$ are ascribed to the vibration modes of the defect in sp^3 carbons (D band) and the graphite sp^2 carbons (G band), respectively. Besides, the ratio of the integrated area of I_D and I_G was found to be 1.16. From Raman spectrum provides the information about the significant disordered morphology of this amorphous PCS contains a large concentration of defects and/or pores, which supports the XRD result. Figure 3.1.c shows a low magnification SEM image. From this image, it can be observed that the carbon nanospheres are homogeneously dispersed with a few localized agglomerations of the metal compounds seen on the surface and that can be assigned to the presence of some Fe-oxides in the carbon matrix. Thus, the further investigation obtained from the EDX analysis (Figure 3.1.d) confirmed the presence of Fe (2.69 at %) together with other metallic elements (Al and Cu) from the sample holder.

Figure 3.2.a depicts the porous structure of carbon employing in SEM, where it can be found that no bulky aggregation of the carbon spheres is observed. In order to observe the microstructure, PCS was further investigated by TEM analysis, as shown in Figure 3.2.b. The low magnification TEM images in Figure 3.2.b confirms that the PCS is formed by individual and isolated spherical particles. These images also confirm the presence of tiny metallic particles embedded in the carbonaceous matrix. Meanwhile, figure 3.2.c shows that PCS possess fine micropore channels without any detectable existence of mesopores or macropores.

To obtain the additional information about the textural features of this carbon, nitrogen adsorption-desorption measurements were performed, and the results are plotted in figure 3.2.d and 3.2.e. As revealed from figure 3.2.d, PCS shows a type I profile isotherm (according to the IUPAC classification), which indicates that the PCS is predominantly microporous in nature.^[33] The calculated DFT specific surface area were found to be $2072\text{ m}^2\text{ g}^{-1}$, which is at least 2.5 times higher than other carbon synthesized from similar phenolic resins.^[8, 34-37] This is due to the use of FeCl_3 catalysts during the preparation of resorcinol formaldehyde gel, which also worked as activation agent during the pyrolysis of the gel. Many studies validated the high efficacy of FeCl_3 as activation agent for synthesis of highly porous carbon from different precursors such as resin, waste biomass, coal tar etc.^[19-21] The pore size distribution analysis calculated by the 2D-NLDFT model shows that the PCS carbon has total pore volume of $1.33\text{ cm}^3\text{ g}^{-1}$ out of which micropore volume is $1.05\text{ cm}^3\text{ g}^{-1}$, which is almost 80 % of the total pore volume.

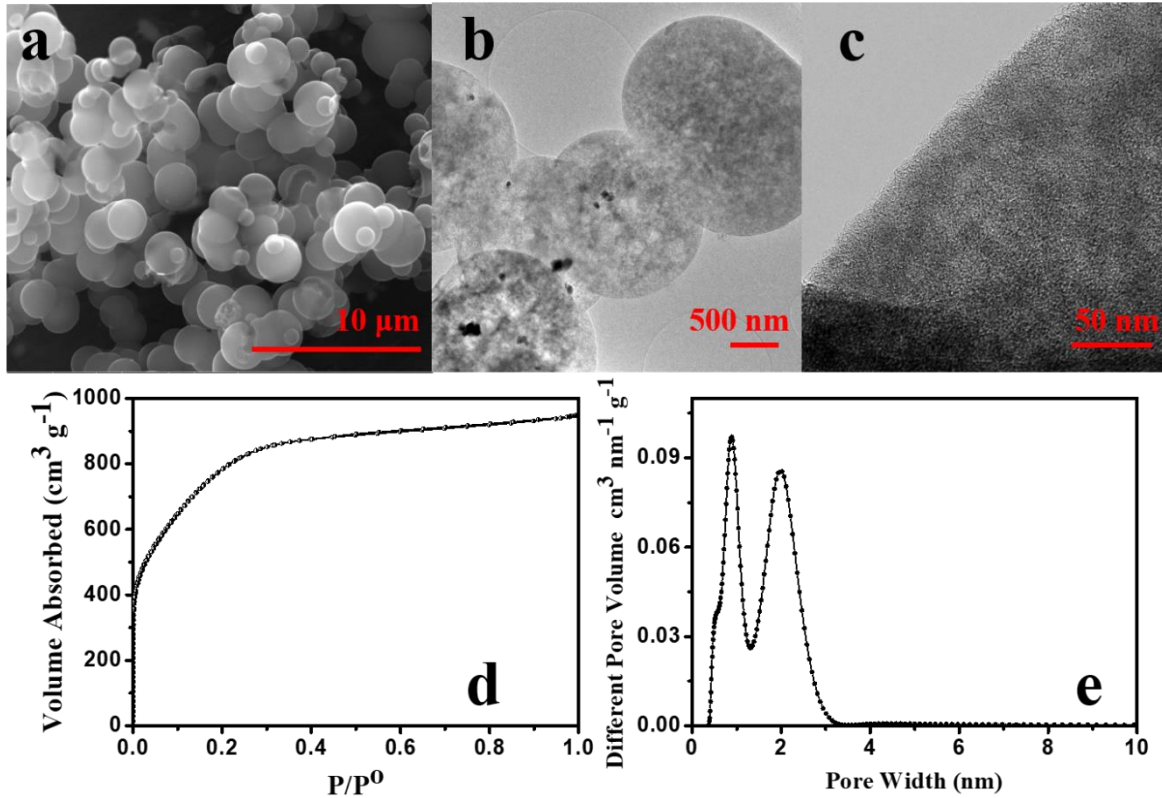
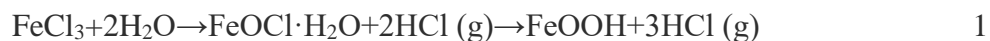


Figure 3.2. (a) SEM and (b) TEM image of the microspherical PCS, (c) high magnification TEM image of the outer surface of the PCS, (d) N₂ adsorption-desorption isotherm, and (e) pore size distribution curve.

Many studies suggested that Fe₃O₄ and Fe₂O₃ formed during the pyrolysis of FeCl₃ containing carbon precursors promote the formation of micropores.^[22, 38-39] These micropores are derived from the interstices of the remaining turbostratic framework in the carbon spheres. The pore size distribution is observed to be broad in the range of 0.4-3.0 nm with two peaks at 0.9 and 2.0 nm. The chemical transformation of FeCl₃ during this activation process is explained in the following steps (Eq. 1-6) ^[19]:

At 200-330 °C: decomposition of FeCl₃·6H₂O into amorphous Fe-species



At 330-700 °C: formation of Fe₂O₃ from FeOOH, which reacts with carbon to form Fe₃O₄





At 700-800 °C: Reaction of Fe_2O_3 and Fe_3O_4 with carbon to form metallic Fe.



Therefore, these results confirmed that PCS mostly contain pores within the micro- and small mesopores range, which could be highly beneficial for the formation of the electrical double layer in both aqueous and organic electrolytes.

3.4. Electrochemical characterization

3.4.1. Electrode processing and cell assembly

Electrodes were processed by mixing the synthesized PCS material (90 wt. %), super-C65 conducting carbon additive (5 wt. %), and a polytetrafluorethylene (PTFE) binder (5 wt. %, from a 60 wt. % aqueous dispersion). The mixture was homogenized and was kneaded continuously to form a dough with good plasticity, followed by uniformly rolling the dough until forming a self-standing film with a thickness of nearly 40 μm . 11 mm diameter disk-shaped self-standing electrodes were punched out from the film and dried at 120 °C overnight. The mass loading for the tested electrodes was kept uniform in the range of 4-5 mg/cm^2 . The electrochemical performances of the fabricated electrodes were assessed in a special symmetrical three-electrode SwagelokTM cell system as shown in Figure 3.3.

Two carbon electrodes of similar mass loading with a porous glass fibre membrane (Whatman GFB) in between them were sandwiched between two stainless steel current collectors and assembled within a Teflon SwagelokTM airtight T type cell, which formed a two-electrode EDLC cell. A third reference electrode was introduced in the cells, which is kept equidistant from both carbon electrodes for differentiating the potential evolution of each of them with the scan rate and the cut-off voltage being enforced between the positive and negative electrodes. Three different electrolytes (Aqueous alkaline (6M KOH), aqueous neutral (1M Li_2SO_4), and organic

(1M Tetraethylammonium tetrafluoroborate [TEABF₄] in acetonitrile) were used in this study to test the electrochemical performance. For aqueous alkaline and neutral electrolytes, two different types of calomel reference electrodes namely Hg/HgO in 0.1M NaOH and Hg/HgSO₄ in 0.1M K₂SO₄, respectively were used. For organic electrolytes, an Ag wire was used as a quasi-reference electrode. The Ag wire was polished with emery paper and etched in nitric acid solution to remove surface oxides and impurities.

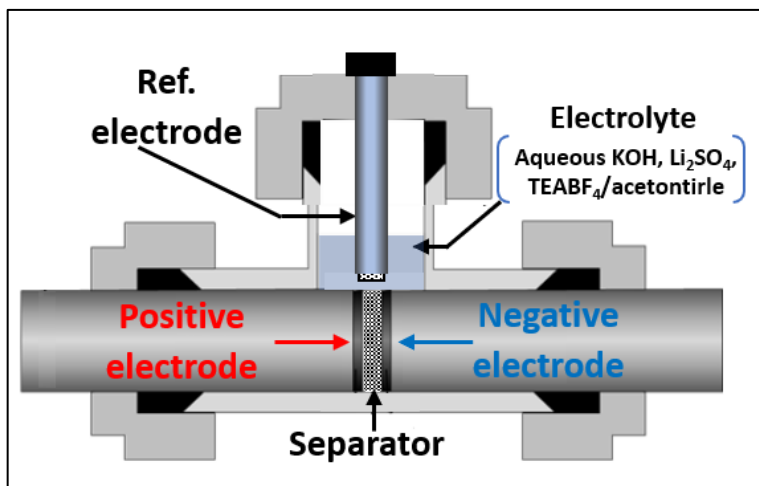


Figure 3.3. Three electrode SwagelokTM-type cell configurations for testing symmetric EDLC.

3.4.2. Electrochemical evaluation

The high specific surface area and appropriate porosity of PCS could envision the potential of this material as electrode material for EDL capacitors. Thus, three different electrolytes, *i.e.* aqueous alkaline, aqueous neutral, and organic electrolytes were selected to evaluate the correlation of textural features of PCS materials with the ionic size and conductivity of the electrolytes. High salt concentration in the solvent is required to reach high ionic conductivity of the electrolyte, which is necessary to achieve good capacitive performance, especially at high current densities. For aqueous alkaline electrolyte, this is not an issue because they can achieve high concentration although it can increase the corrosive degradation.

For neutral aqueous media, some salts such as K₂SO₄ cannot achieve very high concentration due to its solubility limit. On the other side, many studies claimed that 1M Li₂SO₄ as neutral electrolyte has not only excellent conductivity but also can operate in a wide electrochemical potential range.^[28, 32] For organic electrolytes, the conductivity is dependent on both salt and

solvent. Among the commonly used solvents, acetonitrile has a lot of advantages, such as low viscosity, high dielectric constant and most of the electrolyte salts can get easily desolvated also in this media, which can enhance the capacitive performance significantly.^[28] Therefore, the electrolytes chosen for this study were 6M KOH (aqueous), 1M Li₂SO₄ (aqueous), and 1.5M TEABF₄ (acetonitrile), respectively.

Another important factor for selecting these three electrolytes is their difference in the ionic size of cations and anions. For KOH electrolyte, the ionic size of the cation is smaller than anion, whereas it is completely opposite in case of TEABF₄ based electrolytes.^[28] In the case of Li₂SO₄ electrolyte, the ionic size of cation and anion are nearly equal. Since the cations and anions are electroadsorbed in negative and positive electrode to form the electric double layer, thus their differences in ionic size can directly influence the degree of electroadsorption and thereby affecting the overall charge storage performance.^[40-41] Several studies has been reported on the effect of ionic size on electrochemical charge storage behavior in different types of aqueous and organic electrolytes.^[42-46] In this context, Chen *et al.* has carried out an interesting study, where they have used biomass derived porous carbon to compare the effect of three types of aqueous electrolyte (acidic, alkaline and neutral) and organic electrolyte on EDL charge storage behaviour.^[29] However, their study does not have much information on the charge storage behavior in individual electrodes of a two-electrode cell. From this perspective, the electrochemical study carried out in this work has gone through a detailed evaluation of charge storage properties in the individual electrode by fabricating a special three-electrode SwagelokTM cell (Figure 3.3), where two PCS electrodes are coupled with a reference electrode.

Figure 3.4. shows CV profiles recorded at 5 mV s⁻¹ scan rate and GC-GD profiles recorded at 0.1 A g⁻¹ in the three different electrolytes. All CV curves show rectangular and symmetric profiles whatever the electrolyte used, A sharp shift of capacitive current transient at the cut-off voltage limit is also observed in all CVs.^[47] This behavior can be interpreted as a nearly ideal EDL mechanism, indicating a typical characteristic of good microporous carbon with high electrical conductivity. The electrosorption behavior of the different electrolyte ions in the micropores of PCS materials can be observed from the electrochemical response of the individual electrodes as shown in Figure 3.4.

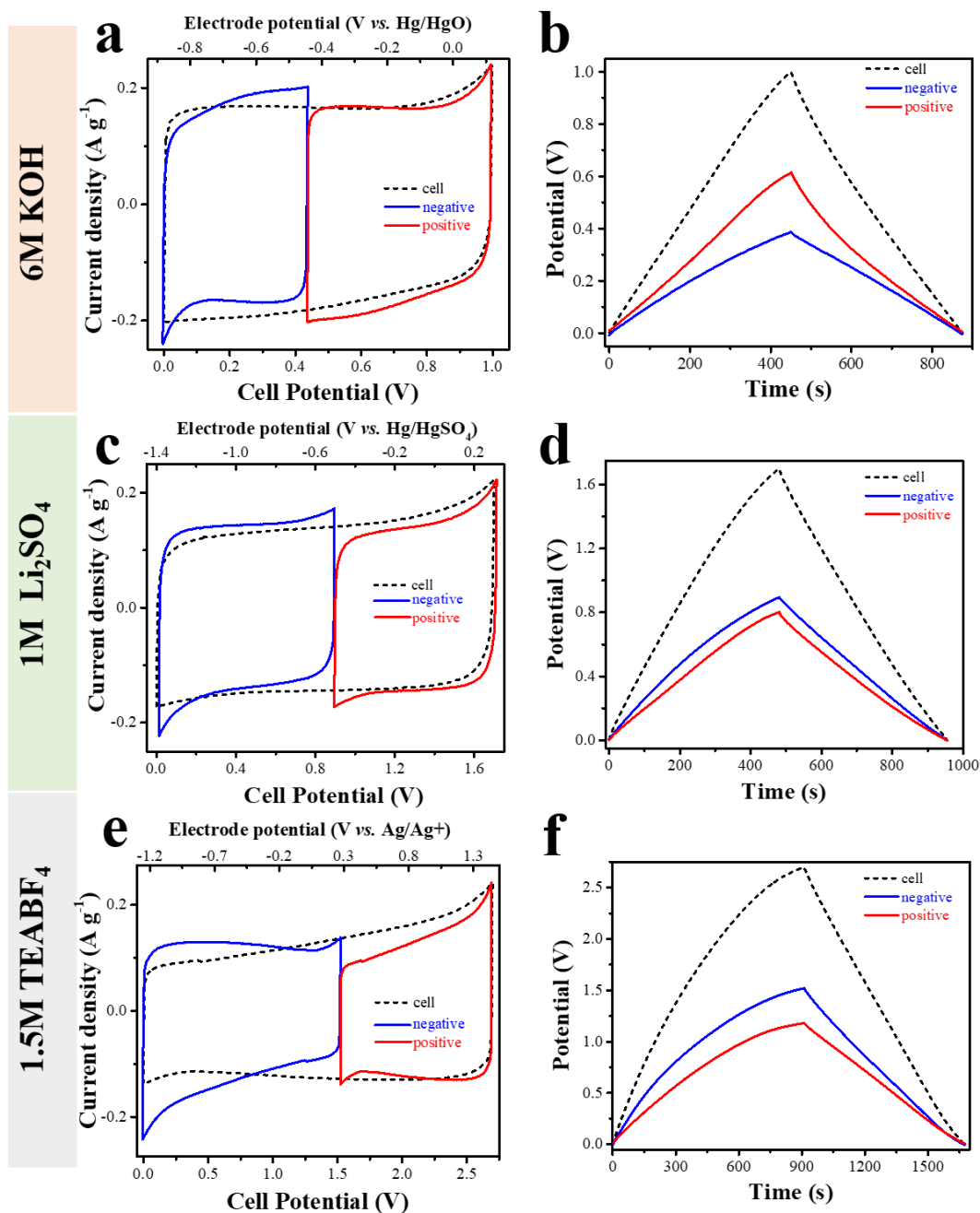


Figure 3.4. Cyclic voltammograms at a scan rate of 5 mV s^{-1} and galvanostatic charge-discharge profiles at the current density of 0.1 A g^{-1} for the tested EDLCs in different electrolytes, (a and b) 6M KOH, (c and d) 1M Li₂SO₄, and (e and f) 1.5M TEABF₄. Cell voltage (black dashed line) vs. potential evolution of individual electrodes: positive electrode in red and negative electrode marked in blue.

It can be observed that in the case of KOH electrolyte (Figure 3.4.a), the CV curve associated to the positive electrode has a larger area compared to the negative electrode, which means the electrosorption of hydrated OH^- ion stores the charge more favorably in larger voltage window than the K^+ ion. This is due to the larger size of hydrated OH^- ion (0.63 nm) compared to the K^+ ion (0.33 nm) in the 6M KOH solution. [28, 42-43] However, CV profile recorded in Li_2SO_4 electrolyte (Figure 3.4.c) exhibits both positive and negative electrodes has almost equal CV area, which indicates that both electrodes have nearly similar charge storage behavior. The ionic size of the hydrated Li^+ and SO_4^{2-} ions are also almost the same in size (*i.e.* 0.38 nm). [40, 48]. Therefore, the contribution from both cation and anion towards charge storage is as well very identical. In case of a cell measured using 1M TEABF_4 /acetonitrile as electrolyte (Figure 3.4.e), the CV area in the negative electrode was found to be larger than the positive electrode, indicating that the TEA^+ ion has bigger ionic radii in both solvated and desolvated form than BF_4^- ion, which explains electroadsorption of TEA^+ ion are more favorable compared to the BF_4^- ion. [1, 46, 49]

Ideally, the charge built up in the positive and negative electrode is equivalent to each other, *i.e.* $Q_+ = Q_-$, which can be rewritten as

$$C_+ \Delta E_+ m_+ = C_- \Delta E_- m_- \quad 7$$

Where, C_+ is the capacitance, ΔE_+ the voltage range, m_+ the mass of the positive electrode, and C_- , ΔE_- , m_- corresponds to the negative electrode values. Since the electrode mass is kept almost equal for both positive and negative, thus the capacitance in each electrode is inversely proportional to the voltage evolution.

Figure 3.4.b, d, and f show the GC-GD profiles recorded at 0.1 A g^{-1} current density. In the case of both aqueous electrolytes, the symmetric GC-GD profiles exhibit equal charge and discharge time with negligible iR drop. The GC-GD profile registered in the organic electrolyte also shows a symmetric profile with almost negligible iR drop but with a slightly longer charge time than discharge. Moreover, figure 3.4.b shows the GC-GD profiles of individual electrodes in KOH electrolyte, where the potential evolution in the positive electrode is found to 60 % of the total voltage evolution. This indicates that the negative electrode delivers 60% of the total specific capacitance. [43] Whereas, in Li_2SO_4 electrolyte, the GC-GD profiles (Figure 3.4.d) of individual electrodes display almost equal voltage evolution in both positive and negative electrodes,

suggesting their similar contribution towards the total capacitance. In the case of TEABF₄ electrolyte (Figure 3.4.f), the potential swing of negative electrode is found to be larger than that observed for the positive electrode, meaning that the positive electrode has a larger contribution on the capacitance of the cell.

Figure 3.5.a, c and e show the CV patterns registered at increasing sweep rates from 10-100 mV s⁻¹. It is clearly observed that the profile remains stable with a negligible shift from the ideal EDL behavior in the whole range. This validates the optimum porosity of the PCS material, which allows the unrestricted ion movement throughout its porous network. It is worth to point out the absence of redox peak in CV curves, especially in the KOH electrolyte that supposed to appear due to the presence of residual iron oxide crystal in the PCS material. This indicates that the iron oxides are embedded within the carbonaceous matrix and avoiding its direct exposure to the electrolytes. Figure 3.5.b, d and f show the GC-GD profiles of the PCS electrodes in the three different electrolytes in the current density range of 1.0-10 A g⁻¹. It can be noticed that the appearance of iR drop in KOH electrolyte is significantly smaller than the other two electrolytes by comparing their GC-GD profiles of 1 A g⁻¹. It is noteworthy to mention that the iR drop in aq. Li₂SO₄ electrolyte is higher than the TEABF₄/acetonitrile.

Figure 3.6.a shows the specific capacitance evolution calculated from the discharge branch at different current rates (0.1 to 10 A g⁻¹). It can be observed that the electrode tested in aq. KOH electrolyte showed the highest specific capacitance of 168 F g⁻¹ at 0.1 A g⁻¹ compared to 110 and 114 F g⁻¹ that observed in aq. Li₂SO₄ and TEABF₄ in acetonitrile, respectively. Furthermore, the specific capacitance retention values of these EDLCs are found to be 73 (aq. KOH), 67 (aq. Li₂SO₄), and 73 % (TEABF₄/acetonitrile) even at the high current density of 10 A g⁻¹.

This huge difference in the capacitive performance can be attributed to two main factors. (1) Aq. KOH electrolyte has a much higher conductivity of 544 mS cm⁻¹ compared to 77.6 and 59 mS cm⁻¹ in aq. Li₂SO₄ and TEABF₄/ acetonitrile respectively.^[28, 40, 50] (2) Aq. KOH electrolyte can also contribute pseudocapacitive charge storage in the microporous carbon through the redox interaction of OH⁻ ion with the surface functional moieties.^[28, 32, 40] Thus, the higher capacitance retention behavior at high current density in aq. KOH than Li₂SO₄ can be attributed to the faster ionic mobility of solvated K⁺ and OH⁻ ions than the Li⁺ and SO₄⁻ ions. Moreover, the poor wettability of aqueous neutral electrolytes with porous carbon material can also be the reason for

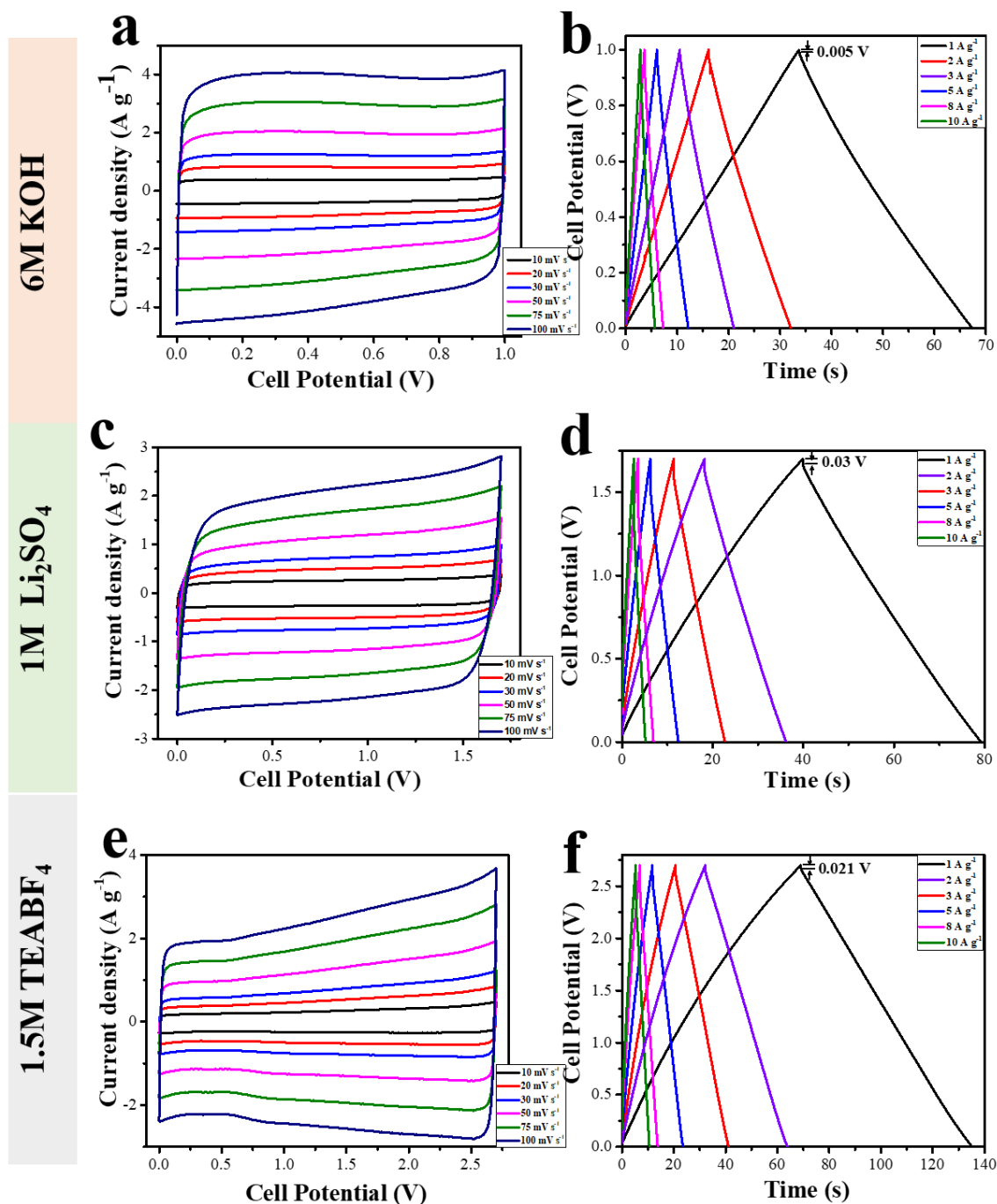


Figure 3.5. Cyclic voltammograms at different scan rates and galvanostatic charge-discharge profiles at different current densities for the tested EDLCs in different electrolytes, (a and d) 6M KOH, (b and e) 1M Li₂SO₄, and (c and f) 1.5M TEABF₄.

lowering the capacitance retention of aq. Li₂SO₄ compared to the acidic, alkaline, or organic electrolyte.^[28] This capacitance fading behavior can be related to the higher iR drop (*i.e.* 0.03V)

measured in the Li_2SO_4 electrolyte as it can be compared to the other two electrolytes observed in figure 3.5.d.

On the other side, the excellent capacitance retention of 73 % that showed in the organic $\text{TEABF}_4/\text{acetonitrile}$ electrolyte indicates the pore distribution in the synthesized PCS material is well suited to accommodate the bigger organic salt ions in both solvated and desolvated form.^[28, 32, 40] This result suggests that the PCS materials hold the possibility to perform good charge storage behavior also in the ionic liquid electrolytes.

After the rate performance tests, the EIS analysis was performed on all the cells with an open circuit potential after leaving them with a rest period of 1 h. Figure 3.6.b shows the comparative Nyquist plots obtained from the EIS analysis, indicates the typical curves of the porous carbon electrodes. The insignificant semicircle of aq. KOH and $\text{TEABF}_4/\text{acetonitrile}$ electrolytes indicate that the cells exhibit very low interfacial resistance. Whereas the electrode in aq. Li_2SO_4 electrolyte shows the formation of a quite prominent semicircle in high to medium frequency range. This can be directly attributed to the poor wettability of the porous carbon electrode in the aqueous neutral electrolyte as explained above.

The internal cell resistance in each electrolyte was measured by extrapolating the low-frequency region of the Nyquist curves to X-axis. As expected, the electrode in KOH electrolyte shows the lowest ESR of 0.25Ω compared to 1.45Ω and 0.75Ω that showed in aq. Li_2SO_4 electrolyte and $\text{TEABF}_4/\text{acetonitrile}$ electrolyte, respectively, which supports the GC-GD results explained above. The low-frequency region of all the Nyquist curves showed vertical straight lines parallel to the Y-axis, which validates the formation of EDL type charge storage in all the electrolytes. From the middle to low-frequency region in aq. Li_2SO_4 electrolyte, a small diversion in Y-axis is indicating the ion diffusion resistance in this electrolyte was much higher than the other two.

Figure 3.6.c demonstrates the comparative Ragone plots corresponding energy vs. power densities for all the EDLCs. The highest energy densities obtained for the cells in aq. KOH, aq. Li_2SO_4 and $\text{TEABF}_4/\text{acetonitrile}$ electrolytes are 5.8 , 10.8 , and 28.4 Wh kg^{-1} at 50 , 85 , and 133 W kg^{-1} power density, respectively. Therefore, the energy density in the $\text{TEABF}_4/\text{acetonitrile}$ electrolyte was almost 5 and 2.5 times more than aq. KOH and aq. Li_2SO_4 electrolytes. Moreover, the energy density in TEABF_4 electrolyte still retained 19 Wh kg^{-1} at a high-power density of

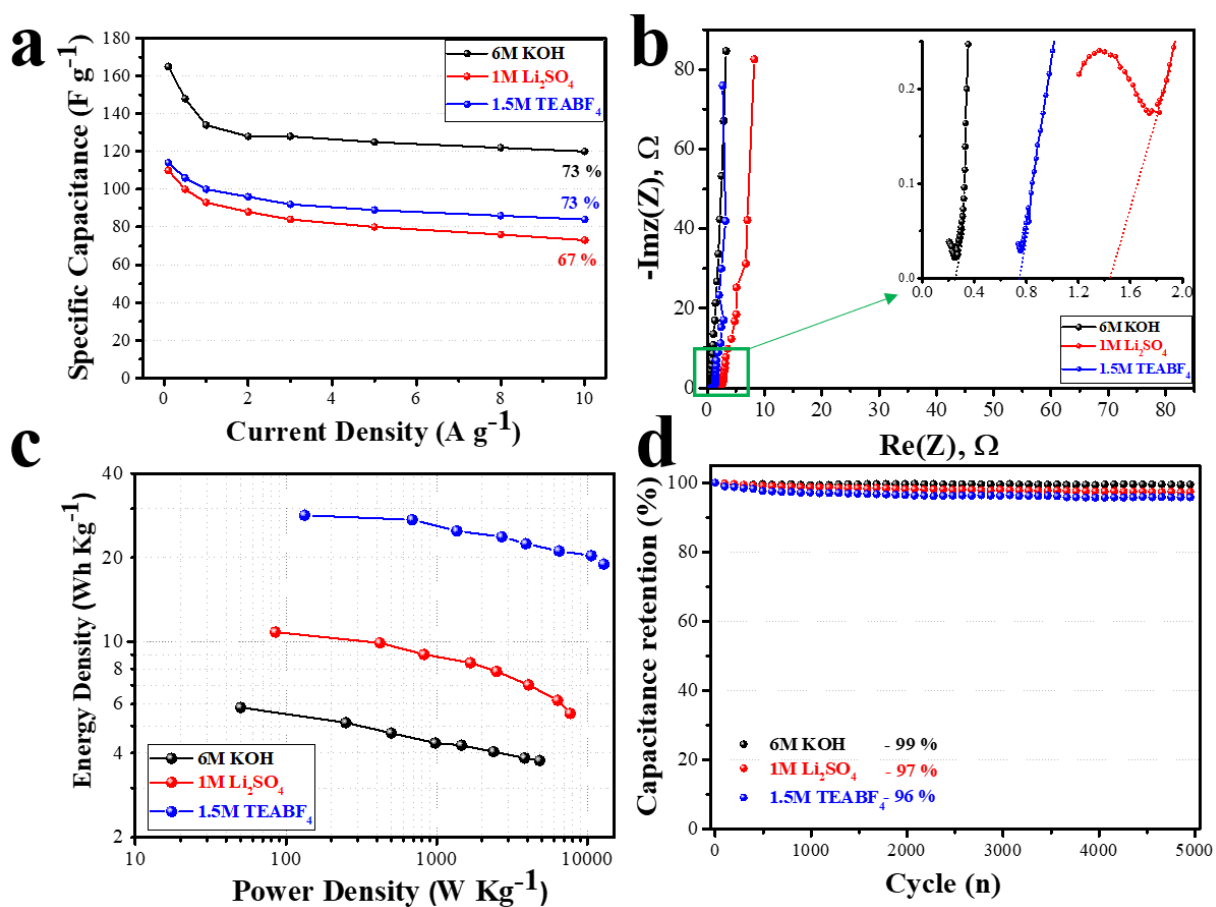


Figure 3.6. Comparative (a) rate capability, (b) Nyquist plots (registered after the rate performance evaluation) (c) Ragone plots, and (d) cyclic stability performance for the tested EDLCs in different electrolytes.

12.9 $kW kg^{-1}$ which is very promising for commercial applications. The cells in aq. KOH and aq. Li_2SO_4 electrolyte retained the energy density of 3.8 and 5.6 $Wh kg^{-1}$ at a high-power density of 4.8 and 7.7 $kW kg^{-1}$.

The long-term stability of these full cells was also accomplished by performing GC-GD tests at 3 $A g^{-1}$ for 5000 cycles. From the resultant cycling stability plots in Figure 3.6.d, it can be observed that all the EDLCs was achieved excellent capacitance retention of 99, 97, and 96 % of its initial capacitance, which is really impressive.

3.5. Conclusion

In summary, sol-gel derived porous carbon spheres using FeCl_3 as a catalyst were tested as electrode material for an electric double layer capacitor. Three different electrolytes based on ionic size dissimilarity in cations and anions were used in this study. In aqueous 6M KOH electrolyte, the negative electrode was found to deliver more capacitance compared to the positive electrode due to the smaller size of cation, whereas it is completely opposite in case of organic TEABF₄/acetonitrile electrolyte. On the other hand, aqueous Li_2SO_4 electrolyte showed similar charge storage performance on both electrodes. Due to high ionic conductivity and additional pseudocapacitive contribution, the KOH electrolyte was found to deliver the highest specific capacitance of 168 F g^{-1} at 0.1 A g^{-1} for the porous carbon sphere electrode. Both KOH and TEABF₄/acetonitrile showed excellent rate performance of 73 % at 10 A g^{-1} , closely followed by the Li_2SO_4 electrolyte. In overall, the porous carbon spheres showed maximum energy and power density of 28.4 Wh kg^{-1} and 12.9 kW kg^{-1} , respectively. These results along with the simplicity and scalability of the synthesis process make this synthesized porous carbon spheres a potential candidate for commercial exploration.

Bibliography

1. Béguin, F.; Presser, V.; Balducci, A.; Frackowiak, E., Carbons and electrolytes for advanced supercapacitors. *Advanced materials* **2014**, *26*, 2219-2251.
2. Miller, J. R., Engineering electrochemical capacitor applications. *Journal of Power Sources* **2016**, *326*, 726-735.
3. González, A.; Goikolea, E.; Barrena, J. A.; Mysyk, R., Review on supercapacitors: technologies and materials. *Renewable and Sustainable Energy Reviews* **2016**, *58*, 1189-1206.
4. Miller, J. R.; Burke, A. F., Electrochemical capacitors: Challenges and opportunities for real-world applications. *Electrochemical Society Interface* **2008**, *17*, 53-57.
5. Pandolfo, A. G.; Hollenkamp, A. F., Carbon properties and their role in supercapacitors. *Journal of Power Sources* **2006**, *157*, 11-27.
6. Wang, L.; Hu, X., Recent advances in porous carbon materials for electrochemical energy storage. *Chemistry—An Asian Journal* **2018**, *13*, 1518-1529.
7. Al-Muhtaseb, S. A.; Ritter, J. A., Preparation and properties of resorcinol–formaldehyde organic and carbon gels. *Advanced materials* **2003**, *15*, 101-114.
8. Hasegawa, G.; Kanamori, K.; Nakanishi, K., Facile preparation of macroporous graphitized carbon monoliths from iron-containing resorcinol–formaldehyde gels. *Materials Letters* **2012**, *76*, 1-4.
9. Calvo, E. G.; Ania, C. O.; Zubizarreta, L.; Menéndez, J.; Arenillas, A., Exploring new routes in the synthesis of carbon xerogels for their application in electric double-layer capacitors. *Energy & fuels* **2010**, *24*, 3334-3339.
10. Xu, Y.; Wang, S.; Yan, M.; Zhang, L.; Zhai, Z.; Liu, Z., Synthesis of carbon aerogels based on resorcinol–formaldehyde/hydroxyethyl cellulose/carbon fiber and its electrochemical properties. *Journal of Porous Materials* **2018**, *25*, 1505-1511.
11. Kakunuri, M.; Sharma, C. S., Resorcinol-formaldehyde derived carbon xerogels: A promising anode material for lithium-ion battery. *Journal of Materials Research* **2018**, *33*, 1074.
12. Despetis, F.; Barral, K.; Kocon, L.; Phalippou, J., Effect of aging on mechanical properties of resorcinol-formaldehyde gels. *Journal of Sol-Gel Science and Technology* **2000**, *19*, 829-831.
13. Saliger, R.; Bock, V.; Petricevic, R.; Tillotson, T.; Geis, S.; Fricke, J., Carbon aerogels from dilute catalysis of resorcinol with formaldehyde. *Journal of non-crystalline solids* **1997**, *221*, 144-150.
14. Zhu, Y.; Hu, H.; Li, W.; Zhang, X., Resorcinol-formaldehyde based porous carbon as an electrode material for supercapacitors. *Carbon* **2007**, *45*, 160-165.

15. Maldonado-Hódar, F.; Ferro-García, M.; Rivera-Utrilla, J.; Moreno-Castilla, C., Synthesis and textural characteristics of organic aerogels, transition-metal-containing organic aerogels and their carbonized derivatives. *Carbon* **1999**, *37*, 1199-1205.
16. Berthon, S.; Barbieri, O.; Ehrburger-Dolle, F.; Geissler, E.; Achard, P.; Bley, F.; Hecht, A.-M.; Livet, F.; Pajonk, G. M.; Pinto, N., DLS and SAXS investigations of organic gels and aerogels. *Journal of non-crystalline solids* **2001**, *285*, 154-161.
17. Kiciński, W.; Szala, M.; Nita, M., Structurally tailored carbon xerogels produced through a sol-gel process in a water-methanol-inorganic salt solution. *Journal of sol-gel science and technology* **2011**, *58*, 102-113.
18. Maldonado-Hódar, F.; Moreno-Castilla, C.; Rivera-Utrilla, J.; Hanzawa, Y.; Yamada, Y., Catalytic graphitization of carbon aerogels by transition metals. *Langmuir* **2000**, *16*, 4367-4373.
19. Xu, Z.; Zhou, Y.; Sun, Z.; Zhang, D.; Huang, Y.; Gu, S.; Chen, W., Understanding reactions and pore-forming mechanisms between waste cotton woven and FeCl₃ during the synthesis of magnetic activated carbon. *Chemosphere* **2020**, *241*, 125120.
20. Yang, J.; Zhao, Y.; Ma, S.; Zhu, B.; Zhang, J.; Zheng, C., Mercury removal by magnetic biochar derived from simultaneous activation and magnetization of sawdust. *Environmental science & technology* **2016**, *50*, 12040-12047.
21. Boudou, J.; Bégin, D.; Alain, E.; Furdin, G.; Marêché, J.; Albinia, A., Effects of FeCl₃ (intercalated or not in graphite) on the pyrolysis of coal or coal tar pitch. *Fuel* **1998**, *77*, 601-606.
22. Oliveira, L. C.; Pereira, E.; Guimaraes, I. R.; Vallone, A.; Pereira, M.; Mesquita, J. P.; Sapag, K., Preparation of activated carbons from coffee husks utilizing FeCl₃ and ZnCl₂ as activating agents. *Journal of hazardous materials* **2009**, *165*, 87-94.
23. Zazo, J.; Bedia, J.; Fierro, C.; Pliego, G.; Casas, J.; Rodriguez, J., Highly stable Fe on activated carbon catalysts for CWPO upon FeCl₃ activation of lignin from black liquors. *Catalysis today* **2012**, *187*, 115-121.
24. Rastegar, H.; Bavand-Vandchali, M.; Nemati, A.; Golestani-Fard, F., Catalytic graphitization behavior of phenolic resins by addition of in situ formed nano-Fe particles. *Physica E: Low-dimensional Systems and Nanostructures* **2018**, *101*, 50-61.
25. Thompson, E.; Danks, A.; Bourgeois, L.; Schnepf, Z., Iron-catalyzed graphitization of biomass. *Green Chemistry* **2015**, *17*, 551-556.
26. Ōya, A.; Ōtani, S., Catalytic graphitization of carbons by various metals. *Carbon* **1979**, *17*, 131-137.
27. Carriazo, D.; Gutiérrez, M. C.; Jiménez, R.; Ferrer, M. L.; del Monte, F., Deep-Eutectic-Assisted Synthesis of Bimodal Porous Carbon Monoliths with High Electrical Conductivities. *Particle & Particle Systems Characterization* **2013**, *30*, 316-320.
28. Zhong, C.; Deng, Y.; Hu, W.; Sun, D.; Han, X.; Qiao, J.; Zhang, J., *Electrolytes for electrochemical supercapacitors*. CRC press: 2016.

29. Chen, Z.; Wang, X.; Ding, Z.; Wei, Q.; Wang, Z.; Yang, X.; Qiu, J., Biomass-based Hierarchical Porous Carbon for Supercapacitors: Effect of Aqueous and Organic Electrolytes on the Electrochemical Performance. *ChemSusChem* **2019**, *12*, 5099-5110.
30. Lewandowski, A.; Olejniczak, A.; Galinski, M.; Stepniak, I., Performance of carbon-carbon supercapacitors based on organic, aqueous and ionic liquid electrolytes. *Journal of Power Sources* **2010**, *195*, 5814-5819.
31. Balducci, A., Electrolytes for high voltage electrochemical double layer capacitors: A perspective article. *Journal of Power Sources* **2016**, *326*, 534-540.
32. Béguin, F.; Frackowiak, E., *Supercapacitors: materials, systems, and applications*. John Wiley & Sons: 2013.
33. Sing, K. S., Reporting physisorption data for gas/solid systems with special reference to the determination of surface area and porosity (Recommendations 1984). *Pure and applied chemistry* **1985**, *57*, 603-619.
34. Chen, H.; Zhou, M.; Wang, Z.; Zhao, S.; Guan, S., Rich nitrogen-doped ordered mesoporous phenolic resin-based carbon for supercapacitors. *Electrochimica Acta* **2014**, *148*, 187-194.
35. Przepiórski, J.; Tryba, B.; Morawski, A. W., Adsorption of carbon dioxide on phenolic resin-based carbon spheres. *Applied surface science* **2002**, *196*, 296-300.
36. Wang, M.-X.; Huang, Z.-H.; Kang, F.; Liang, K., Porous carbon nanofibers with narrow pore size distribution from electrospun phenolic resins. *Materials Letters* **2011**, *65*, 1875-1877.
37. Lenghaus, K.; Qiao, G. G.; Solomon, D. H.; Gomez, C.; Rodriguez-Reinoso, F.; Sepulveda-Escribano, A., Controlling carbon microporosity: the structure of carbons obtained from different phenolic resin precursors. *Carbon* **2002**, *40*, 743-749.
38. Zhu, X.; Qian, F.; Liu, Y.; Matera, D.; Wu, G.; Zhang, S.; Chen, J., Controllable synthesis of magnetic carbon composites with high porosity and strong acid resistance from hydrochar for efficient removal of organic pollutants: an overlooked influence. *Carbon* **2016**, *99*, 338-347.
39. Ahmed, M. J.; Theydan, S. K., Adsorptive removal of p-nitrophenol on microporous activated carbon by FeCl₃ activation: equilibrium and kinetics studies. *Desalination and Water Treatment* **2015**, *55*, 522-531.
40. Zhong, C.; Deng, Y.; Hu, W.; Qiao, J.; Zhang, L.; Zhang, J., A review of electrolyte materials and compositions for electrochemical supercapacitors. *Chemical Society Reviews* **2015**, *44*, 7484-7539.
41. Pal, B.; Yang, S.; Ramesh, S.; Thangadurai, V.; Jose, R., Electrolyte selection for supercapacitive devices: a critical review. *Nanoscale Advances* **2019**, *1*, 3807-3835.
42. Karthik, M.; Redondo, E.; Goikolea, E.; Roddatis, V.; Doppiu, S.; Mysyk, R., Effect of mesopore ordering in otherwise similar micro/mesoporous carbons on the high-rate performance

of electric double-layer capacitors. *The Journal of Physical Chemistry C* **2014**, *118*, 27715-27720.

43. Garcia-Gomez, A.; Barranco, V.; Moreno-Fernandez, G.; Ibañez, J.; Centeno, T.; Rojo, J., Correlation between capacitance and porosity in microporous carbon monoliths. *The Journal of Physical Chemistry C* **2014**, *118*, 5134-5141.

44. Zhu, J.; Xu, Y.; Wang, J.; Lin, J.; Sun, X.; Mao, S., The effect of various electrolyte cations on electrochemical performance of polypyrrole/RGO based supercapacitors. *Physical Chemistry Chemical Physics* **2015**, *17*, 28666-28673.

45. Wu, H.; Wang, X.; Jiang, L.; Wu, C.; Zhao, Q.; Liu, X.; Yi, L., The effects of electrolyte on the supercapacitive performance of activated calcium carbide-derived carbon. *Journal of power sources* **2013**, *226*, 202-209.

46. Koh, A. R.; Hwang, B.; Roh, K. C.; Kim, K., The effect of the ionic size of small quaternary ammonium BF₄ salts on electrochemical double layer capacitors. *Physical Chemistry Chemical Physics* **2014**, *16*, 15146-15151.

47. Bhattacharjya, D.; Yu, J.-S., Activated carbon made from cow dung as electrode material for electrochemical double layer capacitor. *Journal of Power Sources* **2014**, *262*, 224-231.

48. Li, Y.; Zhang, C.; Jiang, Y.; Wang, T.-J.; Wang, H., Effects of the hydration ratio on the electrosorption selectivity of ions during capacitive deionization. *Desalination* **2016**, *399*, 171-177.

49. Redondo, E.; Ségalini, J.; Carretero-González, J.; Goikolea, E.; Mysyk, R., Relation between texture and high-rate capacitance of oppositely charged microporous carbons from biomass waste in acetonitrile-based supercapacitors. *Electrochimica Acta* **2019**, *293*, 496-503.

50. Jiang, J.; Liu, B.; Liu, G.; Qian, D.; Yang, C.; Li, J., A systematically comparative study on LiNO₃ and Li₂SO₄ aqueous electrolytes for electrochemical double-layer capacitors. *Electrochimica Acta* **2018**, *274*, 121-130.

CHAPTER – 4

Optimization of aqueous asymmetric supercapacitors by using nickel cobalt oxide and superactivated polymer-derived carbon as electrode materials

We investigated the performance of an aqueous asymmetric supercapacitor (AAS) assembled by using novel nanostructured NiCo_2O_4 as the positive electrode and a polymer derived superactivated carbon (SAC) as the negative electrode. The combination of both the nanostructured NiCo_2O_4 and the carbon with hierarchical porosity and ultrahigh specific surface area (above $3000 \text{ m}^2 \text{ g}^{-1}$) led to excellent rate performances and long stability of the system. The optimization of the AAS device is further achieved through the variation of mass ratio between positive and negative electrodes. The optimized AAS full cell exhibits reversibility within the 0.0-1.5 V operative voltage region, delivering a specific cell capacity of 24.6 mAh g^{-1} at a current density of 1 A g^{-1} . This results in a remarkable energy density of 13 Wh kg^{-1} at a power density of 26.2 kW kg^{-1} and an excellent cycling durability above 87% of the initial capacity after 10,000 charge–discharge cycles.

4.1. Introduction

Aqueous electrolytes-based supercapacitor have always higher ionic conductivity, are non-flammable, cheaper and are more environmental friendly than those ones operating with organic electrolytes.^[1, 2] In contrast, the utilization of aqueous electrolyte in symmetric supercapacitors tends to show much lower energy density due to their narrow electrochemical stability window. Therefore, it is a tremendous challenge to improve the energy density of aqueous electrochemical capacitor without compromising its environmental benignity, cost and power density. On this note, aqueous asymmetric supercapacitor (AAS) combining a battery-type positive and an EDLC type negative electrode has allured widespread attention in the energy storage field to become an inexpensive alternative or supplement to LIBs in many applications.^[2]

Activated carbons are traditionally chosen as negative electrodes for AAS because of their high specific surface area, chemical stability, good conductivity and low cost.^[3-4] Other nanostructured carbons such as stacked graphene films, graphene oxides or carbon nanotubes have been also postulated as promising candidates for the negative electrode.^[5-6] For the positive electrode, various faradaic-type materials including mono or multi-metallic transition compounds and conductive polymers are mostly investigated due to their excellent charge storage capability by reversible redox reactions.^[5,7,8-14] Among the various transition metal oxides, a binary metal oxide, $\text{Ni}_x\text{Co}_{(3-x)}\text{O}_4$, has been discovered to hold tremendous promise due to its excellent theoretical capacity (over 2000 F g^{-1} in terms of capacitance) along with high electronic conductivity facilitating high rate performance compared to its monometallic counterparts.^[15-17] Moreover, nano-sized positive electrode materials are highly desired, since in this case, redox active functional groups concentration is maximized and its accessibility is improved, leading to better rate performances and reversibility.^[18-24]

Regarding activated carbons, the large concentration of ultramicropores (pore size $<0.7 \text{ nm}$) and tortuous microporosity, inherent to the activation processes of preformatted rigid precursors using steam, CO_2 , KOH or NaOH ,^[25] strongly decrease their performance at high current rates, resulting in a failing balance of the high capacity exhibited by the positive electrodes.^[7,10] In this context, we have synthesized a novel and straightforward synthetic process to easily obtain a very high surface area carbon by the simultaneous polymerization, carbonization and chemical

activation of a mixture of melamine and terephthalaldehyde with KOH (activating agent). These super-activated carbons showed an excellent performance when tested as active electrode material in symmetric EDLCs in different aqueous electrolytes.^[26] The combination of high specific surface area and its hierarchical structure of pores at the meso and microscale favors the ion transport making of it an excellent candidate to be used as carbonaceous material for high power asymmetric energy storage devices.

Apart from the characteristic properties of individual electrode materials, the mass-balance between positive and negative electrodes is an important parameter to investigate during testing of the electrochemical performance of advanced hybrid supercapacitors. Mass balance of the negative and positive electrode allows to control the potential span of each electrode in an asymmetric cell and is thus the key to achieve a high energy density with high cycle life without compromising the power density.

The research study presented in this chapter, was designed a robust AAS cell and studied the role of electrode mass-balance on the electrochemical performance. In this system, we are using our lab synthesized a high surface area porous carbon (SAC) as the negative electrode and NiCo₂O₄ nano-thorns assembled into floral-like spheres as the positive electrode.

4.2. Material synthesis

The super-activated carbon (hereafter denoted as SAC) was synthesized as previously described elsewhere.^[26] Briefly, 1.24 g of melamine, 1.36 g of terephthalaldehyde and 5.0 g of KOH were finely ground in an agate mortar and then directly heated in the furnace at 250 °C for 3 h and then at 800 °C for 1 h with a heating ramp of 1 °C min⁻¹ in Ar atmosphere. The carbonized material was washed several times with 3 M HCl and DI water, then dried at 120 °C in an oven.

NiCo₂O₄ was synthesized in the following way: 0.126 g of Ni (NO₃)₂·6H₂O, 0.251 g of Co(NO₃)₂·6H₂O and 0.462 g of urea were mixed under continuous stirring for 30 min in 10 mL of DI water. Then, the clear solution was poured in a Teflon-lined autoclave and kept in oven for 180 °C for 2 h. The purple precipitates were collected by centrifugation and washed with ethanol and DI water several times. After drying at 60 °C for 6 h, the samples were calcined in air at 300 °C for 3 h.

4.3. Physicochemical characterization

The structure and morphology of the NiCo_2O_4 was studied by scanning electron microscopy (SEM). Figure 4.1.a clearly shows that the material is composed of dendritic microspheres formed by the assembly of NiCo_2O_4 nanothorns, where it is prominent that the hollow core morphology of these floral spheres wall is a tightly packed bundle of nanothorn-like crystalline sheets of NiCo_2O_4 . These types of self-assembled hierarchical structures are generally obtained by hydro/solvothermal synthesis where urea plays the role of both the self-template organizer and the precipitator.

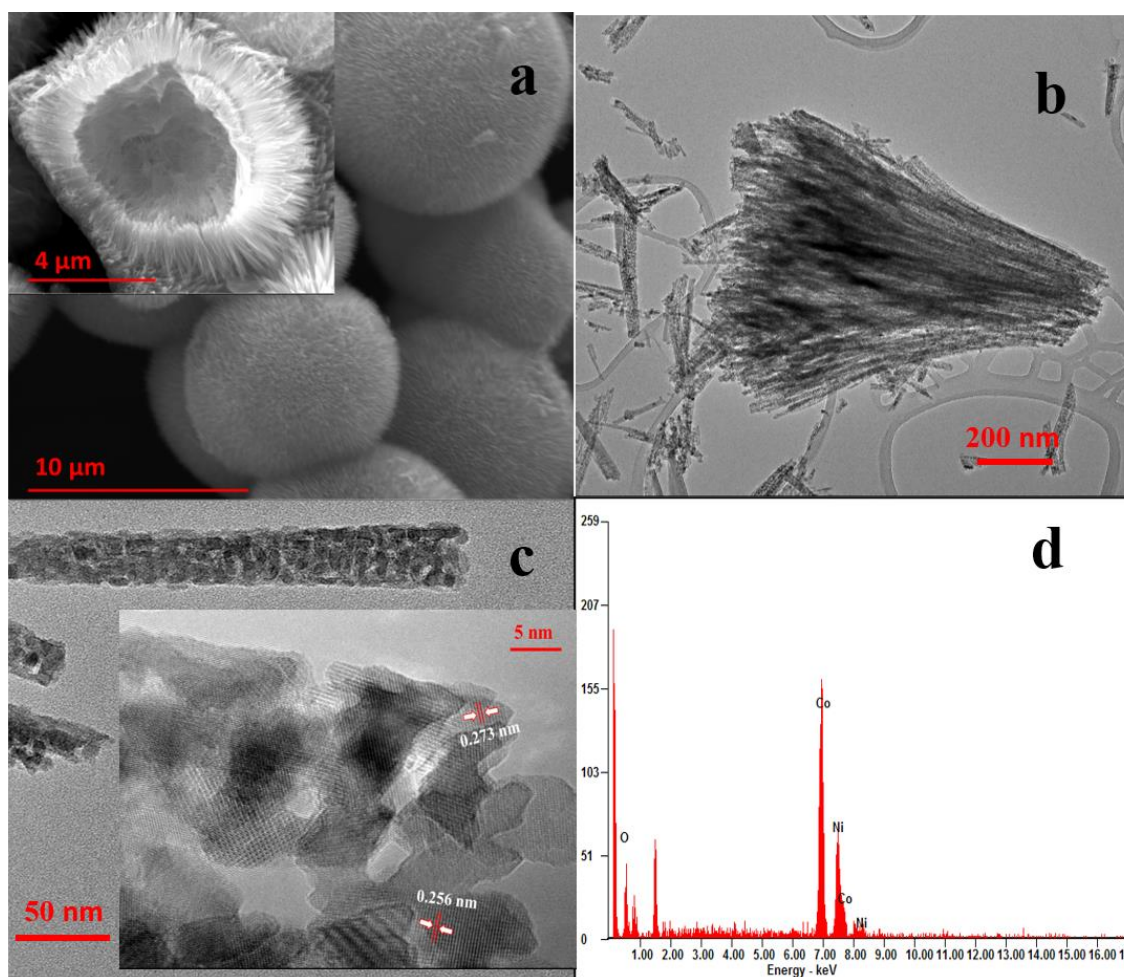


Figure 4.1. (a) SEM image (inset: higher magnification SEM image of the sphere surface), (b) & (c) TEM image showing the assembly of small crystalline nanoparticles into nano-thorn (inset: high magnification TEM image) and (d) EDX spectra recorded for this NiCo_2O_4 material.

Meanwhile, in Figure 4.1.b and c, transmission electron microscopy (TEM) images reveal that the thorn bundles are decorated with a stone-pillar-like array with well-defined porous structures, which may help the electrolyte ions accessing the surface. The inset of Figure 4.1.c indicates the well-distinct polycrystallinity of each grain with the spacing between the adjacent fringes of ~ 0.273 nm, which is in agreement to the theoretical (111) interplane distance within the NiCo_2O_4 spinel phase. According to Energy dispersive X-ray (EDX) analysis (Figure 4.1.d), the atomic ratio between Ni and Co is similar to the ratio used in the pristine solution media.

The X-ray diffraction (XRD) pattern registered for the synthesized nickel cobalt oxide is depicted in Figure 4.2.a. As it can be observed, the pattern shows well-defined diffraction peaks at 18.9° , 30.9° , 36.6° , 44.6° , 55.4° , 59.0° and 64.8° , which can be assigned to the (111), (200), (311), (400), (422), (511) and (440) lattice planes indexed for the crystalline NiCo_2O_4 according to the standard JCPDS file no. 73-1702. It is worth noting that only these peaks are observed, discarding the presence of other crystalline impurity phases in the sample. Besides, these XRD findings are in good agreement with the above mentioned EDX analysis *i.e.* the formation of crystalline NiCo_2O_4 spinel phase. To get more information on the textural properties of this sample, the oxide was investigated by nitrogen gas adsorption-desorption technique.

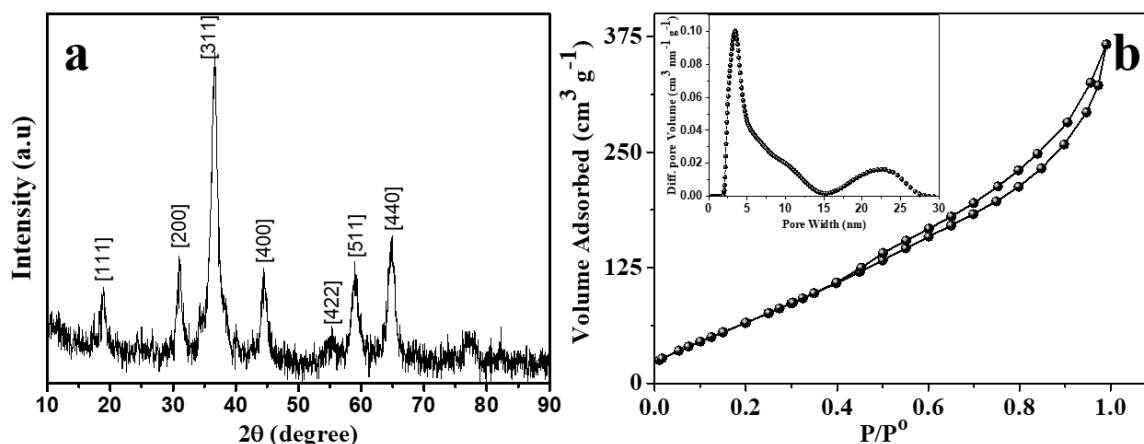


Figure 4.2. (a) XRD profile and (b) Nitrogen adsorption desorption isotherms (inset: pore size distribution curve) of NiCo_2O_4 .

The isotherm registered for the NiCo_2O_4 , shown in Figure 4.2.b, exhibits a profile in between type II and type IV according to the IUPAC classification,^[27] with a small hysteresis loop (H3)

in the relative pressure region between 0.4 and 1.0. These isotherms are characteristic of mesoporous materials containing slit-shaped pores. It is worth to highlight the quite large BET specific surface area calculated for this mixed metal oxide that reached $255 \text{ m}^2\text{g}^{-1}$. The pore size distribution calculated from the adsorption branch through the Barrett-Joyner-Halenda (BJH) approach shows a bimodal distribution with two pore systems centered at $\sim 4.0 \text{ nm}$ and $\sim 22 \text{ nm}$, which correspond to the interparticle voids between primary crystalline particles within the thorns and to the pores between adjacent thorns in the NiCo_2O_4 flowers, respectively, giving rise to a total pore volume of $0.56 \text{ cm}^3\text{g}^{-1}$.

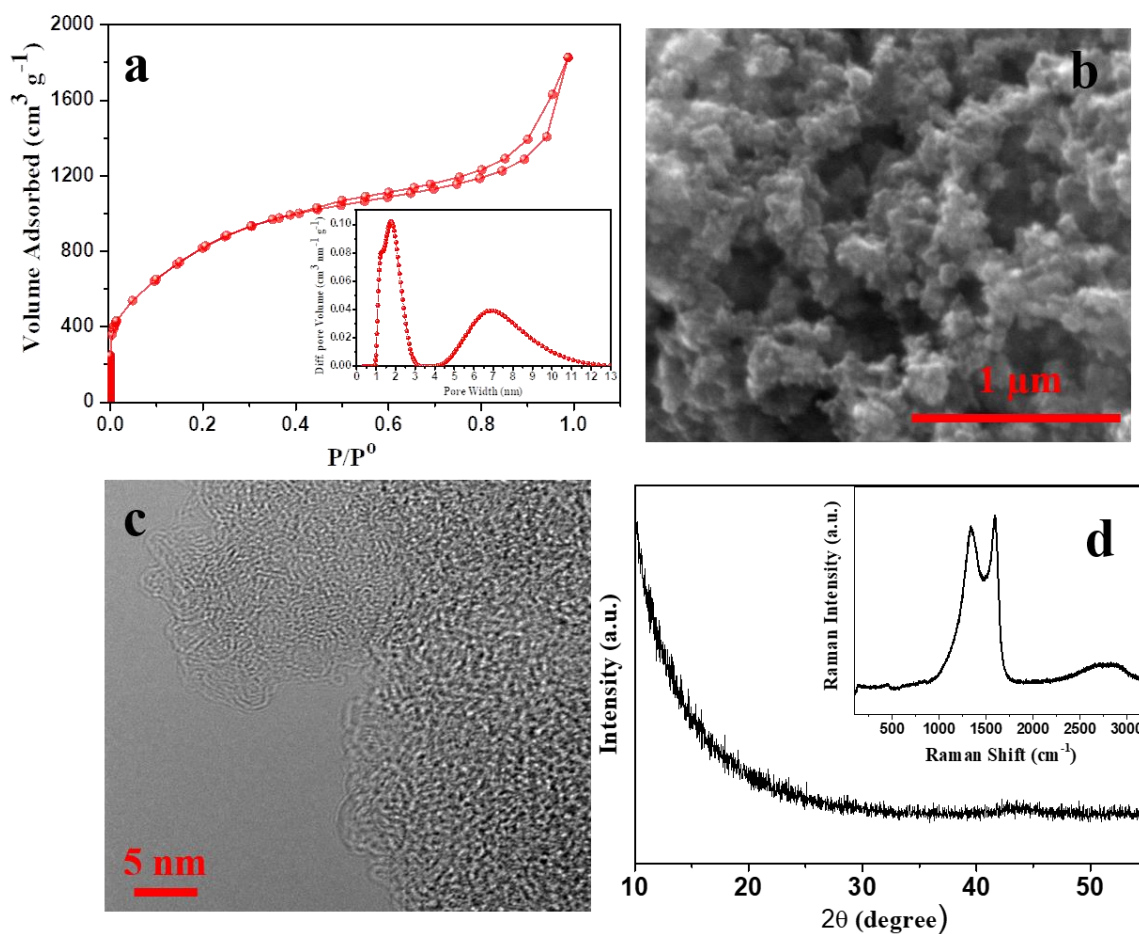


Figure 4.3. (a) Nitrogen adsorption desorption isotherms (inset: pore size distribution curve), (b) SEM image and (c) TEM image registered for the SAC, (d) XRD pattern (inset: Raman spectrum).

The nitrogen adsorption-desorption isotherm registered for the SAC is shown in Figure 4.3.a. This isotherm shows a profile between type I and II with a H4-type hysteresis loop according to the IUPAC classification.^[27] The adsorption at high relative pressures indicates the presence of medium size or large mesopores in SAC.

The BET specific surface area and pore volume of SAC are calculated to be $3071 \text{ m}^2\text{g}^{-1}$ and $2.8 \text{ cm}^3\text{g}^{-1}$, respectively. The inset of Figure 4.3.a depicts the pore size distribution curve of this carbon, which clearly shows that SAC comprises a bimodal distribution of micro-mesopores with pores of 1–3 nm combined with mesopores ranging from 4.5 to 8 nm.

A more detailed structural characterization of this carbon was performed by SEM and TEM analysis. The SEM image (Figure 4.3.b) illustrates the rough surface of the carbon showing irregular-shaped carbon particles of approximately ~50 nm. The inter-particle voids in carbon can be the reason for the high content of mesopores in this material ($1.8 \text{ cm}^3\text{g}^{-1}$), which overall endows the SAC with a good amount of hierarchical porosity at different pore lengths. On the other hand, the high magnification TEM image (Figure 4.3.c) shows the presence of maggot-like shaped nanopores randomly distributed along the sample.

The XRD pattern of the SAC in Figure 4.3.d shows a smooth profile without the presence of any significant diffraction peak, which is characteristic of the highly porous amorphous carbons. The Raman spectrum registered for the SAC (inset of Figure 4.3.d) shows a typical profile of amorphous carbons; two predominant bands at nearly 1350 cm^{-1} and 1580 cm^{-1} , which correspond to the D and G bands respectively, are observed together with a broad and low intense peak recorded at 2700 cm^{-1} which is ascribed to the G stretching mode.

The D band is generally activated by surface defects and it is used to measure the degree of disorder within the carbon materials whereas G band results from the bond stretching vibration of sp^2 carbon pairs.^[26,28] Furthermore, the presence of the G band in carbon-based materials indicates the perfection of hexagonal symmetry which leads to the formation of a partially graphitic structure. The obtained spectrum supports the amorphous nature characteristic of carbon walls, which contains a large number of defects and pores, which is in good agreement with the XRD measurement.

4.4. Electrochemical characterization

4.4.1. Electrode processing and cell assembly

Electrochemical performance of NiCo_2O_4 was first assessed in a conventional three-electrode configuration using a 6M KOH aqueous solution as electrolyte. The electrodes were prepared by mixing 60 wt% of NiCo_2O_4 with 30 wt% of carbon black (CB) and 10 wt% of polytetrafluorethylene (PTFE) in the presence of a few drops of ethanol. The dough was kneaded continuously until reaching plasticity, uniformly rolled until a thickness of nearly 40 μm , punched out into disk shaped (12 mm in diameter) and finally dried at 120°C overnight.

Working electrodes were prepared by compressing these disk-shaped electrodes ($\sim 2.12 \text{ mg cm}^{-2}$) onto a 2 mm thick Nickel foam (99.8% pure, MTI Corp.) that served as current collector. A Pt coiled wire and a Hg/HgO (saturated in 1M NaOH) electrode were used as counter and reference electrodes, respectively. The counter electrode was cleaned prior the measurements with acidic piranha solution to remove any surface impurities.

Symmetric SAC//SAC supercapacitors were built using a two-electrode configuration and electrodes with similar masses ($\sim 2.3 \text{ mg cm}^{-2}$) were assembled into SwagelokTM-type cells. The disk-shaped electrodes with $\sim 130 \mu\text{m}$ thickness were prepared following the above-mentioned process by mixing 90 wt% of the SAC with 5 wt% of CB and 5 wt% of PTFE. A porous glass fiber (Whatman GFB) membrane was used as a separator between them and stainless-steel rods as current collectors. The electrodes and the separator were wetted with a few drops of 6M KOH aqueous electrolyte.

Asymmetric cells of Ni-Co-oxide//SAC were built using four different mass ratios of positive and negative electrodes, *i.e.* 1:1, 1:2, 1:3 and 1:4, respectively in SwagelokTM-type two-electrode cells. Porous glass fiber was used as separator, stainless steel current collectors, and 6M KOH as an electrolyte.

4.4.2. Electrochemical performance of the positive electrode (NiCo_2O_4)

The electrochemical activity of the synthesized nanostructured NiCo_2O_4 was firstly investigated in a three-electrode configuration using 6M KOH aqueous solution as the electrolyte.

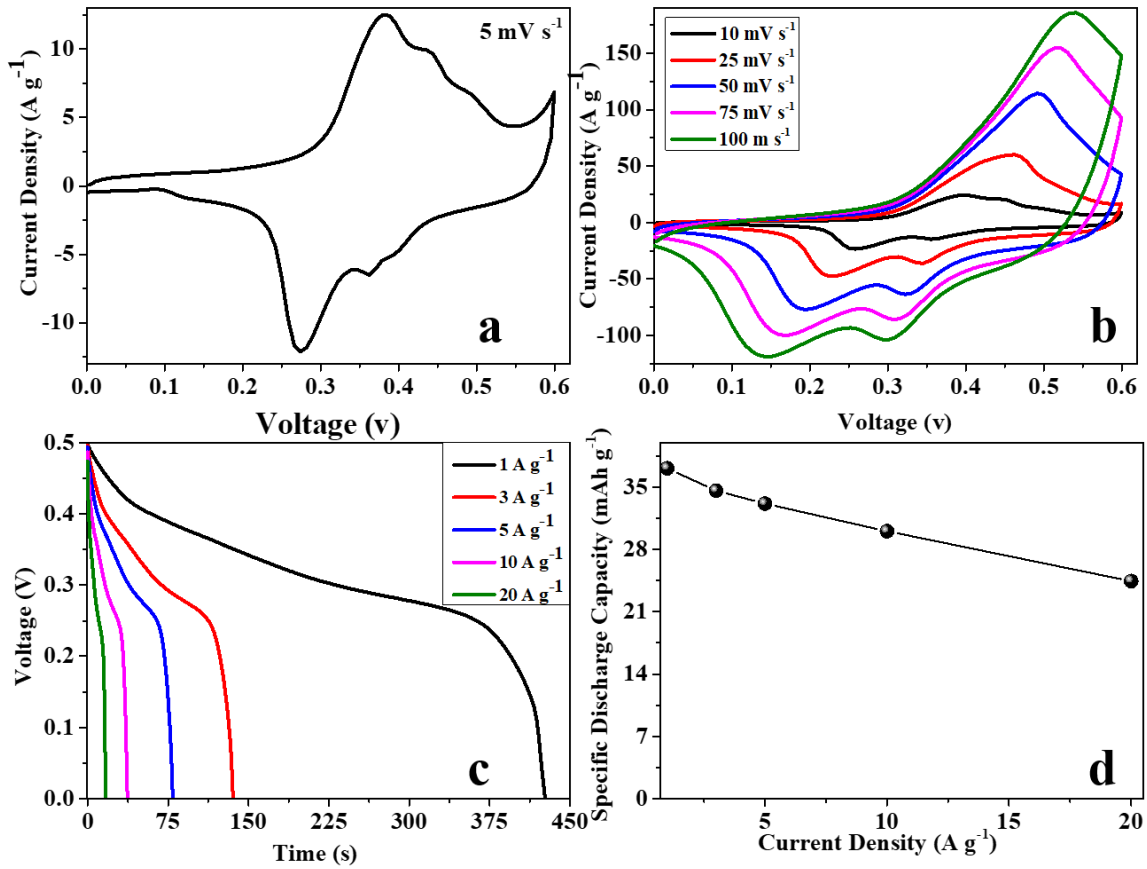
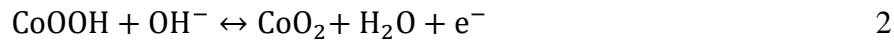
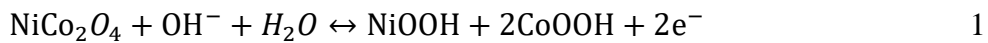


Figure 4.4. (a) CV curve registered at 5 mV s⁻¹ and (b) at higher sweep rates (10-100 mV s⁻¹) for the NiCo₂O₄. (c) Galvanostatic discharge curves recorded at indicated current densities (1-20 A g⁻¹) and (d) Capacity evolution vs. Current for the NiCo₂O₄.

Figure 4.4.a displays the CV curve registered for the working electrode containing NiCo₂O₄ at a sweep rate of 5 mV s⁻¹ in the potential range between 0 V and 0.6 V vs. Hg/HgO. A pair of well-defined cathodic and anodic peaks are observed at *ca.* 0.38 V and 0.27 V.^[29] Another pair of small yet distinguishable redox peaks can also be observed around 0.44 V and 0.36 V vs. Hg/HgO. All these peaks can be ascribed to the reversible transitions between the oxidation states Co³⁺/Co⁴⁺ and Ni²⁺/Ni³⁺ accompanying with the hydroxyl ion in the alkaline electrolyte as given in Eq. 1 and 2.^[29-31]



With increasing the scan rate, the oxidation peaks of the CV curve shift towards more positive potentials while the reduction peaks shift more negative direction (Figure 4.4.b), indicating some uncompensated resistance in the cell, most likely the slow redox kinetics as previously reported elsewhere.^[30]

Figure 4.4.c displays the galvanostatic discharge curves of NiCo₂O₄ floral spheres at different current densities from 1 to 20 A g⁻¹ in the potential range of 0.0–0.50 V. The non-linear characteristic of the discharge curves prove that this material has battery-like faradaic charge storage behavior rather than pseudocapacitive.

Nevertheless, the cell exhibited a specific capacity of 37 mAh g⁻¹ at a discharge rate of 1 A g⁻¹ and excellent capacity retention of ~66% at the high current density of 20 A g⁻¹ (Figure 4.4.d). The results suggest that the porous architecture of this binary metal oxide electrode is ideally suited as a positive electrode material for fast and efficient AAS.

4.4.3. Electrochemical performance of the negative electrode (SAC)

The electrochemical performance of SAC electrodes was tested in two-electrode configuration using 6M KOH aqueous solution as the electrolyte. Figure 4.5.a shows the CV profiles at various scan rates ranging from 5 to 100 mV s⁻¹ between 0 and 1.0 V. All of the CV curves show large areas with near rectangular-like shapes, which is a characteristic feature for an ideal EDLC behaviour with good dynamic charge propagation.^[26]

A sharp change in capacitive current transient upon altering the polarization direction near voltage limits (0.0 and 1.0 V) signifies a very low internal resistance of the cell. This can be attributed to the presence of a high amount of medium or large-sized mesopores and the high electrical conductivity of the SAC-based electrode. The SAC comprises bimodal micro-mesoporosity which promotes an unrestricted access of electrolyte ions to the available active surface. This highly porous carbon framework helps absorbing more electrolyte ions on the active electrode surface and also ensures the efficacy of double layer capacitance.^[28]

Galvanostatic charge-discharge (CD) curves were registered for SAC at various current densities between the 0.0 and 1.0 V voltage range are included in figure 4.5.b.

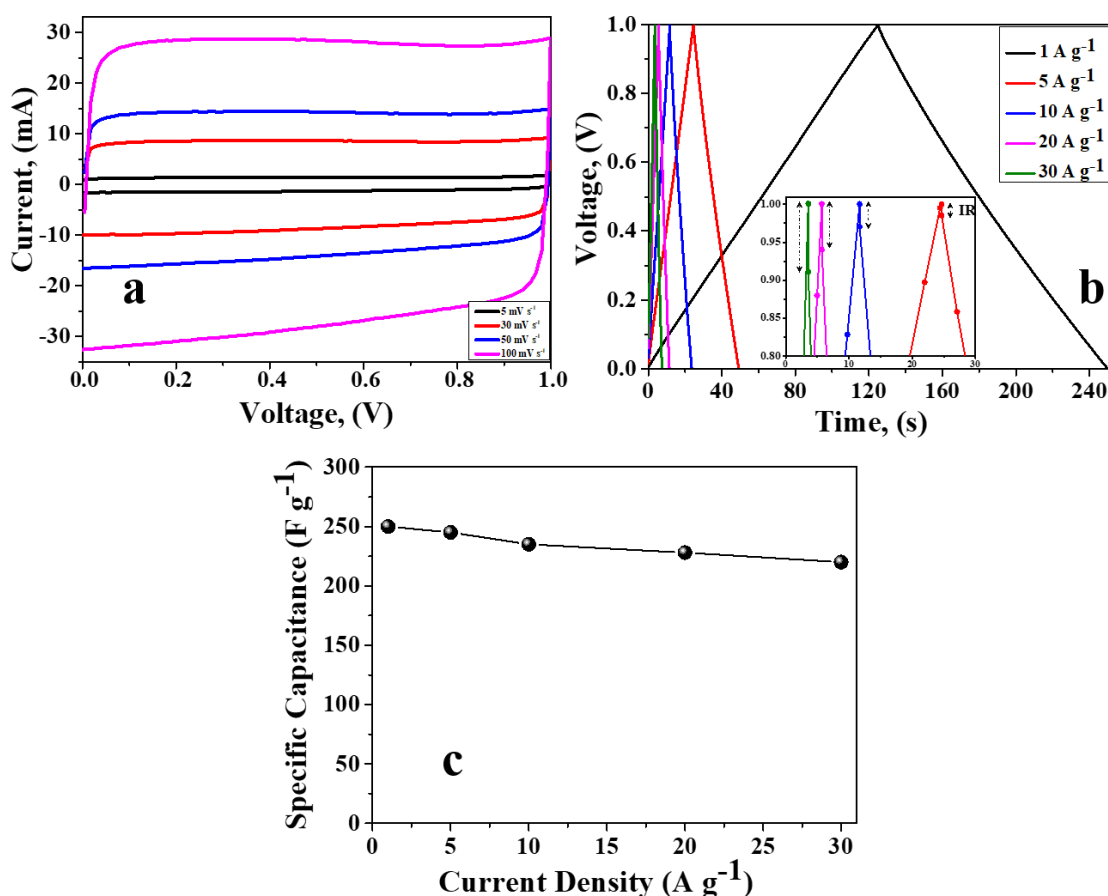


Figure 4.5. (a) CV curves registered at indicated sweep rates, (b) charge-discharge curve at labeled current densities, inset shows a magnified view of the 0.8-1.0 V region, and (c) specific capacitance evolution of SAC sample at different current rates.

It is worth noticing that this material exhibits a triangular CD profile with almost 100% of coulombic efficiency (*i.e.* charge time = discharge time) and the very low ohmic drop associated to each cycle even at very high current rates (see the inset in figure 4.5.b).

The specific capacitance value calculated for this sample at 1 A g⁻¹ correspond to 250 F g⁻¹, and it shows an excellent capacitance retention up to 220 F g⁻¹ at a high current density of 30 A g⁻¹. The excellent rate capability exhibited by this carbon, as evidenced by the high capacitance retention of ~88% of its initial value at 30 A g⁻¹ as (Figure 4.5.c) support the use of the SAC carbon as attractive candidate to be used as negative electrode for AAS system.

4.4.4. Electrochemical performance of the NiCo₂O₄//SAC asymmetric supercapacitor

AAS full cells were fabricated by assembling nanostructured NiCo₂O₄ and SAC as positive vs. negative electrodes, respectively, and using a 6M KOH aqueous solution as the electrolyte. To evaluate and optimize the electrochemical performance of the AAS cells, four different mass ratios *i.e.*, 1:1, 1:2, 1:3 and 1:4 of positive vs. negative electrodes respectively were investigated by changing only the negative electrode mass with respect to a fixed positive electrode mass (Figure 4.6.). It was observed that increasing the mass of the negative electrode has a noticeable impact on the overall performance of the asymmetric cells.

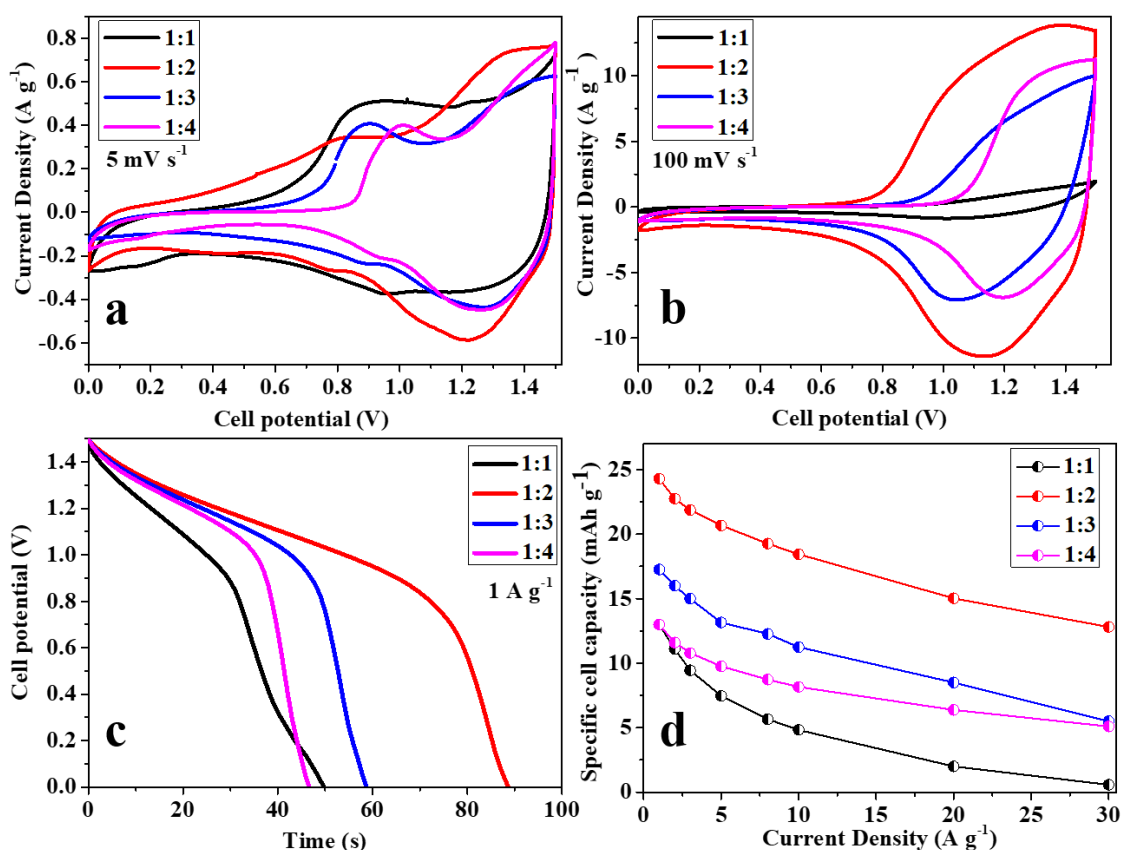


Figure 4.6. (a) Comparative CV profiles at low potential scan rate of 5 mV s⁻¹ and (b) high scan rate of 100 mV s⁻¹, (c) Comparative discharge curve at current density of 1 A g⁻¹ and (d) rate capability of AAS device [NiCo₂O₄//SAC].

Figure 4.6.a and b show CV curves registered for the AAS cells assembled using different electrode mass ratios at low and high scan rates of 5 and 100 mV s⁻¹ in the 0.0-1.5 V potential

range. All of the AAS cells exhibit a combinative CV geometry consisting of both faradaic and EDLC type contribution. Some prominent redox peaks can be observed in the voltage range of 0.8 to 1.5 V resulting from faradaic charge storage in the positive electrode, whereas the potential below 0.8 is mostly non-faradaic in nature. No oxygen evolution was observed until the operating voltage of 1.5 V, which is estimated to be the appropriate operating potential for an AAS device. As can be observed, the charging and discharging current densities gradually increase as the sweep rate is increased indicating the fast-kinetic reversibility of this AAS system.^[32]

The specific capacity and rate capability of these AAS cells was determined by means of galvanostatic charge-discharge tests at different current rates within the 0.0-1.5 V voltage range. Figure 4.6.c shows the comparative discharge profiles corresponding to the AAS cells with different mass ratios registered at 1 A g⁻¹. As can be clearly observed, all of them exhibit a non-linear potential vs. time profile, which indicates the contribution of faradaic battery-type storage mechanisms.

Figure 4.6.d shows the variation of the calculated specific cell capacities of the AAS cells for different current densities up to 30 A g⁻¹. The capacity retention at high current rates of all the AAS cells, except for the 1:1 ratio, are found to be high, which could be ascribed to the praiseworthy contribution from SAC by generating fast electron conduction path as well as a good stability. We found that there is a significant enhancement of electrochemical capacity with the increase in mass of the negative electrode compared to the positive but with a limitation up to certain level.

The best specific capacity was obtained for the 1:2 ratio, reaching specific capacity values of 24.6 mAh g⁻¹ at 1 A g⁻¹ and 15 mAh g⁻¹ at 30 A g⁻¹, while no enhancement was observed with further increase in the negative electrode mass. This can be explained because the necessary charge was already stabilized by the negative electrode in 1:2 ratio AAS cell, which is sufficient enough to utilize the full capacity of the positive electrode.

We can relate this with the principle of charge balance ($Q_+ = Q_-$) from individual performance of NiCo₂O₄ and SAC electrodes. Further increase in the mass of the negative electrode (up to four times that of the positive electrode), become ineffective to increase the cell capacity. Although the electrochemical behaviour as well as capacitive performances of 1:3 and 1:4 ratio AAS cells

are not hugely different from that of the best performed 1:2 ratio, but when it comes to 1:1 ratio, the capacity performance is quite low compared to others and the corresponding results are given in table 4.1.

Table 4.1. Comparative electrochemical parameters calculated for the different AAS devices

AAS device electrode name (Positive//Negative) [NiCo ₂ O ₄ //SAC]	Capacity, Q _D (mAh g ⁻¹)	Coulombic efficiency (η_i)	ED (Wh kg ⁻¹) ^[a] & PD (kW kg ⁻¹) ^[b] at Current Densities				
			1 A g ⁻¹	10 A g ⁻¹	20 A g ⁻¹	30 A g ⁻¹	
1:1	12.9	71.5	ED	12.0	7.5	3.6	0.5
			PD	0.8	5.0	7.4	16.7
1:2	24.6	88.1	ED	24.3	20.7	18.4	13
			PD	1.0	5.1	10.0	26.2
1:3	17.3	87.1	ED	17.3	13.7	11.2	5.1
			PD	1.0	5.5	10.1	18.4
1:4	13.9	85.3	ED	13.8	10.1	8.05	3.5
			PD	1.0	5.2	9.85	20.5

[a] ED: Energy density. [b] PD: Power density

This clearly indicates that a sufficient mass of the negative electrode was not available in this cell to balance charge storage capacity of the positive electrode. It is evident that the charge balance approach is playing an important role in full cell asymmetric device. This difference in performance is also manifest from the equivalent series resistance (ESR) vs current density plots of the AAS cells where the 1:1 ratio shows a much higher ESR compared to negligible values of the other cells (Figure 4.7.a).

Moreover, figure 4.7.b represents the Ragone plots of the corresponding energy vs power densities for all of the AAS cells. The cell with 1:2 ratio has achieved a high energy density of 24.3 Wh kg⁻¹ at a power density of 1.0 kW kg⁻¹ (current density of 1 A g⁻¹). Furthermore, this cell still retains 13 Wh kg⁻¹ energy density value at high power density of 26.2 kW kg⁻¹, which is very promising towards the development of high energy aqueous supercapacitors.

From all these GC-GD results, it was found that the 1:2 AAS cell shows the best performance in terms of both specific capacity and rate capability. So, this 1:2 AAS cell is selected to investigate the long-term stability by performing GC-CD cycles at 5 A g⁻¹ current density. From the resultant cyclic stability plot in Figure 4.7.c, it can be observed that the specific cell capacity increases steadily at the initial ~200 cycles.

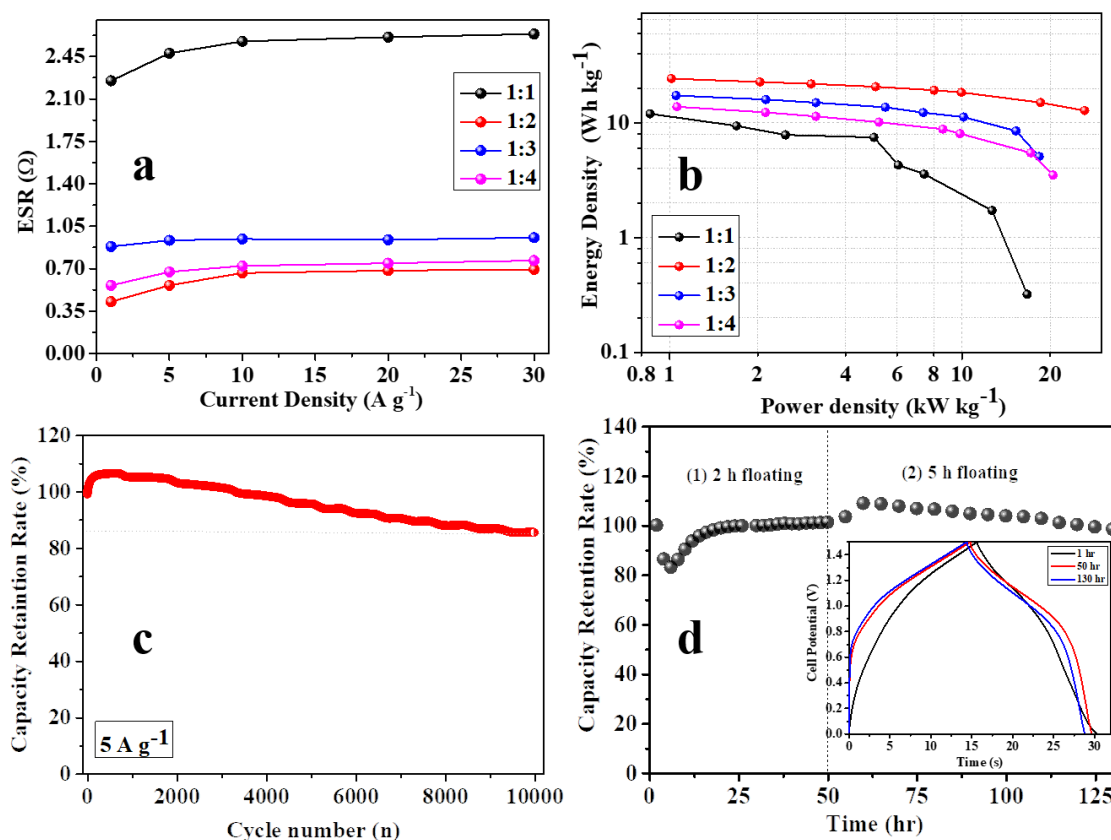


Figure 4.7. (a) Plots of cumulative ESR values, (b) comparative Ragone plots, (c) cycling stability and (d) Stability tests performed under floating conditions for the optimized AAS using positive: negative 1:2 ratio and (inset GC-GD registered at indicated times during the floating tests. of 1:2 AAS device $[NiCo_2O_4//SAC]$ measured at $5 A g^{-1}$.

This slight activation process could be ascribed to the gradual penetration of the electrolyte into the active material surface.^[33-34] Subsequently, after reaching the maximum capacity at around 200 cycles, it stabilizes up to 1000 cycles and then it decreased slowly. After 10,000 cycles of charge-discharge, this AAS cell still delivered about 87% of its initial capacity, which is an outstanding cycling performance compared to the reported results in similar AAS systems.^[30,32]

Such high stability can be attributed to its unique material morphology, which can resist the volume changes in the active electrode in presence of electrolyte insertion/extraction process.^[32-37]

Additional stability tests were performed under floating potential (Figure 4.7.d). This procedure can be considered a more realistic evaluation for cells and further confirms the outstanding stability of this optimized AAS even under this harsh cycling conditions. We have also compared our best AAS results with commercially available Norit carbon by maintaining same mass balance and found that SAC carbon shows better performance than Norit carbon, which predicts our lab synthesized SAC carbon has much more potential to give excellent stability (figure 4.8.a-d and table 4.2). Commercially available Norit activated carbons has the surface area of $\sim 1000 \text{ m}^2 \text{ g}^{-1}$ with high inner porosity and as a consequence, a large interior surface. In comparison with SAC, norit as a negative electrode is not capable to balance sufficient charge storage in this particular AAS system.

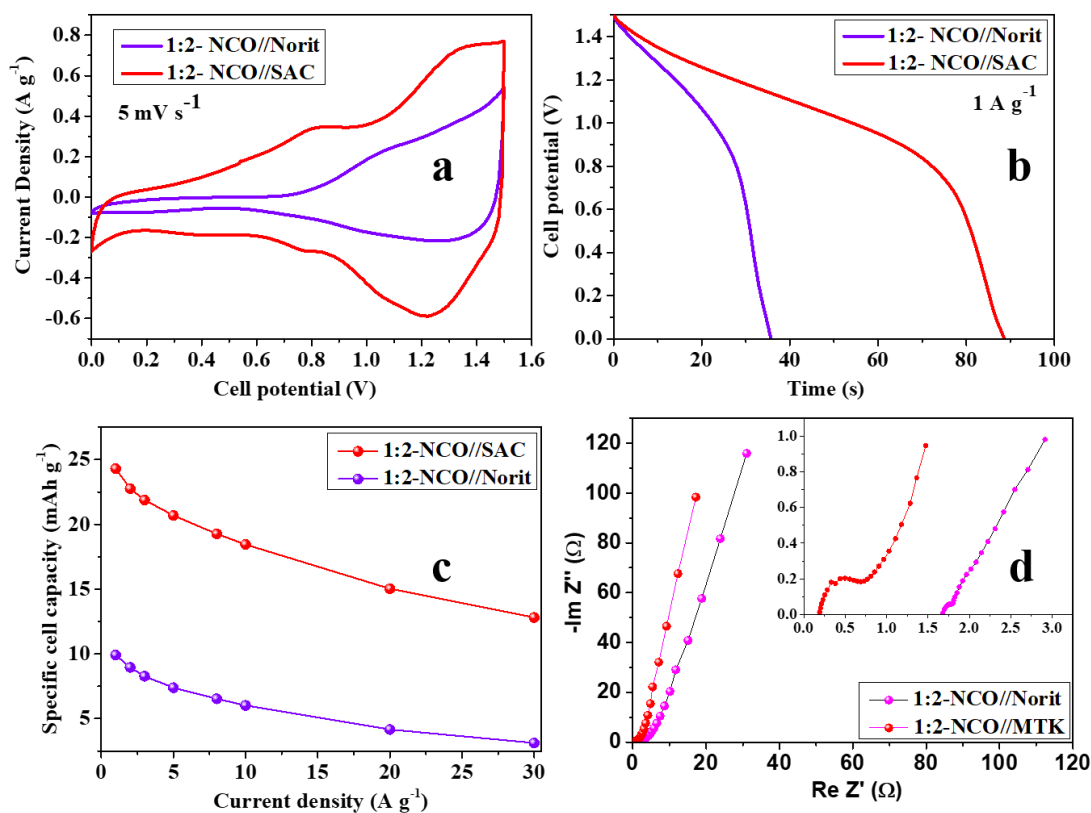


Figure 4.8. (a) CV curves registered at 5 mV s^{-1} , (b) GC-GD recorded at current density 1 A g^{-1} , (c) cell specific capacity evolution, and (d) Nyquist plot for the 1:2 AAS device [NiCo₂O₄//SAC] (Red) and other AAS [NiCo₂O₄//Norit] assembled using commercially available activated carbon (purple).

This result confirms that through a judicious selection of the positive and negative electrodes and careful balance between their amounts we can successfully design advanced a low-cost aqueous hybrid supercapacitor system to compete with the commercially available counterparts. Table 4.2. summarizes the electrochemical performance of this 1:2 ratio AAS cell, compared with other recently reported results in similar AAS devices. It can be observed that the present [NiCo₂O₄//SAC (1:2)] device outperform most of the previously reported AAS cells not only in terms of energy and power densities, but also in terms of much better cycling stability.

Table 4.2. Summary of some representative electrochemical values reported elsewhere for previous Ni-Co-Oxide/hydroxide based asymmetric supercapacitor together with the results obtained in the present study.

AAS device electrode name(Positive//Negative)	Electrolyte	AAS capacitance F g ⁻¹ at 1 A g ⁻¹	Cycling stability Retention	ED (Wh kg ⁻¹) & PD (kW kg ⁻¹) at Current Density				
				1A g ⁻¹	10A g ⁻¹	20A g ⁻¹	30A g ⁻¹	
Ni-Co Oxide//APDC ¹	2M KOH	188	89% upto 4000 cycles at 5 A g ⁻¹	ED	67	52	41.6	-
				PD	0.8	8.0	16	-
NiCo ₂ O ₄ //AC ²	2 M KOH	77.3	108.1% upto 10000 cycles at 3 A g ⁻¹	ED	24.15	16.50	13.75	12.06
				PD	0.23	2.30	4.60	6.67
NCH11/G/NF//AC ³	2 M KOH	108	84.4% upto 2000 cycles at 4 A g ⁻¹	ED	33.75	20.84	-	-
				PD	0.75	7.5	-	-
Ni-Co-Oxide//AC* ⁴	1 M KOH	60	85% upto 2000 cycles at 8 mA	ED	12	9.5	7.4	-
				PD	0.09	0.95	1.90	-
NiCo ₂ O ₄ -rGO//AC ⁵	2 M KOH	96	83% upto 2500 cycles at 1 A g ⁻¹	ED	22.5	18	10.46	-
				PD	0.66	6.60	13	-
NiCo ₂ O ₄ //RGO ⁶	6 M KOH	101.7	93.5% upto 10000 cycles at 5 A g ⁻¹	ED	23.87	18.77	15.28	13.82
				PD	0.66	6.70	13.89	19.75
C7N3//AC ⁷	2 M KOH	82	86.4% upto 10000 cycles at 2 A g ⁻¹	ED	34.92	19.94	-	-
				PD	0.875	8.75	-	-
1: 2 AAS device [NiCo₂O₄//MTK]	6 M KOH	81	87% upto 10000 cycles at 5 A g ⁻¹	ED	24.312	20.68	18.45	13.00
				PD	1.015	5.06	10	26.25
1: 2 AAS device [NiCo ₂ O ₄ //Norit]	6 M KOH	33	-	ED	12.00	8.5	6.4	2.08
				PD	1.05	5.09	11.5	19.08
Ni, Co-HC//HPC ⁸	PVA/KOH	100	100% upto 19,000 cycles at 2 A g ⁻¹	ED	37	30	-	-
				PD	0.8	8.5	-	-

AC= Activated Carbon, APDC= Activated polyaniline derived carbon, RGO= reduced graphene oxide, NCH11/G/NF=Ni-Co binary hydroxide deposited on graphene coated Nickel foam (Ni and Co precursor molar ratio of 1:1), C7N3= Ni-Co-Oxide (Ni and Co precursor molar ratio of 3:7), ED: Energy Density, PD: Power density; * current density in A cm⁻²

4.5. Conclusions

The present work shows the energy storage potential of a novel aqueous asymmetric system, which is formed by coupling a superactivated carbon as negative electrode and a nanostructured NiCo₂O₄ as positive electrode, and further highlights the impact of the mass balance between both electrodes for the optimum performance of the system. The electrochemical studies evidence the importance of the hierarchical structures of the active materials to maintain good capacity retention at high current densities. The optimization of the electrode mass balance within the AAS devices leads not only to both excellent energy and power densities but also to outstanding stability. It was found that the best positive: negative mass ratio in this particular AAS device is 1:2 ratio, which allow delivering maximum gravimetric energy density of 24.3 Wh kg⁻¹ at 1.0 kW kg⁻¹ and still showing 13 Wh kg⁻¹ at 26.2 kW kg⁻¹. Most importantly, this AAS device exhibits excellent long-term cycling stability up to 10,000 cycles with only 13% capacity decay which is outstanding among its peers.

Bibliography

1. Choi, H. S.; Park, C. R. Theoretical guidelines to designing high performance energy storage device based on hybridization of lithium-ion battery and supercapacitor. *J. Power Sources* **2014**, 259, 1-14.
2. Wang, R.; Yan, X. Superior asymmetric supercapacitor based on Ni-Co oxide nanosheets and carbon nanorods. *Sci. Rep.* **2014**, 4, 3712.
3. Zhu, Y.; Wang, J.; Wu, Z.; Jing, M.; Hou, H.; Jia, X.; Ji, X. An electrochemical exploration of hollow NiCo₂O₄ submicrospheres and its capacitive performances. *J. Power Sources* **2015**, 287, 307–315
4. Liu, J.; Jiang, J.; Cheng, C.; Li, H.; Zhang, J.; Gong, H.; Fan, H. J. Co₃O₄ Nanowire@MnO₂ ultrathin nanosheet core/shell arrays: a new class of high-performance pseudocapacitive materials. *Adv. Mater.* **2011**, 23, 2076-2081.
5. Tang, Z.; Tang, C. h.; Gong, H. A high energy density asymmetric supercapacitor from nano-architected Ni(OH)₂/carbon nanotube electrodes. *Adv. Funct. Mater.* **2012**, 22, 1272-1278.
6. Cai, X.; Lim, S. H.; Poh, C. K.; Lai, L.; Lin, J.; Shen, Z. High-performance asymmetric pseudocapacitor cell based on cobalt hydroxide/graphene and polypyrrole/graphene electrodes. *J. Power Sources* **2015**, 275, 298-304.
7. Xu, J.; Wang, Q.; Wang, X.; Xiang, Q.; Liang, B.; Chen, D.; Shen, G. Flexible asymmetric supercapacitors based upon Co₉S₈ Nanorod//Co₃O₄@RuO₂ nanosheet arrays on carbon cloth. *ACS Nano* **2013**, 7, 5453-5462.
8. Mai, L.-Q.; Yang, F.; Zhao, Y.-L.; Xu, X.; Xu, L.; Luo, Y.-Z. Hierarchical MnMoO₄/CoMoO₄ heterostructured nanowires with enhanced supercapacitor performance. *Nat. Commun.* **2011**, 2, 381.
9. Wang, Y.-G.; Cheng, L.; Xia, Y.-Y. Electrochemical profile of nano-particle CoAl double hydroxide/active carbon supercapacitor using KOH electrolyte solution. *J. Power Sources* **2006**, 153, 191-196.
10. Wang, H.; Gao, Q.; Hu, J. Asymmetric capacitor based on superior porous Ni–Zn–Co oxide/hydroxide and carbon electrodes. *J. Power Sources* **2010**, 195, 3017-3024.

11. Wu, Z.; Zhu, Y.; Ji, X. NiCo₂O₄-based materials for electrochemical supercapacitors. *J. Mater. Chem. A* **2014**, 2, 14759-14772.
12. Malak, A.; Fic, K.; Lota, G.; Vix-Guterl, C.; Frackowiak, E. Hybrid materials for supercapacitor application. *J. Solid State Electrochem.* **2010**, 14, 811-816.
13. An, C.; Wang, Y.; Huang, Y.; Xu, Y.; Xu, C.; Jiao, L.; Yuan, H. Novel three-dimensional NiCo₂O₄ architectures: solvothermal synthesis and electrochemical properties. *CrystEngComm* **2014**, 16, 385-392.
14. Wang, Y.-M.; Zhang, X.; Guo, C.-Y.; Zhao, Y.-Q.; Xu, C.-L.; Li, H.-L. Controllable synthesis of 3D Ni_xCo_{1-x} oxides with different morphologies for high-capacity supercapacitors. *J. Mater. Chem. A* **2013**, 1, 13290.
15. Zhao, Y.; Zhang, X.; He, J.; Zhang, L.; Xia, M.; Gao, F.; Morphology controlled synthesis of nickel cobalt oxide for supercapacitor application with enhanced cycling stability. *Electrochim. Acta* 2015, 17, 451-56
16. Chen, W.; Xia, C.; Alshareef, H. N. One-step electrodeposited nickel cobalt sulfide nanosheet arrays for high-performance asymmetric supercapacitors. *ACS nano* **2014**, 8, 9531-9541.
17. Huang, L.; Chen, D.; Ding, Y.; Feng, S.; Wang, Z. L.; Liu, M. Nickel-cobalt hydroxide nanosheets coated on NiCo₂O₄ Nanowires grown on carbon fiber paper for high-performance pseudocapacitors. *Nano Lett.* **2013**, 13, 3135-3139.
18. Lu, X.; Huang, X.; Xie, S.; Zhai, T.; Wang, C.; Zhang, P.; Yu, M.; Li, W.; Liang, C.; Tong, Y. Controllable synthesis of porous nickel-cobalt oxide nanosheets for supercapacitors. *J. Mater. Chem.* **2012**, 22, 13357-13364.
19. Yuan, C.; Li, J.; Hou, L.; Zhang, X.; Shen, L.; Lou, X. W. D. Ultrathin mesoporous NiCo₂O₄ nanosheets supported on Ni foam as advanced electrodes for supercapacitors. *Adv. Funct. Mater.* **2012**, 22, 4592-4597.
20. Zhao, Z.; Geng, F.; Bai, J.; Cheng, H.-M. Facile and controlled synthesis of 3D nanorods-based urchinlike and nanosheets-based flowerlike cobalt basic salt nanostructures. *J. Phys. Chem. C* **2007**, 111, 3848-3852.

21. Wang, X.; Sumboja, A.; Lin, M.; Yan, J.; Lee, P. S. Enhancing electrochemical reaction sites in nickel-cobalt layered double hydroxides on zinc tin oxide nanowires: a hybrid material for an asymmetric supercapacitor device. *Nanoscale* **2012**, *4*, 7266-7272.
22. Carriazo, D.; Patiño, J.; Gutiérrez, M.C.; Ferrer, M. L.; del Monte, F. Microwave-assisted synthesis of NiCo₂O₄-graphene oxide nanocomposites suitable as electrodes for supercapacitors. *RSC Adv.* **2013**, *3*, 13690-13695.
23. Zhu, J.; Jiang, J.; Sun, Z.; Luo, J.; Fan, Z.; Huang, X.; Zhang, H.; Yu, T. 3D Carbon/Cobalt-Nickel mixed-oxide hybrid nanostructured arrays for asymmetric supercapacitors. *Small* **2014**, *10*, 2937-2945.
24. Salunkhe, R. R.; Tang, J.; Kamachi, Y.; Nakato, T.; Kim, J. H.; Yamauchi, Y. A concept for asymmetric supercapacitors using 3D nanoporous carbon and cobalt oxide electrodes synthesized from single metal organic framework. *ACS nano* **2015**, *9*, 6288-6296.
25. Bleda-Martínez, M. J.; Maciá-Agulló, J. A.; Lozano-Castelló, D.; Morallón, E.; Cazorla-Amorós, D.; Linares-Solano, A. Role of surface chemistry on electric double layer capacitance of carbon materials. *Carbon* **2005**, *43*, 2677-2684.
26. Diez, N.; Mysyk, R.; Zhang, W.; Goikolea, E.; Carriazo, D. One-pot synthesis of highly activated carbons from melamine and terephthalaldehyde as electrodes for high energy aqueous supercapacitors. *J. Mater. Chem. A* **2017**, *5*, 14619-14629.
27. Sing, K. S. W. .; Everett, D. H.; Haul, R. A. W.; Moscou, L.; Pierotti, R. A.; Rouquerol, J.; Siemieniewska, T. ; Reporting physisorption data for gas/solid systems with special reference to the determination of surface area and porosity. *Pure Appl. Chem.* **1985**, *57*, 603-619.
28. Panja, T.; Bhattacharjya, D.; Yu, J.-S. Nitrogen and phosphorus co-doped cubic ordered mesoporous carbon as a supercapacitor electrode material with extraordinary cyclic stability. *J. Mater. Chem. A* **2015**, *3*, 18001-18009.
29. Hu, G.; Tang, C.; Li, C.; Li, H.; Wang, Y.; Gong, H. The sol-gel-derived nickel-cobalt oxides with high supercapacitor performances. *J. Electrochem. Soc.* **2011**, *158*, A695.

30. Liu, X.; Shi, S.; Xiong, Q.; Li, L.; Zhang, Y.; Tang, H.; Gu, C.; Wang, X.; Tu, J. Hierarchical NiCo₂O₄@NiCo₂O₄ core/shell nanoflake arrays as high-performance supercapacitor materials. *ACS Appl. Mater. Inter.* **2013**, *5*, 8790-8795.
31. Li, Y.; Hasin, P.; Wu, Y. Ni_(x)Co_(3-x)O₍₄₎ nanowire arrays for electrocatalytic oxygen evolution. *Adv. Mater.* **2010**, *22*, 1926-1929.
32. Oh, K.-H.; Gund, G.-S.; Park, H.-S. Stabilizing NiCo₂O₄ hybrid architectures by reduced graphene oxide interlayers for improved cyclic stability of hybrid supercapacitors. *J. Mater. Chem. A* **2018**, 10.1039/C8TA04038A
33. Lei, Y.; Li, J.; Wang, Y.; Gu, L.; Chang, Y.; Yuan, H.; Xiao, D. Rapid microwave-assisted green synthesis of 3D hierarchical flower-shaped NiCo₂O₄ microsphere for high-performance supercapacitor. *ACS Appl. Mater. Inter.* **2014**, *6*, 1773-1780.
34. Yang, Y.; Li, L.; Ruan, G.; Fei, H.; Xiang, C.; Fan, X.; Tour, J. M. Hydrothermally formed three-dimensional nanoporous Ni(OH)₂ thin-film supercapacitors. *ACS nano* **2014**, *8*, 9622-9628.
35. Laheear, A.; Przygocki, P.; Abbas, Q.; Beguin, F. Appropriate methods for evaluating the efficiency and capacitive behavior of different types of supercapacitors. *Electrochem commun* **2015**, *60*, 21-25.
36. Tie, D.; Huang, S.; Wang, J.; Zhao, Y.; Ma, J.; Zhang, J.; Zhao, Y. Hybrid energy storage devices: advanced electrode materials and matching principles. *Energy Storage Mater.*, 2018, 21
37. Bai, Y.; Wang, W.; Wang, R.; Sun, J.; Gao, L. Controllable synthesis of 3D binary nickel–cobalt hydroxide/graphene/nickel foam as a binder-free electrode for high-performance supercapacitors. *J. Mater. Chem. A* **2015**, *3*, 12530-12538.
38. Tang, C.; Tang, Z.; Gong, H. Hierarchically porous Ni-Co oxide for high reversibility asymmetric full-cell supercapacitors. *J. Electrochem. Soc.* **2012**, *159*, A651-A656.
39. Wang, X.; Liu, W. S.; Lu, X.; Lee, P. S. Dodecyl sulfate-induced fast faradic process in nickel cobalt oxide–reduced graphite oxide composite material and its application for asymmetric supercapacitor device. *J. Mater. Chem.* **2012**, *22*, 23114-23119.
40. Chen, H.; Jiang, J.; Zhang, L.; Qi, T.; Xia, D.; Wan, H. Facilely synthesized porous NiCo₂O₄ flowerlike nanostructure for high-rate supercapacitors. *J. Power Sources* **2014**, *248*, 28-36.

41. Zhang, J.; Liu, F.; Cheng, J.; Zhang, X. Binary nickel–cobalt oxides electrode materials for high-performance supercapacitors: influence of its composition and porous nature. *ACS Appl. Mater. Inter.* **2015**, *7*, 17630-17640.
42. Zhao, Y.; Ma, H.; Huang, S.; Zhang, X.; Xia, M.; Tang, Y.; Ma, Z. F. Monolayer nickel cobalt hydroxyl carbonate for high performance all-solid-state asymmetric supercapacitors. *ACS Appl. Mater. Interfaces* **2016**, *8*, 22997-23005

CHAPTER – 5

Optimization of a novel dual-carbon lithium hybrid capacitor
by cell potential window approach

The major challenge of hybrid metal-ion capacitor is to improve the energy-power output along without sacrificing the cycle life. To extract the best performance of a hybrid device, two main factors need to be considered, which are, electrode material excellence and device engineering. Besides, we can also significantly improve the overall electrochemical performance of a lithium-ion capacitor (LIC) cell by optimizing the safe operational potential window. Herein, we introduce a new LIC device by assembling a polymer derived spongy hard carbon (SHC) and an activated carbon (PAC), as negative and positive electrodes, respectively. In this system, the semi-graphitic 3D like network of SHC is used for lithium intercalation (battery-type) and the high specific surface area of PAC for fast ions adsorption (capacitor-type), that leads a remarkable capacity values and very stable rate performances even at high current rates. Apart from the high energy-power density target, to improve the overall performance of the LIC device in terms of operational safety point of view, a detailed potential window variation study is also performed. Among the tested variations, the potential range of 1.5-4.0V was found to be the operationally safest with very good reversibility as well as no chances of Li plating even at a high current density of 10 A g^{-1} . At such high current density, this LIC device is capable to provide a specific cell capacity of 25 mAh g^{-1} within an incredibly discharge time of only 9 seconds, which corresponds to an energy density of 64 Wh kg^{-1} at an extreme power density of 28 kW kg^{-1} . Furthermore, within this operational potential range, this hybrid device exhibited an excellent capacity retention of 82% even after 10,000 charge-discharge cycles.

5.1. Introduction

Most common dual carbon hybrid supercapacitors use graphite as negative electrode, which shows a theoretical capacity of 372 mAh g^{-1} according to the LiC_6 stoichiometry.^[1-2] However, graphite exhibits slow Li^+ intercalation kinetics that limits the charge-discharge efficiency at high applied current.^[3-5] On the other hand, graphitizable carbon (soft carbon) and non-graphitizable carbon (hard carbon) have been studied as anode material for LIBs and also for metal ion hybrid capacitors.^[6-7] Graphene layers of soft carbons often get stacked due to their random orientation.^[1] This turbostratic misalignment has the ability to provide better charge-discharge capacity at higher current rates but the capacity gradually deteriorates due to their structural deformations during the prolonged cycling. In contrast, HCs or non-graphitizable carbons contain mainly graphene layers not stacked in a parallel way like in a “house of cards” model, where lithium ions can intercalate in the pores and cavities formed by the carbon sheets.^[8-9] Thus, HCs can provide not only high charge discharge capacity ($\sim 740 \text{ mAh g}^{-1}$ for Li_2C_6) but also excellent cyclability. For this reason, in recent years, several research works have been focused on the development of different HCs to better understand their morphological effects as negative electrodes in both batteries and hybrid system.

Recently, 3D porous carbons with high surface area and hierarchically interconnected pore architectures have shown excellent energy storage capacity and rate capability, enabling high mass loading supercapacitor and secondary batteries.^[2, 10-12] In this regard, nanostructured spongy porous carbons are not only interesting because Li storage can be maximized but also because they facilitate electron conduction in their carbon matrix through their porous structure, which ultimately helps to enhance electrolyte kinetics.^[10, 13-14] Besides, during the pre-lithiation process, Li^+ ion can also easily accommodate inside the porous network without major obstacles, which helps to sustain the extreme mechanical strain for longer utilization.^[15] Also, from the economic and easy to scale up point of view, high surface area activated carbons (ACs) synthesized by a single step process from cheap carbon precursors have drawn the attention because of their meso-microporous structure, which is highly suitable for fast electrolyte diffusion.^[16-17] Therefore, above mentioned materials with their preferable porous nature are among the most suitable choices as the negative and positive electrodes respectively for dual carbon hybrid LIC systems.

Apart from materials, cell optimization has also a great impact on the electrochemical on the electrochemical performance of LIC devices. Due to the difference in ion diffusion kinetics of HC anodes and AC cathodes, they exhibit a very different capacity retention performance when the current density increases. This creates a severe charge imbalance at high current rates that leads to Li plating on the anode, resulting in a severe capacity fading as well as an unsafe process.^[18]

In this chapter, we are introducing a facile synthetic route towards the 3D nanostructured spongy shaped hard carbon (SHC) as anode material. This SHC anode was coupled with a high surface area polymer derived activated carbon (PAC) cathode in a full LIC cell system. The individual electrochemical performance shows the excellent utilization of their corresponding porosity and textural properties when used as anode and cathode in a LIC cell. Besides, the performance of the hybrid LIC system was further improved by optimizing the cell potential window to avoid the lithium plating at high current densities. Through this approach, we are able to define a safe and very stable operative potential window, where the system can work very efficiently without compromising its energy and power density values along with an extended self-life for long term operation.

5.2. Material synthesis

For the synthesis of the polymeric molecular framework, first 0.081 g of Triton-X-100 was dispersed properly in 50 mL de-ionized (DI) water. In this mixture, 450 μ L of aniline and 340 μ L of pyrrole were added under continuous stirring until the complete dissolution was ensured and then this solution was kept in an ice-bath to maintain a temperature of 3-5 $^{\circ}$ C. For the oxidative polymerization, already precooled (3-5 $^{\circ}$ C) aqueous ammonium persulfate solution (0.8 g was dissolved in 1 mL of DI water) was added to the above solution and stirred for a few minutes. Then, 2 mL of phosphoric acid (85%) were added quickly and the resulting solution was cooled down at 4 $^{\circ}$ C for one day. Finally, the obtained very dense dark-grayish colored precipitate was collected and continuously washed with DI water for several times by centrifugation. This polymeric sediment was kept in a freeze-drier to maintain the interconnected microscopic structure of the polymeric frame. Finally, the product was carbonized at 800 $^{\circ}$ C under Ar

atmosphere for 2 h with a heating ramp rate of $3\text{ }^{\circ}\text{C min}^{-1}$ to get the final SHC material. The calculated overall yield of HSC was $\sim 40\%$.

For the synthesis of the PAC, first, 1.1 g of resorcinol, 0.68 g of terephthalaldehyde and 5.0 g of KOH were vigorously mixed in an agate mortar and then the mixture was carbonized in a tubular furnace. The annealing temperature was first set to $250\text{ }^{\circ}\text{C}$ for 3 h and then using a heating ramp rate of $1\text{ }^{\circ}\text{C min}^{-1}$ the sample was kept at $800\text{ }^{\circ}\text{C}$ for 1 h under Ar atmosphere. Finally, the carbonized product was washed several times with 3M hydrochloric acid and DI water until the pH value was ~ 7 . The final PAC material was dried in a vacuum furnace at $120\text{ }^{\circ}\text{C}$ overnight. The calculated overall yield of PAC was $\sim 30\%$.

5.3. Physicochemical characterization

The polymer-derived SHC was prepared by using a simple synthetic route of “molecular framework” strategy, involving a crosslinking polymerization of two monomers (aniline and pyrrole) in the presence of phosphoric acid which acts as catalyst. In this process, initially a combination of these two hydrophobic monomers was introduced with a surfactant (Triton X-100) to form a polymeric micelle. In this synthesis, Triton X-100 is used to locally confine the polymer and restrict its growing, to reduce the polymer particles sizes. A molecular cross-linked conjugated polymeric network was formed by an addition of an oxidizing agent (aqueous ammonium persulfate) and a cross-linker (phosphoric acid). During the thermal annealing process, the phosphate linkage (P-O-C bonds) in phosphoric acid not only helps to retain the volatile molecular species but also maintains the interlinked network very well.^[10, 19] Thus, the obtained yield of SHC after the carbonization process is much higher compared to the other polymer-derived carbons or biomass-derived carbons without much collapsing its carbonaceous microstructure.

The interconnected porous network gives this SHC a spongy shaped texture, which can be clearly observed from the SEM image in Figure 5.1.a. More in-depth information of this carbon nanostructure is further confirmed from the TEM image (Figure 5.1.b). The carbon cluster contains small spherical-like dispersed homogenous nanoparticles with uniform size between ~ 30 to ~ 40 nm. There are lots of void areas left between the particles which form a 3D like interconnected network. This interparticle void space ($\sim 4 - 8$ nm) can also be confirmed from the

pore size distribution (PSD) profiles in the inset of Figure 5.1.c. Besides, the N₂ adsorption-desorption isotherm indicates a profile in between type I and II with H3 type hysteresis according to the IUPAC classification, signaling the microporous characteristics of this carbon that form monolayers and partial multilayers under the low to medium pressure pore-filling range.^[20] Due to the presence of a large amount of micropores, the calculated BET specific surface area was found to be 440 m² g⁻¹ with a bimodal pore size distribution exhibiting both pores below 1 nm as well as mesopores with a mean pore size of 6 nm.

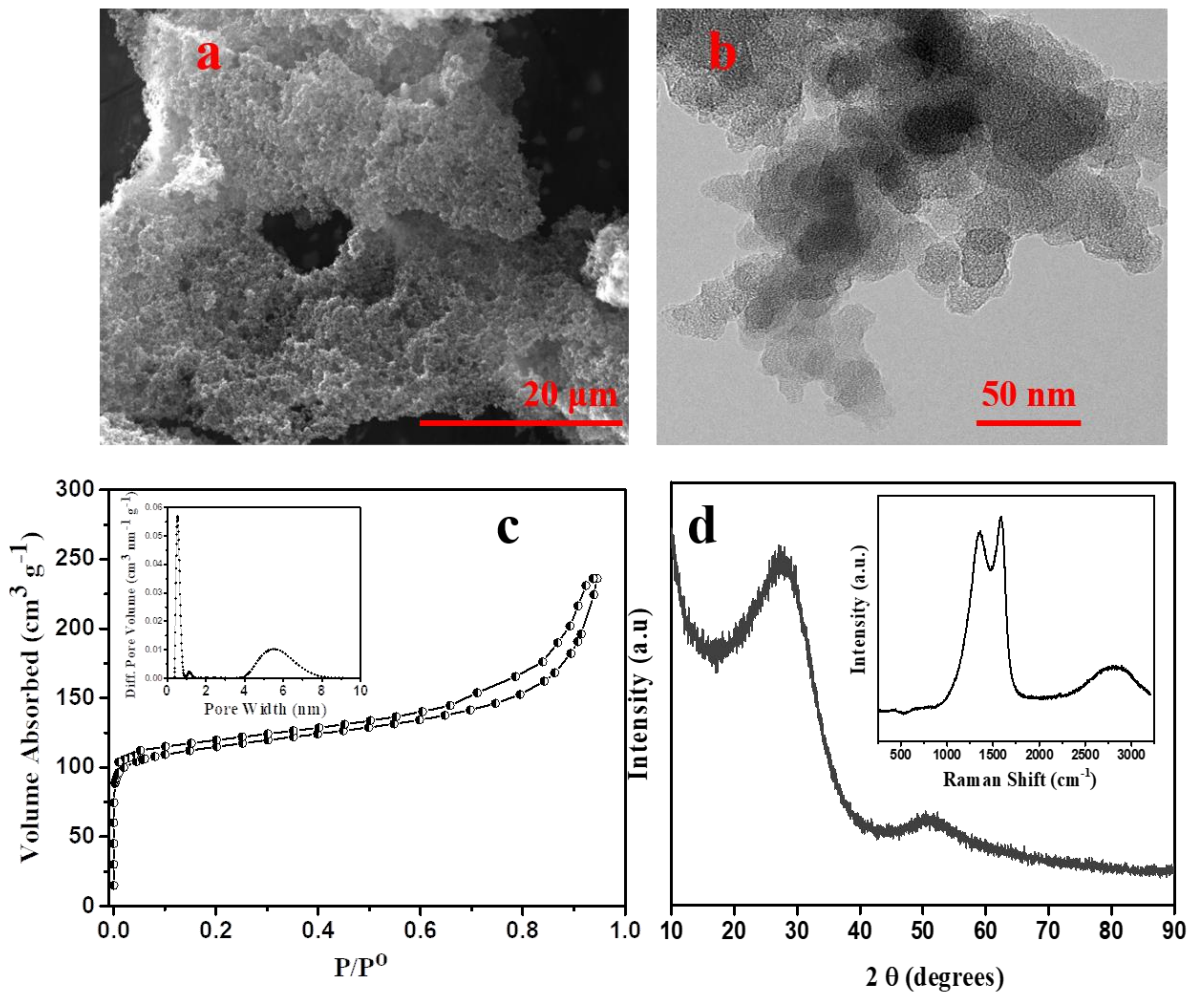


Figure 5.1. (a) SEM image and (b) TEM image, (c) Nitrogen adsorption–desorption isotherms (inset: pore size distribution curve) and (d) XRD pattern (inset: Raman spectrum) of the SHC).

The XRD pattern (Figure 5.1.d) of SHC displays the two typical broad diffraction peaks corresponds to (002) and (100) planes, indicates the turbostratic nature of this carbon with low

graphitization degree. The interlayer spacing at the (002) plane was found to be 3.30 Å, which is very close to that of graphite (3.34 Å). From the Scherrer equation, the thickness of the graphitic domain size was calculated to be 7.7 Å, suggesting that they are formed by 2 to 3 stacked layers of graphene. The Raman spectrum (inset of Figure 5.1.d) illustrates two distinctive peaks at nearly 1356 cm⁻¹ and 1583 cm⁻¹, which correspond to the D-band (defects in the carbon lattice) and G-band (stretching vibration in C-C bonds), respectively. The integrated ratio of D and G bands in the structure is often widely used to reveal the level of the defect quantity in graphitic materials. The integrated area of I_D/I_G was found to be 0.86, confirming that this carbonaceous material has a low graphitization degree.^[21-22] Moreover, another pair of broad peaks can be distinguishable in the region of 2500-3200 cm⁻¹ corresponding to 2D and D+G bands, which appear due to the lattice disordered induced band of this material.

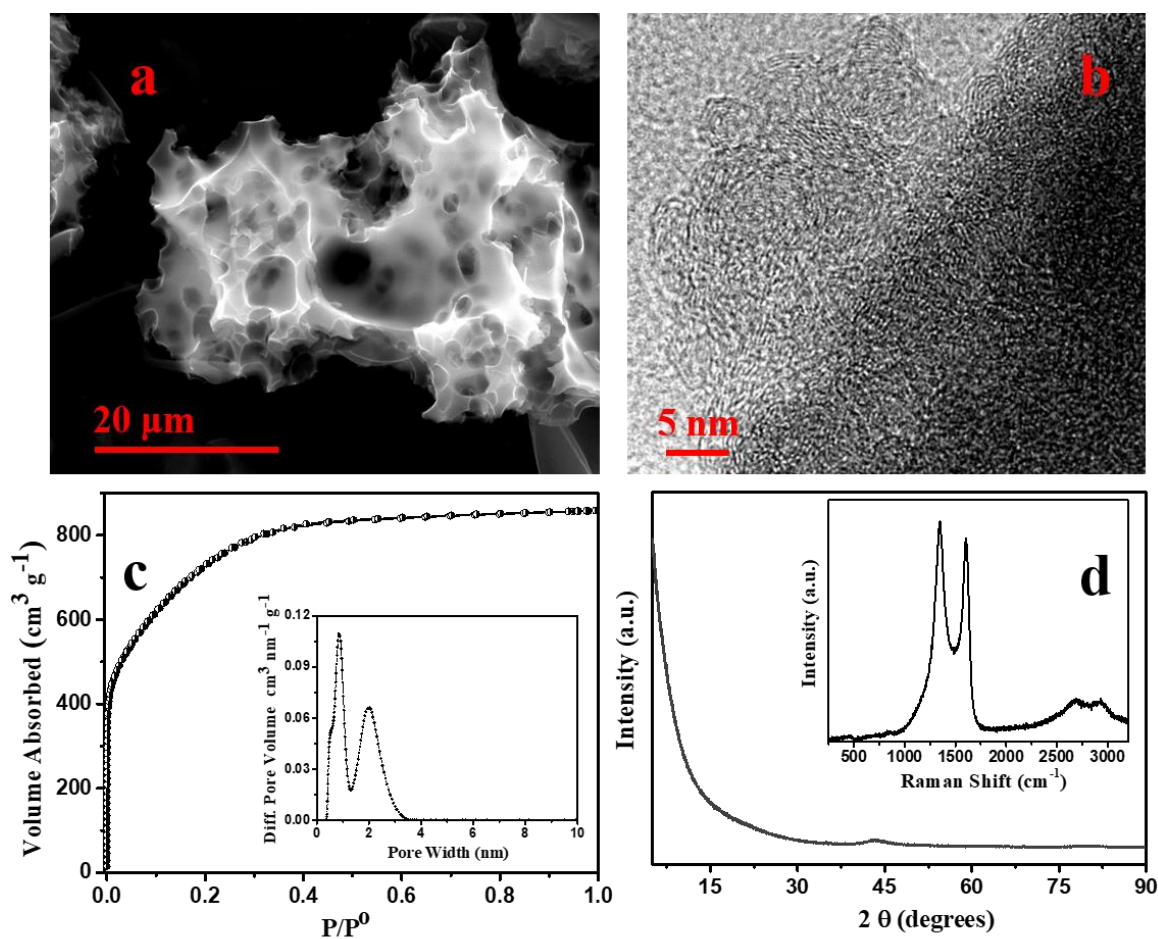


Figure 5.2. (a) SEM image, (b) TEM image, (c) N₂ adsorption-desorption isotherms (inset: pore size distribution curve) and (d) Raman spectrum registered for the PAC.

Figure 5.2.a represents the SEM image of the PAC. According to the micro-images the material is formed by non porous large particles that contain some voids, which are formed as consequence of the gas evolution during the resin condensation process. A closer evaluation of the material's texture is done by transmission electron microscopy. High resolution TEM image (Figure 5.2.b.) show the presence of graphene layers and worm-type micropores randomly distributed on the surface that are produced by the in-situ chemical activation of the material. The formation of this microporous structure can also be confirmed from the N₂ adsorption-desorption isotherm (Figure 5.2.c), indicating this carbon has type I isotherm.^[20] The BET specific surface area and the pore volume was found to be 2090 m² g⁻¹ and 1.32 cm³ g⁻¹, respectively. The PSD profile (inset of Figure 5.2.c) indicates the material exhibits a combination of meso- and microporosity.

This hierarchical pore distribution observed in the PAC can be effective for an EDLC type electrode where the ion diffusion process can be facilitated through the porous structure and, therefore, the physisorption of the electrolyte ions can be eased. The smooth XRD profile (Figure 5.2.d) also suggests a highly porous amorphous characteristics for this carbon. Besides, the ratio of the integrated area of *I_D* and *I_G* from the Raman spectrum was found to be 1.33 (inset of Figure 5.2.d), which also suggests a significantly disordered morphology containing a large concentration of defects and/or pores, which can be related with the XRD measurements.^[21-22]

Additional textural information extracted from the nitrogen adsorption-desorption isotherms are given in table 5.1

Table 5.1.: Textural information obtained from N₂ adsorption-desorption measurement.

Samples	V _T (cm ³ g ⁻¹)	BET	DFT				Dubinin-Radushkevich Equation		
		SSA (m ² g ⁻¹)	SSA (m ² g ⁻¹)	Micro-SSA (m ² g ⁻¹)	V _{T-DFT} (cm ³ g ⁻¹)	V _{micro} (cm ³ g ⁻¹)	Micro-SSA (m ² g ⁻¹)	Average micropore size (nm)	V _{DR-micro} (cm ³ g ⁻¹)
SHC	0.33	440	570	499	0.36	0.14	416	0.83	0.172
PAC	1.32	2090	2111	1907	1.21	0.98	1353	1.32	0.895

V_T : Total pore volume by applying Gurvitch rule; SSA: Specific Surface Area; V_{T-DFT} : Total pore volume calculated from DFT method by applying 2D-NLDFT theory; V_{DR-micro} : Micropore volume obtained from Dubinin-Radushkevich Equation

5.4. Electrochemical characterization

5.4.1. Electrode processing and cell assembly

The SHC anode electrode slurry was prepared by mixing 90 wt% of active material, 5 wt% of Super P C65 carbon black and 5 wt% of polyvinylidene fluoride (PVdF) as a binder in N-methyl-2-pyrrolidone (NMP). All the components were mixed under vigorous magnetic stirring for at least 1 h. Then, this SHC slurry was coated onto a copper (Cu) foil current collector. Similar procedure was used for the preparation of positive electrodes based on PAC. but this slurry was coated onto aluminium foil. All laminates were immediately dried under dynamic vacuum at 80 °C for at least 12 h. The mass loading of the positive and negative electrode was kept in the range of 1.4-1.6 mg cm⁻². The electrochemical characterization of both anode and cathodes was performed in individual airtight Swagelok T-cells in a three-electrode configuration. Metallic lithium was used as both the counter and the reference electrode. In the case of the anode, the three-electrode cell was cycled within the potential range of 0.002 V to 2 V *vs.* Li/Li⁺, whereas for the measurement of the cathode, this was set within the 1.5-4.2 V *vs.* Li/Li⁺ potential range.

Lithium hybrid capacitor full cells were assembled by using SHC as negative and PAC as positive electrode Swagelok-type T-cell. The mass ratio between negative and positive electrode was maintained in a 1:1 mass ratio. A porous glass fiber membrane separator (Whatman GFB) and stainless steel current collectors were used to assemble the cells along with 1 M LiPF₆ in EC:DMC (1:1) electrolyte. Three different potential windows or cell voltages were set for analysis, *i.e.* 1.5-4.2 V, 1.5-4.0 V and 2.0-4.0 V, respectively. A metallic Li was used as reference to record the potential evolution in individual electrode of the full cell. Before performing electrochemical measurements, a preconditioning step was performed in both negative and positive electrodes to maximize the output voltage. In this step, the negative electrode (SHC) was cycled at least five times between 0.002-2.0 V *vs.* Li/Li⁺ at the current rate of 0.1C in order to prelithiate and to form a stable solid electrolyte interface (SEI). A cut-off potential of 0.002 V *vs.* Li/Li⁺ was set in order to avoid any chances of lithium plating. Once this pre-lithiation process was finished, the positive electrode (PAC) was also charged up to a cut-off potential of 4.2 V *vs.* Li/Li⁺. After this preconditioning, the LIC full cells were set for further extensive electrochemical characterization under different potential windows as mentioned above.

5.4.2. Electrochemical performance of anode (SHC)

First, the performance of the SHC anode material was investigated in a half-cell configuration (T-type Swagelok) using Li foil as both the counter and the reference electrode and the obtained results are presented in figure 5.3. For this SHC anode, first cyclic voltammetry (CV) measurements were performed at 1 mV s^{-1} within a potential range of 0.002-2.0 V vs. Li/Li⁺. In the first cycle, a broad reduction peak is positioned in between $\sim 1.2 \text{ V}$ to 0.5 V (Figure 5.3.a), which correlates to the solid electrolyte interface (SEI) formation due to the reductive decomposition of organic compounds of the carbonate solvent from the electrolyte.

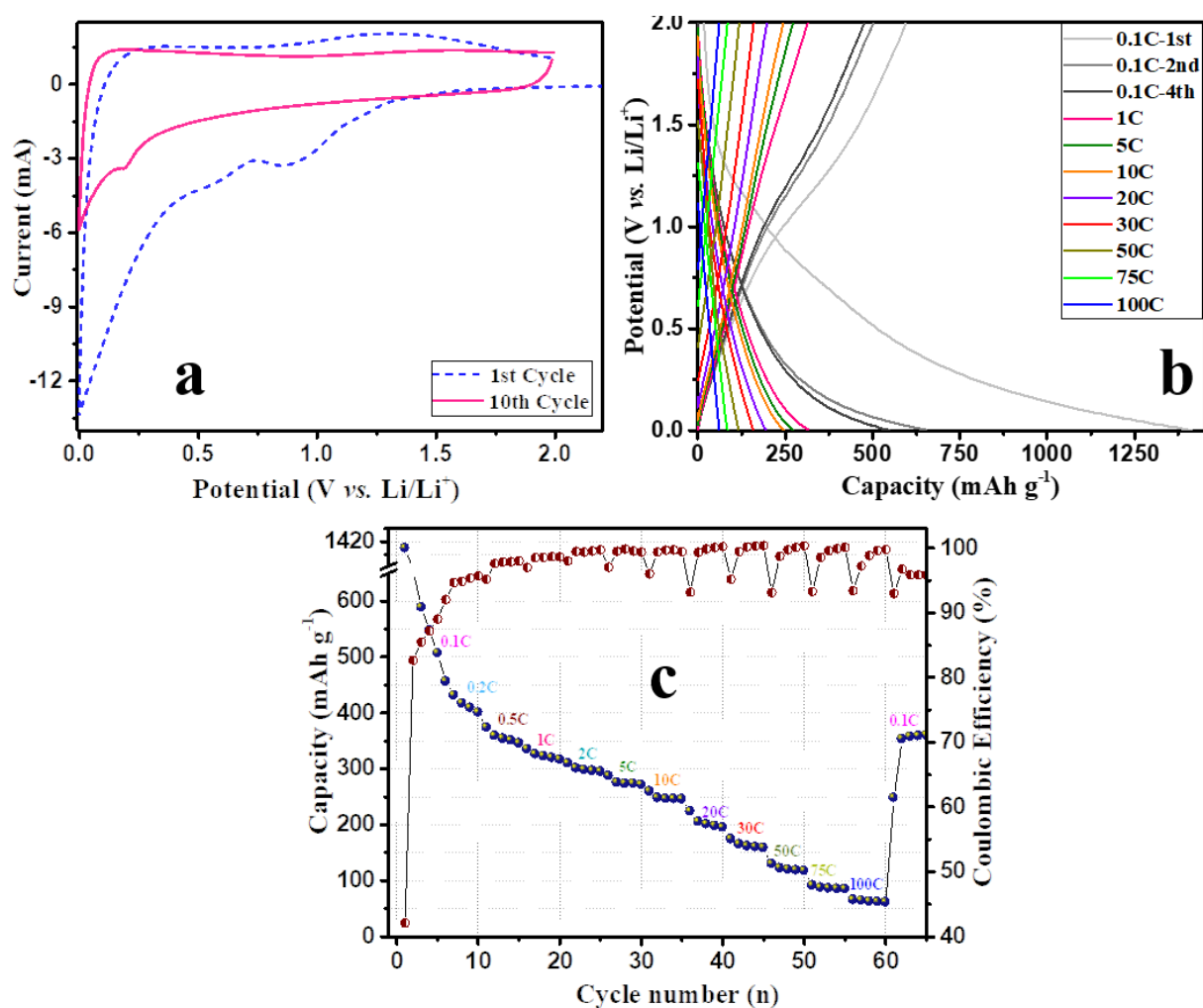


Figure 5.3. Electrochemical characterization of SHC as anode in half-cell configuration tested between 0.002 and 2.0 V; (a) CVs vs. Li/Li⁺, (b) GC-GD vs. Li/Li⁺, and (c) rate capability and coulombic efficiency.

When the anode material undergoes the reduction process at low potentials close to the electrode potential of metallic Li, both the solvent and the salt of the electrolyte solution become thermodynamically unstable. The composition of the SEI layer mostly corresponds to the formation of insoluble inorganic compounds such as Li_2CO_3 and can also partially contain LiF (decomposition product of the LiPF_6 salt).^[4, 23] In general, it is expected that the SEI overgrowth is noticeable with continuous operation, but in our case, no such significant increment has evidenced after 10th cycle. In the CV profile (Figure 5.3.a), the diffusion-controlled lithium ion insertion occurs in between 0.45 V to 0.00 V, where the starting point of the steep slope near 0.45 V indicates that the ion insertion occurs first within the interlayers of the graphene-like disordered sheets and later into the randomly distributed sealed and open micropores of those stacked turbostratic interlayers (*i.e.* near the plateau like region of ~0.25 V to 0.00 V).^[24]

In this context, it is well known that hard carbon as anode materials can be described as “house of card” like model. In this model, the disordered structure of the material consists of cross-linked interlayer carbon sheets (graphene like layers), where the ions can easily intercalate on each side of these sheets.^[25] CV results are in a good agreement with galvanostatic charge-discharge (GC-GD) measurements performed at 0.1C rate (0.037 A g^{-1} considering a theoretical capacity of graphite at 372 mA h g^{-1}).

As shown in Figure 5.3.b, a distinguishable sloping down and/or plateau-like region are noticeable at the same potential range as that observed in the CV. The first discharge curve shows a very high specific capacity of 1415 mAh g^{-1} . However, the first charge specific capacity was found to be $\sim 596 \text{ mAh g}^{-1}$. It gives a initial coulombic efficiency (CE) of $\sim 42\%$. This is due to the due to its high specific surface area of SHC containing abundant micropores, which intensifies the electrolyte decomposition and SEI formation. The second charge-discharge cycle shows that the discharge capacity was quickly stabilized at 652 mAh g^{-1} with a impressive CE of 83 %. In the subsequent cycles at 0.1C, the discharge capacity and CE values become stabilized at and at the end of 10th cycle, the discharge capacity and CE reaches 400 mAh g^{-1} and 96%.

Figure 5.3.b also shows the charge discharge profiles of SHC anode at increasing current rate upto 100C (37.2 A g^{-1}). It can be readily observed that discharge curves shows a decreasing trend of the plateau formation with increase in current rate, which can be ascribed to decrease in Li

insertion-extraction ability of SHC anode. However, the rate capability test results (Figure 5.3.c) shows a substantial capacity retention upto high applied current rate of 100C. At an applied current of 10C the delivered capacity value was 250 mAh g⁻¹, which corresponds to a 42% of capacity retention considering the initial reversible capacity set in the 5th cycle, likewise at 30C the materials still maintains 26% of the initial capacity. With this notation, even at 100C rate, the SHC anode can ensure 61 mAh g⁻¹, which demonstrates the applicability of the material even at such extreme and demanding conditions. Besides, 96% of the initial reversible capacity was successfully retrieved when the applied current was set again at 0.1C rate, indicating that the microstructure of this carbonaceous material is adequately capable to sustain such harsh conditions.

These electrochemical features points out that SHC could be a good candidate to be used as high energy battery type electrode in hybrid supercapacitors.

5.4.3. Electrochemical performance of cathode (PAC)

The electrochemical characterization of the PAC within a potential range of 1.5-4.2 V vs. Li/Li⁺ is shown in Figure 5.4. The CV profiles at low scan rate of 5 and 10 mV s⁻¹ shows quasi-rectangular butterfly-shaped profiles with minima around OCP (Figure 5.4.a), which is an indicative of a capacitive charge storage. with minima around OCP (Figure 5.4.a) is a clear indicative of a capacitive charge storage low electrolytic distributed resistance.^[26-27] This type of CV profile is typically shown by phenolic resin-based activated carbon and is attributed to the potential dependence of the ion penetration into nanopores, which is assumed to be minimal at the OCP.^[27] The CV profiles at increasing scan rate up to 10 mV s⁻¹ shows that the quasi-rectangular CV pattern is retained, although with some charge polarization.

Figure 5.4.b shows the GC-GD profiles at different current densities of the PAC cathode. These ideally symmetric GC-GD curves also evidence the capacitive charge storing behavior of the PAC cathode. Besides, the iR drop increment is very minute even when it is tested at high current density of 10 A g⁻¹. In the rate performance profile (Figure 5.4.c) the specific capacity and capacitance values at different current densities are depicted. At a current density of 1 A g⁻¹ these values are 129 mAh g⁻¹ and 173 F g⁻¹, respectively, and even at the very demanding current density of 30 A g⁻¹, the decrease in capacity (or capacitance) is only 20%, evidencing that this

AC can maintain a very stable performance without a major deterioration in LiPF₆ electrolyte. Therefore, these results confirm that the hierarchical and interconnected pore structures of this PAC cathode is highly capable to provide high power density for hybrid system due to their uninterrupted fast ionic diffusion onto the electrode surface.

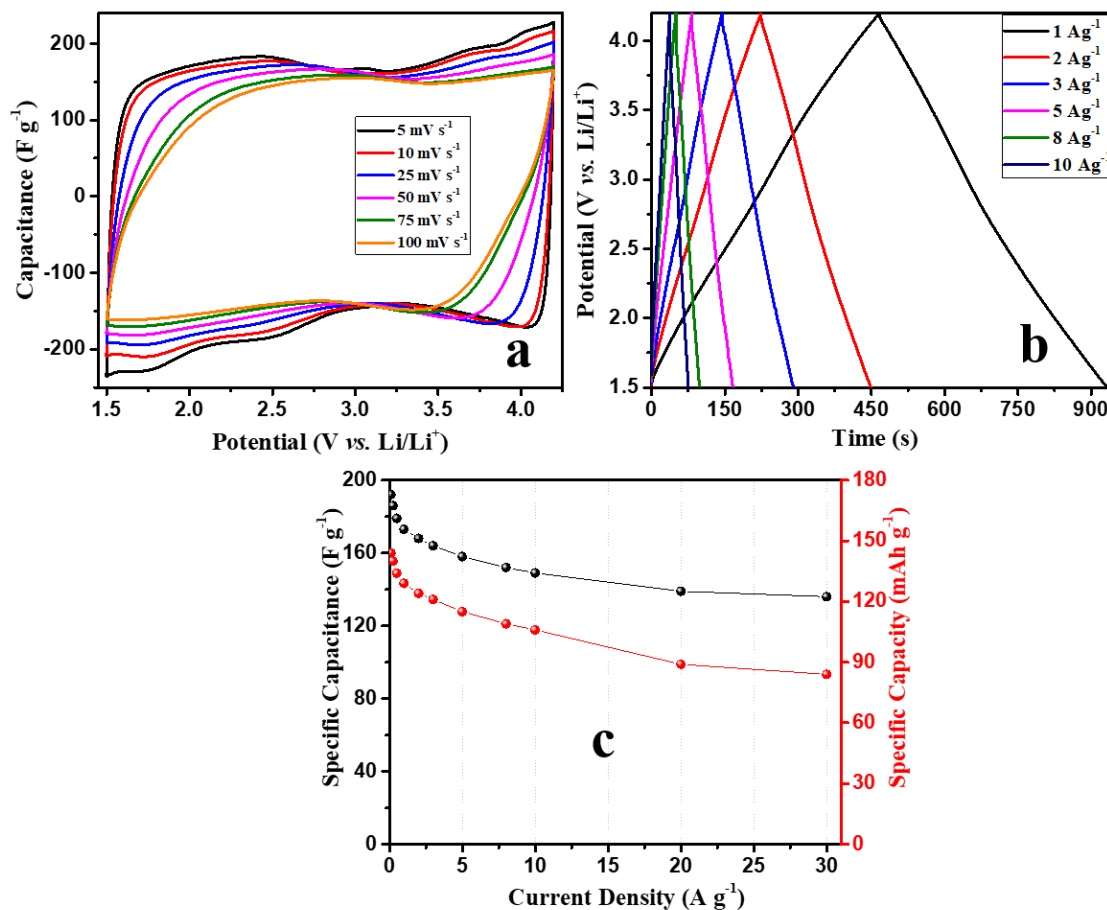


Figure 5.4. Electrochemical characterization of PAC cathode in half-cell configuration tested between 1.5 to 4.2 V vs. Li/Li⁺; (a) CVs at different scan rates from 5 mV s⁻¹ to 100 mV s⁻¹, (c) GC-GDs, and (c) capacity and capacitance values vs. current densities.

5.4.4. Electrochemical performance of the SHC//PAC hybrid LIC

The individual electrochemical performance of each electrode material suggests the possibility of using both the polymer-derived SHC and PAC in a hybrid system capable of working for high power requirements. The main challenge of the hybrid technology is, in fact, to improve the energy density without compromising the power outcome. For this reason, the mass ratio

(SHC:PAC) is adjusted to maximize the performance at high current densities. The specific capacity values of both materials at different current densities are summarized in Figure 5.5.a.

At a high applied current density of 10 A g^{-1} , the SHC and the PAC deliver 168 mAh g^{-1} and 106 mAh g^{-1} , suggesting a SHC:PAC mass ratio of 1.5:1 for the full cell set up. This ultimate theoretical prediction of the capacity balancing ratio might be risky considering both lithium plating and a faster SHC electrode degradation at high current densities. Thus, for the sake of a safe-handling and stable performance, we decided to construct a full cell using a SHC:PAC mass ratio of 1:1 instead. Besides, we also performed a prelithiation step of SHC negative electrode, a lithium metal foil was introduced in the system as third electrode and SHC was first discharged-charged at 0.1C rate for 5 cycles in between the 2V and 0.002 vs. Li/Li^+ . This step is an effective approach to replenish the Li^+ lost during initial discharge process, which substantially enhances the LIC performances (high coulombic efficiency, superior rate capability, high capacity retention, and high energy and power density).^[28] This prelithiation process also forms a uniform SEI layer in the negative electrode, which safeguards further decomposition of electrolyte on the negative electrode. Then the lower cut-off potential was set at 0.2V vs. Li/Li^+ to avoid any possibilities of lithium plating. Thereafter the PAC positive electrode was charged at 0.1C rate up to 4.2V vs. Li/Li^+ .

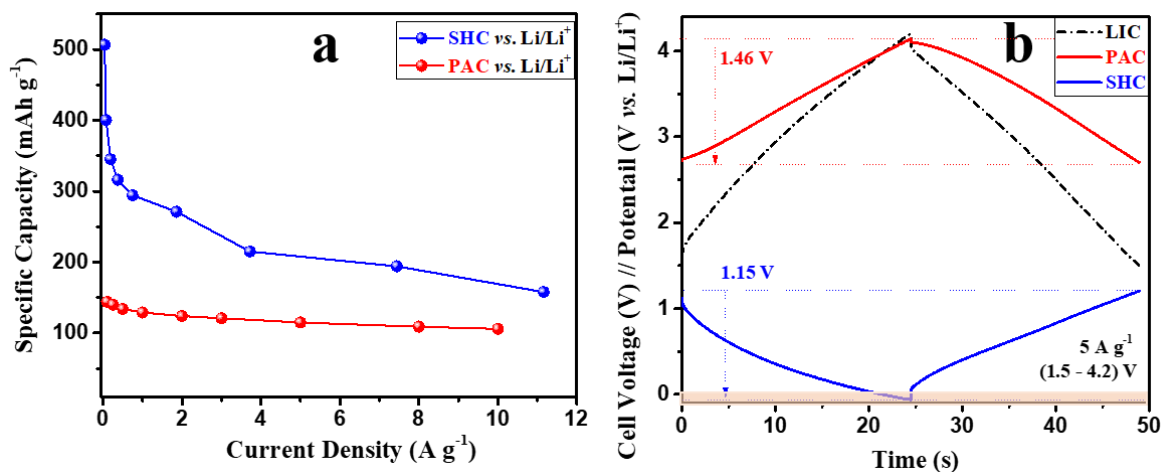


Figure 5.5. (a) Specific capacity of the SHC vs. PAC at different applied current densities, and (b) GC-GD profiles of each electrode at different current density of 5 A g^{-1} of 1.5-4.2 V LIC cell (yellow colored marked zone indicates Li Plating).

After this preconditioned process, the full cell was set for further electrochemical characterization. In order to give an in-depth electrochemical evaluation to set a practical potential range of the hybrid system, first, we selected a wide potential range of 1.5-4.2 V. At this potential range, it was expected that the cell must perform without any hindrance. While testing the full cell, we noticed that the full cell was started to suffer from lithium plating at the current density of 5 A g^{-1} during the operation (Figure 5.5.b).

To avoid this lithium plating, we decided to decrease the maximum cathode potential from 4.2 to 4.0 V. Meanwhile, we also lowered the minimum cathode potential from 1.5 to 2.0 V. Thus, to optimize the intrinsic and extrinsic parameters limiting upon the overall cell performance, we fixed two different sets of potential range *i.e.* 1.5-4.0 V and 2.0-4.0 V for further evaluation.

In Figure 5.6, all the GC-GD curves of LICs (SHC:PAC=1:1) summarizes the individual potential swing of the SHC anode and PAC cathode (plotted *vs.* Li/Li+) at different current densities with various potential range, *i.e.* 1.5-4.2 V, 1.5-4.0 V and 2.0-4.0 V, respectively.

Among these three different potential range variation, it is clearly illustrating that the 1.5-4.2 V is performing better than the rest at low current densities while at the high current density of 10 A g^{-1} , the best performance is obtained from the potential range of 1.5-4.0V without any chances of lithium plating along with a full cell discharge time of 9s. From this individual potential swings at the high current density (10 A g^{-1}), evidencing that the reduction of the maximum cathode potential from 4.2 to 4.0 V is facilitating the SHC anode to achieve the charge balance by utilizing the maximum potential swing of PAC cathode (1.73 V) in 1.5-4.0 V cell.

These measurements reveal that the use of the highest cathodic potential (*i.e.* 4.2 V) may unsettle the charge balance in between the anode and cathode that leads to lithium plating chances at high current rates by extreme usage of anodic potential. Even by reducing the minimum cathodic potential from 1.5 to 2.0 V, we also observed that the LIC cell is able to balance perfectly the overall charge distribution among cathodes and anodes, but the full utilization of the anode is not happening here by reducing this slight potential scale. Thus, the obtained full cell discharge time of 2.0-4.0 V is quite lesser than the 1.5-4.0 V.

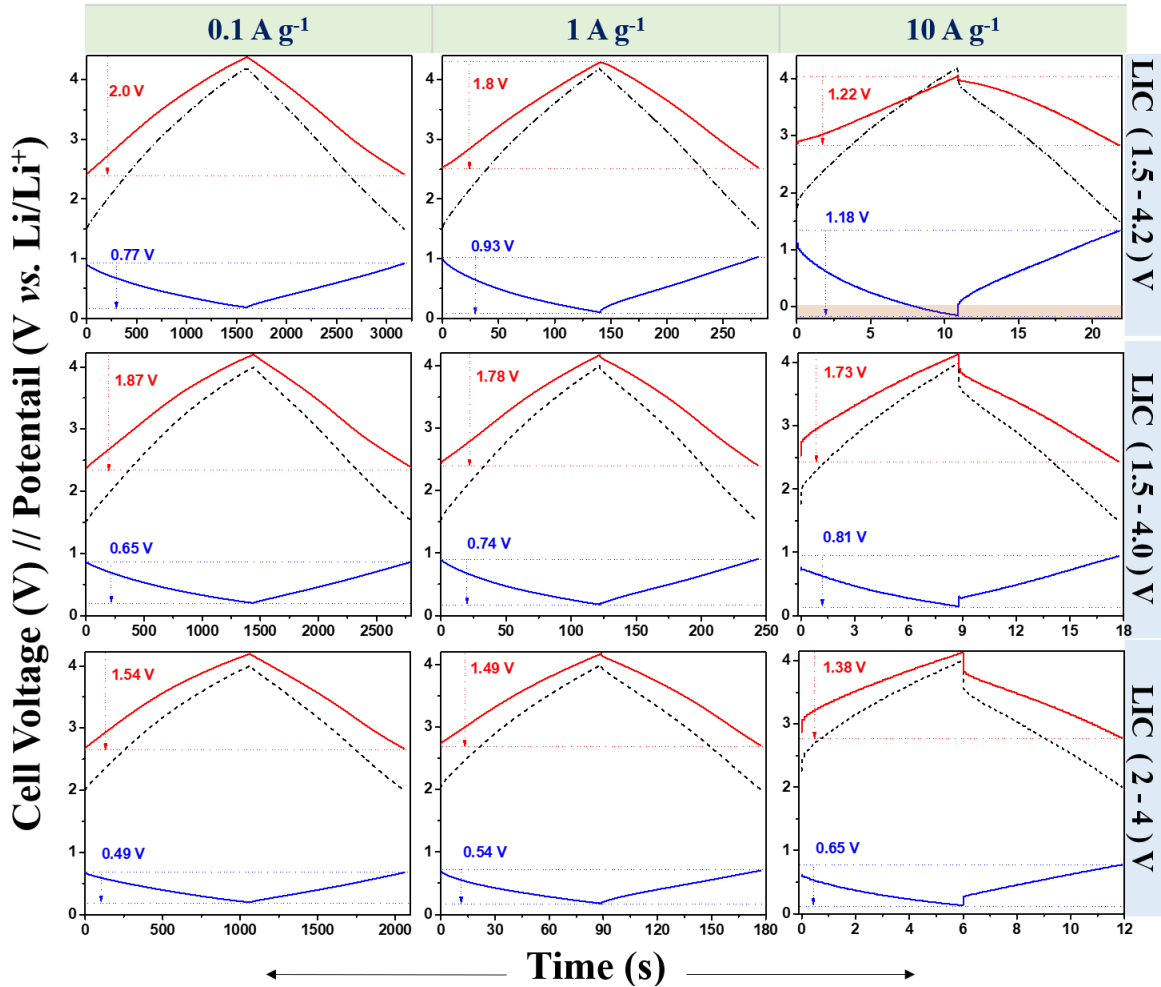


Figure 5.6. Comparative GC-GD profiles of each electrode in SHC//PAC full LICs measured at different current densities of 0.1, 1 and 10 A g^{-1} , (yellow colored marked zone indicates Li Plating).

Figure 5.7.a shows the evolution of the specific cell capacity at different current densities. It is visible that 1.5-4.2 V potential range reveals the highest obtained capacity values, though this LIC cell was suffering from lithium plating (yellow marked points at higher current rates). Thus, the safest and reliable full cell capacity value can be taken into account from the potential range of 1.5-4.0 V. At high applied current the electrochemical performance started to differ with the variation in potential window range, even though the mass ratio of SHC and PAC was maintained same in each LIC cells of (*i.e.* 1:1).

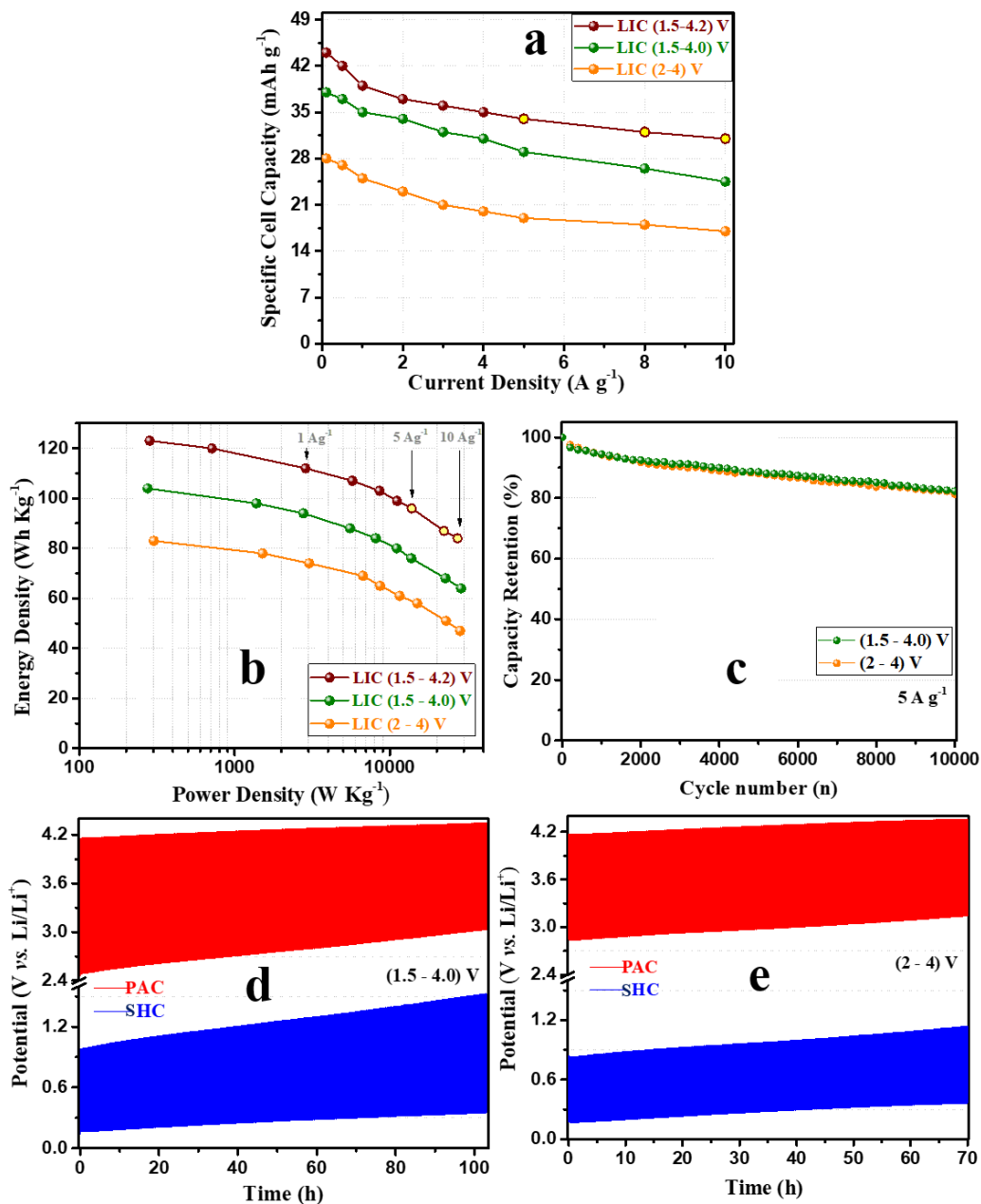


Figure 5.7. Comparative (a) rate capability and (b) Ragone Plot of SHC//PAC full cells by applying the variation in the potential range [(1.5-4.2V), (1.5-4.0V), (2.0-4.0V)]; (b) cycling stability at the current density of 5 A g^{-1} and potential swings of each electrode of the (c) 1.5-4.0V and (d) 2-4.0 V LIC cells during the cycling test.

A Ragone plot is displayed in Figure 5.7.b, evaluating how all these LIC devices perform when turned to the energy-to-power proportion. From this plot it can be claimed that the LIC fixed within

the 1.5-4.0 V range not only shows the most reliable behaviour but also shows a good energy and power values compared to the others. So, the obtained energy density value from this LIC was 104 Wh kg^{-1} at the power density of 275 W kg^{-1} and this potential range can maintain an energy density of 64 Wh kg^{-1} at an extreme power density of 28 kW kg^{-1} , which means the full cell discharge time can be attained within 9s.

Following performance of each cell, we decided to perform the cycling test of 1.5-4.0 V and 2.0-4.0 V LIC cells at the current density of 5 A g^{-1} (Figure 5.7.c). For a better evaluation of the stability of the cell, the potential swing of each electrode has been monitored during the cyclability tests.

The cycling stability test of 1.5-4.0 V LIC cell (Figure 5.7.d) shows that there is a shift in anodic potential minima and cathodic potential maxima towards the positive direction. Moreover, it is pointing a prominent gradual expansion in the anode potential range and concurrent shrinkage of cathodic potential range with time. On the other hand, the potential swing of 2.0-4.0 V LIC cell (Figure 5.7.e) shows the shift in anodic and cathodic potential range without any expansion/shrinkage of anode/cathode potential window. This behaviour has been previously explained by Sun et al. which claimed that the capacity fading upon cycling is related to the slow irreversible Li deposition on the anode, that causes the expansion of the anodic potential window and this can not fully compensate the charge balance in the cathode, resulting in the shrinkage of the cathode potential window.^[18] However, the results from our study shows that after 10,000 cycles, both cells revealed the same capacity retention rate.

Therefore, it can be inferred that the expansion/shrinkage of anode/cathode potential window does not affect the capacity fade as much as the drifting of anodic and cathodic potential towards the positive direction. This drifting can result in the imbalance of lithiation-delithiation process that fades the overall cell capacity with time.

Hence, the overall results of this study suggest that the 1.5-4.0 V range is more suitable for LIC in terms of energy and power density along with cyclic stability. Table 5.2 summarizes the electrochemical performance of this 1.5-4.0 V LIC, compared with other recently reported results in similar dual carbon LIC devices.

Table 5.2. summarizes the electrochemical performance of this 1.5-4.0V LIC, compared with other recently reported results in similar dual carbon LIC devices.

Device Configuration Negative Electrode//Positive Electrode	Cell Voltage (V)	Max Energy (Wh kg ⁻¹) @ Power (W kg ⁻¹)	Energy (Wh kg ⁻¹) @ max Power (W kg ⁻¹)	Cycling Performance	Ref.
HC // AC	2-4	82@100	14@20000	97% over 600 cycles	[25]
HC // AC	1.4-4.3	80@150	65@2350	82% over 10000 cycles	[1]
HC // bio-mass derived mesoporous carbon	1.7-4.2	121@300	50@9000	81% over 8000 cycles	[29]
Polymer derived HC// AC	1.5-4.2	150@150	70@25000	83% over 10000 cycles	[30]
HC // AC	2-4	73.6@60	36@11900	96.5% over 500 cycles	[18]
HC // AC	2-4	85.7@600	20@7600	96.0% over 5000 cycles	[31]
Bio-mass derived- HC // AC	1.5-4.2	100@150	22@18000	94% over 10000 cycles	[32]
This Work (SHC//PAC)	1.5-4.0	104@275	64@28000	82% over 10000 cycles	-

5.5. Conclusions

The performance of hybrid metal-ion capacitor field has been predominantly linked to the excellence in electrode material in the reported literature until now less importance has been given to the cell design. The observation made from this study confirms that the variation in individual electrode potential can also significantly impact on the overall cell performance for the prolonged application. With the careful control of the cathodic potential limit not only can help to avoid the decomposition of the electrolyte but also can save electrode from intrinsic degradation behaviour. Thus, the selection of the safe operational potential range is firmly related with risk-free device handling that enables its long cyclability. The quality and integrity of the electrode materials also matter to obtain a high-performance LIC system. Thus, the LIC device

designed with our lab-synthesized exclusive nano-architected carbonaceous materials along with potential window variation provides very promising results towards the development of the safe hybrid energy storage devices for future applications.

Bibliography

1. Kim, J.-H.; Kim, J.-S.; Lim, Y.-G.; Lee, J.-G.; Kim, Y.-J., Effect of carbon types on the electrochemical properties of negative electrodes for Li-ion capacitors. *Journal of Power Sources* **2011**, *196*, 10490-10495.
2. Wang, X.; Liu, L.; Niu, Z., Carbon-based materials for lithium-ion capacitors. *Materials Chemistry Frontiers* **2019**, *3*, 1265-1279.
3. Li, G.; Yang, Z.; Yin, Z.; Guo, H.; Wang, Z.; Yan, G.; Liu, Y.; Li, L.; Wang, J., Non-aqueous dual-carbon lithium-ion capacitors: a review. *Journal of Materials Chemistry A* **2019**, *7*, 15541-15563.
4. Ding, J.; Hu, W.; Paek, E.; Mitlin, D., Review of hybrid ion capacitors: from aqueous to lithium to sodium. *Chemical reviews* **2018**, *118*, 6457-6498.
5. Dahn, J.; Seel, J., Energy and capacity projections for practical dual-graphite cells. *Journal of the Electrochemical Society* **2000**, *147*, 899.
6. Sivakkumar, S. R.; Pandolfo, A., Evaluation of lithium-ion capacitors assembled with pre-lithiated graphite anode and activated carbon cathode. *Electrochimica Acta* **2012**, *65*, 280-287.
7. Smith, P. H.; Tran, T. N.; Jiang, T. L.; Chung, J., Lithium-ion capacitors: Electrochemical performance and thermal behavior. *Journal of power sources* **2013**, *243*, 982-992.
8. Noel, M.; Suryanarayanan, V., Role of carbon host lattices in Li-ion intercalation/de-intercalation processes. *Journal of Power Sources* **2002**, *111*, 193-209.
9. Dunn, B.; Kamath, H.; Tarascon, J.-M., Electrical energy storage for the grid: a battery of choices. *Science* **2011**, *334*, 928-935.
10. To, J. W.; Chen, Z.; Yao, H.; He, J.; Kim, K.; Chou, H.-H.; Pan, L.; Wilcox, J.; Cui, Y.; Bao, Z., Ultrahigh surface area three-dimensional porous graphitic carbon from conjugated polymeric molecular framework. *ACS central science* **2015**, *1*, 68-76.
11. Pandolfo, A. G.; Hollenkamp, A. F., Carbon properties and their role in supercapacitors. *Journal of Power Sources* **2006**, *157*, 11-27.
12. Evers, S.; Nazar, L. F., New approaches for high energy density lithium-sulfur battery cathodes. *Accounts of chemical research* **2013**, *46*, 1135-1143.
13. Xu, F.; Tang, Z.; Huang, S.; Chen, L.; Liang, Y.; Mai, W.; Zhong, H.; Fu, R.; Wu, D., Facile synthesis of ultrahigh-surface-area hollow carbon nanospheres for enhanced adsorption and energy storage. *Nature communications* **2015**, *6*, 1-12.

14. Zhou, C.; Han, J.; Song, G.; Guo, R., Fabrication of poly (aniline-co-pyrrole) hollow nanospheres with Triton X-100 micelles as templates. *Journal of Polymer Science Part A: Polymer Chemistry* **2008**, *46*, 3563-3572.
15. Roberts, A. D.; Li, X.; Zhang, H., Porous carbon spheres and monoliths: morphology control, pore size tuning and their applications as Li-ion battery anode materials. *Chemical Society Reviews* **2014**, *43*, 4341-4356.
16. Díez, N.; Mysyk, R.; Zhang, W.; Goikolea, E.; Carriazo, D., One-pot synthesis of highly activated carbons from melamine and terephthalaldehyde as electrodes for high energy aqueous supercapacitors. *Journal of Materials Chemistry A* **2017**, *5*, 14619-14629.
17. Zheng, Z.; Gao, Q., Hierarchical porous carbons prepared by an easy one-step carbonization and activation of phenol-formaldehyde resins with high performance for supercapacitors. *Journal of Power Sources* **2011**, *196*, 1615-1619.
18. Sun, X.; Zhang, X.; Liu, W.; Wang, K.; Li, C.; Li, Z.; Ma, Y., Electrochemical performances and capacity fading behaviors of activated carbon/hard carbon lithium ion capacitor. *Electrochimica Acta* **2017**, *235*, 158-166.
19. Solum, M.; Pugmire, R.; Jagtoyen, M.; Derbyshire, F., Evolution of carbon structure in chemically activated wood. *Carbon* **1995**, *33*, 1247-1254.
20. Sing, K. S., Reporting physisorption data for gas/solid systems with special reference to the determination of surface area and porosity (Recommendations 1984). *Pure and applied chemistry* **1985**, *57*, 603-619.
21. Pimenta, M.; Dresselhaus, G.; Dresselhaus, M. S.; Cancado, L.; Jorio, A.; Saito, R., Studying disorder in graphite-based systems by Raman spectroscopy. *Physical chemistry chemical physics* **2007**, *9*, 1276-1290.
22. Sole, C.; Drewett, N. E.; Hardwick, L. J., In situ Raman study of lithium-ion intercalation into microcrystalline graphite. *Faraday Discussions* **2014**, *172*, 223-237.
23. Chan, C. K.; Ruffo, R.; Hong, S. S.; Cui, Y., Surface chemistry and morphology of the solid electrolyte interphase on silicon nanowire lithium-ion battery anodes. *Journal of Power Sources* **2009**, *189*, 1132-1140.
24. Xing, W.; Dahn, J., Study of irreversible capacities for Li insertion in hard and graphitic carbons. *Journal of the Electrochemical Society* **1997**, *144*, 1195.
25. Stevens, D.; Dahn, J., The mechanisms of lithium and sodium insertion in carbon materials. *Journal of The Electrochemical Society* **2001**, *148*, A803.
26. Panja, T.; Bhattacharjya, D.; Yu, J.-S., Nitrogen and phosphorus co-doped cubic ordered mesoporous carbon as a supercapacitor electrode material with extraordinary cyclic stability. *Journal of Materials Chemistry A* **2015**, *3*, 18001-18009.

-
27. Hahn, M.; Baertschi, M.; Barbieri, O.; Sauter, J.-C.; Kötz, R.; Gallay, R., Interfacial capacitance and electronic conductance of activated carbon double-layer electrodes. *Electrochemical and Solid State Letters* **2003**, *7*, A33.
28. Abe, Y.; Saito, T.; Kumagai, S., Effect of prelithiation process for hard carbon negative electrode on the rate and cycling behaviors of lithium-ion batteries. *Batteries* **2018**, *4*, 71.
29. Jayaraman, S.; Jain, A.; Ulaganathan, M.; Edison, E.; Srinivasan, M.; Balasubramanian, R.; Aravindan, V.; Madhavi, S., Li-ion vs. Na-ion capacitors: A performance evaluation with coconut shell derived mesoporous carbon and natural plant based hard carbon. *Chemical Engineering Journal* **2017**, *316*, 506-513.
30. Arnaiz, M.; Nair, V.; Mitra, S.; Ajuria, J., Furfuryl alcohol derived high-end carbons for ultrafast dual carbon lithium ion capacitors. *Electrochimica Acta* **2019**, *304*, 437-446.
31. Zhang, J.; Liu, X.; Wang, J.; Shi, J.; Shi, Z., Different types of pre-lithiated hard carbon as negative electrode material for lithium-ion capacitors. *Electrochimica Acta* **2016**, *187*, 134-142.
32. Ajuria, J.; Redondo, E.; Arnaiz, M.; Mysyk, R.; Rojo, T.; Goikolea, E., Lithium and sodium ion capacitors with high energy and power densities based on carbons from recycled olive pits. *Journal of Power Sources* **2017**, *359*, 17-26.

CHAPTER – 6

Development of dual-carbon lithium-ion hybrid capacitor with electrode mass variation approach for the improvement of rate performance and cycling stability

Most lithium-ion capacitor (LIC) devices include graphite or non-porous hard carbon as negative electrode often failing when demanding high energy at high power densities. Herein, we introduce a new LIC formed by the assembly of polymer-derived hollow carbon spheres (HCS) and an activated carbon (AC), as negative and positive electrodes, respectively. The hollow microstructure of HCS and the ultra large specific surface area of AC shown maximize lithium insertion/diffusion and ions adsorption in each of the electrodes, leading to individual remarkable capacity values and rate performances. To optimize the performance of the LIC not only in terms of energy and power densities but also from a stability point of view, a rigorous mass balance study is also performed. Optimized LIC, using a 2:1 negative to positive electrode mass ratio, shows very good reversibility within the operative voltage region of 1.5–4.2 V and it is able to deliver specific cell capacity of 28 mAh g⁻¹ even at a high current density of 10 A g⁻¹. This leads to an energy density of 68 Wh kg⁻¹ at an extreme power density of 30 kW kg⁻¹. Moreover, this LIC device shows an outstanding cyclability, still retaining more than 92% of the initial capacity after 35,000 charge–discharge cycles.

6.1. Introduction

As anode material, hard carbon signifies high specific capacity and favorable cyclic performance in LIBs and LICs.^[1-7] Among the different nanostructured hard carbon materials, carbon nanosheets, nanospheres, carbon nano pipes or carbon nanofibers have been recently investigated as negative electrodes for LICs. Tuning the microstructure of these hard carbons at the nanoscale brought about significant improvements in terms of structural stability, transport kinetics, cyclability, and coulombic efficiency (CE).^[5, 8-10] The morphology of hollow carbon spheres (HCSs) results particularly convenient since they provide electrolyte reservoirs and fasten Li^+ intercalation/deintercalation processes through the thin carbon walls.^[11, 12] Additionally, their ample inner space can buffer the volume changes undergone during charge/discharge processes, thus improving the mechanical stability of the electrode.^[12, 13]

As the positive electrode, activated carbons (ACs) are preferentially chosen due to their large specific surface areas and open porosity, which allows fast ionic transport to the whole surface of the electrode.^[2, 14] We have synthesized a novel and straightforward synthetic route for the preparation of ultra-high specific surface area ACs. This synthesis strategy, consisting of a facile one-step process in which polymerization, carbonization and chemical activation of the carbon precursors occur all at once and yields carbons with specific surface areas slightly above $3000 \text{ m}^2 \text{ g}^{-1}$ and a hierarchical micro-mesoporous structure. Both their suitable porous structure and easy preparation make them a suitable choice as positive electrode materials in LIC systems.^[15]

The performance of hybrid supercapacitors can be improved through the optimization of the mass balance between the positive and the negative electrode.^[16] Thus, different mass balances translate into different working potential spans and, therefore, a different degree of utilization of each electrode, which can be used to maximize the energy density of the device. Indeed, most of the scientific reports focus on the best-obtained energy/power results, not paying much attention to safety and stability.

In this chapter, we present a facile synthetic route towards HCSs by the pyrolysis of nitrogen containing monomers. This material was coupled in a full cell with our lab-synthesized

superactivated carbon as the positive electrode. The optimization of the mass balance of the electrodes, within an operative potential window of 1.5-4.2 V, was also investigated.

6.2. Material synthesis

The HCS were synthesized by the carbonization of polymeric hollow spheres under a dynamic inert atmosphere. For the synthesis of the co-polymeric hollow nanospheres, 0.08 g of Triton-X-100 was dispersed in 50 mL deionized water, and then 0.456 mL of aniline and 0.346 mL of pyrrole were added to the mixture under continuous stirring that was kept until complete dissolution. Then, the solution was kept under continuous stirring in an ice bath to maintain a temperature of 3-5 °C. For the oxidative polymerization, aqueous ammonium persulfate (0.8 g was dissolved in 1 mL DI water) was precooled at 3-5°C and added to the above solution. The mixture was stirred for a few minutes and the resulting solution was kept in the refrigerator for 24 h at 4 °C. Finally, the obtained dark greenish polymer precipitate was collected by centrifugation and washed with DI water several times. The product was freeze-dried to maintain the microscopic structure of the polymeric hollow spheres and then carbonized at 800 °C in Ar atmosphere for 2 h using a heating rate of 3 °C min⁻¹.

For the synthesis of superactivated carbon (AC), at first, 1.24 g of melamine, 1.36 g of terephthalaldehyde and 5.0 g of KOH were grounded using an agate mortar and then the mixture was carbonized under Ar atmosphere. The temperature was first raised up to 250 °C for 3 h and then increased to 800 °C for 1 h using heating ramps of 1 °C min⁻¹. (CAUTION: certain amount of potassium cyanide may be formed during the carbonization process, so carbon should be carefully manipulated, and the wastes treated accordingly). Then the final product was washed several times with 3 M HCl, and DI water followed by drying at 120 °C in a furnace.^[15]

6.3. Physicochemical characterization

The schematic diagram included in Figure 6.1. summarizes the approach followed for the preparation of the HCS that will serve as negative electrode in this study. First, polymeric hollow microspheres were prepared by a simple strategy that involves the interfacial co-polymerization of aniline and pyrrole in the presence of Triton X-100.^[13, 17] Due to their different hydrophobicity,

the molecules of aniline mainly sit at the outer layer of the micelle-water interface, whereas the more hydrophobic pyrrole molecules tend to diffuse towards the inner wall of the micellar core.

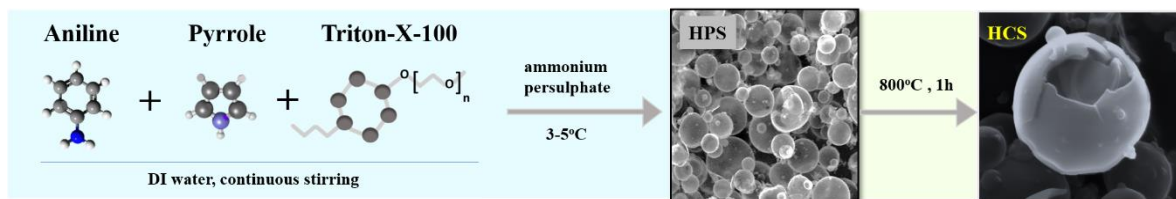


Figure 6.1 Schematic diagram of the synthesis process of hollow polymer spheres (HPS) and hollow carbon spheres (HCS).

Polymerization leads to the formation of hollow polymeric spheres (HPS) and its posterior carbonization under inert atmosphere yields HCS. The HCS maintain the pristine microstructure of the HPSs but undergo a slight shrinkage of their size (Figure 6.2.a and b).

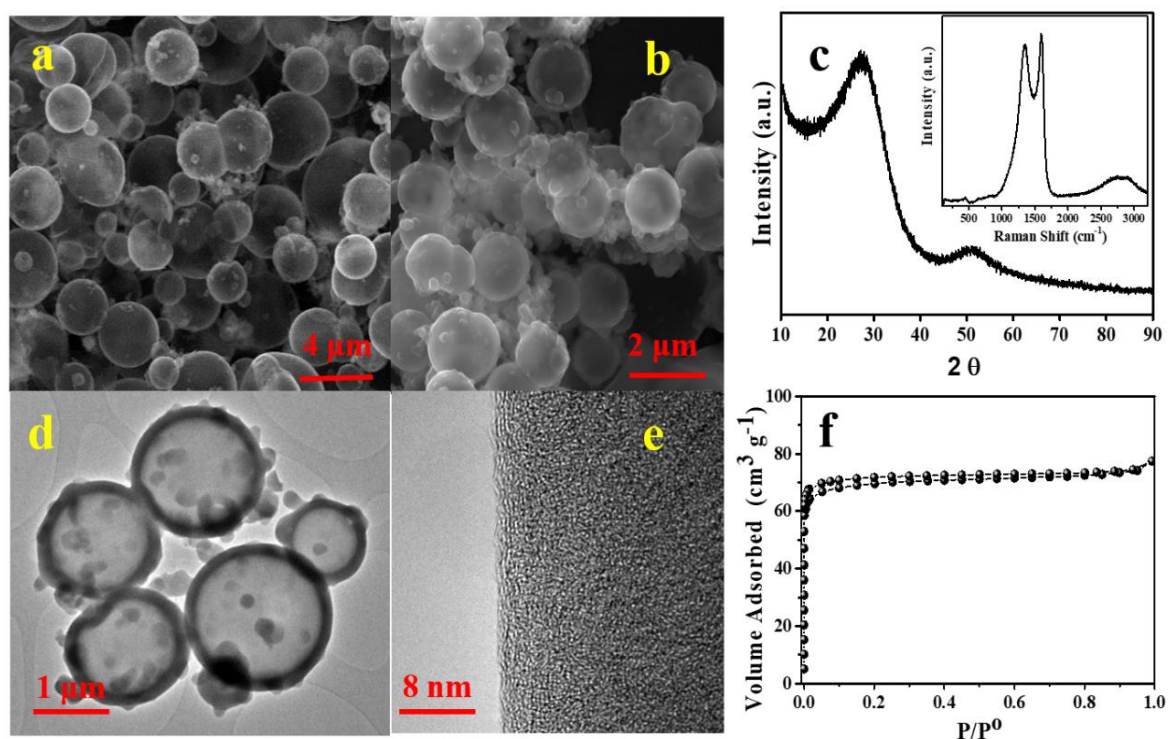


Figure 6.2. (a) SEM images of HPS and (b) HCS obtained after the pyrolysis of HPS, (c) XRD pattern recorded for HCS (inset: Raman spectrum registered for HCS), (d) low magnification. The TEM image of HCS and (e) high magnification TEM image of HCS outer surface, (f) N₂ adsorption-desorption isotherms registered for HCS.

The thickness of the carbon walls was of *ca.* 110 nm (Figure 6.2.d). XRD pattern of the carbonized sample (Figure 6.2.c) shows two low intensity and broad X-ray diffraction peaks at $\sim 26^\circ$ and $\sim 50^\circ$ (2θ) angles, which correspond to the (002) and (100) planes characteristic of disordered carbons with a low degree of graphitization. The Raman spectrum (Figure 6.2.c, inset) shows two predominant bands at $\sim 1356\text{ cm}^{-1}$ and $\sim 1594\text{ cm}^{-1}$, which reflect the defects in the carbon lattice (D-band) and the stretching vibration in C-C bonds (G-band), respectively. Additionally, two broad and very low intense peaks can be identified in the $2500\text{-}3000\text{ cm}^{-1}$ region that are ascribed to the G' stretching mode. Defects in the forms of edges and surface imperfections like defects, cracks, cavities, and active sites act as catalytic sites, which can be active for formation of solid-electrolyte interface (SEI) layer formation as well as lithiation-delithiation process in the negative electrode of the LIC cell.^[18]

The high-resolution TEM images (Figure 6.2.e) evidenced the presence of micropores in the carbon shells. To get additional information about the textural features of these carbon spheres, nitrogen gas adsorption-desorption measurements were carried out. The N_2 adsorption-desorption isotherm registered for the HCSs (Figure 6.2.f) shows a profile in between types I and IV according to the IUPAC classification, with a H4 hysteresis loop.^[19] The large adsorption of nitrogen at low relative pressures confirmed the microporous nature of the material. Due to the presence of a large amount of micropores, the BET specific surface area calculated for this material was $282\text{ m}^2\text{ g}^{-1}$. We have also performed the elemental analysis of the HCS carbon to obtain the nitrogen content in this anode material. This analysis showed that HCS carbon has 9.1 wt.% nitrogen in the framework. It is well-known that the incorporation of nitrogen-containing groups in the carbon network not only improves electronic and ionic conductivity but also provides active sites and enhances ion adsorption leading to an increase in capacity and rate capability.^[13, 20]

Physicochemical characterization of the superactivated carbon prepared by the *in-situ* polymerization, carbonization, and activation of melamine and terephthalaldehyde is included in Figure 6.3. SEM images (Figure 6.3.a) show irregular-shaped carbon utricles with a size of $\sim 50\text{ nm}$ and a very rough surface. High magnification TEM image (Figure 6.3.b) reveal that the sample contained randomly distributed nanopores. The N_2 adsorption-desorption isotherm registered for this activated carbon exhibits a profile in between type I and IV with a

distinguishable capillary condensation step in the relative pressure range of 0.3-0.6.^[15] The abrupt increase of N₂ absorption at low relative pressures is indicative of its highly microporous structure. Indeed, the specific surface area and pore volume calculated for this material was as high as 3180 m² g⁻¹ and 2.8 cm³ g⁻¹, respectively.

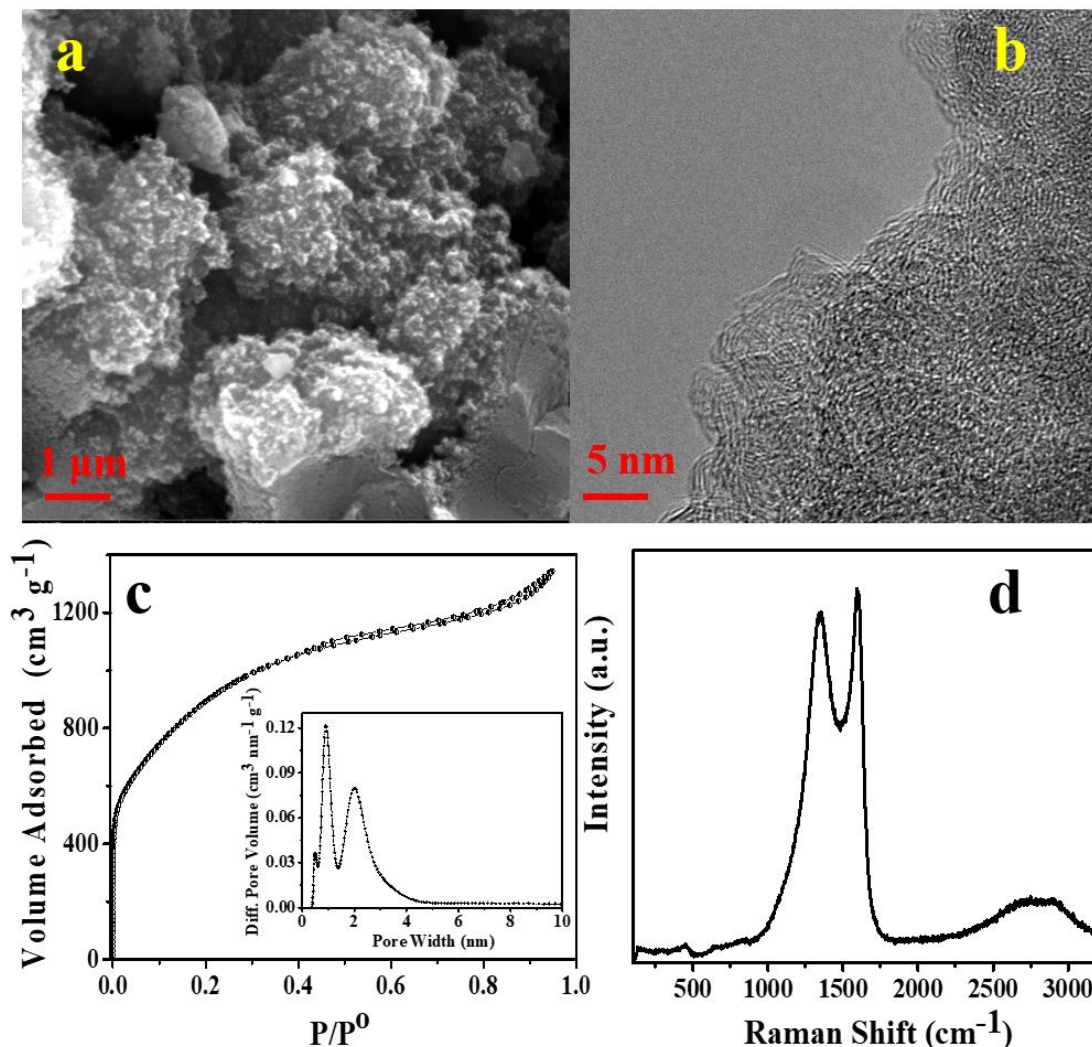


Figure 6.3. (a) SEM image, (b) TEM image, (c) N₂ adsorption-desorption isotherms (inset: pore size distribution curve) and (d) Raman spectrum registered for the AC.

The pore size distribution calculated from the isotherm data (inset in Figure 6.3.c) shows the contribution of pores with two sizes in the micro- and mesopore range, centered at *ca.* 1.0 nm and 2.3 nm, respectively. The ultra-large specific surface area combined with the hierarchical

distribution of pore sizes, *i.e.* the physical adsorption of a large number of ions with a low diffusion resistance, make this carbon good candidate as an EDLC electrode material.

The Raman spectrum in Figure 6.3.d displays the typical D and G bands at $\sim 1350\text{ cm}^{-1}$ and $\sim 1590\text{ cm}^{-1}$, respectively, pointing out that a significant amount of graphitic carbon is still present in the carbonaceous network despite the large concentration of defects and/or pores in sample.^[20]

6.4. Electrochemical characterization

6.4.1. Electrode processing and cell assembly

The negative electrode slurry was prepared by mixing 90 wt% of hollow spherical carbon (HCS) with 5 wt% Super-C C65 carbon black (Imerys Graphite & Carbon, Willebroek, Belgium) and 5% polyvinylidene fluoride (PVdF) in N-methyl-2-pyrrolidone (NMP). The components were mixed under vigorous stirring for at least 1 h using a magnetic stirrer. The obtained HCS-based slurry was coated onto a copper foil current collector. For the positive electrode slurry, the activated carbon, Super-C C65, and PVdF were mixed in a weight mass ratio of 90:5:5 in NMP solution under continuous stirring for 1 h and then the AC-based slurry was laminated onto an aluminum foil. Laminates were placed immediately into a vacuum oven for drying at 80 °C for 12 h under constant vacuum. The mass loading of the positive electrode was of 1-1.3 mg cm⁻² while the loading in the negative electrode ranged from 1.4 to 2.6 mg cm⁻².

The electrochemical characterization of the anode was evaluated in a three-electrode configuration using an airtight Swagelok T-cell. Metallic Li was used as both the counter and the reference electrode, and the anode was cycled within the potential range of 0.002 to 2.0 V. The same cell assembly procedure was followed to perform the electrochemical characterization of the cathode within the 1.5-4.2 V potential range.

Lithium hybrid supercapacitor full cells (HCS//AC) were assembled using four different negative-to-positive electrode mass ratios: (1.1:1), (1.3:1), (1.7:1) and (2:1). A three-electrode configuration (Swagelok T-cell) with a metallic Li reference was chosen in order to record the individual electrode potential changes. Stainless steel current collectors and a porous glass fiber separator (Whatman GFB) were used and the electrolyte used was 1 M LiPF₆ in EC:DMC (1:1). Before testing, the negative and positive electrodes were preconditioned to maximize the output

voltage. Thus, the HCS electrode was cycled at least five times between 0.002 and 2 V *vs.* Li/Li⁺ at 0.1C rate to form solid electrolyte interphase (SEI) and supply enough lithium to compensate the initial irreversible cycles. After that, a cut-off potential of 0.2 V *vs.* Li/Li⁺ was set to evade any chances of lithium plating. The AC electrode was also charged up to a cut-off potential of 4.2 V *vs.* Li/Li⁺. After this pre-lithiation process, the LICs full cells were built for their extensive electrochemical characterization.

6.4.2. Electrochemical performance of Anode (HCS)

First, the performance of HCS as anode material was investigated in a half-cell configuration (T-type Swagelok) using Li foil as both the counter and the reference electrode. The cell cycled within the potential range of 0.002–2.0 V *vs.* Li⁺/Li. Figure 6.4.a illustrates the 1st, 5th and the 10th cyclic voltammograms (CVs) recorded at 1 mV s⁻¹. It can be observed that most of the capacity is stored below 1.0 V. In the first CV, a broad reduction peak can be distinguished between ~1.0 to 0.3 V, which resembles the formation of a SEI layer due to the carbonate solvent decomposition.^[21] The intercalation of Li⁺ into the HCS takes place between 0.3 and 0.01 V, while the deintercalation process shows a maximum current peak at 0.23 V. The Galvanostatic charge-discharge curves (GCD) performed between 2.0 V and 0.002 V at different current rates are shown in Figure 6.4.b. The first discharge at 0.1C (C = 372 mA h g⁻¹) from its open circuit potential shows two distinct plateaus at ~1.0 V and ~0.25 V corresponding to SEI formation and Li⁺ intercalation, which are in good agreement with the CV. The first discharge shows a very large specific capacity of *ca.* 910 mA h g⁻¹, whereas the first charge shows a specific capacity of 523 mA h g⁻¹ corresponding to an irreversible capacity loss of ~43%. Such high irreversible capacity loss measured in the first cycle is attributed not only to the formation of the SEI layer caused by the decomposition of carbonate electrolyte but also due to the irreversible reaction of Li⁺ with oxygen-containing functional groups present in the HCS.^[22] It can be observed in the second and fourth charge-discharge curves that there is an additional charge storage between 1.5 and 0.25 V in addition to the Li⁺ intercalation between 0.25 and 0.01 V. This explains the high specific discharge capacity values of 500 and 430 mA h g⁻¹, respectively. These additional specific capacity values are attributed to the highly disordered nature of HCS carbon that promotes Li⁺ storage through other mechanisms such as excess bulk storage, storage in cavities

and nanopores, interfacial/surface storage and the effect of heteroatoms, which gradually decreases during the subsequent cycles stabilizing after the fifth cycle.^[23]

The HCS anode showed excellent capacity retention at increased current rates (Figure 6.4.d). Thus, 173 mA h g⁻¹ and 100 mA h g⁻¹ were achieved at 10C and 30C (measured in the 5th cycle registered at each current rate), which corresponds to a retention of the initial capacity of ~40% and ~24%, respectively. Even after testing at the very high current rate of 100C, 87% of the initial capacity was retrieved when the current rate was set again to 0.1C.

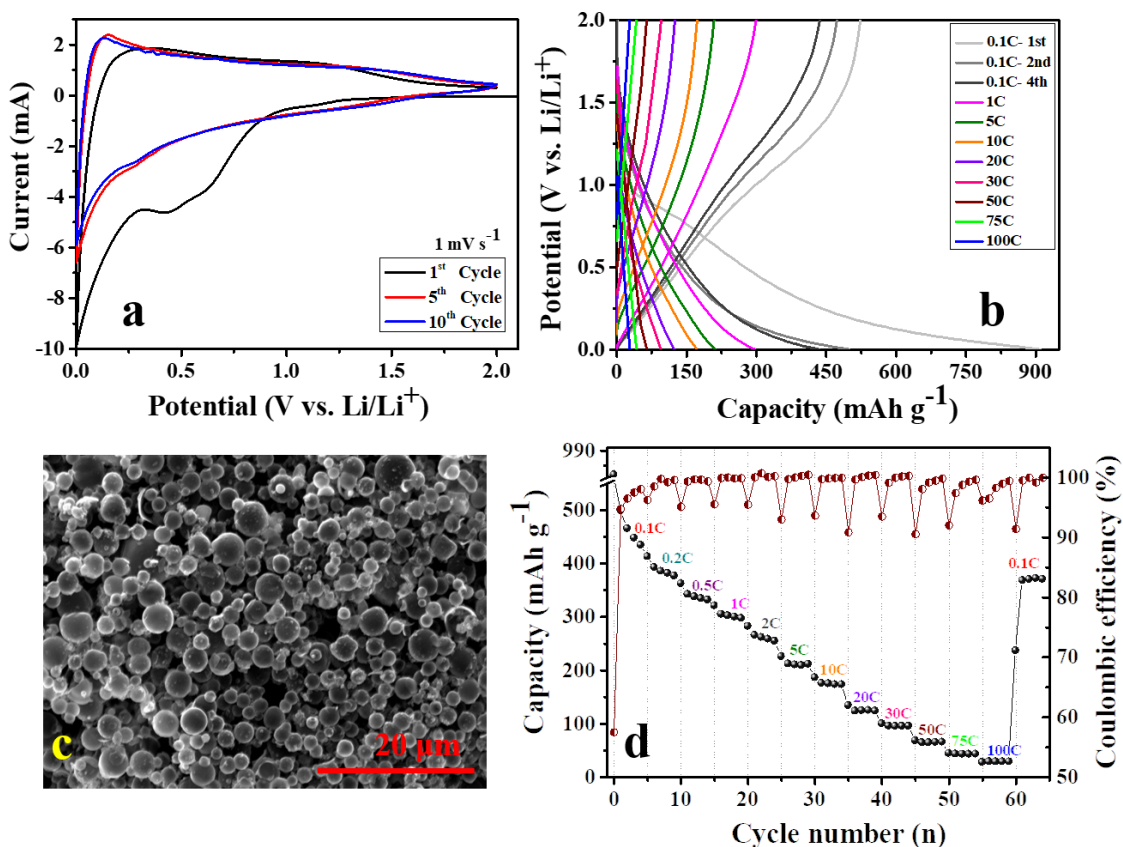


Figure 6.4. Electrochemical characterization of hollow carbon spheres as an anode in half-cell configuration tested between 0.002 and 2.0 V; (a) CVs vs. Li/Li⁺, (b) GC-GD vs. Li/Li⁺, (c) SEM image of HCS electrode surface and (d) rate capability and coulombic efficiency.

The SEM images registered for an anode containing HCS and the binder show that the carbon spheres are well dispersed, which ensures that lithium ions can easily access all the available microporous carbon surfaces (Figure 6.4.c). Additionally, the microstructure of the HCS is

undoubtedly responsible for such advanced rate performance. Both the interparticle space and the spherical voids in the core of the HCSs act as ion-buffering reservoirs, which shorten the diffusion path towards the thin microporous carbon shell.^[12, 13] It is also noteworthy that although the CE in the first cycle was merely 57%, it quickly raised up to 95% in the next cycles and stabilized at a value of 98% in the subsequent cycles and maintained even at the high current rate. Such high CE indicates that this carbon architecture is very capable of enduring the mechanical stress induced at harsh current rates.

6.4.3. Electrochemical performance of cathode (AC)

The capacitive performance of the superactivated carbon was evaluated in the potential range of 1.5-4.2 V vs. Li⁺/Li using LiPF₆ in 1:1 (EC:DMC) as the electrolyte (figure 6.5).

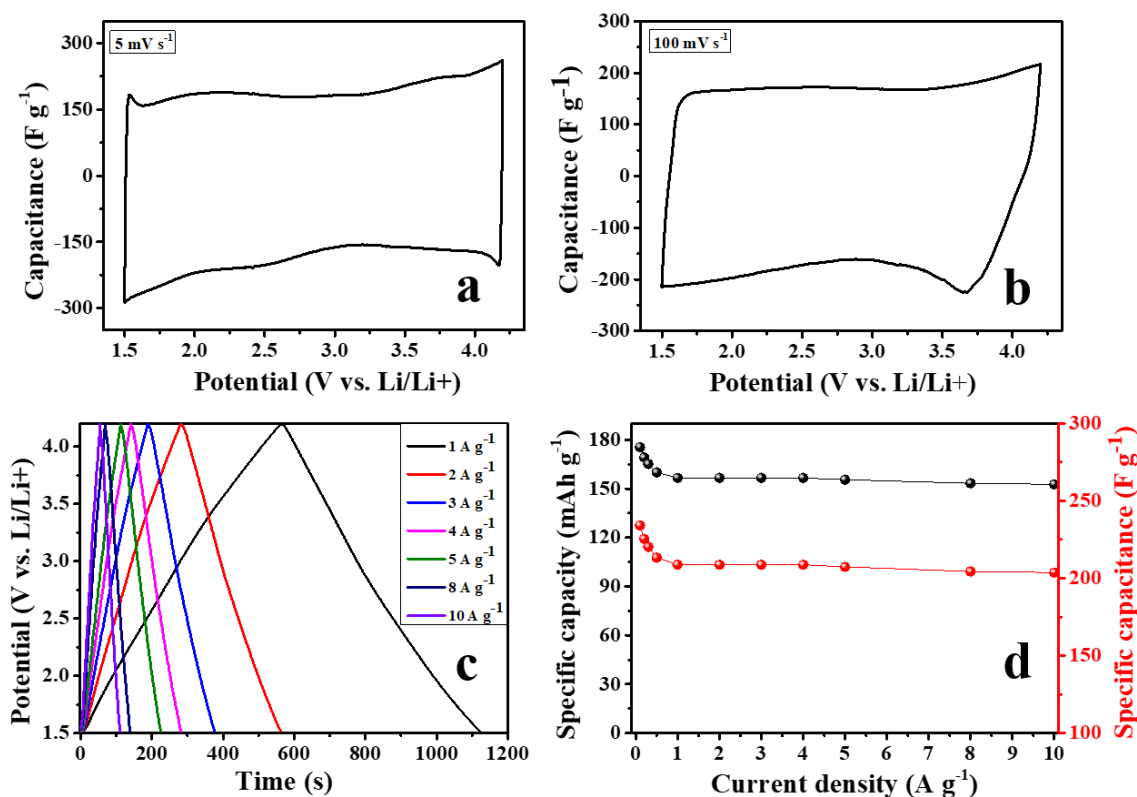


Figure 6.5. Electrochemical characterization of AC cathode in half-cell configuration tested between 1.5 to 4.2 V; (a) & (b) CVs at low and high scan rate of 5 mV s⁻¹ and 100 mV s⁻¹ (vs. Li/Li⁺), (c) GC-GDs vs. Li/Li⁺, and (d) capacity vs. current density (rate performance).

Figures 6.5.a and b include the CV curves registered at 5 and 100 mV s⁻¹. At the lowest scan rate, the plot is square-shaped and very symmetric, evidencing the capacitive behavior of the material. Generally, the open circuit potential of activated carbon cathodes falls in between the potential range of 3.0-3.1 V vs. Li/Li⁺ in a Li-ion electrolyte.

Therefore, the electrical double layer stores ions of opposite charge depending on the potential range, *i.e.* it adsorbs PF₆⁻ anions from 3.0 to 4.2 V and Li⁺ cations from 3.0 to 1.5 V. Even at the high sweep rate of 100 mV s⁻¹ the plot shows the characteristic rectangular-shaped profile, pointing out the fast and effective polarization undergone due to the charge separation at the electrode/electrolyte interface.

Figure 6.5.c shows the GC-GD profiles of the AC cathode at different current densities. The symmetric triangular-shaped GC-GD curves showing almost 100% of CE confirm the purely capacitive behavior of the superactivated carbon. Interestingly, this AC achieved a specific capacitance of 208 F g⁻¹ at 1 A g⁻¹, and retained 203 F g⁻¹ at a high discharge rate of 10 A g⁻¹ (Figure 6.5.d). Such good capacitance retention is favored by the extremely high specific surface area of the AC combined with its hierarchical and interconnected porous network, which allows the unimpeded diffusion of electrolyte ions onto the active carbon surface.^[15, 16] The excellent rate capability observed together with the absence of ohmic drop at the beginning of the discharge branches point out this activated carbon as a promising positive electrode material for LIC systems.

6.4.4. Electrochemical performance of the HCS//AC hybrid LIC

In view of the good performances exhibited by both carbonaceous materials, LIC full cells were assembled using HCS and AC as anode and cathode electrodes, respectively. As a rule of thumb in asymmetric capacitor configuration, there should be charge balance between anode and cathode based on the specific capacity and potential window.^[24] However, this rule does not always result in optimum performance in case of Li-ion capacitor. This is because there is stark difference between the kinetics of faradaic lithiation in anode and non-faradaic PF₆⁻ adsorption on cathode. This difference results in contrasting specific capacity performance of anode and cathode at low and high current densities (Figure 6.6.a), which make it almost impossible to estimate the charge balance effectively only by considering the specific capacity at low current.

Therefore, to evaluate and optimize the electrochemical performance of the full cell as well as to achieve the best possible performance in terms of specific capacity, cycling stability and safety, a variation of the electrode mass ratio was investigated. Thus, four LIC cells were assembled using anode/cathode electrode mass ratios of 1.1, 1.3, 1.7 and 2.0.

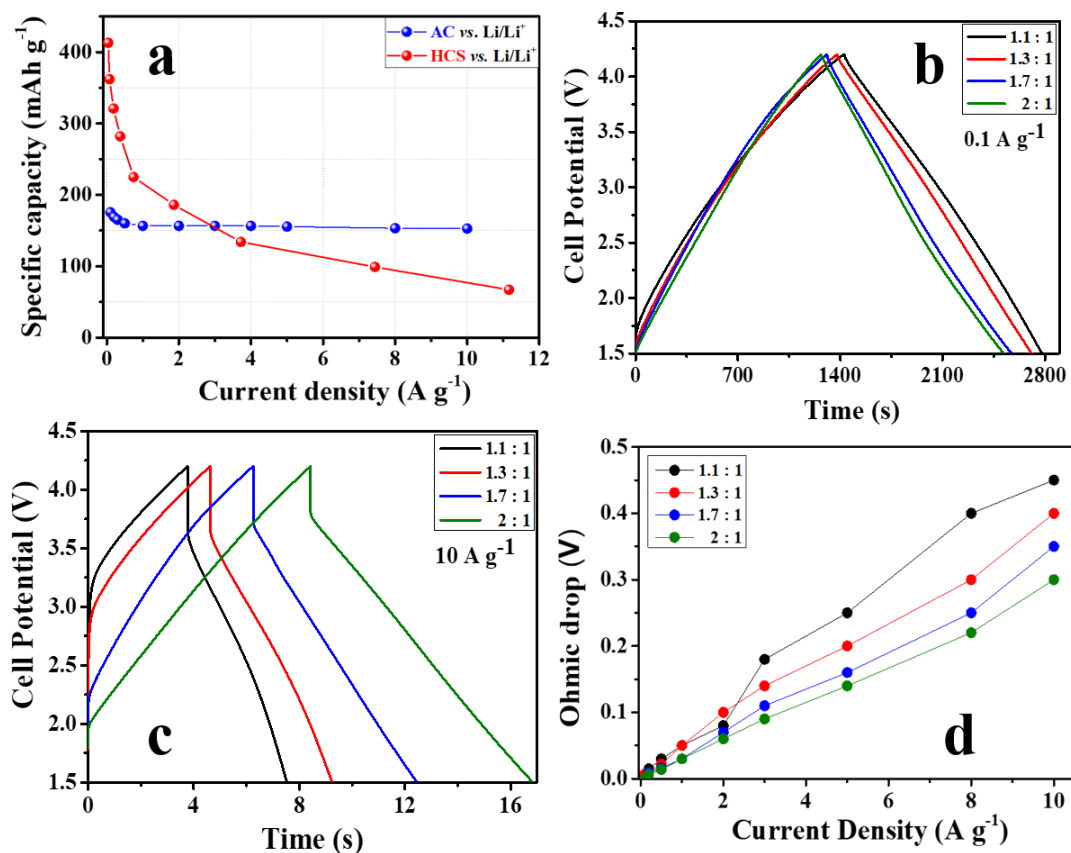


Figure 6.6. (a) Specific capacity of HCS vs. AC at different applied current densities, comparative electrochemical characterization of HCS//AC full cells with different electrode mass ratios: GC-GDs at a current density of (b) 0.1 A g⁻¹ and (c) 10 A g⁻¹, and (d) ohmic drop values with respect to different current densities.

In Figure 6.6.b and c, the GC-GD curves recorded for these four LIC cells at 0.1 and 10 A g⁻¹, respectively, in the 1.5-4.2 V potential range are summarized. At the lowest current density, a progressive decrease of the discharge time was observed when the mass ratio was increased from 1.1:1 to 2:1. This trend is inverted when the current density is increased to 10 A g⁻¹. At this current rate, a prominent decrease in the ohmic drop combined with an increase in the discharge time

(almost twice higher) is observed when the mass ratio is increased from 1.1 to 2.0. The effect of mass ratio is also clearly exhibited from Ohmic drop vs. current density plots of all LIC cells is shown in Figure 6.6.d. The better electrochemical performance of the high mass ratio LIC cell seems to be the deeper utilization (larger operating voltage) of the EDLC electrode during the fast-anionic adsorption-desorption process.

Thus, the LICs with the lower mass ratios seem to be limited by the anode. Figure 6.7.a shows the evolution of the specific capacity with the current density for all the studied LIC cells. At current densities below 1 A g^{-1} the lower mass ratio (1.1:1) LIC cell shows the highest specific capacity, whereas the LIC cell assembled using the 2.0:1 electrode mass ratio shows the best rate capability and the largest value of specific capacity at high current rates, achieving 28 mAh g^{-1} at a current density of 10 A g^{-1} .

Figure 6.7.b represents the comparative Ragone plots calculated for the different LICs. At the lowest current density, the 1.1:1 cell achieved an energy density of 141 Wh kg^{-1} , and this value slightly decreased with the increase of the mass ratio down to the 117 Wh kg^{-1} reached by the 2.0:1 cell. With the increase of the applied current, the differences between the different cells become more noticeable. Indeed, at the highest current density (8 seconds of discharge) the LIC with the highest loading in the negative electrode obtained an energy density as high as 68 Wh kg^{-1} at a power density of 30 kW kg^{-1} .

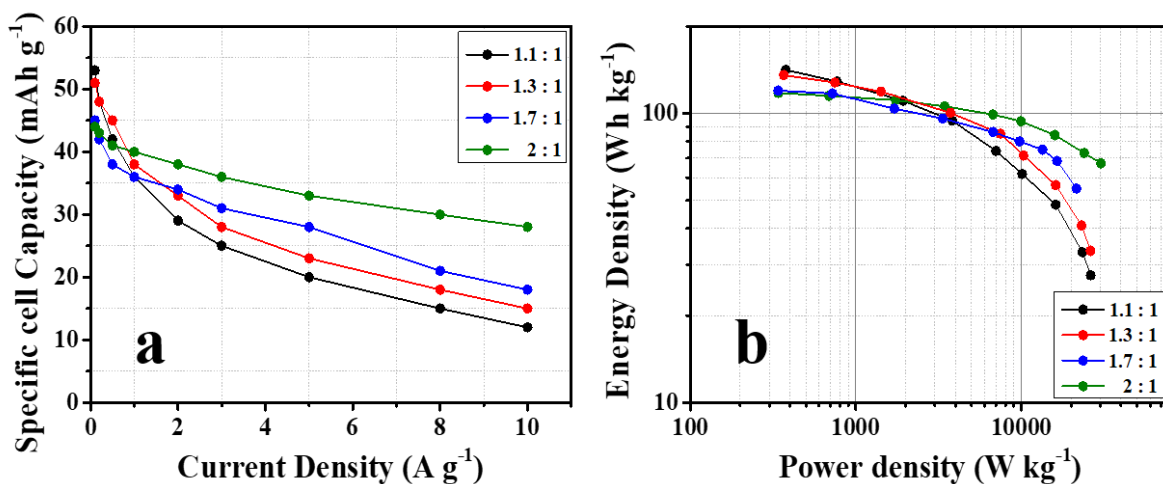


Figure 6.7. Comparative (a) rate capability and (b) Ragone plot of HCS//AC full cells.

In order to get deeper insights into the electrochemical performance of the LICs, the performance of each electrode was monitored. The GC-GD profiles registered for the AC cathodes and the HCS anodes (plotted vs. Li/Li⁺) at a current density of 1 A g⁻¹ are shown in Figure 6.8.a-d.

In the 1.1:1 LIC cell (Figure 6.8.a) the anode potential swing is significantly high (~1.85 V), which evidences a high utilization of the anode for the Li⁺ intercalation-deintercalation process. Therefore, this configuration allows extraction of the highest amount of charge stored thus delivering the highest specific capacity. However, since the anodic process is kinetically much slower than the adsorption-desorption of PF₆⁻ occurring in the positive electrode, this configuration limits the charge extraction at high current densities. This anode potential swing is gradually decreased from ~1.38 to ~0.34 V, as it can be observed from Figures 6.8.b, c, and d, with an increase in anode/cathode mass ratio.

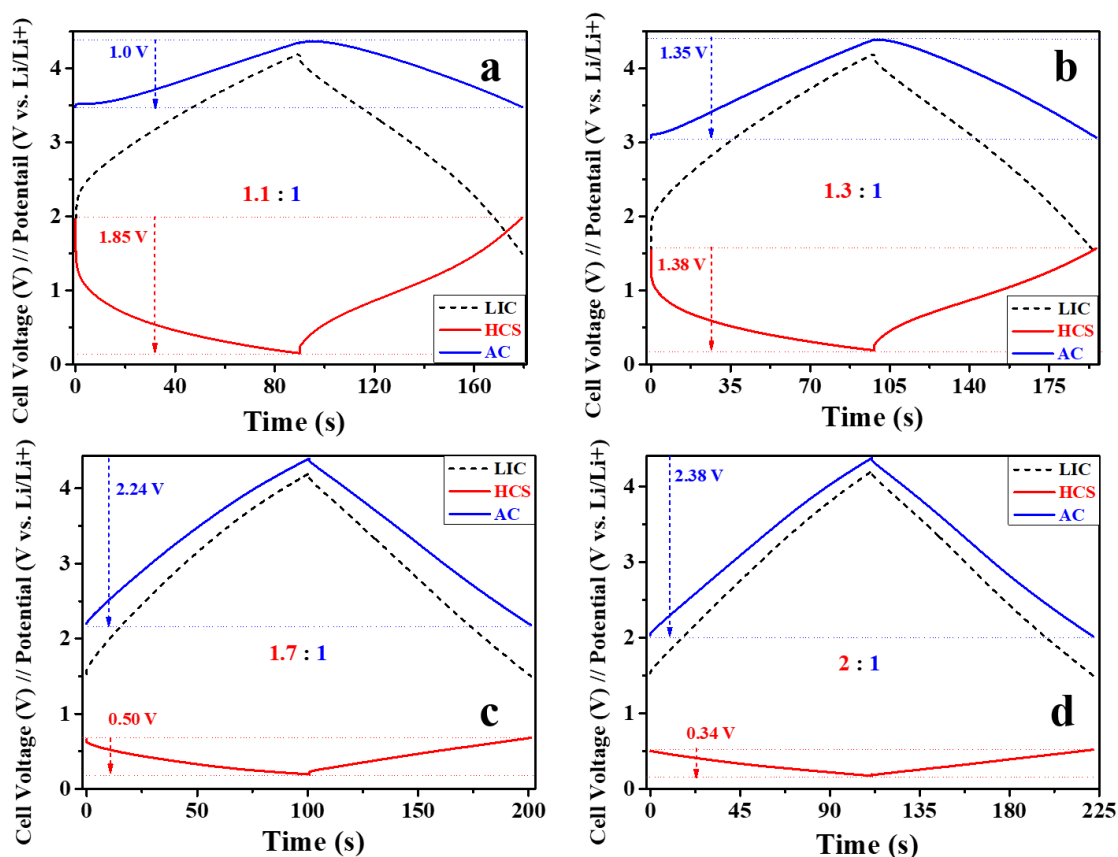


Figure 6.8. Comparative GC-GD profiles of each electrode in LICs with different electrode mass ratios at a current density of 1 A g⁻¹. The cells were run in the 1.5 – 4.2 V potential range.

This decrease results in less utilization of anode capacity but results in less particle volume expansion, electrolyte decomposition and lithium consumption. On its behalf, with the increase in anode/cathode mass ratio, the potential swing in the cathode increased significantly from 1.0 V (1.1:1 cell) to 2.38 V (2:1 cell) thus gradually enhancing the cathode capacity. Therefore, the 2:1 electrode mass ratio guarantees the best rate capability of the cell taking advantage of high utilization of the porous electrode surface. On the other hand, the lower polarization registered in the anode limits the extraction of the anode capacity, and thus, it results in a full cell of less specific capacity. However, concurrently this lower anode polarization avoids the chances of lithium plating, which is beneficial in terms of safety as well as durability. Figure 6.9.a-d shows the GC-GD plots of each electrode as well as the corresponding LIC for all cell combinations at a current density of 10 A g^{-1} . These figures almost mirror the observation revealed from Figure 6.8.a-d with additional evidence.

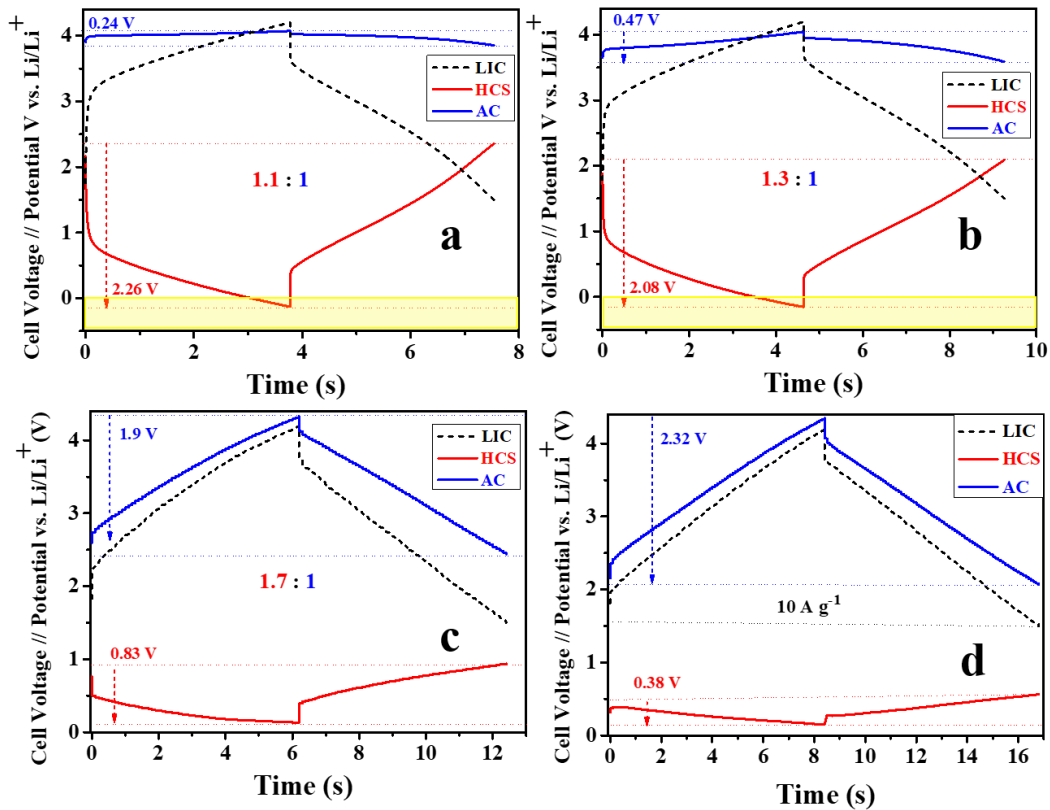


Figure 6.9. GC-GD curves of each electrode in LICs with different electrode mass ratios at an applied current density of 10 A g^{-1} (the yellow colored zone in the Y axis (V) is indicating the lithium plating).

Figure 6.9.d reveals that the 2:1 LIC cell is still fully operative within the 1.5- 4.2 V potential range even at such a high current rate. Moreover, the anode potential swing is still limited to ~ 0.38 V. However, the 1.1:1 LIC cell (Figure 6.9.a) shows a significant increase in anode potential swing up to ~ 2.26 V. This results in severe Li^+ plating on the anode can be seen in 1.1:1 and 1.3:1 LIC cell (yellow color marked area in Figure 6.9.a and b), which not only degrades the cell performance but also aggravates safety issues. The other two mass ratio LIC cells show a gradual decrease in the anode potential swing, thus enhancing the power performance. From all these GC-GD results, it was found that the 2:1 LIC cell shows the best performance in terms of both specific capacity and rate capability. This is due to a steady cathode potential window combined with contended use of the anode *i.e.* CE very close to 100%, which allows the stable performance of the full cell. So, this 2:1 LIC cell is selected to investigate the long-term stability by performing GC-CD cycles at 10 A g^{-1} current density.

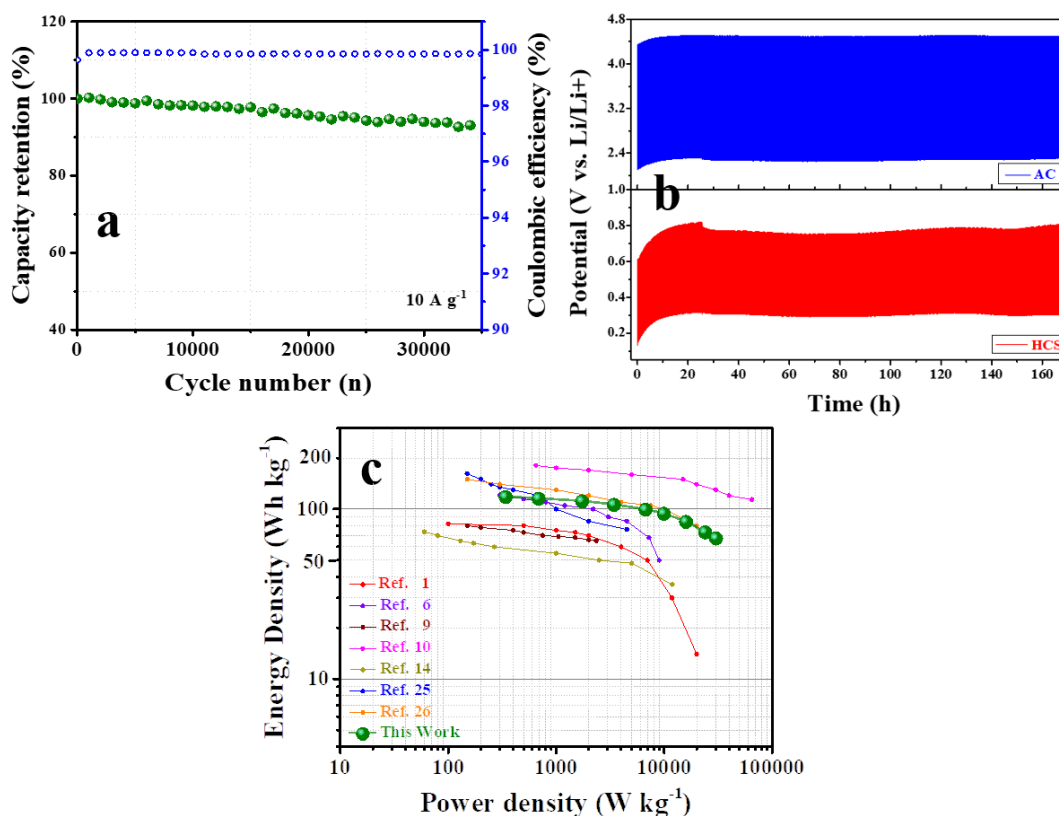


Figure 6.10. Electrochemical performance of the 2:1 LIC: (a) cycling stability; (b) potential swings of each electrode during the cycling test; (c) comparative Ragone plots of our 2:1 LIC and other representative LICs reported in the literature.

The resultant cyclic stability plot in Figure 6.10.a shows that this LIC cell delivered an outstanding cycling performance, retaining 98.7% of its initial capacity after 10,000 cycles, and 92% after 35,000 cycles. The potential swing of each electrode during the cycling test is plotted in Figure 6.10.b. As can be seen, although the cathodic potential window shows a small upward shifting, it remains steady during the whole test, which validates the stable performance of the full cell. For the sake of comparison, Figure 6.10.c collects the Ragone plot of our optimized LIC as well as those of other representative LIC systems recently reported in the literature. It is worth to highlight the excellent energy density measured for our selected LIC, especially in the high-power region in which most of the previously reported LICs suffer from an abrupt decay of their energy densities. [1, 6, 9, 10, 14, 25, 26]

6.5. Conclusions

Micro-sized hollow carbon spheres have been synthesized by an easy procedure. This material exhibits improved performance in the lithium insertion-extraction process especially at very high current rates, which point it as a promising candidate for its use as the negative electrode in LICs. LICs were assembled by coupling this micro-structured hollow carbon spheres *versus* a superactivated micro-mesoporous carbon using different electrode mass ratios. The hollow carbon spheres are able to resist the volume changes during repetitive lithiation-delithiation cycles, while the hierarchical porosity of the superactivated carbon offering very low resistance to ion diffusion assured a good response at high current rates. It was found that the best negative/positive electrode mass ratio in this LIC system is 2:1, the cell delivering a maximum gravimetric energy density of 117 Wh kg⁻¹ at 0.34 kW kg⁻¹ and still 68 Wh kg⁻¹ at an extreme power density of 30 kW kg⁻¹. The robustness of the LIC was confirmed by its remarkable long-term stability over 35,000 cycles with only 8% of capacity decay registered. This outstanding performance makes our proposed LIC a promising energy storage system standing out among its peers.

Bibliography

1. Cao, W. J.; Zheng, J. P. Li-ion capacitors with carbon cathode and hard carbon/ stabilized lithium metal powder anode electrodes. *J. Power Sources* **2012**, *213*, 180-185.
2. Sivakkumar, S. R.; Pandolfo, A. G. Evaluation of lithium-ion capacitors assembled with pre-lithiated graphite anode and activated carbon cathode. *Electrochim. Acta* **2012**, *65*, 280-287.
3. Smith, P. H.; Tran, T. N.; Jiang, T. L.; Chung, J.; Lithium-ion capacitors: electrochemical performance and thermal behavior. *J. Power Sources* **2013**, *243*, 982-992.
4. Luo, Y.; Liu, L.; Lei, K.; Shi, J.; Xu, G.; Li, F.; Chen, J. A nonaqueous potassium-ion hybrid capacitor enabled by two-dimensional diffusion pathways of dipotassium terephthalate. *Chem. Sci.* **2019**, *10*, 2048-2052.
5. Ding, J.; Hu, W.; Paek, E.; Mitlin, D. Review of hybrid ion capacitors: from aqueous to lithium to sodium. *Chem. Rev.* **2018**, *118*, 6457-6498.
6. Jayaraman, S.; Jain, A.; Ulaganathan, M.; Edison, E.; Srinivasan, M.P.; Balasubramanian, R.; Aravindan, V.; Madhavi, S. Li-ion vs. Na-ion capacitors: a performance evaluation with coconut shell derived mesoporous carbon and natural plant based hard carbon. *Chem. Eng. J.* **2017**, *316*, 506-513.
7. Sun, X.; An, Y.; Geng, L.; Zhang, X.; Wang, K.; Yina, J.; Huo, Q.; Wei, T.; Zhang, X.; Ma, Y.; Leakage current and self-discharge in lithium-ion capacitor. *J. Electroanal. Chem.* **2019**, 850, 113386.
8. Ajuria, J.; Redondo, E.; Arnaiz, M.; Mysyk, R.; Rojo, T.; Goikolea, E. Lithium and sodium ion capacitors with high energy and power densities based on carbons from recycled olive pits. *J. Power Sources* **2017**, *359*, 17-26.
9. Kim, J. H.; Kim, J. S.; Lim, Y. G.; Lee, J. G.; Kim, Y. J. effect of carbon types on the electrochemical properties of negative electrodes for li-ion capacitors. *J. Power Sources* **2011**, *196*, 10490-10495.

10. Li, C.; Zhang, X.; Wang, K.; Sun, X.; Ma, Y. High-power lithium-ion hybrid supercapacitor enabled by holey carbon nanolayers with targeted porosity. *J. Power Sources* **2018**, *400*, 468-477.
11. Zhang, H.; Noonan, O.; Huang, X.; Yang, Y.; Xu, C.; Zhou, L.; Yu, C. Surfactant-free assembly of mesoporous carbon hollow spheres with large tunable pore sizes. *ACS Nano* **2016**, *104*, 4579-4586.
12. Liu, T.; Zhang, L.; Cheng, B.; Yu, J. Hollow carbon spheres and their hybrid nanomaterials in electrochemical energy storage. *Adv. Energy Mater.* **2019**, *9*, 1803900.
13. Xu, F.; Tang, Z.; Huang, S.; Chen, L.; Liang, Y.; Mai, W.; Zhong, H.; Fu, R.; Wu, D. Facile synthesis of ultrahigh-surface-area hollow carbon nanospheres for enhanced adsorption and energy storage. *Nat. Commun.* **2015**, *6*, 7221.
14. Sun, X.; Zhang, X.; Liu, W.; Wang, K.; Li, C.; Li, Z.; Ma, Y. Electrochemical performances and capacity fading behaviors of activated carbon/hard carbon lithium ion capacitor. *Electrochim. Acta* **2017**, *235*, 158-166.
15. Díez, N.; Mysyk, R.; Zhang, W.; Goikolea, E.; Carriazo, D. One-pot synthesis of highly activated carbons from melamine and terephthalaldehyde as electrodes for high energy aqueous supercapacitors. *J. Mater. Chem. A* **2017**, *5*, 14619-14629.
16. Panja, T.; Díez, N.; Mysyk, R.; Bhattacharjya, D.; Goikolea, E.; Carriazo, D. A robust NiCo₂O₄/superactivated carbon aqueous supercapacitor with high power density and stable cyclability. *ChemElectroChem* **2019**, *6*, 2536-2545.
17. Zhou, C.; Han, J.; Song, G.; Guo, R. Fabrication of poly(aniline-co-pyrrole) hollow nanospheres with triton x-100 micelles as templates. *J. Polym. Sci. A* **2008**, *46*, 3563-3572.
18. Verma, P.; Maire, P.; Novak, P. A review of the features and analyses of the solid electrolyte interphase in li-ion batteries. *Electrochimica. Acta* **2010**, *55*, 6332-6341.

-
19. Sing, K. S. W.; Everett, D. H.; Haul, R. A. W.; Moscou, L.; Pierotti, R. A.; Rouquerol, J.; Siemieniewska, T. Reporting physisorption data for gas/solid systems. *Pure Appl. Chem.* **1985**, *57*, 603-619.
20. Panja, T.; Bhattacharjya, D.; Yu, J. S. Nitrogen and phosphorus co-doped cubic ordered mesoporous carbon as a supercapacitor electrode material with extraordinary cyclic stability. *J. Mater. Chem. A* **2015**, *3*, 18001-18009.
21. An, S. J.; Li, J.; Daniel, C.; Mohanty, D.; Nagpure, S.; Wood III, D. L. The state of understanding of the lithium-ion-battery graphite solid electrolyte interphase (sei) and its relationship to formation cycling. *Carbon* **2016**, *105*, 52-76.
22. Frackowiak, E.; Gautier, S.; Gaucher, H.; Bonnamy, S.; Beguin, F. Electrochemical storage of lithium in multiwalled carbon nanotubes. *Carbon* **1999**, *37*, 61-69.
23. Kaskhedikar, N. A.; Maier, J.; *Adv. Mater.* **2009**, Lithium storage in carbon nanostructures. *21*, 2664–2680.
24. Shao, Y.; El-Kady, M. F.; Sun, J.; Li, Y.; Zhang, Q.; Zhu, M.; Wang, H.; Dunn, B.; Kaner, R. B. Design and mechanisms of asymmetric supercapacitors. *Chemical Reviews* **2018**, *118*, 9233-9280.
25. Sennu, P.; Aravindan, V.; Ganesan, M.; Lee, Y. G.; Lee, Y. S. Biomass-derived electrode for next generation lithium-ion capacitors. *ChemSusChem* **2016**, *9*, 849-854.
26. Arnaiz, M.; Nair, V.; Mitra, S.; Ajuria, J. Furfuryl alcohol derived high-end carbons for ultrafast dual carbon lithium ion capacitors. *Electrochim. Acta* **2019**, *304*, 437-446.
27. Laheear, A.; Przygocki, P.; Abbas, Q.; Beguin, F. Appropriate methods for evaluating the efficiency and capacitive behaviour of different types of supercapacitors. *Electrochem. Commun.* **2015**, *60*, 21-25.

CHAPTER – 7

Conclusions and perspectives

7.1. Conclusions

The thesis has presented different approaches that aimed to improve the electrochemical performance of supercapacitors in different configurations, such as EDLCs, asymmetric and hybrid LIC system. The following descriptions can be concluded from the individual works which were performed to establish the specific objectives of the thesis.

7.1.1. EDLC System

In this work, a straightforward synthetic approach has been developed for the preparation of spherical nanostructured carbons with high specific surface area from the polycondensation polymerization reaction of the resorcinol and formaldehyde precursor in presence of an acid catalyst and its electrochemical characteristics were studied in different electrolytes.

- The presence of an acid catalyst (FeCl_3) fasten the polycondensation process and induce the formation of an interconnected microporous network along the carbon framework, which may maximize the electrical double layer formation and enhance the ions movement through the whole surface of the carbon.
- The electrochemical double-layer capacitive storage capacity of this material was evaluated in different electrolytes, such as aqueous (alkaline and neutral) and organic medium. Selecting different electrolytes based on their operative potential window not only enhances the overall performance but also has a lot of impact on its long-term stability.
- This material shows the best electrochemical performance in aqueous electrolytes due to the fast-kinetic response of electrolyte ions into pores, whereas the organic electrolyte exhibited the best energy-power output because of their wide potential window.
- A more accessible ultramicroporous surface area of the carbon can be utilized in EDLCs by selecting the electrolyte according to the appropriate ionic sizes which can boosts the surface-controlled kinetics during prolong stability performance.

7.1.2. Aqueous asymmetric system

In this work, we have investigated the performance of a robust AAS cell assembled using a proprietary ultrahigh specific surface area carbon as the negative electrode and a nanostructured NiCo_2O_4 as the positive electrode (a combination of EDLC and faradaic type materials), and the impact of the electrode mass balance on the electrochemical performance of the system.

- This electrochemical study evidenced the importance of the hierarchical structures of the active materials to maintain good capacity retention at high current densities.
- The mass balance between positive and negative electrodes showed a huge impact on the electrochemical performance of the resultant advanced hybrid full cells. The mass balance allows controlling the potential span and degree of utilization of each electrode within the asymmetric capacitor.
- The optimization of the electrodes mass balance within the AAS devices led not only to both excellent energy and power densities but also to significant cycling stability.

7.1.3. Hybrid LIC System

In this section, we have developed different hard carbons and activated carbons as a negative and positive electrode for the study of the dual carbon LIC cell. We have performed two sets of studies with the objective to increase the overall electrochemical performance of the full LIC system.

- In the first approach, we demonstrated that the high energy density along with the power density can be achieved by the careful optimization of the full cell operative potential window. For the electrode material, we synthesized a spongy shaped hard carbon and high surface area activated carbon by using a simple method. This study is not only helpful to obtain a safe potential window but also useful for improved overall performance.
- In the second approach, we demonstrated that prolong cycling stability can be achieved by the optimization of mass balance. In this work, we have developed a polymer derived hollow carbon spheres as the negative electrode, which can resist the volume changes during repetitive lithiation-delithiation cycles, while the hierarchical porosity of the superactivated carbon as positive electrode offering very low resistance to ion diffusion

assured a good response at high current rates. The robustness of the LIC was confirmed by its remarkable long-term stability.

- From those above-mentioned approaches, the study was focused to find out excellent electrode material and also a very safe operational method to increase the specific energy density in hybrid LIC full cell. Besides, the obtained results were evidencing the effect on overall electrochemical cell performance after considering those strategies for the development of the full LIC cell.

The Ragone plot in Figure 7.1 summarizes the energy to power values measured for the different systems evaluated in this thesis. In order to study different segments of supercapacitor configuration, the objective of the thesis was to focus on the development of the electrode material along with the strategic cell design to increase the specific energy. Besides, it is worth mentioning that these detailed studies also signify the approach made here in this thesis has a huge impact on the safe handling issues for prolonging applications purpose. However, considering costs as well as stability and reproducibility, dual carbon hybrid LIC system is exhibiting the promising future to compete against the second-generation battery.

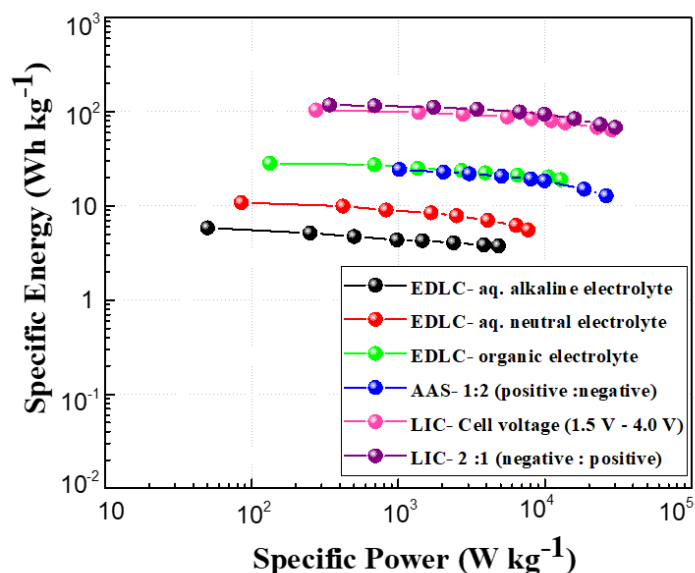


Figure 7.1. Comparative Ragone plots of different supercapacitors based on the studies made in this thesis.

7.2. Perspectives

Recommendations for future research work are discussed as follows.

- Apart from Iron chloride, several other transition metal salts can be used as acid catalysts for the synthesis of graphitic carbon. Most of them are not yet fully investigated to understand their effect on the reaction time and temperature during catalytic activation. The EDL results achieved in this thesis showed better capacitive performance in aqueous alkaline electrolyte compared to aqueous neutral and organic electrolyte due to the microporous nature of the synthesized carbon. Therefore, a detailed study on the role of different acid catalysts towards the development of the new graphitic carbon with tailored porosity might give a direction to understand the relationship of the porous textural properties with different electrolyte ions.
- In this thesis, cobalt is used as one of the binary metal compounds for its excellent electrochemical behaviour for the asymmetric supercapacitors. But compared to toxic and expensive cobalt, other transition metal oxides, like manganese, also can be an attractive alternative as inexpensive and non-toxic metal in combination with nickel to improve the cell voltage, energy, and power densities. Meanwhile, a lightweight, flexible asymmetric cell design can be developed using solid polymer electrolyte. Thus, solid-state asymmetric supercapacitors with high energy and power densities will increase the future research attention for their promising applications in stretchable and wearable electronics.
- In this thesis, the electrochemical pre-lithiation process is utilized for the dual carbon hybrid LIC system by using Lithium metal as an additional electrode in the pre-lithiation step. However, this lab-scale confined strategy is not suitable for large-scale production and it needs to be considered for successful commercialization. The recent advancement of the novel electrode materials and sacrificial cell components as an internal source of Li-ions hold the excellent potential to compensate for the first cycle irreversibility. Thus, there is a huge prospect for future research to resolve this issue by not through developing new materials but also optimizing the overall cell design during the fabrication of hybrid LIC system.

LIST OF TABLES

Table 1.1. Comparative features of the electrochemical capacitors and lithium ion batteries.

Table 1.2. Details of different commercial supercapacitors available in market.

Table 1.3. Comparative specific capacitance values of transition metal oxides reported in literature.

Table 1.4. Relevant properties of ions commonly used in aqueous electrolytes.

Table 1.5. Comparative parameters of the different supercapacitor configurations.

Table 1.6. Different parameters for state-of-art of commercial LIC products.

Table 2.1. The details of the general materials used for the experiments.

Table 4.1. Comparative electrochemical parameters calculated for the different AAS devices

Table 4.2. Summary of some representative electrochemical values reported elsewhere for previous Ni-Co-Oxide/hydroxide based asymmetric supercapacitor together with the results obtained in the present study.

Table 5.1.: Textural information obtained from N₂ adsorption-desorption measurement.

Table 5.2. Summarizes the electrochemical performance of this 1.5-4.0V LIC, compared with other recently reported results in similar dual carbon LIC devices.

LIST OF FIGURES

Figure 1.1. Global energy consumption by countries sourced from Global Energy Statistical yearbook 2020. (Enerdata. 2020, data up to 2019).

Figure.1.2. Ragone Plot of different energy storage devices (Review article by Simon and Gogotsi, 2008).

Figure.1.3. Classification of electrochemical capacitors based on materials, cell configurations and electrolytes.

Figure.1.4. Schematic configuration and basic charge/discharge mechanism of the electrochemical capacitor.

Figure 1.5. Different models of the EDL at a positively charged surface, (a) the Helmholtz model, (b) the Gouy–Chapman model, and (c) the Stern model, showing the IHP and OHP.

Figure 1.6. Schematics of the charge storage processes occurring at (a) electrical double-layer capacitive, (b) pseudocapacitive, and (c) battery-type electrodes.

Figure 1.7. Comparative characteristics of the different types charge storage materials, (a) electrical double-layer capacitive, (b) surface redox pseudocapacitance, (c) intercalation pseudocapacitance, and (d) batteries.

Figure 1.8. (a) Estimated future addressable market of EDLC (Skeleton Technological Group), and (b) commercially available supercapacitor cells [Maxwell 3400 F (top left), Skeleton 3200 F (top right), Ioxus 3000F (bottom left), and JM Energy 3300 F (bottom right)].

Figure 1.9. Fully operative supercapacitor trams in Taiwan and Spain.

Figure 1.10. Pore classification of different pore size parameters.

Figure 1.11. Different carbon structures used in EDLCs.

Figure 1.12. Hierarchical porosity distribution outline in activated carbons.

Figure 1.13. Schematic representation of the templating synthetic approach.

Figure 1.14. Schematic representation of several techniques involved in the production of graphene-based materials.

Figure 1.15. Schematic representation of the potential window span for symmetric and asymmetric capacitor.

Figure 1.16. Hybridization of EDLC and Battery system to develop metal ion capacitors.

Figure 1.17. Textural pattern of (a) graphite, (b) soft carbon, and (c) hard carbon.

Figure 1.18. Structural illustration of the lithium consumption in carbon layer and the typical charge/discharge profile of (a) graphite and (b) hard carbon.

Figure 1.19. Typical voltage profiles of an EDLC and a hybrid supercapacitor (Left), and individual galvanostatic charge-discharge profile of a dual carbon LIC (hard carbon//AC).

Figure 2.1. Working range of various microscopy techniques; CTEM: conventional transmission electron microscopy; HRTEM: high resolution electron microscopy.

Figure 2.2. Schematic representation showing the core component of a SEM.

Figure 2.3. FEI Quanta 200 FEG SEM (Thermofischer).

Figure 2.4. Schematic representation of the core components of an TEM.

Figure 2.5. FEI Tecnai G2 F20 S-TWIN TEM (Thermofischer).

Figure 2.6. Schematic representation of the core components of X-ray diffractometer.

Figure 2.7. Bruker D8 discover XRD system.

Figure 2.8. Schematic representation of the basic Raman spectroscopy configurations.

Figure 2.9. Horiba Ultima Expert 2 ICP-OES system.

Figure 2.10. Different types of adsorption isotherms as classified by IUPAC.

Figure 2.11. Schematic representation of different types of hysteresis pattern and the corresponding pore structures.

Figure 2.12. (a) i-t plot and (b) cyclic voltammograms and the respective equivalent circuits of an ideal supercapacitor. Cyclic voltammograms of a supercapacitor (c) with series resistance (R_s), and of (d) with series and leak resistance (R_l).

Figure 2.13. Illustration of Nyquist diagram.

Figure 2.14. Three electrode configurations in a beaker cell (left) and Swagelok™ T-type cell for testing symmetric and asymmetric supercapacitor.

Figure 2.15. Two electrode configurations in a Swagelok™-type cell.

Figure 2.16. Three electrode Swagelok™-type cell configurations for testing hybrid Lithium ion capacitor.

Figure 3.1. (a) XRD profile, (b) Raman spectra, (c) low magnification SEM image, and (d) EDX spectra of the PCS.

Figure 3.2. (a) SEM and (b) TEM image of the microspherous PCS, (c) high magnification TEM image of the outer surface of the PCS, (d) N₂ adsorption-desorption isotherm, and (e) pore size distribution curve.

Figure 3.3. Three electrode Swagelok™-type cell configurations for testing symmetric EDLC.

Figure 3.4. Cyclic voltammograms at a scan rate of 5 mV s⁻¹ and galvanostatic charge-discharge profiles at the current density of 0.1 A g⁻¹ for the tested EDLCs in different electrolytes, (a and b) 6M KOH, (c and d) 1M Li₂SO₄, and (e and f) 1.5M TEABF₄. Cell voltage (black dashed line) vs. potential evolution of individual electrodes: positive electrode in red and negative electrode marked in blue.

Figure 3.5. Cyclic voltammograms at different scan rates and galvanostatic charge-discharge profiles at different current densities for the tested EDLCs in different electrolytes, (a and d) 6M KOH, (b and e) 1M Li₂SO₄, and (c and f) 1.5M TEABF₄.

Figure 3.6. Comparative (a) rate capability, (b) Nyquist plots (registered after the rate performance evaluation) (c) Ragone plots, and (d) cyclic stability performance for the tested EDLCs in different electrolytes.

Figure 4.1. (a) SEM image (inset: higher magnification SEM image of the sphere surface), (b) & (c) TEM image showing the assembly of small crystalline nanoparticles into nano-thorn (inset: high magnification TEM image) and (d) EDX spectra recorded for this NiCo₂O₄ material.

Figure 4.2. (a) XRD profile and (b) Nitrogen adsorption desorption isotherms (inset: pore size distribution curve) of NiCo₂O₄.

Figure 4.3. (a) Nitrogen adsorption desorption isotherms (inset: pore size distribution curve), (b) SEM image and (c) TEM image registered for the SAC, (d) XRD pattern (inset: Raman spectrum).

Figure 4.4. (a) CV curve registered at 5 mV s⁻¹ and (b) at higher sweep rates (10-100 mV s⁻¹) for the NiCo₂O₄. (c) Galvanostatic discharge curves recorded at indicated current densities (1-20 A g⁻¹) and (d) Capacity evolution vs. Current for the NiCo₂O₄.

Figure 4.5. (a) CV curves registered at indicated sweep rates, (b) charge-discharge curve at labeled current densities, inset shows a magnified view of the 0.8-1.0V region, and (c) specific capacitance evolution of SAC sample at different current rates.

Figure 4.6. (a) Comparative CV profiles at low potential scan rate of 5 mV s⁻¹ and (b) high scan rate of 100 mV s⁻¹, (c) Comparative discharge curve at current density of 1A g⁻¹ and (d) rate capability of AAS device [NiCo₂O₄//SAC].

Figure 4.7. (a) Plots of cumulative ESR values, (b) comparative Ragone plots, (c) cycling stability and (d) Stability tests performed under floating conditions for the optimized AAS using positive: negative 1:2 ratio and (inset GC-GD registered at indicated times during the floating tests. of 1:2 AAS device [NiCo₂O₄//SAC] measured at 5 A g⁻¹.

Figure 4.8. (a) CV curves registered at 5 mV s⁻¹, (b) GC-GD recorded at current density 1 A g⁻¹, (c) cell specific capacity evolution, and (d) Nyquist plot for the 1:2 AAS device [NiCo₂O₄//SAC] (Red) and other AAS [NiCo₂O₄//Norit] assembled using commercially available activated carbon (purple).

Figure 5.1. (a) SEM image and (b) TEM image, (c) Nitrogen adsorption–desorption isotherms (inset: pore size distribution curve) and (d) XRD pattern (inset: Raman spectrum) of the SHC).

Figure 5.2. (a) SEM image, (b) TEM image, (c) N₂ adsorption-desorption isotherms (inset: pore size distribution curve) and (d) Raman spectrum registered for the PAC.

Figure 5.3. Electrochemical characterization of SHC as anode in half-cell configuration tested between 0.002 and 2.0 V; (a) CVs vs. Li/Li⁺, (b) GC-GD vs. Li/Li⁺, and (c) rate capability and coulombic efficiency.

Figure 5.4. Electrochemical characterization of PAC cathode in half-cell configuration tested between 1.5 to 4.2 V vs. Li/Li⁺; (a) CVs at different scan rates from 5 mV s⁻¹ to 100 mV s⁻¹, (c) GC-GDs, and (c) capacity and capacitance values vs. current densities.

Figure 5.5. (a) Specific capacity of the SHC vs. PAC at different applied current densities, and (b) GC-GD profiles of each electrode at different current density of 5 A g⁻¹ of 1.5-4.2 V LIC cell (yellow colored marked zone indicates Li Plating).

Figure 5.6. Comparative GC-GD profiles of each electrode in SHC//PAC full LICs measured at different current densities of 0.1, 1 and 10 A g⁻¹, (yellow colored marked zone indicates Li Plating).

Figure 5.7. Comparative (a) rate capability and (b) Ragone Plot of SHC//PAC full cells by applying the variation in the potential range [(1.5-4.2V), (1.5-4.0V), (2.0-4.0V)]; (b) cycling stability at the current density of 5 A g⁻¹ and potential swings of each electrode of the (c) 1.5-4.0V and (d) 2-4V LIC cells during the cycling test.

Figure 6.1 Schematic diagram of the synthesis process of hollow polymer spheres (HPS) and hollow carbon spheres (HCS).

Figure 6.2. (a) SEM images of HPS and (b) HCS obtained after the pyrolysis of HPS, (c) XRD pattern recorded for HCS (inset: Raman spectrum registered for HCS), (d) low magnification TEM image of HCS and (e) high magnification TEM image of HCS outer surface, (f) N₂ adsorption-desorption isotherms registered for HCS.

Figure 6.3. (a) SEM image, (b) TEM image, (c) N₂ adsorption-desorption isotherms (inset: pore size distribution curve) and (d) Raman spectrum registered for the activated carbon (AC).

Figure 6.4. Electrochemical characterization of hollow carbon spheres as an anode in half-cell configuration tested between 0.002 and 2.0 V; (a) CVs *vs.* Li/Li⁺, (b) GC-GD *vs.* Li/Li⁺, (c) SEM image of HCS electrode surface and (d) rate capability and coulombic efficiency.

Figure 6.5. Electrochemical characterization of AC cathode in half-cell configuration tested between 1.5 to 4.2 V; (a) & (b) CVs at low and high scan rate of 5 mV s⁻¹ and 100 mV s⁻¹ (*vs.* Li/Li⁺), (c) GC-GDs *vs.* Li/Li⁺, and (d) capacity *vs.* current density (rate performance).

Figure 6.6. (a) Specific capacity of HCS *vs.* AC at different applied current densities, comparative electrochemical characterization of HCS//AC full cells with different electrode mass ratios: GC-GDs at a current density of (b) 0.1 A g⁻¹ and (c) 10 A g⁻¹, and (d) ohmic drop values with respect to different current densities.

Figure 6.7. Comparative (c) rate capability and (d) Ragone plot of HCS//AC full cells.

Figure 6.9. GC-GD curves of each electrode in LICs with different electrode mass ratios at an applied current density of 10 A g⁻¹ (the yellow colored zone in the Y axis (V) is indicating the lithium plating).

Figure 6.10. Electrochemical performance of the 2:1 LIC: (a) cycling stability; (b) potential swings of each electrode during the cycling test; (c) comparative Ragone plots of our 2:1 LIC and other representative LICs reported in the literature.

Figure 7.1. Comparative Ragone plots of different supercapacitors based on the studies made in this thesis.

LIST OF ABBREVIATIONS

AAS	Aqueous Asymmetric Supercapacitor
AC	Activated Carbon
ACN	Acetonitrile
AM	Active mass
BET	Brunauer, Emmett and Teller
CDC	Carbide Derived Carbon
CNT	Carbon Nanotubes
CE	Coulombic efficiency
CV	Cyclic Voltammetry
CVD	Chemical Vapor Deposition
DFT	Density Functional Theory
DMC	Dimethyl carbonate
EC	Ethylene carbonate
EMC	Ethyl Methyl Carbonate
EM	Electron Microscopy
EV	Electric Vehicle
EDX	Energy Dispersive X-ray
EDLCs	Electrochemical Double Layer Capacitors
EIS	Electrochemical Impedance Spectroscopy
GC-GD	Galvanostatic charge/discharge
GF	Glass fiber

List of Abbreviation

GO	Graphene Oxide
rGO	reduced Graphene Oxide
HC	Hard Carbon
HEV	Hybrid Electric Vehicle
HRTEM	High-Resolution Transmission Electron Microscopy
IL	Ionic Liquid
IEA	International Energy Agency
IUPAC	International Union of Pure and Applied Chemistry
LIC	Lithium Ion Capacitor
LIB	Lithium Ion Battery
MWCNT	Multi Wall Carbon Nanotubes
NLDFT	Non-Local Density Functional Theory
NIC	Sodium Ion Capacitor
OCP	Open Circuit Potential
PCA	Polymer Derived Activated Carbon
PCS	Porous Carbon Spheres
PSD	Pore Size Distribution
SAC	Super Activated Carbon
SC	Supercapacitor
SEM	Scanning Electron Microscopy/Microscope
SEI	Solid Electrolyte Interphase
SHC	Spongy Hard Carbon
SSA	Specific Surface Area

SWCNT	Single Wall Carbon Nano Tubes
XRD	X-ray Diffraction

LIST OF CONTRIBUTIONS

Publications in International Journals

Panja, T.; Díez, N.; Mysyk, R.; Bhattacharjya, D.; Goikolea, E.; Carriazo, D. A Robust NiCo₂O₄/Superactivated Carbon Aqueous Supercapacitor with High Power Density and Stable Cyclability. *ChemElectroChem* **2019**, *6*, 2536-2545.

Panja, T.; Ajuria, J.; Díez, N.; Bhattacharjya, D.; Goikolea, E.; Carriazo, D. Fabrication of High-performance Dual Carbon Li-ion Hybrid Capacitor: Mass Balancing Approach to Improve the Energy-Power Density and Cycle Life. *Scientific Reports* **2020**, *10*, 1-11.

Oral Presentations

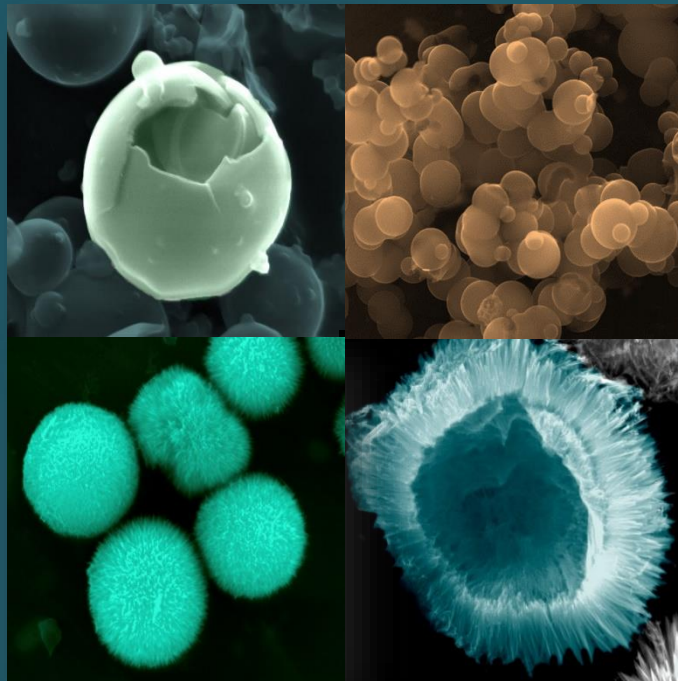
Panja, T.; Díez, N.; Mysyk, R.; Bhattacharjya, D.; Goikolea, E.; Carriazo, D. A Robust NiCo₂O₄/Superactivated Carbon Aqueous Supercapacitor with High Power Density and Stable Cyclability. *Power Our Future (POF) 2019, Vitoria-Gasteiz, Basque Country*.

Poster Presentations

Panja, T.; Díez, N.; Mysyk, R.; Bhattacharjya, D.; Goikolea, E.; Carriazo, D. Nanostructured Nickel Cobalt Oxide for High Power and Energy Density Aqueous Asymmetric Supercapacitor. *Electrochemistry 2018, Ulm, Germany*.

Panja, T.; Ajuria, J.; Díez, N.; Bhattacharjya, D.; Goikolea, E.; Carriazo, D. Advanced Nanostructured Carbons for Lithium Ion Capacitors. *International Symposium on Enhanced Electrochemical Capacitors (ISEECap) Meeting 2019, Nantes, France*.

The electrochemical capacitors or supercapacitors are envisioned as potential next-generation energy storage systems because of their excellent storage capacity, power density, and long-term durability. However, all these advantages are overshadowed by their poor energy density. Thus, this thesis aims to achieve a high-energy supercapacitor device without compromising its power performance to make them more commercially viable for many applications. The research work is associated with the improvement of the supercapacitors in different device configurations, such as EDL, asymmetric, and hybrid LIC systems by integration of advanced material and cell design. The results obtained from the studies of different supercapacitor systems demonstrate that the variation in electrode mass, cell voltage, and electrolyte has a huge impact on the overall electrochemical performance, stability, life expectancy, and safety of the device. Therefore, careful optimization of cell design and advancement in electrode materials retains the high importance driving factors of the supercapacitors for the development of future energy storage technology.



2020